

Connecting chirality and spin in electronic devices

Xu Yang

2020



**university of
 groningen**

faculty of science
 and engineering

zernike institute for
 advanced materials

Zernike Institute PhD thesis series 2020-16

ISSN: 1570-1530

ISBN: 978-94-034-2894-9 (eBook)

ISBN: 978-94-034-2895-6 (Book)

© 2020 Xu Yang

The work described in this thesis was performed in the research group Physics of Nanodevices of the Zernike Institute for Advanced Materials at the University of Groningen, the Netherlands. This work was supported by the Zernike Institute for Advanced Materials.

Cover art: The concepts of chirality and spin illustrated as a spiral and a spinning top.

Cover design: Joanna Smolonska

Printed by: Lovebird design



university of
 groningen

Connecting chirality and spin in electronic devices

PhD thesis

to obtain the degree of PhD at the
 University of Groningen
 on the authority of the
 Rector Magnificus Prof. C. Wijmenga
 and in accordance with
 the decision by the College of Deans.

This thesis will be defended in public on
 Friday 18 September 2020 at 11.00 hours

by

Xu Yang

born on 26 November 1990
 in Gansu, China

Supervisors

Prof. C.H. van der Wal

Prof. B.J. van Wees

Assessment Committee

Prof. B.L. Feringa

Prof. H.S.J. van der Zant

Prof. H.M. Yamamoto

to my parents

Contents

1	Introduction – Unraveling chirality-induced spin selectivity (CISS)	1
1.1	Nature is chiral	2
1.2	A spintronics vision for the future	3
1.3	The rise of CISS	3
1.4	Open questions	6
1.5	This thesis	6
1.6	Guideline to readers	7
	Bibliography	8
2	A symmetry perspective of chirality, spin, and CISS	13
2.1	Symmetry and chirality	14
2.1.1	Molecular symmetry operations	14
2.1.2	Fundamental symmetries of space and time	16
2.1.3	True chirality	17
2.2	Spin-related symmetry implications	18
2.2.1	The Kramers degeneracy theorem	18
2.2.2	Symmetry restrictions on electronic energy band	19
2.2.3	Spin–charge conversion by symmetry breaking	19
2.2.4	The Onsager reciprocity	22
2.3	Chirality-induced physical phenomena	23
2.3.1	Optical rotation and circular dichroism	23
2.3.2	Generalized helicity-induced dichroism	24
2.3.3	Magneto-chiral effects	25
2.4	CISS experiments revisited	26
2.4.1	Photoemission experiments	26
2.4.2	Magnetotransport experiments	26

2.4.3	The role of substrate	27
2.5	Appendices	28
	Bibliography	32
3	Spin-dependent electron transmission model for chiral molecules in mesoscopic devices	39
3.1	An electron transmission model for chiral molecules	41
3.1.1	Reciprocity theorem and spin-flip reflection by chiral molecules	42
3.1.2	Matrix formalism and barrier-CISS center-barrier (BCB) model for CISS molecules	44
3.2	Discussion	46
3.2.1	Two-terminal geometries	46
3.2.2	Four-terminal geometries and experimental designs	49
3.3	Conclusion	55
3.4	Reply to Comment	56
3.5	Appendices	60
	Bibliography	70
4	Detecting chirality in two-terminal electronic nanodevices	73
4.1	Transport matrix formalism beyond Landauer formula	74
4.1.1	Spin-charge conversion in a chiral component	75
4.1.2	Spin-charge conversion in a magnetic tunnel junction	77
4.2	Origin of MR – energy-dependent transport and energy relaxation	77
4.2.1	No MR in the linear response regime	77
4.2.2	Emergence of MR in nonlinear regime	79
4.3	Chiral spin valve	82
4.4	Discussion	84
4.5	Appendices	84
	Bibliography	96
5	Circuit-model analysis for spintronic devices with chiral molecules as spin injectors	99
5.1	Circuit-model analysis	100
5.2	Discussion	105
5.3	Conclusion	107
5.4	Appendices	108
	Bibliography	111

6	Highly anisotropic and nonreciprocal charge transport in chiral van der Waals Tellurium	115
6.1	Highly anisotropic charge transport in Tellurene	116
6.1.1	Angle-resolved mesoscopic conductance	116
6.1.2	Inhomogeneity and chirality effects in 2D conduction	119
6.1.3	Anisotropic temperature dependence	121
6.2	Nonreciprocal charge transport in Tellurene	122
6.2.1	Bias dependence of nonlinear charge transport	122
6.2.2	Discussion on nonlinear mechanisms	123
6.3	Conclusion	124
6.4	Methods	125
6.5	Appendices	126
	Bibliography	129
7	Enhancing and rectifying electron transport through a biomolecular junction comprising Photosystem I and graphene	133
7.1	Binding PSI onto graphene using peptides	134
7.1.1	Sample preparation	134
7.1.2	Peptide improves PSI coverage	135
7.2	Enhanced and rectified PSI-graphene electron transport	137
7.2.1	Point-and-shoot technique for I - V characterization	137
7.2.2	Random positioning method for statistical confirmation	139
7.3	Mechanical tuning of PSI-graphene electron transport	140
7.4	Conclusion	143
7.5	Methods	143
	Bibliography	144
8	Closing remark – Spinchiraltronics	147
8.1	Conclusion	148
8.2	Further questions	150
8.3	Outlook – Spinchiraltronics	151
	Summary	153
	Samenvatting	158
	Acknowledgements	164
	Publications	171
	Curriculum Vitae	173

Chapter 1

Introduction – Unraveling chirality-induced spin selectivity (CISS)

Two hundred years before the start of this PhD project, Biot experimentally observed that the solution of certain organic compounds could rotate linearly polarized light [1]. Depending on the rotation direction, the compound could be classified as either right-handed or left-handed. This handedness would later be termed chirality, following the Greek word for hand, $\chi\epsilon\iota\rho$ (cheir). Interestingly, Biot conducted this famous experiment as part of a combat against the then increasingly prevailing theory that light travels as waves rather than particles. This battle would not settle for another 109 years, until de Broglie formulated the groundbreaking theory of wave-particle duality [2]. In the same year, Pauli outlined his monumental exclusion principle [3], and proposed a classically indescribable degree of freedom of electrons, which we now call spin. That was year 1924, at the height of the establishment of a revolutionary facet of modern physics — quantum mechanics. Decades later, the quantum mechanical understanding of electrons in matter has transformed humanity from an industrial civilization into an information civilization, and is moving forward at an unprecedented pace. This grand journey is now joined by this thesis. Herein, I will connect the concepts of (molecular) chirality and (electronic) spin, and shed light on how their potential interaction, described as chirality-induced spin selectivity (CISS), can be harnessed for future technologies.

1.1 Nature is chiral

Our understanding of nature is founded on iterations of curious *observations* and insightful *interpretations*. Not long after Biot observed the optical rotation of polarized light [1], Fresnel interpreted the phenomenon as a result of velocity difference between right-handed and left-handed circular light waves [4]. He suggested that this might have originated from peculiar constitutions of the optical medium, which allowed to distinguish between right and left handednesses [4, 5]. This later inspired Pasteur that handed molecules and crystals might exist in mirror-imaged three-dimensional forms, which he went on to eventually separate [6], laying the foundation for Le Bel and van 't Hoff to establish the field of stereochemistry [7, 8].

We now refer to the distinguishable pair of mirrored molecules as chiral enantiomers, and describe their difference in terms of fundamental symmetries [5]. We became aware that the optical rotation observed by Biot is in fact quite normal for natural compounds, and the underlying chirality has profound consequences for all life on Earth [9].

Nearly all naturally occurring and biologically active compounds are chiral and exist in only one enantiomeric form. A famous example is the DNA double helix. It encodes essential genetic information for all known organisms, and is uniformly right-handed. Furthermore, 19 out of the 20 natural amino acids are left-handed (the other one is not chiral), and all natural sugars are right-handed.

This biological homochirality gives us the ability to literally taste and smell chirality. For instance, the left-handed form of aspartame tastes sweet and is widely used as artificial sweeteners, whereas the right-handed form is tasteless [10]. Moreover, one enantiomer of carvone carries the refreshing fragrance of mint, while the mirror-imaged form smells like caraway seeds. It is for this reason that distinguishing chiral enantiomers is crucially important for us, particularly when it comes to pharmaceutical applications, since while one enantiomer may be therapeutic, the other can be detrimental.

However, it is not an easy task to distinguish and separate chiral enantiomers without using other chiral agents, because the mirrored forms often exhibit identical physical and chemical properties [11, 12]. Therefore, the observation that molecular *chirality* may interact with electronic *spin*—later termed *chirality-induced spin selectivity* (CISS)—intrigued intensive research interests, not only in the century-old field of stereochemistry, but also in the emerging area of spin electronics, or *spintronics* [13].

1.2 A spintronics vision for the future

The notion of spintronics emerged at the beginning of the 21st century as a promising candidate for next-generation electronics [14–16]. That was when the decades-long exponential growth of the electronics industry was seen to reach fundamental limits set by conventional silicon-based technologies [17]. Unlike the existing technologies that rely solely on the *charge* of electrons, spintronics envisions also using their *spin* degree-of-freedom to process and store digital information.

The realization of spintronics requires to prepare, control, and detect electronic spins, and this can be done using magnetic and electric fields [18, 19]. To understand this, we interpret the spin as the rotational motion of an electron around its own axis, which can be either clockwise or counter-clockwise, commonly referred to as the spin-up or spin-down state [20]. Associated with this spin state is an intrinsic magnetic dipole moment, which interacts with magnetic fields. In a uniform magnetic field, spins precess around the field direction (Larmor precession), whereas in a nonuniform magnetic field, electrons also acquire a spin-dependent linear momentum along the gradient of the field (Stern-Gerlach experiment). Furthermore, a moving electron in an electric field experiences a relativistic effective magnetic field, which also interacts with the spin (*spin-orbit coupling*).

A generic spintronic device, as illustrated by Datta and Das [21], consists of three major components: a spin injector where charge signals are converted into spin signals, a spin transport channel where spin signals are controlled and manipulated, and a spin detector that converts spin signals back to charge signals. Researchers in the field have been looking into mechanisms for efficient interconversion between charge and spin [22–25], for improving spin lifetime and transport distance [26–31], as well as for separating spin signals from undesired charge backgrounds [32–34].

Organic materials have also been considered for spintronic applications for the potential of reducing device size and lowering cost [35–37]. Mostly, they were only used as spin transport channels rather than spin injectors or detectors [38, 39], because their efficiency for interconverting spin and charge was relatively low [40–43]. However, this picture may have changed due to the series of observations described as CISS, where efficient spin–charge interconversion was observed in organic materials that are chiral.

1.3 The rise of CISS

The inception of CISS dates back to a 1999 article published by the Naaman group [44]. In this report, the authors shined circularly polarized light onto a gold substrate in order to generate spin-polarized photoelectrons, which were subsequently transmit-

ted through a thin film of chiral stearyl lysine molecules adsorbed on the substrate. It was observed that the transmission probability of the photoelectrons depended on the circular polarization of the light, as well as on the chirality of the molecules. This suggested a chirality-related spin-selective electron transmission through the molecules.

This type of electron photoemission experiments accounted for a large part of early observations associated with CISS. In many cases, after transmitting through the chiral molecular layer, the spin polarization of the photoelectrons was directly measured, and it could reach as high as tens of percent [45]. The molecules used ranged from large biological systems such as peptides [46, 47], proteins [48, 49], and DNA [45, 50] to small molecules such as 1,2-diphenyl-1,2-ethanediol (DPED) [51] and helicenes [52]. The results on helicenes were particularly surprising, since the nearly 10% spin polarization was achieved through a film of molecules that were atomically thin, consisted of only light-weighted carbon atoms, did not contain any atomic chiral centers, and formed only one helical turn in the secondary structure [52].

Meanwhile, observations based on electron magnetotransport experiments also showed connections between electronic spin (collectively exhibited as magnetization) and molecular chirality. These experiments often used two electrodes, one magnetic and the other not, to apply a charge current through a chiral molecule (or an ensemble of chiral molecules), and observed an electrical resistance that depended on the magnetization direction of the magnetic electrode. This magnetoresistance would also change sign if the opposite chiral enantiomers were used [53–63]. In one case, researchers used a special chiral molecule that could reverse chirality under light illumination, and indeed, they observed that the illumination also induced a sign change of the magnetoresistance [64].

Other experiments, too, found connections between magnetism and chirality. For example, one experiment observed that chiral adsorbates may alter the magnetic atomic-force-microscopy (mAFM) signals obtained on a ferromagnetic substrate [65]. In other cases, the presence of chiral molecules was related to a transverse electrical conduction that usually is associated with the presence of a magnetic field or magnetization [66–68]. A number of electrochemistry experiments showed that in electrochemical cells, the voltage drop across a ferromagnetic electrode with chiral adsorbates might depend on magnetization [48, 61, 69–71]. Also, some photoluminescence and fluorescence experiments demonstrated magnetization-dependent light emission properties of optically responsive chiral structures adsorbed on ferromagnetic substrates [49, 70, 72–74]. Most remarkably, it was recently reported that an achiral ferromagnetic substrate could be used to distinguish and even separate chiral enantiomers [75].

All these exciting observations not only strongly indicate the potential interaction

between molecular chirality and electronic spin, but also urgently call for a thorough theoretical understanding. This understanding should answer two core questions. First, how does chirality interact with spin on a microscopic level? Second, how does this interaction generate the signals in various types of experiments?

A majority of theoretical efforts focused on the first question. They interpreted CISS as a result of spin-orbit coupling (SOC), and numerically calculated the spin-dependent electron transmission through assumed chiral (helical) molecular structures [76–83]. Sometimes, the role of a built-in electric dipole or an electric field was also considered [84–87]. These results were able to qualitatively explain experimental observations, but cannot quantitatively account for the magnitude of the signals. First-principle calculations were scarce and also could not provide quantitative explanations [52, 88].

Very recently, it was proposed that there may exist a non-relativistic counterpart of SOC that could fill up the quantitative gap [89]. This curvature-induced effect parallels earlier observations that curved carbon structures exhibited much stronger SOC than the flat two-dimensional carbon, graphene [90–93]. However, even if this would indeed be applicable to generic chiral molecules, it could still only address the first of the two questions.

When the second question is taken into consideration, it becomes clear that only addressing microscopic mechanisms like SOC cannot fully explain experimental observations. As we will find out in this thesis (Chapter 3 and 4), fundamental symmetry considerations require nonunitary mechanisms within chiral molecules in order for them to generate any spin-polarized electron transmission [78, 94, 95]. This inspires to consider the role of contact and interface effects and spin-flip and spin-absorption mechanisms in the molecules [96–100]. Moreover, nonlinear effects such as orbital magnetization [101], electron-electron interactions [102], and energy relaxation [103] may also significantly contribute.

To date, a comprehensive and quantitative interpretation of various CISS-related observations still remains missing, and it is partly the aim of this thesis to provide some insights.

Before moving on, I would like to point out a few review articles on CISS. For general discussions on the progress of the field, see a series of reviews by Naaman and coauthors [13, 104–106]. For a summary of solid-state-device-based experiments on CISS, see articles by Michaeli *et al.* [62, 107]. For a review of electrochemical experiments on CISS, see Mondal *et al.* [108]. For an overview on experiments that involved photoluminescent chiral molecules or chiral structures, see Abendroth *et al.* [49].

1.4 Open questions

Two decades into the CISS discussion, this growing field is facing a growing amount of open questions. Here, I break the two core questions down into details, in order to address some urgent issues puzzling the theoretical and experimental developments of CISS.

1

1. How does chirality interact with spin on a microscopic level?
 - (a) What are the fundamental restrictions?
 - (b) Can we confirm the spin-orbit origin?
 - (c) Can we distinguish CISS from other spin–charge conversion mechanisms?
2. How does this interaction generate signals observed in various types of experiments?
 - (a) What are the requirements for experimental geometries?
 - (b) Can the magnetic-field- or magnetization-dependent signals be interpreted as due to electronic spin?
 - (c) How to better characterize CISS using (other) spintronic experiments?

1.5 This thesis

This thesis intends to address these open questions by combining the fundamental properties of CISS with theoretical and experimental tools that have guided the development of spintronics, and provide guidelines for future researches. The chapters are arranged as follows.

- **Chapter 1** (this chapter) provides a historical overview of the topic.
- **Chapter 2** approaches the concepts of spin and chirality from a symmetry perspective. It introduces physical principals that are fundamental to spintronics, and physical phenomena that are characteristic to chirality. It addresses the above *Question 1*.
- **Chapter 3** presents a theoretical model that analyzes spin-dependent electron transmission through chiral (molecular) structures, and highlights the limitations of conventional magnetotransport experimental geometries. It addresses the above *Questions 2*.

- **Chapter 4** discusses the important distinctions between observations obtained in the linear and in the nonlinear response regimes, and shows theoretically how nonlinearities can help overcome the limitations of certain experimental geometries. It addresses the above *Question 2*.
- **Chapter 5** provides a theoretical tool for analyzing a common type of electronic device used in CISS experiments, and demonstrates how quantitative analysis can be carried out even when involving highly complicated chiral systems. It addresses the above *Question 2*.
- **Chapter 6** experimentally demonstrates charge transport properties of a chiral two-dimensional van der Waals material, Tellurene. It paves way for further investigations of CISS in solid-state materials.
- **Chapter 7** reports experimental results on charge transport through a bio-molecular junction that contains a photosynthetic protein complex, and shows how the charge transport is affected by biochemical functionalizations. It provides insights for futures CISS researches using bio-organic materials.
- **Chapter 8** concludes the thesis and envisions a future where chirality and spin are incorporated for electronic applications.

1.6 Guideline to readers

Chapter 1 introduces relevant background of the thesis topic, while Chapter 8 summarizes the main findings of the thesis. These two chapters focus on the big picture, and do not require the readers to have any expertise on the topic.

Chapters 2 introduces the theoretical knowledge that are relevant to later discussions. The main text includes essential contents that are sufficient for understanding later chapters, while further technical details are provided in the Appendices for readers who are particularly interested.

Chapters 3 through 7 each focus on one aspect of the thesis topic. These chapters also only include essential arguments in the main text, and leave mathematical derivations and technical discussions to the Appendices. Details related to experiments are provided in the Methods section.

At the end of the thesis, there is an English and a Dutch summary that target general readers who are interested in scientific developments in the field, but have little or no knowledge in this specialized area of physics.

Bibliography

- [1] J.-B. Biot, "Phénomènes de polarisation successive, observés dans des fluides homogènes," *Bull. Soc. Philomath* **190**, p. 1815, 1815.
- [2] L. de Broglie, *Recherches sur la théorie des quanta*. PhD thesis, Migration-université en cours d'affectation, 1924.
- [3] W. Pauli, "Über den Einfluß der Geschwindigkeitsabhängigkeit der Elektronenmasse auf den Zeemaneffekt," *Zeitschrift für Physik* **31**(1), pp. 373–385, 1925.
- [4] M. A. Fresnel, "Considérations théoriques sur la polarisation de la lumière," *Bulletin des Sciences*, pp. 147–158, 1824.
- [5] L. D. Barron, "Fundamental symmetry aspects of molecular chirality," in *New developments in molecular chirality*, pp. 1–55, Springer, Dordrecht, 1991.
- [6] L. Pasteur, "Sur les relations qui peuvent exister entre la forme cristalline, la composition chimique et le sens de la polarisation rotatoire," *Annales Chimie Phys.* **24**, pp. 442–459, 1848.
- [7] J. A. Le Bel, "Sur les relations qui existent entre les formules atomiques des corps organiques et le pouvoir rotatoire de leurs dissolutions," *Bulletin de la Société Chimique de Paris* **22**, pp. 337–347, 1874.
- [8] J. H. van't Hoff, "Sur les formules de structure dans l'espace," *Archives Néerlandaises des Sciences Exactes en Naturelles* **9**, pp. 445–454, 1874.
- [9] W. A. Bonner, "The origin and amplification of biomolecular chirality," *Origins of Life and Evolution of the Biosphere* **21**(2), pp. 59–111, 1991.
- [10] J. Gal, "The discovery of stereoselectivity at biological receptors: Arnaldo Piutti and the taste of the asparagine enantiomers – History and analysis on the 125th anniversary," *Chirality* **24**(12), pp. 959–976, 2012.
- [11] M. Avalos, R. Babiano, P. Cintas, J. L. Jiménez, J. C. Palacios, and L. D. Barron, "Absolute asymmetric synthesis under physical fields: facts and fictions," *Chemical Reviews* **98**(7), pp. 2391–2404, 1998.
- [12] B. L. Feringa and R. A. van Delden, "Absolute asymmetric synthesis: the origin, control, and amplification of chirality," *Angewandte Chemie International Edition* **38**(23), pp. 3418–3438, 1999.
- [13] R. Naaman, Y. Paltiel, and D. H. Waldeck, "Chiral molecules and the electron spin," *Nature Reviews Chemistry* **3**, pp. 250–260, 2019.
- [14] J. M. Shalf and R. Leland, "Computing beyond Moore's law," *Computer* **48**(SAND-2015-8039J), 2015.
- [15] S. A. Wolf, D. D. Awschalom, R. A. Buhrman, J. M. Daughton, S. Von Molnar, M. L. Roukes, A. Y. Chtchelkanova, and D. M. Treger, "Spintronics: a spin-based electronics vision for the future," *Science* **294**(5546), pp. 1488–1495, 2001.
- [16] S. A. Wolf, A. Y. Chtchelkanova, and D. M. Treger, "Spintronics—A retrospective and perspective," *IBM Journal of Research and Development* **50**(1), pp. 101–110, 2006.
- [17] J. D. Meindl, "Beyond Moore's law: The interconnect era," *Computing in Science & Engineering* **5**(1), pp. 20–24, 2003.
- [18] I. Žutić, J. Fabian, and S. D. Sarma, "Spintronics: Fundamentals and applications," *Reviews of Modern Physics* **76**(2), p. 323, 2004.
- [19] S. Bader and S. Parkin, "Spintronics," *Annual Review of Condensed Matter Physics* **1**(1), pp. 71–88, 2010.
- [20] Despite carrying the unit of angular momentum, spin is an intrinsic quantum-mechanical property of elementary particles and has no classical analogue. It is, for every elementary particle, well-defined and immutable. Usually, it is denoted S and labeled with a spin quantum number s , which is $1/2$ for electrons and is 1 for photons. A measurement of a particle's spin along an arbitrarily determined direction will yield discrete values between (and including) $s\hbar$ and $-s\hbar$, with a step size of \hbar . For electrons, this means that there are only two possible measurement outcomes, $\hbar/2$ and $-\hbar/2$, which are referred to as the spin-up and the spin-down states.
- [21] S. Datta and B. Das, "Electronic analog of the electro-optic modulator," *Applied Physics Letters* **56**(7), pp. 665–667, 1990.
- [22] W. Han, K. Pi, K. M. McCreary, Y. Li, J. J. I. Wong, A. G. Swartz, and R. K. Kawakami, "Tunneling spin injection into single layer graphene," *Physical Review Letters* **105**(16), p. 167202, 2010.
- [23] J. Wunderlich, B.-G. Park, A. C. Irvine, L. P. Zárbo, E. Rozkotová, P. Nemeč, V. Novák, J. Sinova, and T. Jungwirth, "Spin Hall effect transistor," *Science* **330**(6012), pp. 1801–1804, 2010.
- [24] M. Gurram, S. Omar, and B. J. van Wees, "Bias induced up to 100% spin-injection and detection polarizations in ferromagnet/bilayer-hBN/graphene/hBN heterostructures," *Nature Communications* **8**(1), p. 248, 2017.
- [25] T. S. Ghiasi, A. A. Kaverzin, P. J. Blah, and B. J. van Wees, "Charge-to-spin conversion by the Rashba–Edelstein effect in two-dimensional van der Waals heterostructures up to room temperature," *Nano Letters* **19**(9), pp. 5959–5966, 2019.
- [26] D. D. Awschalom and M. E. Flatté, "Challenges for semiconductor spintronics," *Nature Physics* **3**(3), p. 153, 2007.
- [27] W. Han, R. K. Kawakami, M. Gmitra, and J. Fabian, "Graphene spintronics," *Nature Nanotechnology* **9**(10), p. 794,

- 2014.
- [28] N. Tombros, C. Jozsa, M. Popinciuc, H. T. Jonkman, and B. J. van Wees, "Electronic spin transport and spin precession in single graphene layers at room temperature," *Nature* **448**(7153), p. 571, 2007.
- [29] W. Han and R. K. Kawakami, "Spin relaxation in single-layer and bilayer graphene," *Physical Review Letters* **107**(4), p. 047207, 2011.
- [30] J. Ingla-Aynés, R. J. Meijerink, and B. J. van Wees, "Eighty-eight percent directional guiding of spin currents with 90 μm relaxation length in bilayer graphene using carrier drift," *Nano Letters* **16**(8), pp. 4825–4830, 2016.
- [31] P. J. Zomer, M. H. D. Guimaraes, N. Tombros, and B. J. van Wees, "Long-distance spin transport in high-mobility graphene on hexagonal boron nitride," *Physical Review B* **86**(16), p. 161416, 2012.
- [32] F. J. Jedema, A. T. Filip, and B. J. van Wees, "Electrical spin injection and accumulation at room temperature in an all-metal mesoscopic spin valve," *Nature* **410**(6826), p. 345, 2001.
- [33] F. J. Jedema, H. B. Heersche, A. T. Filip, J. J. A. Baselmans, and B. J. van Wees, "Electrical detection of spin precession in a metallic mesoscopic spin valve," *Nature* **416**(6882), pp. 713–716, 2002.
- [34] L. J. Cornelissen, J. Liu, R. A. Duine, J. B. Youssef, and B. J. van Wees, "Long-distance transport of magnon spin information in a magnetic insulator at room temperature," *Nature Physics* **11**(12), pp. 1022–1026, 2015.
- [35] W. J. M. Naber, S. Faez, and W. G. van der Wiel, "Organic spintronics," *Journal of Physics D: Applied Physics* **40**(12), p. R205, 2007.
- [36] V. A. Dediu, L. E. Hueso, I. Bergenti, and C. Taliani, "Spin routes in organic semiconductors," *Nature Materials* **8**(9), p. 707, 2009.
- [37] D. Sun, E. Ehrenfreund, and Z. V. Vardeny, "The first decade of organic spintronics research," *Chemical Communications* **50**(15), pp. 1781–1793, 2014.
- [38] V. Dediu, M. Murgia, F. Maticotta, C. Taliani, and S. Barbanera, "Room temperature spin polarized injection in organic semiconductor," *Solid State Communications* **122**(3–4), pp. 181–184, 2002.
- [39] Z. Xiong, D. Wu, Z. V. Vardeny, and J. Shi, "Giant magnetoresistance in organic spin-valves," *Nature* **427**(6977), p. 821, 2004.
- [40] L. Fang, K. D. Bozdog, C.-Y. Chen, P. Truitt, A. Epstein, and E. Johnston-Halperin, "Electrical spin injection from an organic-based ferrimagnet in a hybrid organic-inorganic heterostructure," *Physical Review Letters* **106**(15), p. 156602, 2011.
- [41] K. Ando, S. Watanabe, S. Mooser, E. Saitoh, and H. Siringhaus, "Solution-processed organic spin-charge converter," *Nature Materials* **12**(7), p. 622, 2013.
- [42] D. Sun, K. J. van Schooten, M. Kavand, H. Malissa, C. Zhang, M. Groesbeck, C. Boehme, and Z. V. Vardeny, "Inverse spin Hall effect from pulsed spin current in organic semiconductors with tunable spin-orbit coupling," *Nature Materials* **15**(8), p. 863, 2016.
- [43] H. Liu, C. Zhang, H. Malissa, M. Groesbeck, M. Kavand, R. McLaughlin, S. Jamali, J. Hao, D. Sun, R. A. Davidson, et al., "Organic-based magnon spintronics," *Nature Materials* **17**(4), pp. 308–312, 2018.
- [44] K. Ray, S. P. Ananthavel, D. H. Waldeck, and R. Naaman, "Asymmetric scattering of polarized electrons by organized organic films of chiral molecules," *Science* **283**(5403), pp. 814–816, 1999.
- [45] B. Göhler, V. Hamelbeck, T. Z. Markus, M. Kettner, G. F. Hanne, Z. Vager, R. Naaman, and H. Zacharias, "Spin selectivity in electron transmission through self-assembled monolayers of double-stranded DNA," *Science* **331**(6019), pp. 894–897, 2011.
- [46] I. Carmeli, V. Skakalova, R. Naaman, and Z. Vager, "Magnetization of chiral monolayers of polypeptide: a possible source of magnetism in some biological membranes," *Angewandte Chemie International Edition* **41**(5), pp. 761–764, 2002.
- [47] M. Kettner, B. Göhler, H. Zacharias, D. Mishra, V. Kiran, R. Naaman, C. Fontanesi, D. H. Waldeck, S. Sek, J. Pawłowski, et al., "Spin filtering in electron transport through chiral oligopeptides," *The Journal of Physical Chemistry C* **119**(26), pp. 14542–14547, 2015.
- [48] D. Mishra, T. Z. Markus, R. Naaman, M. Kettner, B. Göhler, H. Zacharias, N. Friedman, M. Sheves, and C. Fontanesi, "Spin-dependent electron transmission through bacteriorhodopsin embedded in purple membrane," *Proceedings of the National Academy of Sciences* **110**(37), pp. 14872–14876, 2013.
- [49] J. M. Abendroth, D. M. Stemer, B. P. Bloom, P. Roy, R. Naaman, D. H. Waldeck, P. S. Weiss, and P. C. Mondal, "Spin selectivity in photoinduced charge-transfer mediated by chiral molecules," *ACS Nano* **13**(5), pp. 4928–4946, 2019.
- [50] S. G. Ray, S. S. Daube, G. Leitus, Z. Vager, and R. Naaman, "Chirality-induced spin-selective properties of self-assembled monolayers of DNA on gold," *Physical Review Letters* **96**(3), p. 036101, 2006.
- [51] M. Á. Niño, I. A. Kowalik, F. J. Luque, D. Arvanitis, R. Miranda, and J. J. de Miguel, "Enantiospecific spin polarization of electrons photoemitted through layers of homochiral organic molecules," *Advanced Materials* **26**(44), pp. 7474–7479, 2014.

- 1
- [52] M. Kettner, V. V. Maslyuk, D. Nürenberg, J. Seibel, R. Gutierrez, G. Cuniberti, K.-H. Ernst, and H. Zacharias, "Chirality-dependent electron spin filtering by molecular monolayers of helicenes," *The Journal of Physical Chemistry Letters* **9**(8), pp. 2025–2030, 2018.
- [53] Z. Xie, T. Z. Markus, S. R. Cohen, Z. Vager, R. Gutierrez, and R. Naaman, "Spin specific electron conduction through DNA oligomers," *Nano Letters* **11**(11), pp. 4652–4655, 2011.
- [54] V. Kiran, S. P. Mathew, S. R. Cohen, I. Hernández Delgado, J. Lacour, and R. Naaman, "Helicenes—A new class of organic spin filter," *Advanced Materials* **28**, pp. 1957–1962, 2016.
- [55] B. P. Bloom, V. Kiran, V. Varade, R. Naaman, and D. H. Waldeck, "Spin selective charge transport through cysteine capped CdSe quantum dots," *Nano Letters* **16**(7), pp. 4583–4589, 2016.
- [56] A. C. Aragonès, E. Medina, M. Ferrer-Huerta, N. Gimeno, M. Teixidó, J. L. Palma, N. Tao, J. M. Ugalde, E. Giral, I. Díez-Pérez, *et al.*, "Measuring the spin-polarization power of a single chiral molecule," *Small* **13**(2), p. 1602519, 2017.
- [57] O. B. Dor, S. Yochelis, S. P. Mathew, R. Naaman, and Y. Paltiel, "A chiral-based magnetic memory device without a permanent magnet," *Nature Communications* **4**, p. 2256, 2013.
- [58] K. S. Kumar, N. Kantor-Uriel, S. P. Mathew, R. Guliamov, and R. Naaman, "A device for measuring spin selectivity in electron transfer," *Physical Chemistry Chemical Physics* **15**(42), pp. 18357–18362, 2013.
- [59] I. Carmeli, K. S. Kumar, O. Heifler, C. Carmeli, and R. Naaman, "Spin selectivity in electron transfer in photosystem I," *Angewandte Chemie International Edition* **53**(34), pp. 8953–8958, 2014.
- [60] S. P. Mathew, P. C. Mondal, H. Moshe, Y. Mastai, and R. Naaman, "Non-magnetic organic/inorganic spin injector at room temperature," *Applied Physics Letters* **105**(24), p. 242408, 2014.
- [61] P. C. Mondal, N. Kantor-Uriel, S. P. Mathew, F. Tassinari, C. Fontanesi, and R. Naaman, "Chiral conductive polymers as spin filters," *Advanced Materials* **27**(11), pp. 1924–1927, 2015.
- [62] K. Michaeli, V. Varade, R. Naaman, and D. H. Waldeck, "A new approach towards spintronics—spintronics with no magnets," *Journal of Physics: Condensed Matter* **29**(10), p. 103002, 2017.
- [63] V. Varade, T. Markus, K. Vankayala, N. Friedman, M. Sheves, D. H. Waldeck, and R. Naaman, "Bacteriorhodopsin based non-magnetic spin filters for biomolecular spintronics," *Physical Chemistry Chemical Physics* **20**(2), pp. 1091–1097, 2018.
- [64] M. Suda, Y. Thathong, V. Promarak, H. Kojima, M. Nakamura, T. Shiraogawa, M. Ehara, and H. M. Yamamoto, "Light-driven molecular switch for reconfigurable spin filters," *Nature Communications* **10**(1), p. 2455, 2019.
- [65] O. B. Dor, S. Yochelis, A. Radko, K. Vankayala, E. Capua, A. Capua, S.-H. Yang, L. T. Baczewski, S. S. P. Parkin, R. Naaman, *et al.*, "Magnetization switching in ferromagnets by adsorbed chiral molecules without current or external magnetic field," *Nature Communications* **8**, p. 14567, 2017.
- [66] G. Bullard, F. Tassinari, C.-H. Ko, A. K. Mondal, R. Wang, S. Mishra, R. Naaman, and M. J. Therien, "Low-resistance molecular wires propagate spin-polarized currents," *Journal of the American Chemical Society* **141**(37), pp. 14707–14711, 2019.
- [67] E. Z. Smolinsky, A. Neubauer, A. Kumar, S. Yochelis, E. Capua, R. Carmieli, Y. Paltiel, R. Naaman, and K. Michaeli, "Electric field-controlled magnetization in GaAs/AlGaAs heterostructures—chiral organic molecules hybrids," *The Journal of Physical Chemistry Letters* **10**(5), pp. 1139–1145, 2019.
- [68] M. Eckshtain-Levi, E. Capua, S. Refaely-Abramson, S. Sarkar, Y. Gavrilov, S. P. Mathew, Y. Paltiel, Y. Levy, L. Kronik, and R. Naaman, "Cold denaturation induces inversion of dipole and spin transfer in chiral peptide monolayers," *Nature Communications* **7**, p. 10744, 2016.
- [69] H. Einati, D. Mishra, N. Friedman, M. Sheves, and R. Naaman, "Light-controlled spin filtering in bacteriorhodopsin," *Nano Letters* **15**(2), pp. 1052–1056, 2015.
- [70] P. C. Mondal, P. Roy, D. Kim, E. E. Fullerton, H. Cohen, and R. Naaman, "Photospintronics: magnetic field-controlled photoemission and light-controlled spin transport in hybrid chiral oligopeptide-nanoparticle structures," *Nano Letters* **16**(4), pp. 2806–2811, 2016.
- [71] T. J. Zwang, S. Hürlimann, M. G. Hill, and J. K. Barton, "Helix-dependent spin filtering through the DNA duplex," *Journal of the American Chemical Society* **138**(48), pp. 15551–15554, 2016.
- [72] P. Roy, N. Kantor-Uriel, D. Mishra, S. Dutta, N. Friedman, M. Sheves, and R. Naaman, "Spin-controlled photoluminescence in hybrid nanoparticles purple membrane system," *ACS Nano* **10**(4), pp. 4525–4531, 2016.
- [73] J. M. Abendroth, N. Nakatsuka, M. Ye, D. Kim, E. E. Fullerton, A. M. Andrews, and P. S. Weiss, "Analyzing spin selectivity in dna-mediated charge transfer via fluorescence microscopy," *ACS Nano* **11**(7), pp. 7516–7526, 2017.
- [74] B. P. Bloom, B. M. Graff, S. Ghosh, D. N. Beratan, and D. H. Waldeck, "Chirality control of electron transfer in quantum dot assemblies," *Journal of the American Chemical Society* **139**(26), pp. 9038–9043, 2017.
- [75] K. Banerjee-Ghosh, O. B. Dor, F. Tassinari, E. Capua, S. Yochelis, A. Capua, S.-H. Yang, S. S. Parkin, S. Sarkar, L. Kronik, *et al.*, "Separation of enantiomers by their enantiospecific interaction with achiral magnetic substrates," *Science* **360**(6395), pp. 1331–1334, 2018.

- [76] S. Yeganeh, M. A. Ratner, E. Medina, and V. Mujica, "Chiral electron transport: scattering through helical potentials," *The Journal of Chemical Physics* **131**(1), p. 014707, 2009.
- [77] E. Medina, F. López, M. A. Ratner, and V. Mujica, "Chiral molecular films as electron polarizers and polarization modulators," *EPL (Europhysics Letters)* **99**(1), p. 17006, 2012.
- [78] A.-M. Guo and Q.-F. Sun, "Spin-selective transport of electrons in DNA double helix," *Physical Review Letters* **108**(21), p. 218102, 2012.
- [79] R. Gutierrez, E. Díaz, R. Naaman, and G. Cuniberti, "Spin-selective transport through helical molecular systems," *Physical Review B* **85**(8), p. 081404, 2012.
- [80] R. Gutierrez, E. Díaz, C. Gaul, T. Brumme, F. Domínguez-Adame, and G. Cuniberti, "Modeling spin transport in helical fields: derivation of an effective low-dimensional Hamiltonian," *The Journal of Physical Chemistry C* **117**(43), pp. 22276–22284, 2013.
- [81] A. A. Eremko and V. M. Loktev, "Spin sensitive electron transmission through helical potentials," *Physical Review B* **88**(16), p. 165409, 2013.
- [82] A.-M. Guo and Q.-F. Sun, "Spin-dependent electron transport in protein-like single-helical molecules," *Proceedings of the National Academy of Sciences* **111**(32), pp. 11658–11662, 2014.
- [83] T.-R. Pan, A.-M. Guo, and Q.-F. Sun, "Spin-polarized electron transport through helicene molecular junctions," *Physical Review B* **94**(23), p. 235448, 2016.
- [84] A.-M. Guo and Q.-F. Sun, "Enhanced spin-polarized transport through DNA double helix by gate voltage," *Physical Review B* **86**(3), p. 035424, 2012.
- [85] K. Michaeli and R. Naaman, "Origin of spin-dependent tunneling through chiral molecules," *The Journal of Physical Chemistry C* **123**(27), pp. 17043–17048, 2019.
- [86] E. Medina, L. A. González-Arraga, D. Finkelstein-Shapiro, B. Berche, and V. Mujica, "Continuum model for chiral induced spin selectivity in helical molecules," *The Journal of Chemical Physics* **142**(19), p. 194308, 2015.
- [87] K. Michaeli, D. N. Beratan, D. H. Waldeck, and R. Naaman, "Voltage-induced long-range coherent electron transfer through organic molecules," *Proceedings of the National Academy of Sciences* **116**(13), pp. 5931–5936, 2019.
- [88] V. V. Maslyuk, R. Gutierrez, A. Dianat, V. Mujica, and G. Cuniberti, "Enhanced magnetoresistance in chiral molecular junctions," *The Journal of Physical Chemistry Letters* **9**(18), pp. 5453–5459, 2018.
- [89] A. Shitade and E. Minamitani, "Geometric spin-orbit coupling and chirality-induced spin selectivity," *arXiv:2002.05371*, 2020.
- [90] H. Min, J. Hill, N. A. Sinitsyn, B. Sahu, L. Kleinman, and A. H. MacDonald, "Intrinsic and Rashba spin-orbit interactions in graphene sheets," *Physical Review B* **74**(16), p. 165310, 2006.
- [91] D. Huertas-Hernando, F. Guinea, and A. Brataas, "Spin-orbit coupling in curved graphene, fullerenes, nanotubes, and nanotube caps," *Physical Review B* **74**(15), p. 155426, 2006.
- [92] F. Kuemmeth, S. Ilani, D. C. Ralph, and P. L. McEuen, "Coupling of spin and orbital motion of electrons in carbon nanotubes," *Nature* **452**(7186), p. 448, 2008.
- [93] G. Steele, F. Pei, E. Laird, J. Jol. H. Meerwaldt, and L. Kouwenhoven, "Large spin-orbit coupling in carbon nanotubes," *Nature Communications* **4**, p. 1573, 2013.
- [94] S. Matityahu, Y. Utsumi, A. Aharony, O. Entin-Wohlman, and C. A. Balseiro, "Spin-dependent transport through a chiral molecule in the presence of spin-orbit interaction and nonunitary effects," *Physical Review B* **93**(7), p. 075407, 2016.
- [95] S. Matityahu, A. Aharony, O. Entin-Wohlman, and C. A. Balseiro, "Spin filtering in all-electrical three-terminal interferometers," *Physical Review B* **95**(8), p. 085411, 2017.
- [96] J. Gersten, K. Kaasbjerg, and A. Nitzan, "Induced spin filtering in electron transmission through chiral molecular layers adsorbed on metals with strong spin-orbit coupling," *The Journal of Chemical Physics* **139**(11), p. 114111, 2013.
- [97] A.-M. Guo, E. Díaz, C. Gaul, R. Gutierrez, F. Domínguez-Adame, G. Cuniberti, and Q.-F. Sun, "Contact effects in spin transport along double-helical molecules," *Physical Review B* **89**(20), p. 205434, 2014.
- [98] D. Nürenberg and H. Zacharias, "Evaluation of spin-flip scattering in chirality-induced spin selectivity using the Riccati equation," *Physical Chemistry Chemical Physics* **21**(7), pp. 3761–3770, 2019.
- [99] X. Yang, C. H. van der Wal, and B. J. van Wees, "Spin-dependent electron transmission model for chiral molecules in mesoscopic devices," *Physical Review B* **99**(2), p. 024418, 2019.
- [100] S. Dalum and P. Hedegård, "Theory of chiral induced spin selectivity," *Nano Letters* **19**(8), pp. 5253–5259, 2019.
- [101] T. Yoda, T. Yokoyama, and S. Murakami, "Current-induced orbital and spin magnetizations in crystals with helical structure," *Scientific Reports* **5**, p. 12024, 2015.
- [102] J. Fransson, "Chirality-induced spin selectivity: The role of electron correlations," *The Journal of Physical Chemistry Letters* **10**(22), pp. 7126–7132, 2019.
- [103] X. Yang, C. H. van der Wal, and B. J. van Wees, "Detecting chirality in two-terminal electronic nanodevices," *Nano*

Letters, 2020.

- [104] R. Naaman and D. H. Waldeck, "Chiral-induced spin selectivity effect," *The Journal of Physical Chemistry Letters* **3**(16), pp. 2178–2187, 2012.
- [105] R. Naaman and D. H. Waldeck, "Spintronics and chirality: Spin selectivity in electron transport through chiral molecules," *Annual Review of Physical Chemistry* **66**, pp. 263–281, 2015.
- [106] R. Naaman, Y. Paltiel, and D. H. Waldeck, "Chirality and spin: A different perspective on enantioselective interactions," *CHIMIA International Journal for Chemistry* **72**(6), pp. 394–398, 2018.
- [107] K. Michaeli, N. Kantor-Uriel, R. Naaman, and D. H. Waldeck, "The electron's spin and molecular chirality—how are they related and how do they affect life processes?," *Chemical Society Reviews* **45**(23), pp. 6478–6487, 2016.
- [108] P. C. Mondal, C. Fontanesi, D. H. Waldeck, and R. Naaman, "Spin-dependent transport through chiral molecules studied by spin-dependent electrochemistry," *Accounts of Chemical Research* **49**(11), pp. 2560–2568, 2016.

Chapter 2

A symmetry perspective of chirality, spin, and CISS

Symmetry is of paramount importance for understanding nature. It is particularly helpful in determining whether a physical phenomenon can exist in a specific material, and whether it can be experimentally detected. Therefore, it would not be proper to attempt to answer the two core questions about CISS (see Chapter 1) without first understanding the fundamental restrictions imposed by symmetry. In this chapter, I will relate chirality and spin to the fundamental symmetries of space and time, and explain how they give rise to certain physical phenomena. From this perspective, I examine experimental observations of CISS and outline further questions that need to be addressed in future researches.

2.1 Symmetry and chirality

The concept of symmetry is carried out by *symmetry operations*. It is an action applied to an object which leaves the object appearing unchanged. The operation can be a physical action, such as a translational or rotational motion, or a mathematical transformation, such as a space-inversion or time-reversal operation. Likewise, the object can be a concrete body, such as a molecule or a crystal, or an abstract concept, such as a Hamiltonian or an arbitrarily defined quantity.

2

2.1.1 Molecular symmetry operations

We illustrate the concepts about symmetry using a simple ball-and-stick model of a tetrahedral molecule, as shown in Fig. 2.1a. Here, a 120° rotation about the vertical axis leaves the molecule indistinguishable from the state prior to the rotation. This rotation is therefore a *symmetry operation* of the molecule. The rotational axis, in this case, is the corresponding *symmetry element*. Also, this molecule is indistinguishable to itself (symmetric) under a mirror reflection (symmetry operation) with respect to a mirror plane (symmetry element) that contains the vertical axis and one of the off-axis atoms.

It is generally considered that there are five types of molecular symmetry operations: *identity* (\hat{E}), *proper rotation* (\hat{C}_n), *reflection* ($\hat{\sigma}$), *inversion* (\hat{i}), and *improper rotation* (\hat{S}_n) [1], and their definitions are summarized in Table 2.1.

Table 2.1: Molecular symmetry operations

Symmetry operation	symmetry element	definition
\hat{E} identity	the object itself	doing nothing
\hat{C}_n n -fold proper rotation	an axis of symmetry	rotating the object by $2\pi/n$ around the axis ^a
$\hat{\sigma}$ reflection	a mirror plane	reflecting the object with respect to the plane ^b
\hat{i} inversion	a center of symmetry	inverting the object with respect to the center
\hat{S}_n n -fold improper rotation	a rotatory reflection axis	an n -fold proper rotation followed by a reflection ^c

^a For an object with multiple rotational axes, the one with largest value n is called the *principal axis* of symmetry.

^b When the mirror plane contains the principal axis of symmetry, it is *vertical*, and the symmetry operation is denoted $\hat{\sigma}_v$. A *horizontal* plane is perpendicular to the principal axis and is denoted $\hat{\sigma}_h$.

^c The reflection mirror plane is perpendicular to the rotational axis.

When a molecule is not symmetric under any improper rotation \hat{S}_n , it is *chiral*. Note that because $\hat{S}_1 \equiv \hat{\sigma}$ and $\hat{S}_2 \equiv \hat{i}$, a chiral molecule also does not have reflection or inversion symmetries (Fig. 2.1b).

These molecule-based symmetry operations can be extended to solid-state crystals, although a thorough analysis must also include translational symmetry operations. For a certain molecule or crystal, its set of symmetry operations form a *symmetry group*, as introduced in Appendix A.

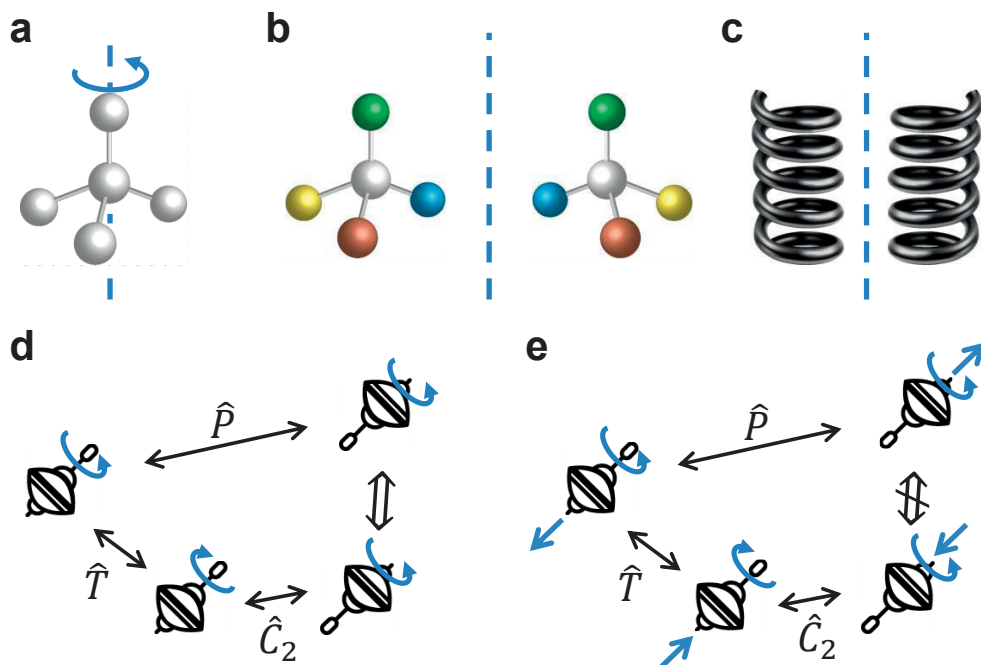


Figure 2.1: Symmetry and chirality for stationary (a, b, c) and moving (d, e) objects. **a.** A tetrahedral molecule (e.g. methane) is transformed to itself by a \hat{C}_3 rotational symmetry operation (axis indicated by the dash-dot line). It also has $\hat{\sigma}_v$ symmetry, for example, with respect to a plane defined by the rotational axis and one of the off-axis atoms. **b.** When the four outer atoms all differ from one another, the tetrahedral molecule is chiral. A mirror reflection (with respect to the dashed line) transforms the molecule to its opposite enantiomer. Each enantiomer alone contains only the trivial identity symmetry operation. **c.** A helix is chiral, it transforms to opposite handedness by improper rotations (including reflection and inversion), but not by proper rotations. Each helix alone is symmetric under \hat{C}_2 proper rotations (rotational axes in the plane perpendicular to the helical screw axis). **d.** A spinning top has two enantiomeric forms of rotation (clockwise *vs.* counter-clockwise) that are interconverted by space-inversion, as well as by time-reversal plus a proper rotation \hat{C}_2 . This rotational motion is therefore not truly chiral. **e.** A spinning top that is moving along its spinning axis is truly chiral, because the two enantiomeric forms of motion (spin parallel to linear momentum *vs.* antiparallel) are interconverted only by space-inversion but not by time-reversal plus any proper rotations.

2.1.2 Fundamental symmetries of space and time

Time-reversal symmetry

The molecular and crystal symmetries only address the stationary constitutions of atoms, but do not consider motion. However, it is the dynamical movements of elementary particles, like electrons or photons, that evoke observable physical phenomena.

In order to describe the symmetry of these time-dependent processes, an additional symmetry operation of *time-reversal* (\hat{T}) is introduced. It manifests as the reversal of all microscopic motion. A system is called time-reversal symmetric (invariant) if it appears unchanged under this operation [2].

Together with *charge-conjugation* (\hat{C} , sign change of electric charge) and *space-inversion* (\hat{P} , reversing the handedness of the space coordinate system), time-reversal (\hat{T}) is one of the most fundamental symmetry operations that has roots in how we describe nature. This is detailed in Appendix B.

Space and time symmetries of physical quantities

Space-inversion \hat{P} and time-reversal \hat{T} are of direct relevance to solid-state physics. Understanding their implications on common physical quantities greatly help understand phenomena related to chirality and spin in electronic devices.

The \hat{P} and \hat{T} operations characterize physical quantities as *odd* and *even*. Vectors that are \hat{P} -odd change sign under space-inversion, and are called *polar vectors*. In contrast, \hat{P} -even vectors retain their sign under \hat{P} , and are called *axial vectors* (or *pseudovectors*). For example, spatial position \mathbf{r} and linear momentum \mathbf{p} both change sign under \hat{P} , and are thus both polar, whereas their cross product, angular momentum $\mathbf{L} = \mathbf{r} \times \mathbf{p}$, retains sign and is thereby axial. Unlike vectors, *scalars* are usually defined without the sense of direction, and are therefore \hat{P} -even. However, a *scalar product* of a polar and an axial vector is \hat{P} -odd, and is called a *pseudoscalar*. An example of a pseudoscalar is *helicity* ($\mathcal{H} = \mathbf{S} \cdot \mathbf{p}/|\mathbf{p}|$), which is the projection of (spin) angular momentum \mathbf{S} (axial) onto the direction of linear momentum \mathbf{p} (polar).

Similarly, \hat{T} distinguishes physical quantities into *time-odd* and *time-even*. Quantities that are time-odd involve motion. For instance, magnetic field \mathbf{B} and magnetization \mathbf{M} are defined by dynamical processes (charge current and electronic spin, respectively), and are thus both \hat{T} -odd. In comparison, the electric field \mathbf{E} is \hat{T} -even, because it is defined by a stationary spatial displacement of electric charges. A summary of common physical quantities and their symmetries under \hat{P} and \hat{T} is given in Table 2.2.

The inclusion of time symmetry and its relevance to magnetism allows us to extend the symmetry classifications of solid-state materials to *time-reversal space groups*,

Table 2.2: Symmetry of physical quantities under \hat{P} and \hat{T} operations

Physical quantity	symmetry under \hat{P}	symmetry under \hat{T}
\mathbf{r} position	odd	even
t time	even	odd
\mathbf{p} linear momentum	odd	odd
\mathbf{k} wavevector	odd	odd
\mathbf{F} force	odd	even
\mathbf{L}, \mathbf{S} angular momenta	even	odd
\mathbf{E} electric field	odd	even
\mathbf{B} magnetic field	even	odd
\mathbf{P} electric polarization	odd	even
\mathbf{M} magnetization	even	odd
\mathcal{H} helicity	odd	even

which are introduced in Appendix A.

2.1.3 True chirality

The concept of *true chirality* was introduced by Barron to define physical quantities that exhibit the same symmetry properties as chiral enantiomers [3–7], and it is based on the fundamental symmetries of space and time:

“True chirality is exhibited by systems that exist in two distinct enantiomeric states that are interconverted by space-inversion, but not by time-reversal combined with any proper spatial rotation.” (Quoted from Ref.6)

Truly chiral systems can distinguish and may even separate opposite chiral enantiomers close to thermodynamic equilibrium, and are therefore important for stereochemistry applications. We illustrate this concept with a few examples.

First, we compare the motion of electrons in two distinct systems: a conducting wire wound into a solenoid, and a collinear alignment of an electric and a magnetic field (both fields are static and uniform). In both systems, electrons can trace a helical path, and the helix can be of either handedness. However, only the helical wire is truly chiral, because its shape, as a stationary geometry, is converted to the opposite handedness by space-inversion but not by time-reversal; whereas the helical motion of electrons in the collinear fields is converted to opposite handedness by both space-inversion and time-reversal (see Table 2.2). In fact, the unawareness of this true chirality consideration has led to numerous failed attempts to separate enantiomers using collinear electric and magnetic fields [6, 8–10].

Another example is the spinning top considered by Barron, see Figure 2.1d-e. It shows that a spinning motion is not truly chiral although it can be in either left-handed or right-handed form, because the two forms are interconverted by both space-inversion and time-reversal (plus a proper rotation). However, a spinning motion combined with a linear motion is truly chiral. The two enantiomeric forms are the parallel and antiparallel alignments of the linear and angular momentum vectors. These two alignments are interconverted only by space-inversion but not time-reversal (plus any proper rotations). The chirality of this combined motion is described by the aforementioned pseudoscalar, helicity \mathcal{H} , which is odd under space-inversion and even under time-reversal.

The latter example can be generalized to the statement that any pseudoscalar that is time-even is truly chiral. As a result, any collinear alignment of a polar and an axial vector, either both time-even or both time-odd, is truly chiral, and the two enantiomeric forms are the parallel and antiparallel alignments of the two vectors [6, 11].

2.2 Spin-related symmetry implications

The heart of spintronics is the spin-dependent electronic property of (solid-state) materials. These properties are quantum mechanical by nature, but can be described semi-classically using the theories of *solid-state physics* [12]. The core of this is the *band theory*, which describes the collective energy and momentum distribution of electrons in a solid using *energy bands* in *reciprocal space*. The spin degree-of-freedom is incorporated by accounting for the *spin-orbit coupling* (SOC). Also, symmetry operations can be applied to an energy band as mathematical operators. These are introduced in Appendix C.

2.2.1 The Kramers degeneracy theorem

Before discussing spintronic effects using the semi-classical picture provided by solid-state physics, we must emphasize again that spin is purely a quantum mechanical concept without any classical analogue. It has a fundamental link with time-reversal symmetry.

As described in Eqn. 2.13, the preservation of time-reversal symmetry manifests as the commutation of the (anti-unitary) operator \hat{T} with the Hamiltonian H . Under this condition, if ψ is an eigenstate of H , $\hat{T}\psi$ is also an eigenstate with the same energy eigenvalue. Further, as pointed out by Kramers [13], if the system has half-integer total spin (e.g. odd-number of electrons), ψ and $\hat{T}\psi$ are orthogonal, and therefore the system has at least a two-fold (spin) degeneracy. This is known as the

Kramers degeneracy theorem.

At thermodynamic equilibrium, the Kramers degeneracy theorem means that there cannot be a net spin polarization without breaking the time-reversal symmetry [14].

The Kramers degeneracy also extends to electron scattering. Bardarson proved that in a generic scattering event where an incoming electron can either be transmitted or reflected, the transmission eigenvalues are also spin-degenerate [15]. As a result, a spin-up and a spin-down electron (of equal energy) must have the same probability to transmit through a two-terminal phase-coherent system (conductor). This *Kramers transmission degeneracy* implies that a phase-coherent electron transport system cannot be used as a spin filter. For example, a 2D topological insulator has spin-polarized conductive edge channels, but it cannot generate a spin-polarized charge current, because the channels on its opposite edges carry opposite spins [16].

2

2.2.2 Symmetry restrictions on electronic energy band

The fundamental space and time symmetries impose restrictions on energy band of a generic electronic system. We consider here the symmetry constraints on two physical quantities that are important to charge and spin transport: the band energy $\epsilon_n(\mathbf{k}, \mathbf{S})$ (here subscript n denotes the n -th energy band, \mathbf{k} is momentum, and \mathbf{S} is spin), and the momentum-space Berry curvature $\Omega_n(\mathbf{k})$.

- (a) If a crystal is symmetric under space-inversion, its energy dispersion must obey $\epsilon_n(\mathbf{k}, \mathbf{S}) = \epsilon_n(-\mathbf{k}, \mathbf{S})$, and its Berry curvature must obey $\Omega_n(\mathbf{k}) = \Omega_n(-\mathbf{k})$. In other words, both the (spin-specific) band energy and the Berry curvature are even functions of wavevector \mathbf{k} .
- (b) If the system is invariant under time-reversal, i.e. there is no magnetic field or magnetization, the energy dispersion must obey $\epsilon_n(\mathbf{k}, \mathbf{S}) = \epsilon_n(-\mathbf{k}, -\mathbf{S})$, and for the Berry curvature $\Omega_n(\mathbf{k}) = -\Omega_n(-\mathbf{k})$. This means that the band energy is symmetric under the simultaneous reversal of momentum and spin, and that the Berry curvature is an odd function of momentum.
- (c) If space-inversion and time-reversal are both preserved, the above requirements imply $\epsilon_n(\mathbf{k}, \mathbf{S}) = \epsilon_n(\mathbf{k}, -\mathbf{S})$, and $\Omega_n(\mathbf{k}) = 0$. Therefore, there is a two-fold spin degeneracy and a vanishing Berry curvature for any momentum \mathbf{k} .

2.2.3 Spin-charge conversion by symmetry breaking

The above restrictions suggest that breaking certain symmetries can give rise to physical properties that are otherwise absent. Fig. 2.2a illustrates an energy band

under space-inversion and time-reversal symmetric conditions. Here the band is an exact overlap of two spin subbands due to the symmetry-required spin-degeneracy for all k values. This degeneracy can be lifted by breaking either the time-reversal or the space-inversion symmetry.

Time-reversal symmetry can be broken by applying an external magnetic field B , which interacts with the magnetic dipole moment μ_S of electrons with an interaction energy $H_B = -\mu_S \cdot B$. This allows to distinguish and separate opposite spin states energetically, as illustrated by the vertical splitting of the two spin subbands in Fig. 2.2b. This is known as the *Zeeman splitting*.

The breaking of space-inversion symmetry is associated with the (crystal) structure of an electronic system. It can take place at surfaces or interfaces, be induced by defects or strain, or be intrinsic to a bulk inversion-asymmetric crystal [17]. This symmetry breaking manifests as a horizontal splitting of the spin subbands in wavevector space due to SOC, as illustrated in Fig. 2.2c. At the Fermi surface, the spin orientations of the conduction electrons are locked to the wavevector k , and this dependence is called a *spin texture*.

Spin texture bridges electronic spin and momentum, and thereby gives rise to spin-dependent electron transport. However, generating an observable spin imbalance still requires to either break the time-reversal symmetry, or to bring the system out of equilibrium, which can be done by a charge current. On one hand, a charge current can induce a nonequilibrium occupation of momentum states, which generates a net spin imbalance [18]. On the other hand, a net spin imbalance can generate a net momentum imbalance, which results in a charge current [19]. These are known as the (inverse) *Edelstein effect*, and are introduced in Appendix D.

In Fig. 2.2d-f we show three typical types of spin textures. For convenience, we also refer to each spin texture as a type of SOC.

The first is the *Rashba SOC*. It arises at surfaces and interfaces, and is caused by an interfacial electric field $E = E\hat{z}$. It produces a winding spin texture where spins are always locked orthogonally to the momentum [20], as illustrated in Fig. 2.2d. It is a commonly observed type of spin texture since most electrical measurements are performed on sample surfaces [21–25].

The second is the *Dresselhaus SOC*. It stems from the lack of inversion symmetry in the bulk due to crystal structure, defects, or strain. An example spin texture is shown in Fig. 2.2e [26]. The combination of Rashba and Dresselhaus SOC can lead to more complicated spin textures, for example, one that all spins are aligned in the $x = y$ direction [22, 27–29].

The third type is the *chiral-Weyl SOC*. It has a radial spin texture where spins are always aligned parallel to the momentum, as illustrated in Fig. 2.2f. This hedgehog-style spin texture can appear in some chiral crystals or Weyl semimetals [30–34].

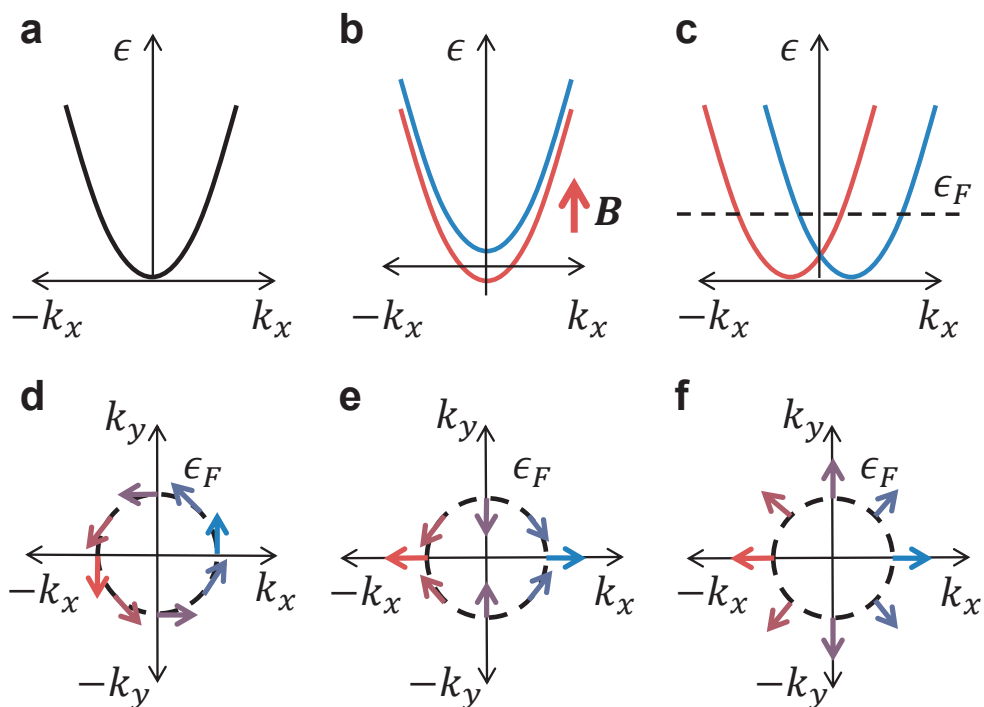


Figure 2.2: Energy band splitting and spin textures induced by symmetry breaking. **a.** A generic energy band under time-reversal and space-inversion symmetric conditions. At each wavevector k_x there exists a two-fold spin degeneracy, and at each energy ϵ , there is a four-fold degeneracy involving two opposite wavevectors and the two opposite spins. **b.** Breaking time-reversal symmetry using an out-of-plane magnetic field B gives rise to Zeeman splitting. The two vertically shifted spin subbands are colored red and blue respectively. **c.** Breaking space-inversion symmetry gives rise to horizontal subband splitting. At each wavevector the opposite spin states no longer have the same energy, and at each energy ϵ , the four-fold degeneracy is split in \mathbf{k} . At the Fermi surface, as indicated by the line cut, the momentum-dependent spin orientations form a spin texture. **d-f.** Three types of two-dimensional spin textures, known as the Rashba type, the Dresselhaus type, and the chiral-Weyl type, respectively.

Examples of these crystals include trigonal tellurium and selenium [35, 36]. Note that here we only consider solid-state materials where an energy band picture is suited. Whether this spin texture can be generalized to chiral molecules or molecular assemblies remains to be investigated.

2.2.4 The Onsager reciprocity

We have described the time-reversal symmetry as the *microscopic reversibility*: it reverses all microscopic motion and leaves the system appearing unchanged. However, macroscopic processes are generally governed by thermodynamics rather than equations of motion of microscopic particles, and are therefore irreversible. Interestingly, as discovered by Onsager, even irreversible processes are subject to constraints imposed by time-reversal symmetry. He proved that correlated macroscopic thermodynamic processes show certain symmetries in their linear response tensors, provided that the system is at the vicinity of thermodynamic equilibrium [37, 38]. This is later celebrated as the *Onsager reciprocity*.

It should be noted at first that the Onsager relations consider systems that undergo a small perturbation around the thermodynamic equilibrium, in a way that the response to the perturbation (for returning to equilibrium) is approximately linearly proportional to the perturbation itself. This is generally referred to as the *linear response regime*, and is where most solid-state electrical measurements are performed. A safe estimate for the range of the linear response regime is that the perturbation to the single-particle energy is within $k_B T$, where k_B is the *Boltzmann constant* and T is temperature [39]. We emphasize that while a perturbation within this range can definitely be considered linear, one outside this range may nevertheless still remain linear.

We illustrate the Onsager reciprocity using the three-dimensional coupled charge and heat transport in solids. The coupled transport equations are [40]

$$\mathbf{j} = S^{(1)}(\mathbf{H}, \mathbf{M})(\mathbf{E} + \frac{1}{e}\nabla\mu) + S^{(2)}(\mathbf{H}, \mathbf{M})\frac{1}{T}\nabla T, \quad (2.1)$$

$$\mathbf{Q} = -S^{(3)}(\mathbf{H}, \mathbf{M})(\mathbf{E} + \frac{1}{e}\nabla\mu) - S^{(4)}(\mathbf{H}, \mathbf{M})\frac{1}{T}\nabla T, \quad (2.2)$$

where \mathbf{j} is charge current density, \mathbf{Q} is heat flux density, \mathbf{E} is electric field, μ is the electrochemical potential of the system, e is elemental charge (positive value), and $S^{(n)}$ are linear response tensors that are dependent on magnetic field \mathbf{H} and magnetization \mathbf{M} .

The Onsager reciprocity then requires [40]

$$S_{ij}^{(1)}(\mathbf{H}, \mathbf{M}) = S_{ji}^{(1)}(-\mathbf{H}, -\mathbf{M}), \quad (2.3)$$

$$S_{ij}^{(2)}(\mathbf{H}, \mathbf{M}) = S_{ji}^{(3)}(-\mathbf{H}, -\mathbf{M}), \quad (2.4)$$

$$S_{ij}^{(4)}(\mathbf{H}, \mathbf{M}) = S_{ji}^{(4)}(-\mathbf{H}, -\mathbf{M}). \quad (2.5)$$

Note that here $S^{(1)}$ is the linear response tensor for (nearly) free electrons in an electric and a magnetic field. It becomes the conductivity tensor $(\sigma)_{\mu\nu}$ when considering

the classical electron transport in a crystal.

At mesoscopic scales, charge transport is also affected by the geometry of the conductor, and the conduction is described by the mesoscopic *conductance* rather than the material-averaged property of *conductivity*. For this, Büttiker extended the Onsager relations into the *reciprocity theorem* of linear conductance [41–43]

$$G_{ij,mn}(\mathbf{H}, \mathbf{M}) = G_{mn,ij}(-\mathbf{H}, -\mathbf{M}), \quad (2.6)$$

where G is linear conductance, whose first pair of subscripts numbers the current contacts, and the second pair denotes the voltage probe. The theorem describes that when an interchange of current and voltage probes is accompanied by the reversal of magnetic field and magnetization, the measured linear conductance remains unchanged [41–43].

In a two-terminal conductor (circuit), the reciprocity theorem reduces to

$$G_{12}(\mathbf{H}, \mathbf{M}) = G_{12}(-\mathbf{H}, -\mathbf{M}), \quad (2.7)$$

which states that the conductance is unaffected by magnetic field and magnetization reversal.

The Onsager relations and the reciprocity theorem hold strictly in the linear response regime, regardless of the microscopic details of the experiment. Its microscopic origin (the microscopic reversibility) is the same as Barron's true chirality consideration for absolute asymmetric synthesis, which is a chemical reaction that starts from achiral (racemic) reactants but yields products with a net enantiomeric excess [44].

2.3 Chirality-induced physical phenomena

Just like spin is linked to the fundamental symmetry of time-reversal, chirality relates to the fundamental symmetry of space-inversion [17]. The presence of chirality gives rise to several interesting physical phenomena, as introduced below.

2.3.1 Optical rotation and circular dichroism

The oldest yet still the most popular way to detect and distinguish chiral enantiomers is the *chiral optical rotation* experiment that Biot discovered in 1815 [45]. It observes the polarization rotation of linearly polarized light after transmitting through

a chiral medium (e.g. solution of chiral molecules or a chiral crystal) [46]. The direction of the rotation is opposite for opposite chiral enantiomers, but the rotation angles are the same. Later, it was discovered that the *ellipticity* of the transmitted light also changes after the chiral medium, and this is known as *circular dichroism* [47, 48].

Fresnel interpreted the linear polarization of light as an equal-amplitude superposition of left and right circular polarizations [49]. In a chiral medium, the opposite circular waves experience different (complex) *refractive indices*, whose real part relates to the group velocity of light, and the imaginary part relates to the absorption coefficient. This induces a difference in both phase and amplitude for the two transmitted circular waves, and therefore gives rise to optical rotation and circular dichroism, respectively.

Because of their common root in refractive index, the dispersion spectra (wavelength dependence) of the optical rotation and circular dichroism relate to each other via the *Kramers-Kronig relations* [50, 51]. Complete knowledge of one spectrum allows the calculation of the other.

Interestingly, optical rotation and circular dichroism are sensitive not only to chirality (the breaking of space-inversion symmetry [17]), but also to magnetism (the breaking of time-reversal symmetry). For the latter the effects are known as Faraday rotation (or Kerr rotation) and magnetic circular dichroism. The different symmetry origins lead to their different application scenarios, as explained from a true chirality point of view in Appendix E.

2.3.2 Generalized helicity-induced dichroism

The chiral optical rotation and circular dichroism can also be interpreted in terms of photon helicity, which, as introduced before, is the (spin) angular momentum projected along the direction of linear momentum (wavevector).

For photons, which are massless spin-one particles, a measurement of its helicity yields either \hbar or $-\hbar$, corresponding to either the left or the right circular polarization, respectively [6, 8]. The opposite helicities represent two forms of photons that are interconverted only by space-inversion but not by time-reversal, and are thereby a pair of truly chiral enantiomers (see again Fig. 2.1e). Because of this true chirality, they interact differently with the chiral medium, which gives rise to optical rotation and circular dichroism.

This helicity interpretation suggests that the dichroism effects can be generalized for other particles too. Indeed, it was proposed and later observed for electrons that their transmission through a vapor of chiral molecules is helicity-dependent [52–55]. A similar effect for neutrons were also proposed [56–58], and a suitable experimental setup was designed [59], but a convincing observation is still not realized.

Although helicity is closely related to spin, it is important to distinguish the helicity dichroism from a general spin-dependent effect [60, 61]. Unlike photons, electrons are spin-half particles with a finite rest mass. As a result, the helicity measurement of a free electron can already yield three values $\hbar/2$, 0, and $-\hbar/2$. It becomes more complicated for a bound electron, since its total angular momentum has both spin and orbital contributions, which codetermine the helicity. Moreover, when relativistic effects are included, the electron helicity also depends on its velocity and the frame of reference [6, 62, 63].

2.3.3 Magnetochiral effects

Another truly chiral physical quantity is the collinear alignment of a wavevector \mathbf{k} and a magnetic field \mathbf{B} . Their parallel and antiparallel alignments are a pair of chiral enantiomers. They can also interact differently with chiral molecules or crystals, and the corresponding effects are generally termed the *magnetochiral effects*. We introduce here two forms of magnetochiral effect, the optical and the electrical ones.

The optical magnetochiral effect concerns the transmission of nonpolarized light (with wavevector \mathbf{k}) through a chiral medium under the influence of a magnetic field \mathbf{B} . The transmission depends on whether \mathbf{k} and \mathbf{B} are parallel or antiparallel. It is effectively described by a term in the refractive index of the chiral medium that scales linearly with $\mathbf{k} \cdot \mathbf{B}$. This term is independent of the polarization of light, but changes sign when the chirality of the medium is reversed. This effect was initially independently predicted for chiral systems as a magnetic-field-dependent dielectric constant [64, 65] and a magnetic-field-induced shift of optical absorption spectrum [66, 67], before being unified by Barron from the true-chirality point of view [11]. It took another two decades until it was finally experimentally verified [68–72], and later confirmed across the electromagnetic spectrum [73–76].

Shortly after the observation of the optical magnetochiral effect, its electrical counterpart was experimentally reported in a twisted (helical) conducting wire [77]. The wavevector \mathbf{k} is here carried by a charge current \mathbf{I} , and the effect manifests as a *dc* electrical resistance that contains a term scaling with $\mathbf{I} \cdot \mathbf{B}$. This term also changes sign with chirality reversal [77]. Later, the same effect was also observed in various materials such as chiral carbon nanotubes [78, 79], chiral molecular crystals [80], chiral magnets [81, 82], and most recently, chiral elemental tellurium [83].

Thanks to the broad concept of wavevector \mathbf{k} , the magnetochiral effect can also be generalized for other waves. Indeed, it was also observed for spin waves [84, 85] and sound waves [86].

2.4 CISS experiments revisited

We now review typical CISS experiments by comparing them with other chirality-related effects, and discuss some major differences.

2.4.1 Photoemission experiments

In CISS photoemission experiments (e.g. [87, 88]), the electron transmission through (a layer of) chiral molecules was described as spin-dependent. These experiments were similar to electron helicity dichroism (e.g. [54]), in the sense that both observed the (averaged) spin polarization of electrons transmitted through a chiral environment. However, the quantitative results were drastically different. For CISS, the polarization was about 60% [88], whereas for electron helicity dichroism, it was only 10^{-4} [54]. More interestingly, the quantitative analyses for electron helicity dichroism suggested its origin as spin-dependent scattering [54], but the same theory would expect much lower spin polarization for CISS, due to the light-weight elements in the DNA molecules [89–91].

This discrepancy draws attention to major differences between the two experiments. First, the electrons traveled through very different environments. In the chiral vapor used in the helicity dichroism experiment, electrons largely traveled through (achiral) space and only occasionally scattered with chiral molecules; while in the CISS photoemission experiment, the electrons supposedly transmitted through the chiral molecules themselves. Second, the chiral molecules were in different conditions. In the helicity dichroism experiment, the molecules were (nearly) not interacting with each other or the environment, whereas for the CISS case, they were densely packed on a gold substrate, and thereby strongly interacting with each other and the substrate. Finally, the chiral molecules underwent different physical processes. In the helicity dichroism experiment, the chiral molecules only interacted with the traveling electrons, while in the CISS experiment, the molecules first interacted with incident photons, and then with the electrons.

These, among other differences, need to be addressed in future experiments in order to provide a more complete picture of CISS.

2.4.2 Magnetotransport experiments

Another major class of CISS experiment is magnetotransport [92–94]. It differs from photoemission in two key aspects. First, in transport experiments, it is the net imbalance of counter-propagating electrons that generates signals, so the single electron transmission picture for photoemission is not suited. Second, the observable in transport experiments is a charge signal (a magnetoresistance, MR), instead of a spin

polarization. Therefore, it is best to compare these experiments to other transport experiments.

The first to compare is the electrical magnetochiral effect, and again there are notable differences. First, the electrical magnetochiral effect is characterized by an additional *dc* resistance ($\Delta R_{eMCh} \propto \pm \mathbf{I} \cdot \mathbf{B}$) introduced by chirality. Evidently, this only generates a second-order correction ($\Delta V = \Delta R_{eMCh} \mathbf{I} \propto \pm I^2 \mathbf{B}$) to the *dc* conduction [80]. In comparison, the MR reported for CISS often reaches tens of percent, and sometimes even appears in the linear response regime (first order) [93]. Second, the electrical magnetochiral effect is caused by a magnetic field, while CISS transport is mostly interpreted as due to magnetization (although a magnetic field is sometimes also present) [93]. Third, the electrical magnetochiral effect generates an MR that is odd in the magnetic field, but CISS transport experiments often report MR that is even in magnetic field/magnetization [92–94].

This encourages us to compare CISS to other transport effects that may not necessarily relate to chirality, for example, the Edelstein effect (Appendix D) [19]. Because of its SOC origin, the Edelstein effect can be observed in the linear response regime, and it generates a spin imbalance from a charge current, similar to the description of CISS. However, this spin imbalance cannot be detected as a charge signal using two-terminal electrical measurements due to the Kramers transmission degeneracy and the Onsager reciprocity. In contrast, CISS describes a spin imbalance that is measured using two-terminal geometries, although it remains unclear whether this happens within the linear response regime.

It may therefore be helpful to consider nonlinear effects. We will show later (Chapter 4) that elementary nonlinear mechanisms like energy-dependent transport and energy relaxation can lift the restrictions of two-terminal measurement geometries [95, 96]. In addition, it is known that charge transport in molecular systems may be highly nonlinear [97, 98], and nonlinear mechanisms may give rise to CISS-like phenomena [99, 100]. To obtain further insight about CISS, it is important that future experiments carefully distinguish results obtained in the linear and nonlinear response regimes.

2.4.3 The role of substrate

We should also not neglect possible extrinsic contributions to the observations of CISS.

A key feature that exists in all CISS experiments is the use of substrates, and for most cases the substrate is either made of a heavy metal like gold, or a ferromagnet like nickel. There have been indications that the substrates were interacting with the adsorbed chiral molecules [101, 102], but it is still unclear what this interaction is and what consequences it may have for electron transport.

This extrinsic aspect has been given attention to [103], but there are very few thorough and quantitative theoretical analyses [104, 105]. Future investigations should therefore address this issue, and carefully assess whether and how the extrinsic mechanisms are related to the intrinsic chirality.

2.5 Appendices

A. Symmetry groups

Molecular point groups

For every molecule, there exists at least one point (not necessarily occupied by an atom) that remains unmoved under all symmetry operations of the molecule. This point is where all corresponding symmetry elements intersect. It identifies the molecule into a specific *point group* [1]. According to the *Schönflies notation system*, the point group of the tetrahedral molecule in Figure 2.1a is denoted C_{3v} , signifying its \hat{C}_3 rotation and $\hat{\sigma}_v$ mirror reflection operations.

Crystal space groups and Bravais lattices

Unlike molecules, crystals extend infinitely in space (for an ideal case). They can be seen as repetitive arrangements of identical clusters of atoms, and thus require additional translational symmetry operations to describe the repetition patterns. These include *translation* (move along a defined vector), *glider plane* (reflection followed by a translation parallel to the reflection plane), and *screw axis* (rotation followed by a translation parallel to the rotational axis).

Based on the point-group and translational symmetry operations, crystals can be categorized into 230 *space groups*, among which 22 groups are chiral and form 11 enantiomeric pairs [106]. Note that while a crystal from a chiral group must be chiral, the opposite does not have to be true. A chiral crystal may belong to 65 different groups known as the *Sohncke groups*, which contain the 22 chiral groups as a subset [107, 108]. A definitive description of all space groups and their notations can be found in the *International Tables for Crystallography* [109].

The 230 space groups can be further classified into 14 *Bravais lattices*, which are networks of *lattice points* that represent the repetitive clusters of atoms. A lattice point can be made unmoved under all point-group symmetry operations of the lattice, and can be transformed to another lattice point under a translation along a *lattice vector* \mathbf{t} . Depending on the angle and length relations among the lattice vectors, Bravais lattices form 7 *crystal systems*: triclinic, monoclinic, orthorhombic, tetragonal, cubic, trigonal, and hexagonal [12].

Time-reversal space groups

When the magnetic properties of a crystal is of interest, the space group discussion must include the \hat{T} symmetry. It reverses all angular momenta, and therefore reverses the magnetization \mathbf{M} of a magnetic crystal.

A general symmetry operator considering all point-group, translational, and time-reversal operations can be expressed as

$$\hat{G} = (\hat{\mathcal{R}} + \mathbf{t})\hat{T}, \quad (2.8)$$

where $\hat{\mathcal{R}}$ is a three-dimensional (proper or improper) rotation matrix and \mathbf{t} is a three-dimensional translation vector.

This then classifies all crystals into 1651 time-reversal space groups, which belong to three categories [40, 110]:

- (a) 230 nonmagnetic space groups, which contain time-reversal as a symmetry element;
- (b) 230 magnetic space groups, corresponding to those of group (a) but without time-reversal;
- (c) The remaining 1191 magnetic groups, whose $\widehat{\mathcal{G}}$ contains time-reversal only in combination with other symmetry operations.

These symmetry groups put restrictions on the anisotropic linear response tensors of a solid-state material to a time-dependent perturbation. For our interest in the linear-regime heat, charge, and spin transport, the translation and inversion operators can be omitted because they are included in the nature of linear response itself. This largely reduces the number of groups that need to be separately treated. Detailed discussions on the shape restrictions of various linear-response tensors can be found in Refs. [40, 111–113].

B. Fundamental symmetries

On a fundamental level, symmetries are related to our subjective perceptions of objective physical processes. Physical processes in nature are governed by fundamental laws, and are not affected by how they are interpreted. However, we adopt scientific interpretations that are built on top of systematic mathematical descriptions, which may contain ingredients that are introduced artificially and cannot be absolutely measured.

These arbitrarily defined ingredients are called *nonobservables*. They are the signs of the elemental charge, the handedness of the space coordinate system, and the arrow of time. For the scope of solid-state physics, we consider them independent of each other [114]. Therefore, reversing each of these signs will leave the entire physical process (including the system in question, all instruments for observation, and the entire associated space and time) appearing unchanged. They are called the charge, parity and time symmetries, and the sign reversals are termed *charge conjugation* (\widehat{C}), *space-inversion* (\widehat{P}), and *time-reversal* (\widehat{T}) [115], as summarized in Table 2.3.

Table 2.3: Summary of fundamental symmetry operations

Symmetry operation	nonobservable	definition
\widehat{C} charge conjugation	the absolute sign of charge	sign reversal of electric charge ^a
\widehat{P} space-inversion	the absolute handedness of space ^b	space coordinate reversal: \mathbf{r} to $-\mathbf{r}$
\widehat{T} time-reversal	the absolute direction of time ^c	time coordinate reversal: t to $-t$

^a This interconverts particles with antiparticles.

^b This can be understood as the absolute chirality (or handedness).

^c This can be understood as the absolute direction of microscopic motion.

As an example, an electric current through a solenoid causes it to interact with a magnet. This interaction does not depend on how we define the electron charge, the solenoid handedness, or the magnetic poles. If we were to change our definition of these quantities, and at the same time consistently reverse their corresponding signs in all mathematical formulas, we will obtain new formulas that still describe exactly the same physical process, and can still make correct predictions.

C. Electrons in solid-state materials

Band theory

In a molecule, electrons are described to be bound to the nuclei backbone (termed *tight binding model*). In contrast, a (conductive) solid has (conduction) electrons that are often assumed to move nearly freely in a periodic potential $V(\mathbf{r})$ (\mathbf{r} denotes space coordinate) provided by the crystal lattice (termed *nearly free electron model*). These conduction electrons can be easily manipulated using electric and magnetic fields, and their motion can be measured accurately as charge currents. Therefore, the *electron transport behavior* in a solid provides a powerful tool to probe its properties.

Quantum mechanics describes an electron using a space- and time-dependent *wave function*, which is obtained by solving the *Schrödinger equation*. Central to this is a *Hamiltonian* operator that describes the total energy of the electron. Under the nearly free electron model, the Hamiltonian of an electron is given by

$$H = -\frac{\hbar^2}{2m}\nabla^2 + V(\mathbf{r}), \quad (2.9)$$

where \hbar is the *reduced Planck constant*, m is the electron mass, and $V(\mathbf{r})$ is the lattice periodic potential satisfying $V(\mathbf{r} + \mathbf{t}) = V(\mathbf{r})$. The eigenfunctions of this Hamiltonian constitute the wave function of the electron (without the time-variant part), which is described by a *Bloch wave*

$$\psi_{\mathbf{k}}(\mathbf{r}) = u_{\mathbf{k}}(\mathbf{r}) \exp(i\mathbf{k} \cdot \mathbf{r}), \quad (2.10)$$

where \mathbf{k} is a *wavevector*, and $u_{\mathbf{k}}(\mathbf{r})$ modulates the wave amplitude with the same period \mathbf{t} .

The wavevector \mathbf{k} determines a crystal momentum $\hbar\mathbf{k}$ and an energy $\epsilon(\mathbf{k})$ of the electron. The relation between \mathbf{k} and $\epsilon(\mathbf{k})$ is called the *dispersion relation*, and captures essential electron transport properties of the crystal. It is mostly continuous with \mathbf{k} but has gaps at k_i (i represents spatial coordinate) values that are integer multiples of π/a_i , where a_i is the lattice spacing in the corresponding direction [116]. The energy gaps separate the allowed energies of an electron into *energy bands*.

In an actual crystal formed by a large but finite number of unit cells, each energy band breaks into the same number of discrete wavevector states, which are equally spaced in k and can each accommodate two valence electrons with opposite spins (two-fold spin *degeneracy*). The electrons in the crystal occupy these states from low to high energy. If a number of bands would be exactly filled with electrons and the rest left completely empty, the crystal would be an *insulator* [117]. Otherwise, if a band would be only partially filled, the crystal would be a *metal* or a *semimetal*. In between the two cases is a *semiconductor*, in which the bands could have been filled like an insulator, but due to a relatively small gap between the highest filled band (*valence band*) and the lowest unfilled one (*conduction band*), electrons occupy a number of states in the latter due to thermal distribution (*Fermi-Dirac distribution*), giving rise to finite conductivity. The *band gap* of a semiconductor is usually comparable to the energy of visible-range photons, and therefore allows for the manipulation of conduction electrons using light.

Spin-orbit coupling

A moving electron in the potential $V(\mathbf{r})$ experiences an effective magnetic field \mathbf{B}_{eff} in its rest frame due to relativistic transformations between electric and magnetic fields

$$\mathbf{B}_{eff} = -\frac{\nabla V(\mathbf{r}) \times \mathbf{p}}{emc^2}, \quad (2.11)$$

where \mathbf{p} is the linear momentum of the electron. This magnetic field interacts with the electron's intrinsic magnetic dipole moment $\boldsymbol{\mu}_S = -g\mu_B\mathbf{S}/\hbar$ ($g \approx 2$, \mathbf{S} is the spin angular momentum of the electron and $\mu_B = e\hbar/2m$ is the Bohr magneton). This interaction is called *spin-orbit coupling* (SOC), and it has energy $H_{SO} = -\boldsymbol{\mu}_S \cdot \mathbf{B}_{eff}/2$ (the factor 1/2 comes from a relativistic correction due to Thomas precession [118]).

The quantum mechanical operator for SOC is

$$H_{SO} = \frac{1}{2} \mu_B \boldsymbol{\sigma} \cdot \mathbf{B}_{eff} = i \frac{\hbar^2}{4m^2 c^2} \boldsymbol{\sigma} \cdot (\nabla V(\mathbf{r}) \times \nabla), \quad (2.12)$$

where momentum \mathbf{p} is replaced by its operator representation $-i\hbar\nabla$, and $\boldsymbol{\sigma} = 2\mathbf{S}/\hbar$ is the *Pauli matrix* vector for spin, whose elements are $\hat{\sigma}_x = \begin{pmatrix} 0 & 1 \\ 1 & 0 \end{pmatrix}$, $\hat{\sigma}_y = \begin{pmatrix} 0 & -i \\ i & 0 \end{pmatrix}$, $\hat{\sigma}_z = \begin{pmatrix} 1 & 0 \\ 0 & -1 \end{pmatrix}$.

For an electron in a crystal, the term H_{SO} is added to the original Hamiltonian (Eqn. 2.9) to take into account spin-orbit effects. As a result, Eqn. 2.10 is no longer a solution to the Schrödinger equation. The new solution contains spin as a variable, and writes $\psi_{\mathbf{k},\mathbf{S}}(\mathbf{r})$. It is still a Bloch wave, but the two-fold spin degeneracy for each \mathbf{k} -state is lifted. Consequently, the crystal now has spin-dependent dispersion relation $\epsilon(\mathbf{k}, \mathbf{S})$, and the exact dependence is determined by the crystal symmetry.

Symmetry operation on energy bands

In general, the crystal symmetry operator \hat{G} leaves the crystal, as well as its potential $V(\mathbf{r})$, appearing unchanged. Consequently, as pointed out by Wigner, \hat{G} commutes with the Hamiltonian H of the nearly free electrons in the crystal [2]. It further implies that, if ψ is a Bloch eigenstate of H with energy ϵ , $\hat{G}\psi$ is also a Bloch eigenstate of H with exactly the same energy. This is shown by applying \hat{G} to the entire Schrödinger equation

$$\hat{G}(H\psi) = \hat{G}(\epsilon\psi) \Rightarrow H(\hat{G}\psi) = \epsilon(\hat{G}\psi). \quad (2.13)$$

The symmetry operator \hat{G} therefore transforms the old eigenstate $\psi_{\mathbf{k},\mathbf{S}}(\mathbf{r})$ to the new one $\hat{G}\psi_{\mathbf{k},\mathbf{S}}(\mathbf{r})$, which has the same energy.

In order to obtain $\hat{G}\psi_{\mathbf{k},\mathbf{S}}(\mathbf{r})$, one can apply \hat{G} to the original Schrödinger equation, and then modify the indices of wavevector \mathbf{k} to \mathbf{k}' and spin \mathbf{S} to \mathbf{S}' , in order to reconstruct a new Schrödinger equation that has the same energy eigenvalue. The transformations $\mathbf{k} \Rightarrow \mathbf{k}'$ and $\mathbf{S} \Rightarrow \mathbf{S}'$ then describe the symmetry operations on the energy band. The transformed wave function $\hat{G}\psi_{\mathbf{k},\mathbf{S}}(\mathbf{r})$ also provides symmetry information about phase-related properties, such as the Berry curvature.

Table 2.4: Symmetry operations on an energy band

Symmetry operation \hat{G}	transformation of \mathbf{k}, \mathbf{S}	transformation of wave function
Lattice translation: $\mathbf{r} \Rightarrow \mathbf{r} + \mathbf{t}$	$\mathbf{k} \Rightarrow \mathbf{k},$ $\mathbf{S} \Rightarrow \mathbf{S}.$	$\hat{G}\psi_{\mathbf{k},\mathbf{S}}(\mathbf{r}) = \psi_{\mathbf{k},\mathbf{S}}(\mathbf{r}) \exp(i\mathbf{k} \cdot \mathbf{t}) = \psi_{\mathbf{k},\mathbf{S}}(\mathbf{r}).$ ^a
Proper rotation: $\mathbf{r} \Rightarrow \hat{\mathcal{R}}_{\mathbf{r}} \mathbf{r}$	$\mathbf{k} \Rightarrow \hat{\mathcal{R}}_{\mathbf{r}}^{-1} \mathbf{k},$ $\mathbf{S} \Rightarrow \hat{\mathcal{R}}_{\mathbf{S}} \mathbf{S}.$	$\hat{G}\psi_{\mathbf{k},\mathbf{S}}(\mathbf{r}) = \hat{\mathcal{R}}_{\mathbf{S}}^{-1} \psi_{\mathbf{k},\mathbf{S}}(\hat{\mathcal{R}}_{\mathbf{r}} \mathbf{r}).$ ^b
Space-inversion: $\mathbf{r} \Rightarrow -\mathbf{r}$	$\mathbf{k} \Rightarrow -\mathbf{k},$ $\mathbf{S} \Rightarrow \mathbf{S}.$	$\hat{G}\psi_{\mathbf{k},\mathbf{S}}(\mathbf{r}) = \psi_{\mathbf{k},\mathbf{S}}(-\mathbf{r}).$
Time-reversal: $t \Rightarrow -t, i \Rightarrow -i.$ ^c	$\mathbf{k} \Rightarrow -\mathbf{k},$ $\mathbf{S} \Rightarrow -\mathbf{S}.$	for $\psi_{\mathbf{k},\mathbf{S}}(\mathbf{r}) = \alpha \uparrow\rangle + \beta \downarrow\rangle,$ $\hat{G}\psi_{\mathbf{k},\mathbf{S}}(\mathbf{r}) = -\beta^* \uparrow\rangle + \alpha^* \downarrow\rangle.$ ^d

^a Lattice translation is by definition an intrinsic symmetry of all Bloch waves.

^b $\hat{\mathcal{R}}_{\mathbf{r}}$ and $\hat{\mathcal{R}}_{\mathbf{S}}$ denote the same rotation, but act in real space and spin space respectively.

^c The time-reversal operator \hat{T} is antiunitary, it reverse t and converts all complex values to their complex conjugate [2]. For a spin-half system $\hat{T}^2\psi = -\psi$.

^d The $*$ denotes complex conjugate, $|\uparrow\rangle, |\downarrow\rangle$ are spin angular momentum eigenvectors for \mathbf{S} , and α, β contain the spatial coordinate. Note that the inner product $\langle \hat{G}\psi_{\mathbf{k},\mathbf{S}} | \psi_{\mathbf{k},\mathbf{S}} \rangle = 0$, indicating that the two time-reversed states are orthogonal, and have opposite spins.

In Table 2.4 we list the symmetry operations on an energy band and the corresponding transformed wave functions $\hat{G}\psi_{\mathbf{k},\mathbf{S}}(\mathbf{r})$.

D. The Edelstein effect

When SOC is considered and for an inversion-asymmetric crystal, the Fermi surface contains a spin texture, which correlates spin orientation with wavevector states.

At equilibrium, opposite wavevector states are always equally occupied. Consequently, if the crystal preserves time-reversal symmetry, $\epsilon_n(\mathbf{k}, \mathbf{S}) = \epsilon_n(-\mathbf{k}, -\mathbf{S})$ provides that opposite spin states are also always equally occupied. Therefore, conduction electrons on the Fermi surface will always have balanced spins, i.e. there cannot be a net spin imbalance (spin accumulation). However, if the equilibrium is broken, for example by a charge current, the opposite wavevector states (along the current direction) will no longer be equally occupied. This consequently gives rise to a net spin imbalance. Such a current-induced spin accumulation is the *Edelstein effect*, or *Rashba-Edelstein effect*, since it was originally calculated by Edelstein for a Rashba-type spin texture [19].

There also exists an Onsager reciprocal effect, the inverse Edelstein effect, where a spin accumulation injected into an inversion asymmetric crystal gives rise to a charge current. The Edelstein and inverse Edelstein effects demonstrate the interconversion between charge and spin signals without evoking magnetism, and prove promising for spintronic applications. Both effects have been thoroughly theoretically studied and experimentally confirmed [18, 119–124].

E. True chirality and optical rotations

The two types of (chiral and magnetic) optical rotation effects can be distinguished from the true chirality point of view.

For the chiral optical rotation, the system in question is the solution of chiral molecules, and the observable is the rotation of light polarization. A space-inversion operation reverts the chirality of all molecules in the solution, and therefore changes the sign of the observed optical rotation, but a time-reversal operation leaves the molecules unchanged. Therefore, the experiment is truly chiral.

The Faraday rotation also rotates linearly polarized light in an (achiral) medium, but only upon the application of a longitudinal magnetic field. For this, the system in question is the medium and the applied magnetic field, and the observable is again the optical rotation. The achiral medium itself is unchanged under both space-inversion and time-reversal, so the symmetry of the observable is solely determined by the symmetry of the magnetic field, which, as we already knew, is odd under time-reversal and even under space-inversion. As a result, the Faraday rotation experiment is not truly chiral.

Because of this distinction, Faraday rotation is used in optical isolators [125], which is usually mounted at the output of a laser to block reflected beams. It rotates both the output and the reflected linearly polarized laser beams by 45° to the same direction with respect to the magnetic field, so that the reflected beam becomes orthogonally polarized to the output, and can be blocked by a linear polarizer. This cannot be done by a chiral optical rotator, which rotates the output and reflected beams with respect to their (opposite) propagation directions, and the two rotations always cancel each other out.

Bibliography

- [1] P. W. Atkins and R. S. Friedman, *Molecular quantum mechanics*, ch. 5, pp. 125–165. Oxford University Press Inc., New York, 5 ed., 2011.

- [2] E. P. Wigner, *Group theory: and its application to the quantum mechanics of atomic spectra*, Academic Press Inc., New York, 1959.
- [3] L. D. Barron, "Optical activity and time reversal," *Molecular Physics* **43**(6), pp. 1395–1406, 1981.
- [4] L. D. Barron, "True and false chirality and parity violation," *Chemical Physics Letters* **123**(5), pp. 423–427, 1986.
- [5] L. D. Barron, "True and false chirality and absolute asymmetric synthesis," *Journal of the American Chemical Society* **108**(18), pp. 5539–5542, 1986.
- [6] L. D. Barron, "Fundamental symmetry aspects of molecular chirality," in *New developments in molecular chirality*, pp. 1–55, Springer, Dordrecht, 1991.
- [7] M. Avalos, R. Babiano, P. Cintas, J. L. Jiménez, J. C. Palacios, and L. D. Barron, "Absolute asymmetric synthesis under physical fields: facts and fictions," *Chemical Reviews* **98**(7), pp. 2391–2404, 1998.
- [8] H. Zocher and C. Török, "About space-time asymmetry in the realm of classical general and crystal physics," *Proceedings of the National Academy of Sciences* **39**(7), p. 681, 1953.
- [9] P. Gerike, "A new absolute asymmetric synthesis," *Naturwissenschaften* **62**(1), pp. 38–39, 1975.
- [10] C. A. Mead, A. Moscovitz, H. Wynberg, and F. Meuwese, "The influence of an electric and magnetic field in chemical reactions," *Tetrahedron Letters* **18**(12), pp. 1063–1064, 1977.
- [11] L. Barron and J. Vrbancich, "Magneto-chiral birefringence and dichroism," *Molecular Physics* **51**(3), pp. 715–730, 1984.
- [12] C. Kittel and P. McEuen, *Introduction to solid state physics*, John Wiley & Sons, Inc, Hoboken, NJ, USA, 8 ed., 2005.
- [13] H. A. Kramers, "Théorie générale de la rotation paramagnétique dans les cristaux," *Proc. Acad. Amst* **33**, pp. 959–972, 1930.
- [14] The two degenerate spin states have opposite wavevectors, since wavevector changes sign under time-reversal operation. This pair of states is called a Kramers pair.
- [15] J. H. Bardarson, "A proof of the Kramers degeneracy of transmission eigenvalues from antisymmetry of the scattering matrix," *Journal of Physics A: Mathematical and Theoretical* **41**(40), p. 405203, 2008.
- [16] M. Z. Hasan and C. L. Kane, "Colloquium: topological insulators," *Reviews of Modern Physics* **82**(4), p. 3045, 2010.
- [17] Note here the difference between space-inversion \hat{P} and (molecular or crystal) inversion \hat{i} . The \hat{P} operation acts on the frame of reference but not on the physical object itself, while \hat{i} does the opposite. The \hat{P} operation does not have a center of inversion, and manifests as the reversal of the handedness of the space coordinate system, while \hat{i} has a center of inversion, and manifests as inverting spatial positions with respect to the center. A strict notion of space-inversion \hat{P} includes not only inversion \hat{i} , but also any improper rotations \hat{S}_n . Therefore, an \hat{i} -asymmetric crystal can still be symmetric under \hat{P} , unless it is chiral. However, in solid-state physics, the notions of space-inversion and inversion are usually not distinguished. Nevertheless, it is important to bear in mind their differences.
- [18] T. Furukawa, Y. Shimokawa, K. Kobayashi, and T. Itou, "Observation of current-induced bulk magnetization in elemental tellurium," *Nature Communications* **8**(1), p. 954, 2017.
- [19] V. M. Edelstein, "Spin polarization of conduction electrons induced by electric current in two-dimensional asymmetric electron systems," *Solid State Communications* **73**(3), pp. 233–235, 1990.
- [20] The interfacial electric field gives rise to an additional SOC term in the Hamiltonian $H_R = \alpha_R (\mathbf{E} \times \mathbf{k}) \cdot \boldsymbol{\sigma}$, with α_R being the Rashba parameter.
- [21] A. Soumyanarayanan, N. Reyren, A. Fert, and C. Panagopoulos, "Emergent phenomena induced by spin-orbit coupling at surfaces and interfaces," *Nature* **539**(7630), p. 509, 2016.
- [22] A. Manchon, H. C. Koo, J. Nitta, S. Frolov, and R. Duine, "New perspectives for Rashba spin-orbit coupling," *Nature Materials* **14**(9), p. 871, 2015.
- [23] K. Kondou, R. Yoshimi, A. Tsukazaki, Y. Fukuma, J. Matsuno, K. Takahashi, M. Kawasaki, Y. Tokura, and Y. Otani, "Fermi-level-dependent charge-to-spin current conversion by Dirac surface states of topological insulators," *Nature Physics* **12**(11), p. 1027, 2016.
- [24] J.-C. Rojas-Sánchez, S. Oyarzún, Y. Fu, A. Marty, C. Vergnaud, S. Gambarelli, L. Vila, M. Jamet, Y. Ohtsubo, A. Taleb-Ibrahimi, et al., "Spin to charge conversion at room temperature by spin pumping into a new type of topological insulator: α -Sn films," *Physical Review Letters* **116**(9), p. 096602, 2016.
- [25] J. Mendes, O. A. Santos, L. Meireles, R. Lacerda, L. Vilela-Leão, F. Machado, R. Rodríguez-Suárez, A. Azevedo, and S. Rezende, "Spin-current to charge-current conversion and magnetoresistance in a hybrid structure of graphene and yttrium iron garnet," *Physical Review Letters* **115**(22), p. 226601, 2015.
- [26] The Dresselhaus Hamiltonian contains terms to the third order of wavevectors, and usually results in a spin texture that is three-dimensional. We show here in Fig. 2.2e only a reduced form where the only element breaking the inversion symmetry is the crystal strain in the z -direction, so that the spin texture only appears in the x - y plane.

- [27] N. Averkiev and L. Golub, "Giant spin relaxation anisotropy in zinc-blende heterostructures," *Physical Review B* **60**(23), p. 15582, 1999.
- [28] A. Sasaki, S. Nonaka, Y. Kunihashi, M. Kohda, T. Bauernfeind, T. Dollinger, K. Richter, and J. Nitta, "Direct determination of spin-orbit interaction coefficients and realization of the persistent spin helix symmetry," *Nature Nanotechnology* **9**(9), p. 703, 2014.
- [29] L. Hu, H. Huang, Z. Wang, W. Jiang, X. Ni, Y. Zhou, V. Zielasek, M. G. Lagally, B. Huang, and F. Liu, "Ubiquitous spin-orbit coupling in a screw dislocation with high spin coherency," *Physical Review Letters* **121**(6), p. 066401, 2018.
- [30] It may appear at time-reversal-invariant (or rotation-protected) spin-degenerate k -states, which are known as Kramers-Weyl nodes, where the two spin subbands cross.
- [31] G. Chang, B. J. Wieder, F. Schindler, D. S. Sanchez, I. Belopolski, S.-M. Huang, B. Singh, D. Wu, T.-R. Chang, T. Neupert, *et al.*, "Topological quantum properties of chiral crystals," *Nature Materials* **17**(11), pp. 978–985, 2018.
- [32] S. Wang, B.-C. Lin, A.-Q. Wang, D.-P. Yu, and Z.-M. Liao, "Quantum transport in Dirac and Weyl semimetals: a review," *Advances in Physics: X* **2**(3), pp. 518–544, 2017.
- [33] M. J. Duff, "Twenty years of the Weyl anomaly," *Classical and Quantum Gravity* **11**(6), p. 1387, 1994.
- [34] K.-S. Kim and J.-H. Han, "Interplay between chiral magnetic and Kondo effects in Weyl metal phase," *Current Applied Physics* **19**(3), pp. 236–240, 2019.
- [35] M. Hirayama, R. Okugawa, S. Ishibashi, S. Murakami, and T. Miyake, "Weyl node and spin texture in trigonal tellurium and selenium," *Physical Review Letters* **114**(20), p. 206401, 2015.
- [36] M. Sakano, M. Hirayama, T. Takahashi, S. Akebi, M. Nakayama, K. Kuroda, K. Taguchi, T. Yoshikawa, K. Miyamoto, T. Okuda, *et al.*, "Radial spin texture in elemental tellurium with chiral crystal structure," *Physical Review Letters* **124**(13), p. 136404, 2020.
- [37] L. Onsager, "Reciprocal relations in irreversible processes. I.," *Physical Review* **37**(4), p. 405, 1931.
- [38] L. Onsager, "Reciprocal relations in irreversible processes. II.," *Physical Review* **38**(12), p. 2265, 1931.
- [39] S. Datta, *Electronic transport in mesoscopic systems*, Cambridge University Press, 1997.
- [40] W. H. Kleiner, "Space-time symmetry of transport coefficients," *Physical Review* **142**(2), p. 318, 1966.
- [41] M. Büttiker, "Symmetry of electrical conduction," *IBM Journal of Research and Development* **32**(3), pp. 317–334, 1988.
- [42] M. Büttiker, "Four-terminal phase-coherent conductance," *Physical Review Letters* **57**(14), p. 1761, 1986.
- [43] M. Büttiker, "Role of quantum coherence in series resistors," *Physical Review B* **33**(5), p. 3020, 1986.
- [44] L. D. Barron, "Reactions of chiral molecules in the presence of a time-non-invariant enantiomorphous influence: a new kinetic principle based on the breakdown of microscopic reversibility," *Chemical Physics Letters* **135**(1-2), pp. 1–8, 1987.
- [45] J.-B. Biot, "Phénomènes de polarisation successive, observés dans des fluides homogènes," *Bull. Soc. Philomath* **190**, p. 1815, 1815.
- [46] J. T. Yang, "Remembrance of things past," in *Circular dichroism and the conformational analysis of biomolecules*, pp. 1–24, Springer, Boston, 1996.
- [47] J. A. Schellman, "Symmetry rules for optical rotation," *Accounts of Chemical Research* **1**(5), pp. 144–151, 1968.
- [48] N. Berova, K. Nakanishi, R. W. Woody, and R. Woody, *Circular dichroism: principles and applications*, Wiley-VCH, New York, 2 ed., 2000.
- [49] M. A. Fresnel, "Considérations théoriques sur la polarisation de la lumière," *Bulletin des Sciences*, pp. 147–158, 1824.
- [50] J. D. Jackson, *Classical Electrodynamics*, Wiley-VCH, New York, 2 ed., 1975.
- [51] B. Y.-K. Hu, "Kramers–Kronig in two lines," *American Journal of Physics* **57**(9), p. 821, 1989.
- [52] D. M. Campbell and P. S. Farago, "Spin-dependent electron scattering from optically active molecules," *Nature* **318**(6041), p. 52, 1985.
- [53] D. M. Campbell and P. S. Farago, "Electron optic dichroism in camphor," *Journal of Physics B: Atomic and Molecular Physics* **20**(19), p. 5133, 1987.
- [54] S. Mayer and J. Kessler, "Experimental verification of electron optic dichroism," *Physical Review Letters* **74**(24), p. 4803, 1995.
- [55] K. Blum and D. Thompson, "Chiral effects in electron scattering by molecules," *Advances in Atomic Molecular and Optical Physics* **38**, pp. 39–86, 1998.
- [56] P. Kabir, G. Karl, and E. Obryk, "Optical activity for neutrons," *Physical Review D* **10**(5), p. 1471, 1974.
- [57] V. F. Sears, "Electromagnetic neutron-atom interactions," *Physics Reports* **141**(5), pp. 281–317, 1986.
- [58] N. F. Ramsey, "Dipole moments and spin rotations of the neutron," *Physics Reports* **43**(10), pp. 409–421, 1978.
- [59] W. Snow, E. Anderson, L. Barrón-Palos, C. Bass, T. Bass, B. E. Crawford, C. Crawford, J. Dawkins, D. Esposito, J. Fry, *et al.*, "A slow neutron polarimeter for the measurement of parity-odd neutron rotary power," *Review of Scientific Instruments* **86**(5), p. 055101, 2015.

- [60] A. Garay and J. Ahlgren-Beckendorf, "Differential interaction of chiral β -particles with enantiomers," *Nature* **346**(6283), p. 451, 1990.
- [61] R. A. Rosenberg, "Spin-polarized electron induced asymmetric reactions in chiral molecules," in *Electronic and Magnetic Properties of Chiral Molecules and Supramolecular Architectures*, pp. 279–306, Springer, 2010.
- [62] D. M. Lazarus and J. S. Greenberg, "Measurement of the velocity dependence of the helicity of beta particles from Co^{60} ," *Physical Review D* **2**(1), p. 45, 1970.
- [63] Y. B. Zel'Dovich and D. Saakyan, "Asymmetry of breakup of optically active molecules by longitudinally polarized relativistic electrons," *Soviet Journal of Experimental and Theoretical Physics* **51**, p. 1118, 1980.
- [64] N. Baranova, Y. V. Bogdanov, and B. Y. Zel'Dovich, "Electrical analog of the faraday effect and other new optical effects in liquids," *Optics Communications* **22**(2), pp. 243–247, 1977.
- [65] N. Baranova and B. Y. Zel'Dovich, "Theory of a new linear magnetorefractive effect in liquids," *Molecular Physics* **38**(4), pp. 1085–1098, 1979.
- [66] G. Wagnière and A. Meier, "The influence of a static magnetic field on the absorption coefficient of a chiral molecule," *Chemical Physics Letters* **93**(1), pp. 78–81, 1982.
- [67] G. Wagniere, "Magnetochiral dichroism in emission. Photoselection and the polarization of transitions," *Chemical Physics Letters* **110**(5), pp. 546–551, 1984.
- [68] G. Rikken and E. Raupach, "Observation of magneto-chiral dichroism," *Nature* **390**(6659), p. 493, 1997.
- [69] P. Kleindienst and G. H. Wagnière, "Interferometric detection of magnetochiral birefringence," *Chemical Physics Letters* **288**(1), pp. 89–97, 1998.
- [70] G. Rikken and E. Raupach, "Pure and cascaded magnetochiral anisotropy in optical absorption," *Physical Review E* **58**(4), p. 5081, 1998.
- [71] M. Vallet, R. Ghosh, A. Le Floch, T. Ruchon, F. Bretenaker, and J.-Y. Thépot, "Observation of magnetochiral birefringence," *Physical Review Letters* **87**(18), p. 183003, 2001.
- [72] G. Rikken and E. Raupach, "Enantioselective magnetochiral photochemistry," *Nature* **405**(6789), p. 932, 2000.
- [73] S. Tomita, K. Sawada, A. Porokhnyuk, and T. Ueda, "Direct observation of magnetochiral effects through a single metamolecule in microwave regions," *Physical Review Letters* **113**(23), p. 235501, 2014.
- [74] Y. Okamura, F. Kagawa, S. Seki, M. Kubota, M. Kawasaki, and Y. Tokura, "Microwave magnetochiral dichroism in the chiral-lattice magnet Cu_2OSeO_3 ," *Physical Review Letters* **114**(19), p. 197202, 2015.
- [75] M. Ceolín, S. Goberna-Ferrón, and J. R. Galán-Mascarós, "Strong hard X-ray magnetochiral dichroism in paramagnetic enantiopure molecules," *Advanced Materials* **24**(23), pp. 3120–3123, 2012.
- [76] R. Sessoli, M.-E. Boulon, A. Caneschi, M. Mannini, L. Poggini, F. Wilhelm, and A. Rogalev, "Strong magneto-chiral dichroism in a paramagnetic molecular helix observed by hard X-rays," *Nature Physics* **11**(1), p. 69, 2015.
- [77] G. Rikken, J. Fölling, and P. Wyder, "Electrical magnetochiral anisotropy," *Physical Review Letters* **87**(23), p. 236602, 2001.
- [78] V. Krstić, S. Roth, M. Burghard, K. Kern, and G. Rikken, "Magneto-chiral anisotropy in charge transport through single-walled carbon nanotubes," *The Journal of Chemical Physics* **117**(24), pp. 11315–11319, 2002.
- [79] J. Wei, M. Shimogawa, Z. Wang, I. Radu, R. Dormaier, and D. H. Cobden, "Magnetic-field asymmetry of nonlinear transport in carbon nanotubes," *Physical Review Letters* **95**(25), p. 256601, 2005.
- [80] F. Pop, P. Auban-Senzier, E. Canadell, G. L. Rikken, and N. Avarvari, "Electrical magnetochiral anisotropy in a bulk chiral molecular conductor," *Nature Communications* **5**, p. 3757, 2014.
- [81] T. Yokouchi, N. Kanazawa, A. Kikkawa, D. Morikawa, K. Shibata, T. Arima, Y. Taguchi, F. Kagawa, and Y. Tokura, "Electrical magnetochiral effect induced by chiral spin fluctuations," *Nature Communications* **8**(1), p. 866, 2017.
- [82] R. Aoki, Y. Kousaka, and Y. Togawa, "Anomalous nonreciprocal electrical transport on chiral magnetic order," *Physical Review Letters* **122**(5), p. 057206, 2019.
- [83] G. Rikken and N. Avarvari, "Strong electrical magnetochiral anisotropy in tellurium," *Physical Review B* **99**(24), p. 245153, 2019.
- [84] S. Seki, Y. Okamura, K. Kondou, K. Shibata, M. Kubota, R. Takagi, F. Kagawa, M. Kawasaki, G. Tatara, Y. Otani, et al., "Magnetochiral nonreciprocity of volume spin wave propagation in chiral-lattice ferromagnets," *Physical Review B* **93**(23), p. 235131, 2016.
- [85] Y. Iguchi, S. Uemura, K. Ueno, and Y. Onose, "Nonreciprocal magnon propagation in a noncentrosymmetric ferromagnet LiFe_3O_8 ," *Physical Review B* **92**(18), p. 184419, 2015.
- [86] T. Nomura, X.-X. Zhang, S. Zherlitsyn, J. Wosnitzer, Y. Tokura, N. Nagaosa, and S. Seki, "Phonon magnetochiral effect," *Physical Review Letters* **122**(14), p. 145901, 2019.
- [87] K. Ray, S. P. Ananthavel, D. H. Waldeck, and R. Naaman, "Asymmetric scattering of polarized electrons by organized organic films of chiral molecules," *Science* **283**(5403), pp. 814–816, 1999.
- [88] B. Göhler, V. Hamelbeck, T. Z. Markus, M. Kettner, G. F. Hanne, Z. Vager, R. Naaman, and H. Zacharias, "Spin se-

- lectivity in electron transmission through self-assembled monolayers of double-stranded DNA," *Science* **331**(6019), pp. 894–897, 2011.
- [89] R. Fandreyer, D. Thompson, and K. Blum, "Attenuation of longitudinally polarized electron beams by chiral molecules," *Journal of Physics B: Atomic, Molecular and Optical Physics* **23**(17), p. 3031, 1990.
- [90] J. Tennyson, "Electron–molecule collision calculations using the R-matrix method," *Physics Reports* **491**(2–3), pp. 29–76, 2010.
- [91] S. Yeganeh, M. A. Ratner, E. Medina, and V. Mujica, "Chiral electron transport: scattering through helical potentials," *The Journal of Chemical Physics* **131**(1), p. 014707, 2009.
- [92] Z. Xie, T. Z. Markus, S. R. Cohen, Z. Vager, R. Gutierrez, and R. Naaman, "Spin specific electron conduction through DNA oligomers," *Nano Letters* **11**(11), pp. 4652–4655, 2011.
- [93] V. Kiran, S. P. Mathew, S. R. Cohen, I. Hernández Delgado, J. Lacour, and R. Naaman, "Helicenes—A new class of organic spin filter," *Advanced Materials* **28**, pp. 1957–1962, 2016.
- [94] M. Suda, Y. Thathong, V. Promarak, H. Kojima, M. Nakamura, T. Shiraogawa, M. Ehara, and H. M. Yamamoto, "Light-driven molecular switch for reconfigurable spin filters," *Nature Communications* **10**(1), p. 2455, 2019.
- [95] X. Yang, C. H. van der Wal, and B. J. van Wees, "Detecting chirality in two-terminal electronic nanodevices," *Nano Letters*, 2020.
- [96] R. Jansen, A. Spiesser, H. Saito, Y. Fujita, S. Yamada, K. Hamaya, and S. Yuasa, "Nonlinear electrical spin conversion in a biased ferromagnetic tunnel contact," *Physical Review Applied* **10**(6), p. 064050, 2018.
- [97] K. Michaeli, D. N. Beratan, D. H. Waldeck, and R. Naaman, "Voltage-induced long-range coherent electron transfer through organic molecules," *Proceedings of the National Academy of Sciences* **116**(13), pp. 5931–5936, 2019.
- [98] F. Evers, R. Korytár, S. Tewari, and J. M. van Ruitenbeek, "Advances and challenges in single-molecule electron transport," *Review of Modern Physics* **92**(3), p. 035001.
- [99] E. Díaz, A. Contreras, J. Hernández, and F. Domínguez-Adame, "Effective nonlinear model for electron transport in deformable helical molecules," *Physical Review E* **98**(5), p. 052221, 2018.
- [100] J. Fransson, "Chirality-induced spin selectivity: The role of electron correlations," *The Journal of Physical Chemistry Letters* **10**(22), pp. 7126–7132, 2019.
- [101] K. Banerjee-Ghosh, O. B. Dor, F. Tassinari, E. Capua, S. Yochelis, A. Capua, S.-H. Yang, S. S. Parkin, S. Sarkar, L. Kronik, *et al.*, "Separation of enantiomers by their enantiospecific interaction with achiral magnetic substrates," *Science* **360**(6395), pp. 1331–1334, 2018.
- [102] O. B. Dor, S. Yochelis, A. Radko, K. Vankayala, E. Capua, A. Capua, S.-H. Yang, L. T. Baczewski, S. S. P. Parkin, R. Naaman, *et al.*, "Magnetization switching in ferromagnets by adsorbed chiral molecules without current or external magnetic field," *Nature Communications* **8**, p. 14567, 2017.
- [103] R. Naaman, Y. Paltiel, and D. H. Waldeck, "Chirality and spin: A different perspective on enantioselective interactions," *CHIMIA International Journal for Chemistry* **72**(6), pp. 394–398, 2018.
- [104] S. Dalum and P. Hedegård, "Theory of chiral induced spin selectivity," *Nano Letters* **19**(8), pp. 5253–5259, 2019.
- [105] D. Nürenberg and H. Zacharias, "Evaluation of spin-flip scattering in chirality-induced spin selectivity using the Riccati equation," *Physical Chemistry Chemical Physics* **21**(7), pp. 3761–3770, 2019.
- [106] C. Bradley and A. Cracknell, *The mathematical theory of symmetry in solids: representation theory for point groups and space groups*, Oxford University Press, 2009.
- [107] M. Nespolo, M. I. Aroyo, and B. Souvignier, "Crystallographic shelves: space-group hierarchy explained," *Journal of Applied Crystallography* **51**(5), pp. 1481–1491, 2018.
- [108] H. D. Flack, "Chiral and achiral crystal structures," *Helvetica Chimica Acta* **86**(4), pp. 905–921, 2003.
- [109] T. Hahn, U. Shmueli, and J. W. Arthur, *International tables for crystallography*, vol. 1, Reidel Dordrecht, 1983.
- [110] D. B. Litvin, "Magnetic space-group types," *Acta Crystallographica Section A: Foundations of Crystallography* **57**(6), pp. 729–730, 2001.
- [111] Y. C. Akgoz and G. A. Saunders, "Space-time symmetry restrictions on the form of transport tensors. I. Galvanomagnetic effects," *Journal of Physics C: Solid State Physics* **8**(9), p. 1387, 1975.
- [112] Y. C. Akgoz and G. A. Saunders, "Space-time symmetry restrictions on the form of transport tensors. II. Thermomagnetic effects," *Journal of Physics C: Solid State Physics* **8**(18), p. 2962, 1975.
- [113] M. Seemann, D. Ködderitzsch, S. Wimmer, and H. Ebert, "Symmetry-imposed shape of linear response tensors," *Physical Review B* **92**(15), p. 155138, 2015.
- [114] To be more accurate, the combination of all three is a universal symmetry operation, and is called the *CPT symmetry*. Each of them three alone may be violated in certain physical phenomena (e.g. processes involving the weak interaction), but these violations are beyond the scope of this thesis.
- [115] T. D. Lee, *Symmetries, asymmetries, and the world of particles*, University of Washington Press, Seattle, 1988.
- [116] This is due to the formation of standing waves when the Bloch wavelengths ($\lambda = 2\pi/k$) are comparable to the

- size of a unit cell in the crystal lattice. The region between the first pair of gaps from origin, i.e. from $-\pi/a_i$ to π/a_i , is called the *first Brillouin zone*.
- [117] Accounting for spin, this requires even number of valence electrons from each unit cell.
 - [118] L. H. Thomas, "The motion of the spinning electron," *Nature* **117**(2945), p. 514, 1926.
 - [119] K. Shen, G. Vignale, and R. Raimondi, "Microscopic theory of the inverse Edelstein effect," *Physical Review Letters* **112**(9), p. 096601, 2014.
 - [120] W. Zhang, M. B. Jungfleisch, W. Jiang, J. E. Pearson, and A. Hoffmann, "Spin pumping and inverse Rashba-Edelstein effect in NiFe/Ag/Bi and NiFe/Ag/Sb," *Journal of Applied Physics* **117**(17), p. 17C727, 2015.
 - [121] Q. Shao, G. Yu, Y.-W. Lan, Y. Shi, M.-Y. Li, C. Zheng, X. Zhu, L.-J. Li, P. K. Amiri, and K. L. Wang, "Strong Rashba-Edelstein effect-induced spin-orbit torques in monolayer transition metal dichalcogenide/ferromagnet bilayers," *Nano Letters* **16**(12), pp. 7514–7520, 2016.
 - [122] T. S. Ghiasi, A. A. Kaverzin, P. J. Blah, and B. J. van Wees, "Charge-to-spin conversion by the Rashba-Edelstein effect in two-dimensional van der Waals heterostructures up to room temperature," *Nano Letters* **19**(9), pp. 5959–5966, 2019.
 - [123] L. A. Benítez, W. S. Torres, J. F. Sierra, M. Timmermans, J. H. Garcia, S. Roche, M. V. Costache, and S. O. Valenzuela, "Tunable room-temperature spin galvanic and spin Hall effects in van der Waals heterostructures," *Nature Materials* **19**, pp. 170–175, 2020.
 - [124] V. Sih, R. Myers, Y. Kato, W. Lau, A. Gossard, and D. Awschalom, "Spatial imaging of the spin Hall effect and current-induced polarization in two-dimensional electron gases," *Nature Physics* **1**(1), p. 31, 2005.
 - [125] F. J. Sansalone, "Compact optical isolator," *Applied Optics* **10**(10), pp. 2329–2331, 1971.

Chapter 3

Spin-dependent electron transmission model for chiral molecules in mesoscopic devices

Various device-based experiments have indicated that electron transfer in certain chiral molecules may be spin-dependent, a phenomenon known as the Chiral Induced Spin Selectivity (CISS) effect. However, due to the complexity of these devices and a lack of theoretical understanding, it is not always clear to what extent the chiral character of the molecules actually contributes to the magnetic-field-dependent signals in these experiments. To address this issue, we report here an electron transmission model that evaluates the role of the CISS effect in two-terminal and multi-terminal linear-regime electron transport experiments. Our model reveals that for the CISS effect, the chirality-dependent spin transmission is accompanied by a spin-flip electron reflection process. Furthermore, we show that more than two terminals are required in order to probe the CISS effect in the linear regime. In addition, we propose two types of multi-terminal nonlocal transport measurements that can distinguish the CISS effect from other magnetic-field-dependent signals. Our model provides an effective tool to review and design CISS-related transport experiments, and to enlighten the mechanism of the CISS effect itself.

3

This chapter is published as:

X. Yang, C. H. van der Wal & B. J. van Wees, "Spin-dependent electron transmission model for chiral molecules in mesoscopic devices," *Phys. Rev. B* **99**, 024418 (2019)

DOI: 10.1103/PhysRevB.99.024418

X. Yang, C. H. van der Wal & B. J. van Wees, "Reply to 'Comment on 'Spin-dependent electron transmission model for chiral molecules in mesoscopic devices''," *Phys. Rev. B* **101**, 026404 (2020)

DOI: 10.1103/PhysRevB.101.026404

3

Developments in the semiconductor industry have allowed integrated circuits to rapidly shrink in size, reaching the limit of conventional silicon-based electronics. One idea to go beyond this limit is to use the spin degree-of-freedom of electrons to store and process information (spintronics) [1]. A spintronic device usually contains two important components: a spin injector and a spin detector, through which electrical or optical signals and spin signals can be interconverted. Conventionally, this conversion is done with bulky solid-state materials, but the recently discovered Chiral Induced Spin Selectivity (CISS) effect suggests that certain chiral molecules or their assemblies are capable of generating spin signals as well. This effect describes that electrons acquire a spin polarization while being transmitted through certain chiral (helical) molecules. Notably, experimental observations of the CISS effect suggest its existence, but complete theoretical insight in its origin is still lacking [2, 3]. The CISS effect is thus not only relevant for spintronic applications, but also fundamentally interesting.

The CISS effect has been experimentally reported in chiral (helical) systems ranging from large biological units such as dsDNA [4, 5] to small molecules such as helicenes [6, 7]. Typically, these experiments can be categorized into either electron photoemission experiments [4, 7–13] or magnetotransport measurements [5, 6, 14–20]. The latter, in particular, are usually based on solid-state devices and are of great importance to the goal of realizing chiral-molecule-based spintronics. Important to realize, in such devices, the CISS-related signals may often be overshadowed by other spurious signals that arise from magnetic components of the devices. Therefore, it is essential to understand the exact role of chiral molecules in these devices and to distinguish between the CISS-related signals and other magnetic-field-dependent signals. However, this has not been addressed, and an effective tool to perform such analyses is still missing.

We provide here a model that is based on the Landauer-Büttiker-type of analysis of linear-regime electron transmission and reflection. Unlike other theoretical works [21–29], our model is derived from symmetry theorems that hold for electrical conduction in general and does not require any assumptions about the CISS effect on a molecular level. With this model, we quantitatively demonstrate how the CISS effect leads to spin injection and detection in linear-regime devices, and analyze whether typical two-terminal and four-terminal measurements are capable of detecting the CISS effect in the linear regime.

3.1 An electron transmission model for chiral molecules

We consider a solid-state device as a linear-regime circuit segment whose constituents are described by the following set of rules:

- A *contact* (pictured as a wavy line segment perpendicular to the current flow, see e.g. Figure 3.1) is described as an electron reservoir with a well-defined chemical potential μ , which determines the energy of the electrons that leave the reservoir. A reservoir absorbs all incoming electrons regardless of its energy or spin;
- A *node* (pictured as a circle, see later figures for four-terminal geometries) is a circuit constituent where chemical potentials for charge and spin are defined. It is described by two chemical potentials μ_{\rightarrow} and μ_{\leftarrow} , one for each spin species with the arrows indicating the spin orientations. At a node a spin accumulation μ_s is defined ($\mu_s = \mu_{\rightarrow} - \mu_{\leftarrow}$). Inside a node the momentum of electrons is randomized, while the spin is preserved. The function and importance of the node will be further addressed in the discussion section;
- A *CISS molecule* (pictured as a helix, color-coded and labeled for its chirality, see e.g. Figure 3.1), a *ferromagnet* (a filled square, see e.g. Figure 3.1), and a *non-magnetic barrier* (a shaded rectangle, see e.g. Figure 3.2) are viewed as two-terminal circuit constituents with energy-conserving electron transmissions and reflections. Each of them is described by a set of (possibly spin-dependent) transmission and reflection probabilities;
- The above constituents are connected to each other via *transport channels* (pictured as line segments along the current flow, see e.g. Figure 3.1), in which both the momentum and the spin of electrons are preserved.

Before proceeding with introducing the model, we would like to highlight the important role of dephasing in the generation of the CISS effect. In a fully phase-coherent two-terminal electron transport system, time-reversal symmetry prohibits the production of spin polarization by a charge current [30]. Consequently, a CISS molecule requires the presence of dephasing in order to exhibit a CISS-type spin-polarizing behavior. The necessity of dephasing has already been addressed by other theoretical works [31–33]. Here we emphasize that the Landauer-Buttiker type of analysis, on which our model is based, does not require phase coherence [34, 35]. Moreover, dephasing can be naturally provided by inelastic processes such as electron-phonon interactions under experimental conditions. Therefore, it is reasonable to assume that a CISS molecule is able to generate a spin polarization in a linear-

regime circuit segment, and our discussions focus on whether this spin polarization can be detected as a charge signal.

In the following part of this article, we first derive a key transport property of CISS molecules and then introduce a matrix formalism to quantitatively describe linear-regime transport devices. Later, in the discussion section, we provide analyses for a few experimental circuit geometries.

3.1.1 Reciprocity theorem and spin-flip reflection by chiral molecules

In order to characterize the CISS effect without having to understand it on a molecular level, we look at universal rules that apply to any conductor in the linear regime, namely the law of charge conservation and the reciprocity theorem.

The reciprocity theorem states that for a multi-terminal circuit segment in the linear regime, the measured conductance remains invariant when an exchange of voltage and current contacts is accompanied by a reversal of magnetic field H and magnetization M (of all magnetic components) [36, 37]. Mathematically we write

$$G_{ij,mn}(H, M) = G_{mn,ij}(-H, -M), \quad (3.1)$$

where $G_{ij,mn}$ is the four-terminal conductance measured using current contacts i and j and voltage contacts m and n . In two-terminal measurements, this theorem reduces to

$$G_{ij}(H, M) = G_{ij}(-H, -M), \quad (3.2)$$

meaning that the two-terminal conductance remains constant under magnetic field and magnetization reversal. This theorem emphasizes the universal symmetry independent of the microscopic nature of the transport between electrical contacts. It is valid for any linear-regime circuit segment regardless of the number of contacts, or the presence of inelastic scattering events [37].

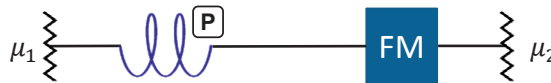


Figure 3.1: A two-terminal circuit segment with a P -type CISS molecule and a ferromagnet between contacts 1 and 2 (with chemical potentials μ_1 and μ_2). The notion P -type represents the chirality of the molecule and indicates that it allows higher transmission for spins *parallel* to the electron momentum. (The opposite chirality allows higher transmission for spins *anti-parallel* to the electron momentum, and is denoted as AP -type.) The ferromagnet (FM) is assumed to allow higher transmission of spins parallel to its magnetization direction, which can be controlled to be either parallel or anti-parallel to the electron transport direction.

By applying the reciprocity theorem to a circuit segment containing CISS molecules, one can derive a special transport property of these molecules. For example, in the two-terminal circuit segment shown in Figure 3.1, the reciprocity theorem requires that the two-terminal conductance remains unchanged when the magnetization direction of the ferromagnet is reversed. Since the two-terminal conductance is proportional to the transmission probability between the two contacts (Landauer-Büttiker) [35], this requirement translates to

$$T_{21}(\Rightarrow) = T_{21}(\Leftarrow), \quad (3.3)$$

where T_{21} describes the transmission probability of electrons injected from contact 1 to reach contact 2, and \Rightarrow and \Leftarrow indicate the magnetization directions of the ferromagnet. This requirement gives rise to a necessary spin-flip process associated with the CISS molecule, as described below.

For ease of illustration, we assume an ideal case where both the ferromagnet and the CISS molecule allow a 100% transmission of the favored spin and a 100% reflection of the other (the general validity of the conclusions is addressed in Appendix A). We consider electron transport from contact 1 to contact 2 (see Figure 3.1) and compare the two transmission probabilities $T_{21}(\Rightarrow)$ and $T_{21}(\Leftarrow)$. For $T_{21}(\Rightarrow)$, the *P*-type CISS molecule (favors spin parallel to electron momentum, see figure caption) allows the transmission of spin-right electrons, while it reflects spin-left electrons back to contact 1. At the same time, the ferromagnet is magnetized to also only allow the transmission of spin-right electrons. Therefore, all spin-right (and none of the spin-left) electrons can be transmitted to contact 2, giving $T_{21}(\Rightarrow) = 0.5$. As for $T_{21}(\Leftarrow)$, while the *P*-type CISS molecule still allows the transmission of spin-right electrons, the ferromagnet no longer does. It reflects the spin-right electrons towards the CISS molecule with their momentum anti-parallel to their spin. As a result, these electrons are reflected by the CISS molecule and are confined between the CISS molecule and the ferromagnet. This situation gives $T_{21}(\Leftarrow) = 0$, which is not consistent with Eqn. 3.3. In order to satisfy Eqn. 3.3, i.e. to have $T_{21}(\Leftarrow) = 0.5$, a spin-flip process has to take place for the spin-right electrons, so that they can be transmitted to contact 2 through the ferromagnet. Such a process does not exist for the ideal and exactly aligned ferromagnet. Therefore, a spin-flip electron reflection process must exist for the CISS molecule. Further analysis (Appendix A) shows that such a spin-flip reflection process completely meets the broader restrictions from Eqn. 3.2. In addition, the conclusion that a spin-flip reflection process must exist is valid for general cases where the ferromagnet and the CISS molecule are not ideal.

In these derivations, the only assumption regarding the CISS molecule is that it allows higher transmission of one spin than the other, which is a conceptual description of the CISS effect itself. Therefore, the spin-flip reflection process has to be regarded as an inherent property of the CISS effect in a linear-regime transport

system, and this is guaranteed by the universal symmetry theorems of electrical conduction [36, 37].

3.1.2 Matrix formalism and barrier-CISS center-barrier (BCB) model for CISS molecules

		Transmission	Reflection
General form		$\mathbb{T} = \begin{pmatrix} t_{\rightarrow\rightarrow} & t_{\leftarrow\rightarrow} \\ t_{\rightarrow\leftarrow} & t_{\leftarrow\leftarrow} \end{pmatrix}$	$\mathbb{R} = \begin{pmatrix} r_{\rightarrow\rightarrow} & r_{\leftarrow\rightarrow} \\ r_{\rightarrow\leftarrow} & r_{\leftarrow\leftarrow} \end{pmatrix}$
Nonmagnetic barrier		$\mathbb{T}_B = \begin{pmatrix} t & 0 \\ 0 & t \end{pmatrix}$	$\mathbb{R}_B = \begin{pmatrix} 1-t & 0 \\ 0 & 1-t \end{pmatrix}$
Ferromagnet		$\mathbb{T}_{FM} = \begin{pmatrix} \frac{1+P_{FM}}{2} & 0 \\ 0 & \frac{1-P_{FM}}{2} \end{pmatrix}$	$\mathbb{R}_{FM} = \begin{pmatrix} \frac{1-P_{FM}}{2} & 0 \\ 0 & \frac{1+P_{FM}}{2} \end{pmatrix}$
<i>P</i> -type ideal CISS molecule		$\mathbb{T}_{0,R}^P = \begin{pmatrix} 1 & 0 \\ 0 & 0 \end{pmatrix}$ $\mathbb{T}_{0,L}^P = \begin{pmatrix} 0 & 0 \\ 0 & 1 \end{pmatrix}$	$\mathbb{R}_{0,R}^P = \begin{pmatrix} 0 & 1 \\ 0 & 0 \end{pmatrix}$ $\mathbb{R}_{0,L}^P = \begin{pmatrix} 0 & 0 \\ 1 & 0 \end{pmatrix}$
<i>AP</i> -type ideal CISS molecule		$\mathbb{T}_{0,R}^{AP} = \mathbb{T}_{0,L}^P$ $\mathbb{T}_{0,L}^{AP} = \mathbb{T}_{0,R}^P$	$\mathbb{R}_{0,R}^{AP} = \mathbb{R}_{0,L}^P$ $\mathbb{R}_{0,L}^{AP} = \mathbb{R}_{0,R}^P$

Figure 3.2: Transmission and reflection matrices (\mathbb{T} and \mathbb{R}) for a non-magnetic barrier (subscript B , here we use the term *barrier*, but it refers to any circuit constituent with spin-independent electron transmission and reflection), a ferromagnet (subscript FM), and ideal *P*-type (superscript P) and *AP*-type (superscript AP) CISS molecules. For the CISS molecules the subscripts R (right) and L (left) denote the direction of the incoming electron flow, and the indicator 0 in the subscripts means these matrices are for an ideal cases where all the matrix elements are either 1 or 0. The matrices for *AP*-type molecules are derived from those for *P*-type molecules under the assumption that opposite chiral enantiomers are exact mirror images of each other, and therefore selects opposite spins with equal probability. Each matrix element represents the probability of a spin-dependent transmission or reflection, with the column/row position indicating the corresponding spin orientations before/after the transmission or reflection (see general form in the top row).

We use matrices to quantitatively describe the spin-dependent transmission and reflection probabilities of CISS molecules and other circuit constituents, as shown in Figure 3.2. At the top of the figure, the general form of these matrices is introduced. Matrix element $t_{\alpha\beta}$ (or $r_{\alpha\beta}$), where α and β is either *left* (\leftarrow) or *right* (\rightarrow), represents the probability of a spin- α electron being transmitted (or reflected) as a spin- β electron, and $\alpha \neq \beta$ indicates a spin-flip process. Here $0 \leq t_{\alpha\beta}, r_{\alpha\beta} \leq 1$, and

the spin orientations are chosen to be either parallel or anti-parallel to the electron momentum in later discussions. Next, the transmission and reflection matrices of a non-magnetic barrier are given. These matrices are spin-independent and are fully determined by a transmission probability t ($0 \leq t \leq 1$), which depends on the material and dimensions of the barrier. Here we use the term *barrier*, but it refers to any circuit constituent with spin-independent electron transmission and reflection. In the third row, we show the transmission and reflection matrices of a ferromagnet. These matrices are spin-dependent, and are determined by the polarization P_{FM} ($0 < |P_{FM}| \leq 1$) of the ferromagnet. Finally, for *P*-type and *AP*-type CISS molecules, we show here an ideal case where all the matrix elements are either 1 or 0. The non-zero off-diagonal terms in the reflection matrices represent the characteristic spin-flip reflections. These ideal CISS molecules are later referred to as *CISS centers*, and will be generalized for more realistic situations.

In accordance with the matrix formalism, we use column vector $\boldsymbol{\mu} = \begin{pmatrix} \mu_{\rightarrow} \\ \mu_{\leftarrow} \end{pmatrix}$ to describe chemical potentials, and column vector $\boldsymbol{I} = \begin{pmatrix} I_{\rightarrow} \\ I_{\leftarrow} \end{pmatrix}$ to describe currents, where each vector element describes the contribution from one spin component (indicated by arrow).



Figure 3.3: A generalized *Barrier-CISS Center-Barrier (BCB)* model for *P*-type CISS molecules. The ideal, 100%-spin-selective CISS Center in the middle introduces the directional spin transmission in a CISS molecule, while the two identical non-magnetic barriers (with transmission probability t) contribute the non-ideal electron transmission and reflection behavior. The overall transmission and reflection matrices of the entire BCB module are fully determined by t and have all elements taking finite values between 0 and 1.

A non-ideal CISS molecule with C_2 symmetry (two-fold rotational symmetry with an axis perpendicular to the electron transport path) can be modeled as a linear arrangement of two identical barriers sandwiching an ideal CISS center, as shown in Figure 3.3 (only the *P*-type is shown). In this *Barrier-CISS Center-Barrier (BCB)* model we consider that all spin-dependent linear-regime transport properties of a CISS molecule exclusively originate from an ideal CISS center inside the molecule, and the overall spin-dependency is limited by the multiple spin-independent transmissions and reflections at other parts (non-magnetic barriers) of the molecule. Therefore, the barrier transmission probability t ($0 < t \leq 1$) fully determines the transmission and reflection matrices of the entire BCB molecule, and consequently determines the spin-related properties of the molecule. The use of an identical barrier on each side

of the CISS center is to address the C_2 symmetry. However, we stress that not all CISS molecules have this symmetry, and the BCB model is still a simplified picture. The model can be further generalized by removing the restriction of the CISS center being ideal, and this case is discussed in Appendix C. Despite being a simplified picture, the BCB model captures all qualitative behaviors of a non-ideal CISS molecule, and at the same time keeps quantitative analyses simple. Therefore, we further only discuss the case of *BCB molecules*, instead of the more generalized *CISS molecules*.

3.2 Discussion

3

In this section, we use different approaches to separately analyze two-terminal and multi-terminal circuit geometries. For two-terminal geometries, we evaluate the conductance of the circuit segment by calculating the electron transmission probability T_{21} between the two contacts. In contrast, for multi-terminal geometries, we take a circuit-theory approach to evaluate the spin accumulation μ_s at the nodes.

A major difference between the two approaches is the inclusion of nodes in multi-terminal geometries. In our description, a node is the only location where spin accumulation can be defined. It can be experimentally realized with a diffusive electron transport channel segment that is much shorter (along the electron transport direction) than the spin-diffusion length λ_s of the channel material. Due to its diffusive nature, a node emits electrons to all directions, so it can be considered as a source of electron back-scattering. Notably, adding a node to a near-ideal electron transport channel (with transmission probability close to 1) significantly alters its electron transmission probability. Nonetheless, this does not affect the validity of our approach because we only address non-ideal circuit segments where electron back-scattering (reflection) already exists due to other circuit constituents (CISS molecules, ferromagnets, or non-magnetic barriers). Note that even when we discuss the use of ideal CISS molecules or ideal ferromagnets, the entire circuit segment is non-ideal due to the reflection of the rejected spins.

In the following discussion, we consider only the P -type BCB molecule, and we use expressions $\mathbb{T}_{R,L}^P$ and $\mathbb{R}_{R,L}^P$ to describe transmission and reflection matrices of the entire BCB module, where the subscripts consider electron flow directions. The derivations of these matrices can be found in Appendix B.

3.2.1 Two-terminal geometries

We discuss here two geometries that are relevant for two-terminal magnetoresistance measurements [38].

The first is an *FM-BCB* geometry, as shown in Figure 3.4. It simulates a common

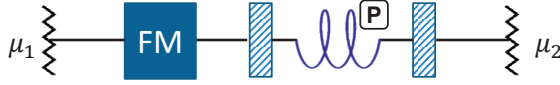


Figure 3.4: An FM-BCB geometry where a ferromagnet and a BCB molecule are connected in series in a two-terminal circuit segment. The magnetization reversal of the ferromagnet does not change the two-terminal conductance.

type of experiment where a layer of chiral molecules is sandwiched between a ferromagnetic layer and a normal metal contact. The other side of the ferromagnetic layer is also connected to a normal metal contact (experimentally this may be a wire that connects the sample with the measurement instrument). Due to the spin-dependent transmission of the chiral molecules and the ferromagnet, one might expect a change of the two-terminal conductance once the magnetization of the ferromagnet is reversed. However, this change is not allowed by the reciprocity theorem (Eqn. 3.2), which can be confirmed with our model, as explained below.

In order to illustrate this, we calculate the electron transmission probabilities for opposite ferromagnet magnetization directions, $T_{21}^{FM-BCB}(\Rightarrow)$ and $T_{21}^{FM-BCB}(\Leftarrow)$, where the arrows indicate the magnetization directions.

For the magnetization direction to the right (\Rightarrow), we first derive the transmission and reflection matrices with the combined contribution from the ferromagnet and the BCB molecule

$$\begin{aligned}
 & \mathbb{T}_{21}^{FM-BCB}(\Rightarrow) \\
 &= \mathbb{T}_R^P \cdot \left(\mathbb{I} + \mathbb{R}_{FM}(\Rightarrow) \cdot \mathbb{R}_R^P + \left(\mathbb{R}_{FM}(\Rightarrow) \cdot \mathbb{R}_R^P \right)^2 + \left(\mathbb{R}_{FM}(\Rightarrow) \cdot \mathbb{R}_R^P \right)^3 + \dots \right) \cdot \mathbb{T}_{FM}(\Rightarrow) \\
 &= \mathbb{T}_R^P \cdot \left(\mathbb{I} - \mathbb{R}_{FM}(\Rightarrow) \cdot \mathbb{R}_R^P \right)^{-1} \cdot \mathbb{T}_{FM}(\Rightarrow),
 \end{aligned} \tag{3.4a}$$

$$\begin{aligned}
 & \mathbb{R}_{11}^{FM-BCB}(\Rightarrow) \\
 &= \mathbb{R}_{FM}(\Rightarrow) + \mathbb{T}_{FM}(\Rightarrow) \cdot \left(\mathbb{I} - \mathbb{R}_R^P \cdot \mathbb{R}_{FM}(\Rightarrow) \right)^{-1} \cdot \mathbb{R}_R^P \cdot \mathbb{T}_{FM}(\Rightarrow),
 \end{aligned} \tag{3.4b}$$

where the $\mathbb{I} = \begin{pmatrix} 1 & 0 \\ 0 & 1 \end{pmatrix}$ is the identity matrix. The addition of the multiple reflection terms is due to the multiple reflections between the ferromagnet and the BCB molecule. Next, we include the contribution from the contacts and derive the trans-

mission and reflection probabilities accounting for both spins

$$T_{21}^{FM-BCB}(\Rightarrow) = (1, 1) \mathbb{T}_{21}^{FM-BCB}(\Rightarrow) \begin{pmatrix} 1/2 \\ 1/2 \end{pmatrix}, \quad (3.5a)$$

$$R_{11}^{FM-BCB}(\Rightarrow) = (1, 1) \mathbb{R}_{11}^{FM-BCB}(\Rightarrow) \begin{pmatrix} 1/2 \\ 1/2 \end{pmatrix}, \quad (3.5b)$$

where the column vector $\begin{pmatrix} 1/2 \\ 1/2 \end{pmatrix}$ describes the normalized input current from contact 1 with equal spin-right and spin-left contributions, and the row vector $(1, 1)$ is an operator that describes the absorption of both spins into contact 2 (calculates the sum of the two spin components).

For the opposite magnetization direction (\Leftarrow), we modify the terms in Eqn. 3.4 and Eqn. 3.5 accordingly. Detailed calculations (see Appendix B) show

$$T_{21}^{FM-BCB}(\Rightarrow) \equiv T_{21}^{FM-BCB}(\Leftarrow) \quad (3.6)$$

for all BCB transmission probabilities t and all ferromagnet polarizations P_{FM} . Therefore, it is not possible to detect any variation of two-terminal conductance in this geometry by switching the magnetization direction of the ferromagnet. In Appendix B we show that it is also not possible to detect any variation of two-terminal conductance by reversing the current, and that the above conclusions also hold for the more generalized CISS model (Appendix C). These conclusions also agree with earlier reports on general voltage-based detections of current-induced spin signals [39].

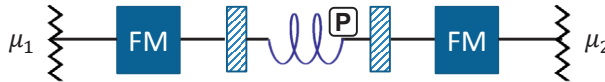


Figure 3.5: A *Spin Valve* geometry with a BCB molecule placed in between two ferromagnets. Unlike a conventional spin valve, here the magnetization reversal of one ferromagnet does not change the two-terminal conductance due to the presence of the BCB molecule.

The second geometry, as shown in Figure 3.5, contains two ferromagnets, and is similar to a spin valve. In a conventional spin valve (a non-magnetic barrier sandwiched between two ferromagnets), the magnetization reversal of one ferromagnet leads to a change of the two-terminal conductance [38] (this does not violate the reciprocity theorem since switching one ferromagnet does not reverse all magnetizations of the entire circuit segment), whereas in the geometry shown in Figure 3.5, this change does not happen due to the presence of spin-flip electron reflections in the BCB molecule. (See Appendix B for more details.) As a result, this geometry is not able to quantitatively measure the CISS effect. We emphasize that here the absence

of the spin-valve behavior is unique for the BCB model, which contains an ideal CISS Center. In Appendix C we show that a further-generalized CISS model regains the spin-valve behavior. Nevertheless, one cannot experimentally distinguish whether the regained spin-valve behavior originates from the CISS molecule or a normal non-magnetic barrier, and therefore cannot draw any conclusion about the CISS effect. In general, it is not possible to measure the CISS effect in the linear regime using two-terminal experiments.

3.2.2 Four-terminal geometries and experimental designs

Four-terminal measurements allow one to completely separate spin-related signals from charge-related signals, and therefore allow the detection of spin accumulations created by the CISS effect [40]. Here we analyze two geometries that are relevant for such measurements. In the first geometry, we use a node connected to BCB molecules to illustrate how spin injection and detection can occur without using magnetic materials (Figure 3.6). In the second geometry, we use two nodes to decouple a BCB molecule from electrical contacts and illustrate the spin-charge conversion property of the molecule (Figure 3.7). In addition, we propose device designs that resemble these two geometries and discuss possible experimental outcomes (Figure 3.8).

Figure 3.6(a) shows a geometry where a node is connected to four contacts. Two of the contacts contain BCB molecules, and the other two contain non-magnetic (tunnel) barriers. We consider an experiment where contacts 1 and 2 are used for current injection and contacts 3 and 4 are used for voltage detection. In terms of spin injection, we first assume that the voltage contacts 3 and 4 are weakly coupled to the node, and do not contribute to the spin accumulation in the node. This means that the chemical potentials of contacts 1 and 2 fully determine the spin-dependent chemical potential (column vector) of the node $\boldsymbol{\mu}_{node} = \begin{pmatrix} \mu_{node \rightarrow} \\ \mu_{node \leftarrow} \end{pmatrix}$. We also assume $\mu_2 = 0$ for convenience since only the chemical potential difference between the two contacts is relevant. Under these assumptions, the node receives electrons only from contact 1, but emits electrons to both contact 1 and 2. Therefore, the incoming current (column vector) into the node is

$$\mathbf{I}_{in} = \frac{G}{e} \mathbb{T}_R^P \mu_1 \begin{pmatrix} 1 \\ 1 \end{pmatrix}, \quad (3.7)$$

and the outgoing current (column vector) from the node is

$$\mathbf{I}_{out} = \frac{G}{e} \left((\mathbb{I} - \mathbb{R}_L^P) + (1 - r_B) \mathbb{I} \right) \boldsymbol{\mu}_{node}, \quad (3.8)$$

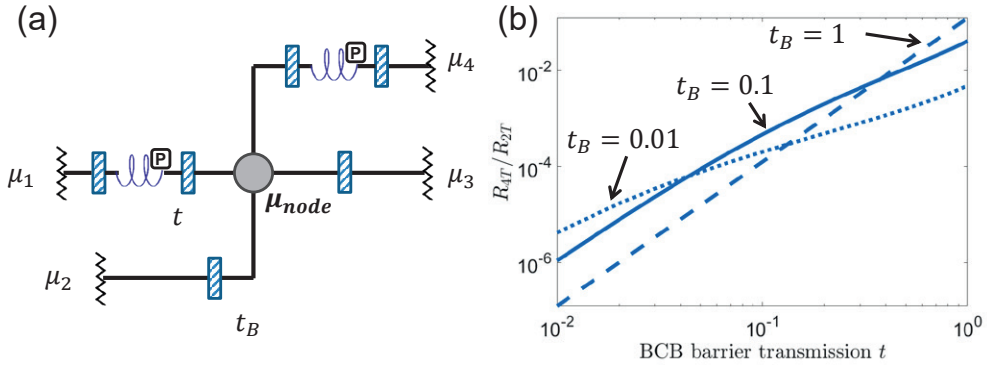


Figure 3.6: (a). A four-terminal geometry that includes a node. Two of the contacts contain BCB molecules, and the other two are coupled to the node via tunnel barriers (with transmission probability t_B). The node is characterized by a spin-dependent chemical potential vector $\boldsymbol{\mu}_{node} \begin{pmatrix} \mu_{node \rightarrow} \\ \mu_{node \leftarrow} \end{pmatrix}$ and each of the four contacts is characterized by a spin-independent chemical potential μ_i , with $i = 1, 2, 3, 4$. (b). Calculated ratio between four-terminal and two-terminal resistances for this geometry, plotted as a function of t (transmission probability of the barriers in BCB molecules) for three t_B (transmission probability of the barriers at the contacts) values.

where $G = Ne^2/h$ is the N -channel, one-spin conductance of the channels connecting the node to each of the contacts, and r_B ($0 \leq r_B \leq 1$) is the reflection probability of the tunnel barrier between the node and contact 2 (different from the barriers in BCB molecules). Due to the spin-preserving nature of the node, at steady state the incoming current is equal to the outgoing current (for both spin components), or $I_{in} = I_{out}$. From this relation we derive

$$\boldsymbol{\mu}_{node} = \left((1 + t_B)\mathbb{I} - \mathbb{R}_L^P \right)^{-1} \mathbb{T}_R^P \mu_1 \begin{pmatrix} 1 \\ 1 \end{pmatrix}, \quad (3.9)$$

where $t_B = 1 - r_B$ is the transmission probability of the tunnel barrier. Next, we derive the spin accumulation in the node

$$\mu_s = \mu_{node \rightarrow} - \mu_{node \leftarrow} = \begin{pmatrix} 1, -1 \end{pmatrix} \boldsymbol{\mu}_{node} = k_{inj} \mu_1, \quad (3.10)$$

where a row vector $\begin{pmatrix} 1, -1 \end{pmatrix}$ is used as an operator to calculate the difference between

the two spin chemical potentials, and

$$k_{inj} = (1, -1) \left((1+t_B)\mathbb{I} - \mathbb{R}_L^P \right)^{-1} \mathbb{T}_R^P \begin{pmatrix} 1 \\ 1 \end{pmatrix}, \quad (3.11)$$

$$\text{with } 0 < k_{inj} \leq \frac{1}{4},$$

is the spin *injection coefficient* for these current contacts. This expression shows that the spin accumulation in the node depends linearly on the chemical potential difference between the current contacts, and the coefficient k_{inj} is determined by both the BCB molecule (with parameter t) and the tunnel barrier connected to contact 2 (with parameter t_B).

With regard to spin detection, we discuss whether the established spin accumulation μ_s in the node can lead to a chemical potential difference (and thus a charge voltage) between the weakly coupled voltage contacts 3 and 4. A contact cannot distinguish between the two spin components, therefore only the charge current (sum of both spins, calculated by applying an operator $(1, 1)$ to a current column vector) is relevant. At steady state, there is no net charge current at any of the voltage contacts,

$$I_3 = \frac{G}{e} (1, 1) \left((1-r_B)\mu_3 \begin{pmatrix} 1 \\ 1 \end{pmatrix} - t_B \boldsymbol{\mu}_{node} \right) = 0, \quad (3.12a)$$

$$I_4 = \frac{G}{e} (1, 1) \left((\mathbb{I} - \mathbb{R}_L^P)\mu_4 \begin{pmatrix} 1 \\ 1 \end{pmatrix} - \mathbb{T}_R^P \boldsymbol{\mu}_{node} \right) = 0, \quad (3.12b)$$

which gives

$$\mu_4 - \mu_3 = k_{det} \mu_s, \quad (3.13)$$

where

$$k_{det} = \frac{1}{2} \frac{(1, 1) \mathbb{T}_R^P \begin{pmatrix} 1 \\ -1 \end{pmatrix}}{(1, 1) \mathbb{T}_L^P \begin{pmatrix} 1 \\ 1 \end{pmatrix}}, \quad (3.14)$$

$$\text{with } 0 < k_{det} \leq \frac{1}{2},$$

is the spin *detection coefficient* for these voltage contacts. This expression shows that the chemical potential difference between the two voltage contacts depends linearly on the spin accumulation in the node, and the coefficient k_{det} is exclusively determined by the BCB molecule (with parameter t).

Combining Eqn. 3.10 and Eqn. 3.13 we obtain

$$\frac{R_{4T}}{R_{2T}} = \frac{\mu_4 - \mu_3}{\mu_1 - \mu_2} = k_{inj} k_{det}, \quad (3.15)$$

where R_{4T} is the four-terminal resistance (measured using contacts 3 and 4 as voltage contacts, while using contacts 1 and 2 as current contacts), and R_{2T} is the two-terminal resistance (measured using contacts 1 and 2 as both voltage and current contacts). This ratio is determined by both the BCB molecule (with parameter t) and the tunnel barrier connected to contact 2 (with parameter t_B), and can be experimentally measured to quantitatively characterize the CISS effect.

As an example, for $t = t_B = 0.5$, we have $k_{inj} \approx 0.11$, $k_{det} \approx 0.17$, and $R_{4T}/R_{2T} \approx 0.02$. In Figure 3.6(b) we plot R_{4T}/R_{2T} as a function of t for three different t_B values. Similar plots for k_{inj} and k_{det} are shown in Appendix B.

The above results show that it is possible to inject and detect a spin accumulation in a node using only BCB molecules and non-magnetic (tunnel) barriers, and these processes can be quantitatively described by the injection and detection coefficients. We stress that the signs of the injection and detection coefficients depend on the type (chirality) of the BCB molecule and the position of the molecule with respect to the contact. Switching the molecule from P -type to AP -type leads to a sign change of the injection or detection coefficient. The sign change also happens if the contact is connected to the opposite side of the BCB molecule. For example, in Figure 3.6(a), contacts 1 and 4 are both connected to the node via P -type BCB molecules, but contact 1 is on the left-hand side of a molecule, while contact 4 is on the right-hand side. Electrons emitted from these two contacts travel in opposite directions through the (same type of) BCB molecules before arriving at the node. As a result, using contact 4 instead of contact 1 as a current contact leads to a sign change of k_{inj} . Similarly, using contact 1 instead of contact 4 as a voltage contact leads to a sign change of k_{det} . Experimentally, one can use three BCB contacts to observe this sign change: A fixed current contact (thus a fixed k_{inj}) in combination with two voltage contacts that use the same type of BCB molecule but are placed on opposite sides of a node (thus opposite signs for k_{det}). The voltages measured by the two voltage contacts (with respect to a common reference contact) will differ by sign. This can be experimentally measured as a signature of the CISS effect.

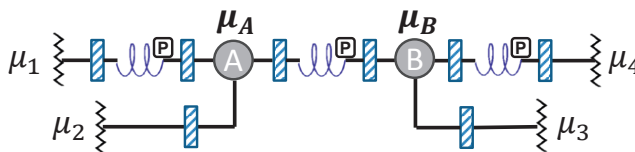


Figure 3.7: A four-terminal geometry involving two nodes A and B , which are connected to each other via a BCB molecule. A spin accumulation difference between the two nodes results in a (charge) chemical potential difference between them, and *vice versa*.

Figure 3.7 shows a geometry where a BCB molecule is between two nodes A

and B , and is decoupled from the contacts. The nodes themselves are connected to contacts in a similar fashion as in the previous geometry. In node A , we consider a chemical potential vector μ_A and a spin accumulation μ_{sA} , which are fully determined by the current contacts 1 and 2. In node B , we consider weakly coupled voltage contacts 3 and 4, so that its chemical potential vector μ_B and its spin accumulation μ_{sB} , are fully determined by μ_A . At steady state, there is no net charge or spin current in node B , which leads to

$$\mu_B = (\mathbb{I} - \mathbb{R}_L^P)^{-1} \mathbb{T}_R^P \mu_A. \quad (3.16)$$

Note that here the matrices only refer to the molecule between the two nodes. For BCB molecules, this expression always gives $\mu_{sB} = 0$, but for a more generalized CISS molecule (as described in Appendix C), this expression can give $\mu_{sB} \neq 0$. This shows that a spin accumulation at one side of a CISS molecule can generate a spin accumulation at the other side of the molecule. Most importantly, for both the BCB model and the more generalized model, Eqn. 3.16 predicts that a spin accumulation difference across a CISS molecule creates a charge voltage across the molecule, and *vice versa* (spin-charge conversion via a CISS molecule). Mathematically written, the expression always provides $\mu_{nA} \neq \mu_{nB}$ when $\mu_{sA} \neq \mu_{sB}$, and $\mu_{sA} \neq \mu_{sB}$ when $\mu_{nA} \neq \mu_{nB}$, where μ_{nA} (or μ_{nB}) is the average chemical potential of the two spin components in node A (or in node B). A more detailed description of this geometry can be found in Appendix C.

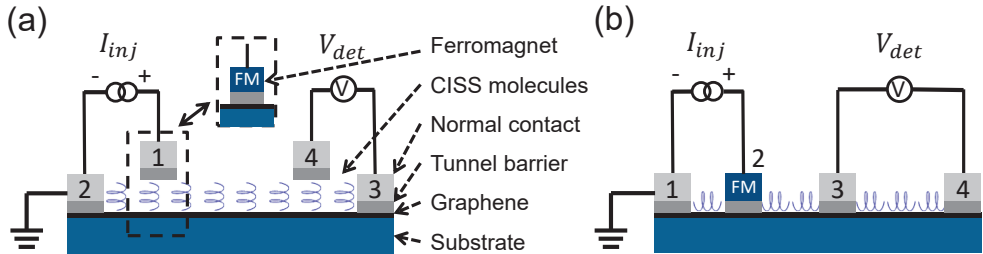


Figure 3.8: Nonlocal device designs with CISS molecules adsorbed on graphene. (a). A device where electrons travel through CISS molecules. All contacts are non-magnetic and are numbered in agreement with Figure 3.6(a). A variation of this device can be achieved by replacing contact 1 with a ferromagnet, see inset. (b). A device where electrons travel in proximity to CISS molecules. A ferromagnetic contact 2 is used for spin injection, but one can also use only non-magnetic contacts, as in Figure 3.7.

Figure 3.8 shows two types of nonlocal devices that resemble the two geometries introduced above. We realize the node function with graphene, chosen for its long spin lifetime and long spin diffusion length [41].

The first type, as shown in Figure 3.8(a), represents the geometry in Figure 3.6(a), where spin injection and detection are both achieved using CISS molecules. A current I_{inj} is injected from contact 1 through CISS molecules into graphene, then driven out to a normal metal contact 2. This current induces a spin accumulation in the graphene layer underneath the current contacts, which then diffuses to the voltage contacts. The voltage contacts then pick up a charge voltage V_{det} in a similar fashion as explained in Figure 3.6(a). With this, the nonlocal resistance can be determined $R_{nl} = V_{det}/I_{inj}$. Further, we can derive (see Appendix B for details)

$$R_{nl} = -k_{inj}k_{det}R_{inj}e^{-\frac{d}{\lambda_s}}, \quad (3.17)$$

where R_{inj} is the resistance measured between the current contacts 1 and 2, d is the distance between contacts 1 and 4, and λ_s is the spin diffusion length of graphene. It is assumed here that the spacing between the current contacts (1 and 2) and the spacing between the voltage contacts (3 and 4) are both much smaller than λ_s . The minus sign comes from the fact that the injection and the detection contacts are on the same side of the graphene channel (both on top), unlike the example in Figure 3.6(a) (one on the left and the other on the right).

A variation of this device is obtained by replacing contact 1 (together with the CISS molecules underneath it) with a ferromagnet, as shown in the inset of Figure 3.8(a). This variation allows one to control the sign of R_{nl} by controlling the magnetization direction of the ferromagnet, which should be aligned parallel or anti-parallel to the helical (chiral) axis of the CISS molecules (out-of-plane, as indicated by the arrows). The nonlocal resistance is therefore

$$R_{nl}(\uparrow) = -R_{nl}(\downarrow) = P_{FM}k_{det}R_{\lambda}e^{-\frac{d}{\lambda_s}}, \quad (3.18)$$

where the arrows indicate the magnetization directions, P_{FM} is the polarization of the ferromagnet, and R_{λ} is the spin resistance of graphene (see Appendix B for more details). In this device, the reversal of the magnetization direction of the ferromagnet leads to a sign change of the nonlocal resistance. Under experimental conditions [42, 43], this nonlocal resistance change $\Delta R_{nl} = R_{nl}(\uparrow) - R_{nl}(\downarrow)$ can reach tens of Ohms (Ω) and is easily detectable.

The second type of device is depicted in Panel (b). It is a variation of the geometry in Figure 3.7, where contact 2 is replaced by a ferromagnet. In this device, instead of traveling through the CISS molecules, the electrons travel through the graphene channel underneath the molecules. It is assumed that due to the proximity of the CISS molecules, the electrons in graphene also experience a (weaker) CISS effect. Whether this assumption is valid remains to be proven. The nonlocal signals produced by this device are derived in Appendix B.

3.3 Conclusion

In summary, we demonstrated that a spin-flip electron reflection process is inherent to the chiral induced spin selectivity (CISS) effect in linear-regime electron transport. Furthermore, we developed a set of spin-dependent electron transmission and reflection matrices and a generalized Barrier-CISS Center-Barrier (BCB) model to quantitatively describe the CISS effect in mesoscopic devices. Based on this formalism, we demonstrated that more than two terminals are needed in order to probe the CISS effect in linear-regime transport experiments. Moreover, we also showed several ways of injecting and detecting spins using CISS molecules and demonstrated that CISS molecules can give rise to spin-charge conversion. In addition, we proposed two types of graphene-based nonlocal devices which can be used to directly measure the CISS effect in the linear regime.

We stress again that the above discussions and proposed devices are all based on linear-regime electron transport. Therefore, our conclusions cannot exclude the two-terminal detection of the CISS effect in the non-linear regime. However, the spin signals in non-linear-regime measurements should approach zero as the two-terminal bias approaches zero (entering the linear regime), and the mechanism that may contribute to such signals has to be different from spin-dependent electron transmission and reflection. A recent work shows that the CISS effect in electron photoemission experiments (three-terminal) can be explained by losses due to spin-dependent electron absorption in chiral molecules [44], but whether a similar process can lead to the detection of the CISS effect in non-linear two-terminal measurements remains to be investigated. In general, our model captures the fundamental role of the CISS effect in linear-regime mesoscopic devices without assuming any microscopic electron transport mechanism inside CISS molecules. Recently, a new type of spin-orbit coupling was predicted for one-dimensional screw dislocations in semiconductor crystals, which has a one-dimensional helical effective electric field. This type of spin-orbit coupling can lead to an enhanced spin lifetime for electrons traveling along the helical axis [45]. Future theoretical work should study whether similar effects exist in chiral or helical molecules.

In general, our model helps to analyze and understand device-based CISS experiments without having to understand the CISS effect on a molecular level. It provides a guideline for future reviewing and designing of CISS-based mesoscopic spintronic devices.

3.4 Reply to Comment

In this section, we emphasize once more the distinction between generating CISS (spin-charge current conversion) in a chiral spin-orbit system and detecting it as magnetoresistance in two-terminal electronic devices. We also highlight important differences between electrical measurement results obtained in the linear response regime and those obtained in the nonlinear regime.

The Comment by R. Naaman and D. H. Waldeck [46] addresses our recent publication “*Spin-dependent electron transmission model for chiral molecules in mesoscopic devices [47]*”. We believe that the Comment is largely based on misunderstandings of Ref. 47, and it is important to clarify these in detail. Therefore, we provide here a point-by-point reply to the Comment and emphasize the important distinctions between the results obtained in the linear response regime and those obtained in the nonlinear regime, because both are experimentally observed using two-terminal electrical measurements. Moreover, we emphasize again the importance of differentiating the conditions for generating a spin polarization in a chiral molecule from those for detecting it as a magnetoresistance signal in a two-terminal electronic device.

1. Comment: *“The paper published by Yang et. al. [47] models spin transmission through chiral molecules in mesoscopic devices. Based on their model, they claim that spin selectivity in electron transport through chiral molecules, in the linear regime, cannot be measured by using a two-terminal device, unless a spin flip process occurs in the molecule.”*

Reply: This summary of Ref. 47 is incorrect. First, the spin-flip reflection is directly related to the presence of spin-polarized transmission. Second, the spin-polarized transmission cannot be detected using a two-terminal electrical measurement in the linear response regime, regardless of the presence of spin-flip reflection.

2. Comment: *“Their simplified, two-terminal model assumes that charge is injected from a source electrode, transits through a chiral molecule and a ferromagnet, and is collected at a drain electrode. In this treatment, the ferromagnet transmits a given spin and reflects the other; but there is no dissipation in the ferromagnet. While the conclusions drawn by the authors may be consistent with the simplified model, the model itself is not realistic enough to account for experiments.”*

Reply: We indeed consider a two-terminal model but it does not involve simplifications for the linear response regime. Note that the role of the source and drain electrodes are interchangeable in the linear response regime because of microscopic reversibility. We have included in the model electron reflections at

all interfaces, including the ferromagnet and the electrodes. The ferromagnet is characterized by a spin polarization parameter, which can be tuned from 0 to 1. The conclusions of the model are valid for all polarization values.

3. Comment: *“Theoretical models for the CISS effect, in two contact spin measurements, exist in the literature already, and the conditions for observing spin polarization have been discussed in detail. As an example, consider the work by Matityahu et. al. which states: “When the helix is connected to two one-dimensional single-mode leads, time-reversal symmetry prevents spin polarization of the outgoing electrons. One possible way to retrieve such a polarization is to allow leakage of electrons from the helix to the environment, via additional outgoing leads.” ”*

Reply: How a spin polarization can be generated by a chiral molecule has indeed been discussed in many publications, including Refs.24, 31, 44 mentioned in the Comment. This is also pointed out in Ref. 47. However, Ref. 47 addresses a completely different issue, which is how such a spin polarization can be detected as a charge signal in transport experiments in the linear response regime. To our best knowledge, this issue is only addressed in one other publication [48], which appeared after Ref.47.

4. Comment: *“In other words, dephasing acts to create asymmetry in the transmission amplitude for spin up versus spin down, and it breaks Onsager’s reciprocity relation.”*

Reply: While dephasing indeed creates transmission asymmetry for opposite spins, it does not break reciprocity. The Onsager’s relation is a thermodynamical theorem, and it holds in the presence of dephasing, see for example Ref.34.

5. Comment: *“For example, Buttiker [49] showed how asymmetry arises for magneto-conductance in a two terminal device. The combination of interactions with a bath and the large electric fields at interfaces (typical of CISS experiments) can result in the observed asymmetry.”*

Reply: This is correct, but the asymmetry can only occur outside the linear response regime, i.e. away from zero bias by at least $V = k_B T / e$ [50].

6. Comment: *“In addition, we note that spin-selective backscattering, as an explanation for the spin selectivity, was also discussed previously [24] and even used to analyze for the extent of spin flipping in experiments [44].”*

Reply: This is the same issue as explained in the above Point 3. Refs. 24, 44 discuss how a spin-polarized current can be generated by chiral molecules, but not how it can be electrically detected in a charge transport experiment.

7. Comment: *“To summarize, two-terminal models have been discussed before, and it was shown that CISS can be observed if dissipation or a combination of non-linearity*

and dissipation are included.”

Reply: See the previous discussions (Points 3-6).

8. Comment: *“The origin of the nonlinearity, to which we refer, is important to clarify. The simplified model used by Yang et al, presents the linear approximation for the conduction, but it does not relate to the actual parameters characterizing the CISS measurements and could prove misleading to some readers.”*

Reply: The model in Ref. 47 is not simplified in the linear response regime, and the results are strict. The model does not intend to present descriptions for the conduction beyond this regime. The model is very relevant for actual CISS measurements since for several of those, such as the ones shown in Fig. 1 in the Comment, the linear response regime can be clearly identified.

9. Comment: *“For charge moves through a system which is smaller, in dimension, than the screening length, the transport does not depend linearly on the field applied [51, 52]. Because the chiral molecules studied, in all the works cited in Ref. 47, are on the scale of few nanometers, upon applying an electric potential the typical field is of the order of 10^8 V/m. Consequently, the electronic states in the molecules ‘mix’; and the electric field has two contributions: mixing of zeroth-order states by the Stark effect and driving current via the potential drop, conduction. For an example of a model based treatment, see the recent work by Michaeli [53]. This limit is different from most conduction studies of mesoscopic structures.”*

Reply: This is irrelevant to the linear response regime. Electron transport is driven by a difference, or a gradient, of the electrochemical potential. In our case it is the difference in Fermi levels in the two electrodes. What the corresponding electric field (distribution) is depends on the electrostatic screening properties of the device, and indeed on whether the device length is shorter or longer than the screening length. In the linear response regime, the calculations of electron transport do not require the (self-consistent) calculations of electrostatic potentials and fields. Outside the linear response regime, though, the effects described in the Comment can indeed play an important role.

10. Comment: *“The non-linearity of the conduction is readily apparent in experiments with two contacts that have already been published. For example, Figure 1A presents the current versus potential curves, that were measured in a magnetic conducting probe AFM configuration and Figure 1B shows the corresponding plot of the conductance versus the applied potential. Figure 1C shows the spin polarization as a function of the applied potential, which is extracted from the measurements shown in Fig. 1A. Note that these data are obtained from “two contact experiments” that have been presented in figures 2 and 3 of a paper [6], referred to as reference 6 by Yang et al. [47].*

The nonlinear response is apparent both in the current dependence on the voltage (Fig 1A), as well as in the other curves."

Reply: Fig. 1A and Fig. 1B (see in the Comment) greatly help us to clarify our point: In all the nonlinear curves in these figures, the linear response regime can be clearly identified, and here it is roughly within ± 0.05 V. According to Ref. 47, the red and blue curves in both Fig. 1A and Fig. 1B should overlap within this bias range, but they do not. More generally, for any CISS measurement using the magnetic conducting AFM technique, the two (averaged) I - V curves should have the same slope at zero bias, and the two (averaged) dI/dV curves should have the same value at zero bias. We emphasize that these requirements originate from the fundamental microscopic reversibility and the laws of thermodynamics. The departures from these requirements as shown in Fig. 1A and Fig. 1B, we think, may be related to the statistical approaches used in these experiments.

11. Comment: *"To illustrate the nonlinearity more clearly, Figure 1D shows a plot of the data from Fig. 1A on a semi-log graph. His plot reveals the exponential growth of the current at low voltage and the deviation of the currents from each other at higher voltages."*

Reply: Figure. 1A and Fig. 1D do not represent the same data, because (1) At a bias of 1 V, the two curves in Fig. 1A reach values of about 0.8 nA and 0.3 nA, respectively, whereas the two curves in Fig. 1D reach about 1.0 nA and 0.4 nA; (2) At zero bias, the two curves in Fig. 1A have different slopes, which is also shown by a difference of dI/dV values of a factor of two to three in Fig. 1B. This must result in a vertical shift between the curves in Fig. 1D over the entire range, but it is not present at low bias. Also, the labeling of the two curves, in the sense that whether it is the H_{DOWN} or the H_{UP} curve that gives higher current, is not consistent in Fig. 1A and Fig. 1D. We therefore will not comment on Fig. 1D.

12. Comment: *"The spin polarization changes dramatically at low potentials; it is basically zero at very low fields and increases as the electric field approaches a maximum of $\sim 5 \times 10^8$ V/m. This observation, which is apparent in most current vs. voltage curves cited in ref. 47, shows that the simplified model developed in ref. 47 is not relevant to the measurements."*

Reply: This description is not inconsistent with our model. According to Ref.47, the polarization calculated as in Fig. 1C should be zero in the linear response regime, and then it may increase with increasing bias. Both curves in Fig. 1C indeed show zero spin polarization at zero bias, which proves the relevance of our model to actual measurements.

13. Comment: *“In summary, the model presented in ref. 47 oversimplifies; it fails to include the dissipation processes occurring at room temperature and it considers a linear limit that is not valid for the measurements on the CISS effect.”*

Reply: This conclusion is incorrect. Ref. 47 considers only the linear response regime which is clearly observed in experiments such as the one shown in Fig. 1 in the Comment, and therefore it is very relevant to actual measurements. Within the linear response regime the model is not simplified.

We emphasize again that Ref. 47 is intended to raise awareness of the consequences of fundamental symmetries and limitations of certain electrical measurement geometries. It also highlights the differences between linear and nonlinear regimes. An extension of our model shows that a magnetoresistance signal in the two-terminal geometries discussed here can indeed be observed in the nonlinear regime [54].

3

3.5 Appendices

A. General validity of the spin-flip reflection process

In the main text, we stated that a spin-flip electron reflection process has to exist in order for spin-dependent transmission through CISS molecules to be allowed by the reciprocity theorem. Mathematically, this statements means that at least one off-diagonal term in the reflection matrices of CISS molecules has to be non-zero. Now we prove the general validity of our statement by limiting all off-diagonal terms of the reflection matrices to zero, and derive violations against the description of the CISS effect. Under this limit, the general form of the transmission and reflection matrices of a CISS molecule is

$$\mathbb{T}_{CISS} = \begin{pmatrix} a & c \\ b & d \end{pmatrix}, \mathbb{R}_{CISS} = \begin{pmatrix} A & 0 \\ 0 & D \end{pmatrix}, \quad (3.19)$$

where $0 \leq a, b, c, d, A, D \leq 1$. For electrons traveling towards the CISS molecule, each spin component can either be transmitted (with or without spin-flip) or reflected, the sum of these probabilities is therefore unity.

$$a + b + A = 1, \quad c + d + D = 1. \quad (3.20)$$

Therefore we have

$$\mathbb{R}_{CISS} = \begin{pmatrix} 1 - a - b & 0 \\ 0 & 1 - c - d \end{pmatrix} \quad (3.21)$$

In addition, we adopt transmission and reflection matrices of a ferromagnet from Figure 3.2.

Next, we consider that the CISS effect exists in the linear regime. This means that (according to the description of the CISS effect) with an input of spin non-polarized electrons, the CISS molecule gives a spin-polarized transmission output (a non-zero spin current I_s). Here we do not make assumptions about the chirality of the molecule or the electron flow direction, so that our conclusions hold for the most general situations. Therefore, we do not assume the sign of I_s , and write

$$I_s = (1, -1) \mathbb{T}_{CISS} \begin{pmatrix} 1/2 \\ 1/2 \end{pmatrix} = \frac{(a + c) - (b + d)}{2} \neq 0, \quad (3.22)$$

where the column vector indicates the spin non-polarized input current, and the row vector is an operator that calculates the difference between the two spin components in the output current.

In order to illustrate the discrepancy between the assumption of not having any spin-flip reflection and the conceptual description of the CISS effect (Eqn. 3.22), we apply the reciprocity theorem to the circuit segment shown in Figure 3.1. For this circuit segment, we calculate the total transmission matrix accounting for the contribution from both the CISS molecule and the ferromagnet, and obtain

$$\mathbb{T}_{21} = \mathbb{T}_{FM} \cdot \left(\mathbb{I} - \mathbb{R}_{CISS} \cdot \mathbb{R}_{FM} \right)^{-1} \cdot \mathbb{T}_{CISS}. \quad (3.23)$$

The transmission probability accounting for both spin species is therefore

$$T_{21} = (1, 1) \mathbb{T}_{21} \begin{pmatrix} 1/2 \\ 1/2 \end{pmatrix}, \quad (3.24)$$

where the row vector is an operator that calculates the sum of both spin species. By substituting the matrices, we can write T_{21} as a function of P_{FM}

$$T_{21}(P_{FM}) = \frac{a(1 + P_{FM})}{1 + a + b + P_{FM}(1 - a - b)} + \frac{d(1 - P_{FM})}{1 + c + d - P_{FM}(1 - c - d)}. \quad (3.25)$$

Here the magnetization reversal of the ferromagnet is equivalent to a sign change of P_{FM} . Therefore, the broader reciprocity theorem requires [36, 37]

$$T_{12}(P_{FM}) \equiv T_{12}(-P_{FM}) \quad (3.26)$$

for all $0 < |P_{FM}| \leq 1$. This requirement gives

$$a = d, \text{ and } b = c,$$

and therefore,

$$(a + c) - (b + d) = 0,$$

which violates Eqn. 3.22.

Therefore, we proved that the spin-flip electron reflection process has to exist in order for the CISS effect to exist in the linear transport regime, and this is a direct requirement from the *Reciprocity Theorem*.

B. Further discussion about the BCB model

Derivation of the BCB transmission and reflection matrices

In the BCB model, we consider a CISS molecule as two normal barriers sandwiching an ideal CISS center. The three parts together determine the transmission and reflection matrices of the molecule. We derive these matrices in two steps. First, we calculate the combined contribution of the left-most barrier and the ideal CISS center as Part 1 (superscript $P1$). Then, we add the second barrier to Part 1 and calculate the total effect.

We adopt the transmission and reflection matrices for a normal barrier and a CISS center from Figure 3.2. Here we only discuss P -type CISS molecules, as the AP -type can be derived using the relations given in Figure 3.2. For Part 1 we have

$$\mathbb{T}_R^{P1} = (\mathbb{T}_{0,R}^P + \mathbb{T}_{0,R}^P \cdot \mathbb{R}_B \cdot \mathbb{R}_{0,R}^P) \cdot \mathbb{T}_B = \begin{pmatrix} t & t(1-t) \\ 0 & 0 \end{pmatrix}, \quad (3.27a)$$

$$\mathbb{R}_R^{P1} = \mathbb{R}_B + \mathbb{T}_B \cdot \mathbb{R}_{0,R}^P \cdot \mathbb{T}_B = \begin{pmatrix} 1-t & t^2 \\ 0 & 1-t \end{pmatrix}, \quad (3.27b)$$

$$\mathbb{T}_L^{P1} = (\mathbb{T}_B + \mathbb{T}_B \cdot \mathbb{R}_{0,R}^P \cdot \mathbb{R}_B) \cdot \mathbb{T}_{0,L}^P = \begin{pmatrix} 0 & t(1-t) \\ 0 & t \end{pmatrix}, \quad (3.27c)$$

$$\mathbb{R}_L^{P1} = \mathbb{R}_{0,L}^P + \mathbb{T}_{0,R}^P \cdot \mathbb{R}_B \cdot \mathbb{R}_{0,R}^P \cdot \mathbb{R}_B \cdot \mathbb{T}_{0,L}^P = \begin{pmatrix} 0 & (1-t)^2 \\ 1 & 0 \end{pmatrix}. \quad (3.27d)$$

Note that here we have a finite number of reflections between the first barrier and the CISS center because the CISS center is ideal. Now we consider Part 1 as one unit and combine it with the second normal barrier

$$\begin{aligned} \mathbb{T}_R^P &= \mathbb{T}_B \cdot (\mathbb{I} - \mathbb{R}_L^{P1} \cdot \mathbb{R}_B)^{-1} \cdot \mathbb{T}_R^{P1} \\ &= \begin{pmatrix} \sigma/(1-t) & \sigma \\ \sigma & \sigma(1-t) \end{pmatrix}, \end{aligned} \quad (3.28a)$$

$$\begin{aligned} \mathbb{R}_R^P &= \mathbb{R}_R^{P1} + \mathbb{T}_L^{P1} \cdot (\mathbb{I} - \mathbb{R}_B \cdot \mathbb{R}_L^{P1})^{-1} \cdot \mathbb{R}_B \cdot \mathbb{T}_R^{P1} \\ &= \begin{pmatrix} \sigma(1-t)^2 - t + 1 & \sigma/(1-t) \\ \sigma(1-t) & \sigma(1-t)^2 - t + 1 \end{pmatrix}, \end{aligned} \quad (3.28b)$$

$$\begin{aligned} \mathbb{T}_L^P &= \mathbb{T}_L^{P1} \cdot (\mathbb{I} - \mathbb{R}_B \cdot \mathbb{R}_L^{P1})^{-1} \cdot \mathbb{T}_B \\ &= \begin{pmatrix} \sigma(1-t) & \sigma \\ \sigma & \sigma/(1-t) \end{pmatrix}, \end{aligned} \quad (3.28c)$$

$$\begin{aligned} \mathbb{R}_L^P &= \mathbb{R}_B + \mathbb{T}_B \cdot (\mathbb{I} - \mathbb{R}_L^{P1} \cdot \mathbb{R}_B)^{-1} \cdot \mathbb{R}_L^{P1} \cdot \mathbb{T}_B \\ &= \begin{pmatrix} \sigma(1-t)^2 - t + 1 & \sigma(1-t) \\ \sigma/(1-t) & \sigma(1-t)^2 - t + 1 \end{pmatrix}, \end{aligned} \quad (3.28d)$$

$$\text{where } \sigma = \frac{t^2(1-t)}{-t^4 + 4t^3 - 6t^2 + 4t}.$$

These results show that in the BCB model, one parameter t ($0 < t \leq 1$) determines the entire set of transmission and reflection probability matrices. Therefore it is possible to plot various transmission or reflection analysis results as functions of t , as shown in the supplementary information. With different t values the BCB model is able to represent a large spectrum of CISS molecules with different "strengths" of the CISS effect. While it is sufficient to illustrate the fundamental role of a CISS molecule in a solid-state device, it is still a simplified picture. We will introduce a more generalized model later in Appendix C.

The FM-BCB geometry

In the main text, we discussed that the two-terminal transmission remains constant under magnetization reversal in the *FM-BCB* geometry, here we illustrate the same result under current reversal. (Note that this is also a restriction from the linear regime.)

The transmission and reflection matrices from contact 2 to contact 1 are

$$\mathbb{T}_{12}^{FM-BCB}(\Rightarrow) = \mathbb{T}_{FM}(\Rightarrow) \cdot \left(\mathbb{I} - \mathbb{R}_R^P \cdot \mathbb{R}_{FM}(\Rightarrow) \right)^{-1} \cdot \mathbb{T}_L^P, \quad (3.29a)$$

$$\mathbb{R}_{22}^{FM-BCB}(\Rightarrow) = \mathbb{R}_L^P + \mathbb{T}_R^P \cdot \left(\mathbb{I} - \mathbb{R}_{FM}(\Rightarrow) \cdot \mathbb{R}_R^P \right)^{-1} \cdot \mathbb{R}_{FM}(\Rightarrow) \cdot \mathbb{T}_L^P, \quad (3.29b)$$

and the corresponding transmission and reflection probabilities accounting for both spins are

$$T_{12}^{FM-BCB}(\Rightarrow) = (1, 1) \mathbb{T}_{12}^{FM-BCB}(\Rightarrow) \begin{pmatrix} 1/2 \\ 1/2 \end{pmatrix}, \quad (3.30a)$$

$$R_{22}^{FM-BCB}(\Rightarrow) = (1, 1) \mathbb{R}_{22}^{FM-BCB}(\Rightarrow) \begin{pmatrix} 1/2 \\ 1/2 \end{pmatrix}. \quad (3.30b)$$

With these expressions, we can calculate the transmission and reflection probabilities as a function of t (BCB transmission probability) for four situations: two current directions and two magnetization directions, and the results are plotted in Figure 3.9(a). Note that for all four situations, the transmission curves (or the reflection curves) completely overlap with each other, this means that neither magnetization reversal nor current reversal can lead to a sign change in the two-terminal conductance. Furthermore, we are able to quantitatively analyze the contribution of each spin component in each of the four situations, and this will be shown in the supplementary information.

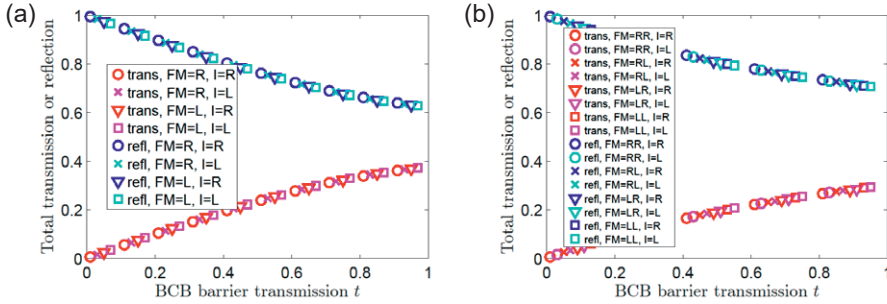


Figure 3.9: Normalized total transmission and reflection of (a) an FM -BCB segment, and (b) a spin-valve segment. Both are plotted as a function of t (BCB barrier transmission). Red and magenta labels (lower group) are for total transmissions accounting for both spin species for different magnetization orientations ($FM=R$ or L , for magnetization *right* or *left*). For the spin-valve cases there are two FM 's and different electron flow directions ($I=R$ or L , for electron flow from *left to right* or from *right to left*). Blue and cyan labels (upper group) are for total reflections. The polarization of the ferromagnet is chosen as $P_{FM} = 0.1$, comparable to experimental conditions with Co contacts.

The spin valve geometry

Similar to the FM -BCB geometry, in order to calculate the two-terminal transmission and reflection probability of the spin valve geometry, we first calculate the transmission and reflection matrices for this geometry. For this, we treat the spin valve geometry as an FM -BCB module and a ferromagnet connected in series, and derive

$$\begin{aligned} & \mathbb{T}_{21}^{SV}(\Rightarrow, \Rightarrow) \\ &= \mathbb{T}_{FM}(\Rightarrow) \cdot \left(\mathbb{I} - \mathbb{R}_{22}^{FM-BCB}(\Rightarrow) \cdot \mathbb{R}_{FM}(\Rightarrow) \right)^{-1} \cdot \mathbb{T}_{21}^{FM-BCB}(\Rightarrow), \end{aligned} \quad (3.31a)$$

$$\begin{aligned} & \mathbb{R}_{11}^{SV}(\Rightarrow, \Rightarrow) \\ &= \mathbb{R}_{11}^{FM-BCB}(\Rightarrow) \\ &+ \mathbb{T}_{21}^{FM-BCB}(\Rightarrow) \cdot \left(\mathbb{I} - \mathbb{R}_{FM}(\Rightarrow) \cdot \mathbb{R}_{22}^{FM-BCB}(\Rightarrow) \right)^{-1} \cdot \mathbb{R}_{FM}(\Rightarrow) \cdot \mathbb{T}_{12}^{FM-BCB}(\Rightarrow), \end{aligned} \quad (3.31b)$$

$$\begin{aligned} & \mathbb{T}_{12}^{SV}(\Rightarrow, \Rightarrow) \\ &= \mathbb{T}_{12}^{FM-BCB}(\Rightarrow) \cdot \left(\mathbb{I} - \mathbb{R}_{FM}(\Rightarrow) \cdot \mathbb{R}_{22}^{FM-BCB}(\Rightarrow) \right)^{-1} \cdot \mathbb{T}_{FM}(\Rightarrow), \end{aligned} \quad (3.31c)$$

$$\begin{aligned}
& \mathbb{R}_{22}^{SV}(\Rightarrow, \Rightarrow) \\
& = \mathbb{R}_{FM}(\Rightarrow) \\
& + \mathbb{T}_{FM}(\Rightarrow) \cdot \left(\mathbb{I} - \mathbb{R}_{22}^{FM-BCB}(\Rightarrow) \cdot \mathbb{R}_{FM}(\Rightarrow) \right)^{-1} \cdot \mathbb{R}_{22}^{FM-BCB}(\Rightarrow) \cdot \mathbb{T}_{FM}(\Rightarrow),
\end{aligned} \tag{3.31d}$$

where the two arrows in the brackets on the left-hand side of the equations indicate the magnetization direction of the two ferromagnets respectively. For the case where the magnetization of one of the ferromagnets is reversed, we can substitute the corresponding magnetization direction with an opposite arrow.

For the two-terminal transmission and reflection probabilities accounting for both spins, we have

$$T_{ij}^{SV} = (1, 1) \cdot \mathbb{T}_{ij}^{SV} \cdot \begin{pmatrix} 1/2 \\ 1/2 \end{pmatrix}, \tag{3.32a}$$

$$R_{ij}^{SV} = (1, 1) \cdot \mathbb{R}_{ij}^{SV} \cdot \begin{pmatrix} 1/2 \\ 1/2 \end{pmatrix}, \tag{3.32b}$$

and we can calculate these probabilities as a function of t (BCB transmission probability) for eight situations: the two ferromagnets each with two magnetization directions, and two opposite current directions, as shown in Figure 3.9(b). Note that for all eight situations, the transmission curves (or the reflection curves) completely overlap with each other, this means that neither magnetization reversal (for either ferromagnet) nor current reversal can lead to a signal change in the two-terminal conductance. Furthermore, we can quantitatively analyze the contribution of each spin component in this geometry, as shown in the Supplemental Material [55].

Injection and detection coefficients

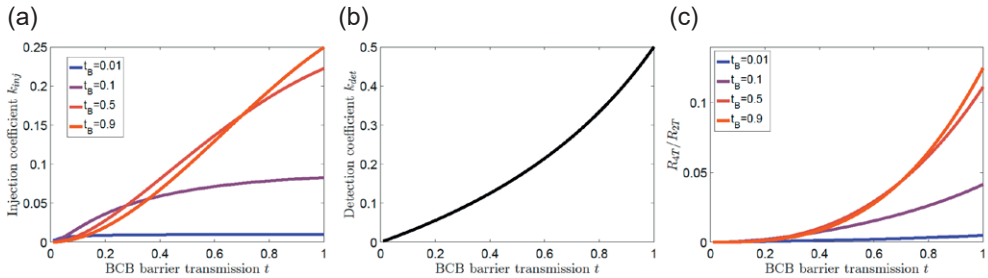


Figure 3.10: (a) Injection coefficient k_{inj} , (b) detection coefficient k_{det} , and (c) ratio between four-terminal and two-terminal resistances, as a function of t (BCB barrier transmission) for various t_B (contact barrier transmission), for the geometry described in Figure 3.6(a) in the main text.

In the main text, we derived the injection and detection coefficients k_{inj} and k_{det} for the four-terminal geometry shown in Figure 3.6(a), and we showed that the product of these two geometries represents the ratio between four-terminal and two-terminal resistances. The injection coefficient depends both on the BCB barrier transmission t and the transmission probability t_B of the barrier at contact 2, whereas the detection coefficient only depends on the BCB barrier transmission t . This difference is due to our assumption of weakly coupled detection contacts. In Fig. 3.10 we plot the injection coefficient k_{inj} , the detection coefficient k_{det} , and the 4T/2T resistance ratio R_{4T}/R_{2T} as a function of t (transmission probability of the barrier in the BCB molecule). Especially, for k_{inj} and R_{4T}/R_{2T} , we set t_B (transmission probability of the barrier in contact 2) to a few different values and illustrate its influence.

Spin-charge conversion

In the main text, we illustrated the spin-charge conversion property of CISS molecules. The chemical potential vectors in the two nodes in Figure 3.7 are related to each other following Eqn. 3.16. We also introduced the scalars of charge chemical potential μ_n (the average of two spin chemical potentials) and spin accumulation μ_s (the difference between two spin chemical potentials). Here we show how these scalar chemical potentials relate to each other.

A vector chemical potential of a node can be rewritten as a sum of two column vectors

$$\begin{aligned}\boldsymbol{\mu} &= \begin{pmatrix} \mu_{\rightarrow} \\ \mu_{\leftarrow} \end{pmatrix} = \begin{pmatrix} \mu_n + \frac{1}{2}\mu_s \\ \mu_n - \frac{1}{2}\mu_s \end{pmatrix} \\ &= \mu_n \begin{pmatrix} 1 \\ 1 \end{pmatrix} + \frac{1}{2}\mu_s \begin{pmatrix} 1 \\ -1 \end{pmatrix}.\end{aligned}\quad (3.33)$$

By rewriting both $\boldsymbol{\mu}_A$ and $\boldsymbol{\mu}_B$ in this fashion, and substituting them into Eqn. 3.16, we obtain

$$\Delta\mu_n \begin{pmatrix} 1 \\ 1 \end{pmatrix} + \frac{1}{2}\Delta\mu_s \begin{pmatrix} 1 \\ -1 \end{pmatrix} = \left(\mathbb{I} - (\mathbb{I} - \mathbb{R}_L^P)^{-1} \mathbb{T}_R^P \right) \boldsymbol{\mu}_A, \quad (3.34)$$

where $\Delta\mu_n = \mu_{nA} - \mu_{nB}$ is the charge chemical potential difference between the two nodes, and $\Delta\mu_s = \mu_{sA} - \mu_{sB}$ is the spin accumulation difference between the two nodes.

For the BCB model,

$$\mathbb{I} - (\mathbb{I} - \mathbb{R}_L^P)^{-1} \mathbb{T}_R^P = \begin{pmatrix} 1 + \frac{1}{t-2} & -1 - \frac{1}{t-2} \\ \frac{1}{t-2} & -\frac{1}{t-2} \end{pmatrix} \quad (3.35)$$

where t is the BCB transmission probability. Substituting this matrix into Eqn. 3.34 gives

$$\Delta\mu_n \begin{pmatrix} 1 \\ 1 \end{pmatrix} + \frac{1}{2}\Delta\mu_s \begin{pmatrix} 1 \\ -1 \end{pmatrix} = \mu_{sA} \begin{pmatrix} 1 + \frac{1}{t-2} \\ \frac{1}{t-2} \end{pmatrix}. \quad (3.36)$$

Note that here the charge chemical potentials in node A (μ_{nA}) drops out of the equation. We emphasize that this is a unique result for the BCB model.

Solving the above vector equation gives

$$\Delta\mu_s = \mu_{sA}, \quad (3.37a)$$

$$\Delta\mu_n = -k_{conv}\Delta\mu_s, \quad (3.37b)$$

where $k_{conv} = t/(4-2t)$ ($0 < k_{conv} \leq 0.5$) is the spin-charge conversion coefficient.

Eqn. 3.37a shows that $\mu_{sB} = \mu_{sA} - \Delta\mu_s = 0$, meaning that a spin accumulation in node A cannot generate a spin accumulation in node B . This result is special for the BCB model and does not hold for a more generalized CISS model (as will be introduced later in Appendix C). Eqn. 3.37b shows that the charge voltage across a BCB molecule linearly depends on the spin accumulation difference across the molecule, and *vice versa* (spin-charge conversion). The conversion coefficient k_{conv} depends on t (BCB barrier transmission). Notably, for BCB molecules this coefficient has the same value as the detection coefficient ($k_{conv} = k_{det}$). This is because the result $\mu_{sB} = 0$ makes node B equivalent to a contact: it is not able to distinguish between two spin components. For a more generalized model (as will be introduced later in Appendix C) the two coefficient take different values. These conclusions were mentioned in the main text, here we showed the proof.

Nonlocal signals

We first discuss the non-local resistance measured with device geometries shown in Figure 3.8(a). In this picture the axes of the CISS molecules are vertical rather than horizontal, therefore the spin orientations are described as spin-up or spin-down. As a result, the spin accumulation is defined as $\mu_s = (\mu_{\uparrow} - \mu_{\downarrow})$.

First, we discuss the case where the spin injection is done through a BCB molecule. The injected spin accumulation underneath contact 1 is

$$\mu_{s,inj} = -k_{inj}\mu_1 = -ek_{inj}I_{inj}R_{inj}, \quad (3.38)$$

where the minus sign is due to the fact that the electrons are traveling downwards through CISS molecules into graphene, as a result, the injected spin accumulation is negative (mostly spin-down). The resistance

$$R_{inj} = R_{12} = \frac{\mu_1 - \mu_2}{eI_{inj}} \quad (3.39)$$

is the resistance measured between the two injection contacts 1 and 2.

Inside graphene, the spin accumulation diffuses to all directions, and therefore the spin accumulation at the detection contact is

$$\mu_{s,det} = \mu_{s,inj}e^{-\frac{d}{\lambda_s}}, \quad (3.40)$$

where λ_s is the spin diffusion length in graphene, and d is the distance between the inner injection and detection contacts (1 and 4) (we have assumed that this distance is much larger than the separation of the two injection contacts or the separation of the two detection contacts).

Further, the voltage detected by the detection contacts is (following Eqn. 3.13)

$$V_{det} = \frac{1}{e}k_{det}\mu_{s,det}. \quad (3.41)$$

With this, we have

$$R_{nl} = \frac{V_{det}}{I_{inj}} = -k_{inj}k_{det}R_{inj}e^{-\frac{d}{\lambda_s}}, \quad (3.42)$$

as in Eqn. 3.17.

For the case where the spin injection is obtained through a ferromagnet, the spin injection becomes

$$\mu_{s,inj} = \pm eP_{FM}I_{inj}R_\lambda, \quad (3.43)$$

where P_{FM} is the polarization of the ferromagnet (with magnetization direction out-of-plane), and R_λ is the spin resistance of graphene. This spin resistance is determined by the spin relaxation length in graphene and the shape of the graphene channel, and is defined as $R_\lambda = R_{sq}\lambda_s/W$, where R_{sq} is the square resistance of graphene and W is the width of the graphene channel (assuming the channel width remains the same across the spin diffusion length). The sign of the injected spin accumulation is determined by the magnetization direction of the ferromagnet, with magnetization-up for positive spin accumulation and magnetization-down for negative spin accumulation.

The diffusion and detection mechanisms are the same as in the previous case. Therefore, the non-local resistance for this situation is

$$R_{nl} = \pm k_{det}P_{FM}R_\lambda e^{-\frac{d}{\lambda_s}}, \quad (3.44)$$

as in Eqn. 3.18. With the help of the ferromagnet, it is possible to switch the sign of the non-local resistance.

Next, for the device shown in Figure 3.8(b), the CISS molecules are aligned in-plane of the device, therefore we assume the ferromagnet also has in-plane magnetization, and we describe spin accumulation again as $\mu_s = \mu_{\rightarrow} - \mu_{\leftarrow}$. We simplify the discussion by assuming the spin injection is mainly contributed by the ferromagnet, and the spin detection is achieved through the spin-charge conversion mechanism of the CISS molecules. The spin accumulation underneath the detection contacts can be generated by two mechanisms: the spin diffusion in graphene (as in the previous case), and the spin-charge conversion between the injection node and the detection node. However, in the BCB model, the spin-charge conversion does not contribute to a spin accumulation underneath the detector contacts. Therefore, we only consider the spin diffusion mechanism. Similar to the previous case, we can derive the nonlocal signal

$$R_{nl} = \pm k_{conv}P_{FM}R_\lambda e^{-\frac{d}{\lambda_s}}, \quad (3.45)$$

where k_{conv} is the spin-charge conversion coefficient described before, but here it concerns the proximity-induced CISS effect in the graphene channel, rather than the CISS molecules themselves. Important to realize, due to the proximity effect, the diffusion length λ_s and the spin resistance R_λ of graphene may differ from the previous case.

C. Generalized CISS Model

The BCB model is a simplified model where the spin-dependent characteristics of a CISS molecule are exclusively originated from an ideal CISS center. However, the assumption of having an ideal spin-flip core in a molecule may not be accurate. Therefore, we assume a general form of transmission and reflection matrices,

$$\mathbb{T}_R^P = \begin{pmatrix} a, & c \\ b, & d \end{pmatrix}, \quad \mathbb{R}_R^P = \begin{pmatrix} A, & C \\ B, & D \end{pmatrix}, \quad (3.46)$$

where

$$0 \leq a, b, c, d, A, B, C, D \leq 1, \quad (3.47a)$$

$$a + b + A + B = c + d + C + D = 1, \quad (3.47b)$$

$$a + c > b + d. \quad (3.47c)$$

Here the first restriction Eqn. 3.47a comes from the fact that all matrix elements are probabilities. The second restriction Eqn. 3.47b addresses that for each spin component, the sum of its probabilities of being transmitted and being reflected equals 1. The third restriction Eqn. 3.47c is the conceptual description of the CISS effect, which shows that a spin polarization arises after transmission through a CISS molecule. This restriction is similar to Eqn. 3.22, but here we determine a sign for the polarization because we have assumed the chirality (P -type) of the molecule and the electron flow direction (R for rightwards).

We still assume that the molecule has C_2 symmetry, so that the transmission and reflection matrices for reversed current can be written as

$$\mathbb{T}_L^P = \begin{pmatrix} 0 & 1 \\ 1 & 0 \end{pmatrix} \cdot \mathbb{T}_R^P \cdot \begin{pmatrix} 0 & 1 \\ 1 & 0 \end{pmatrix}, \quad (3.48a)$$

$$\mathbb{R}_L^P = \begin{pmatrix} 0 & 1 \\ 1 & 0 \end{pmatrix} \cdot \mathbb{R}_R^P \cdot \begin{pmatrix} 0 & 1 \\ 1 & 0 \end{pmatrix}. \quad (3.48b)$$

The matrices for AP -type molecules can be derived according to Figure 3.2. Before we proceed with the mathematical proof, we discuss the validity of these symmetry assumptions.

Since we only consider the electron transport in CISS molecules, the C_2 symmetry that we require only refers to the symmetry in electron transport. Furthermore, this symmetry is also a requirement of the linear regime. A highly asymmetric molecule can still be treated with our model, but only under the assumption that it is composed of a symmetric (C_2) part which contributes to CISS, and asymmetrically distributed normal barriers. In terms of the symmetry relations between the two chiralities, it is by definition that the two chiral enantiomers are exact mirror images of each other, and thereby select opposite spins with equal probability (when placed in the same circuit environment).

We apply the reciprocity theorem to a geometry similar to Figure 3.4 in the main text, but now the BCB molecule is replaced by a generalized CISS molecule. The general reciprocity theorem requires that the two-terminal resistance remains unchanged under magnetization reversal regardless of the polarization of the ferromagnet. Therefore, we assume the ferromagnet is 100% polarized for convenience. Following the same steps as in the FM -BCB geometry, the two terminal transmission probabilities considering two magnetization directions and two current directions become

$$T_{21}(\Rightarrow) = a + b + (c + d) \frac{B}{1 - D}, \quad (3.49a)$$

$$T_{21}(\Leftarrow) = c + d + (a + b) \frac{C}{1 - A}, \quad (3.49b)$$

$$T_{12}(\Rightarrow) = b + d + (a + c) \frac{C}{1 - D}, \quad (3.49c)$$

$$T_{12}(\Leftarrow) = a + c + (b + d) \frac{B}{1 - A}, \quad (3.49d)$$

where the arrows indicate the magnetization direction of the ferromagnet, and the subscripts indicate the electron flow direction. The reciprocity theorem requires these four expressions to have the same value

$$T_{12}(\Rightarrow) = T_{12}(\Leftarrow) = T_{21}(\Rightarrow) = T_{21}(\Leftarrow) = T, \quad (3.50)$$

which can be written as a vector equation

$$\begin{pmatrix} 1 & 1 & \frac{B}{1-D} & \frac{B}{1-D} \\ \frac{C}{1-A} & \frac{C}{1-A} & 1 & 1 \\ \frac{C}{1-D} & 1 & \frac{C}{1-D} & 1 \\ 1 & \frac{B}{1-A} & 1 & \frac{B}{1-A} \end{pmatrix} \cdot \begin{pmatrix} a \\ b \\ c \\ d \end{pmatrix} = T \begin{pmatrix} 1 \\ 1 \\ 1 \\ 1 \end{pmatrix}. \quad (3.51)$$

In order for this equation to be self-consistent, relation

$$A = D$$

is required. Consequently, we can derive

$$b = c, \quad (3.52a)$$

$$a - d = C - B. \quad (3.52b)$$

Therefore, the generalized form of the transmission and reflection matrices of a CISS molecule is

$$\mathbb{T}_R^P = \begin{pmatrix} a & b \\ b & a(1-s) \end{pmatrix}, \quad \mathbb{R}_R^P = \begin{pmatrix} A & B + as \\ B & A \end{pmatrix}, \quad (3.53)$$

with $a + b + A + B = 1$, and s ($0 \leq s \leq 1$) being a quantitative description of the *strength* of the CISS effect in a molecule.

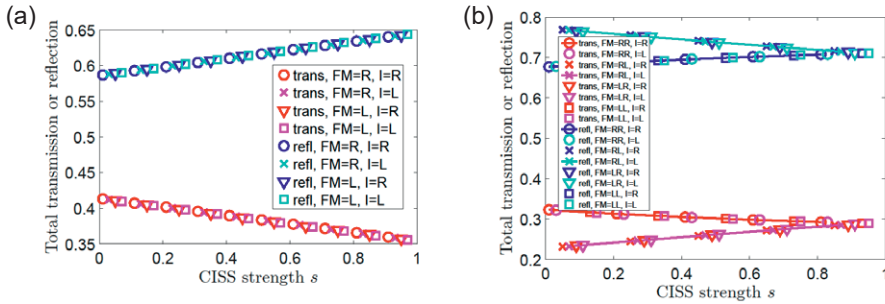


Figure 3.11: Normalized total transmission and reflection of (a) an FM-CISS segment, and (b) a spin-valve segment. Both are plotted as a function of s (generalized CISS strength). Red and magenta labels (lower group) are for total transmissions accounting for both spin species for different magnetization orientations (FM=R or L, for the spin-valve case there are two FM's) and different electron flow directions (I=R or L). Blue and cyan labels (upper group) are for total reflections. The polarization of the ferromagnet is chosen as $P_{FM} = 0.7$.

Next, we discuss the results given by this generalized model for the geometries discussed in the main text, and compare it with the BCB model. We arbitrarily choose the following transmission and reflection matrices for the generalized model

$$\mathbb{T}_R^P = \begin{pmatrix} 0.6 & 0.15 \\ 0.15 & 0.6(1-s) \end{pmatrix}, \quad \mathbb{R}_R^P = \begin{pmatrix} 0.2 & 0.05 + 0.6s \\ 0.05 & 0.2 \end{pmatrix}, \quad (3.54)$$

and use parameter s as the variable to tune the CISS strength.

For the *FM-BCB* geometry (which now becomes *FM-CISS* geometry), we plot the two-terminal transmission and reflection probabilities as a function of s for four situations: two magnetization directions and two current directions. The results show that all four situations give identical results for all CISS strength s , as shown in Figure 3.11(a). This is consistent with the BCB model, just as required by the reciprocity theorem.

For the spin valve geometry, we plot the two-terminal transmission and reflection probabilities as a function of s for eight situations: two ferromagnets each with two magnetization directions, and two current directions. The results are shown in Figure 3.11(b). Unlike the BCB model, here we find different transmission and reflection probabilities for cases where the two magnetization directions are parallel *vs.* anti-parallel. The transmission probability is in general higher when the two ferromagnets are magnetized parallel compared to anti-parallel. Notably, the difference between the two configurations decreases as the CISS strength s increases. This is because with increasing s , electrons have a higher probability of encountering spin-flip reflections. This also explains why in a BCB model, where an ideal spin-flip process is present, switching the magnetization directions does not lead to any conductance variation. The direction of the current has no effect on the transmission and reflection probabilities, as is required by the linear regime.

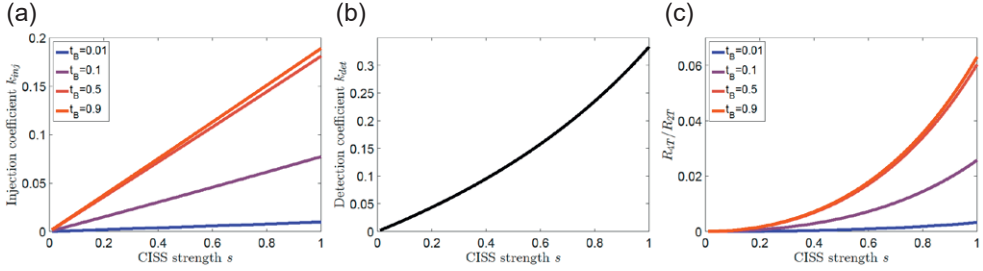


Figure 3.12: (a) Injection coefficient k_{inj} , (b) detection coefficient k_{det} , and (c) ratio between four-terminal and two-terminal resistances, as a function of s (generalized CISS strength) for various t_B (contact barrier transmission), for the geometry described in Figure 3.6(a) in the main text.

For four terminal geometries, we calculate here the spin injection and detection coefficients using the formulas derived in the main text, and we plot these coefficients as a function of the CISS strength s . Figure 3.12(a) shows the injection coefficient as a function of s for a few t_B values. Figure 3.12(b) shows the detection coefficient as a function of s , and Figure 3.12(c) shows the ratio between four-terminal and two-terminal resistances as a function of s .

Last but not least, we discuss the spin-charge conversion property of the generalized CISS molecule. Substituting the corresponding transmission and reflection matrices into Eqn. 3.34, and solving the vector equation, we can obtain relations between the conversion coefficient k_{conv} and the chemical potential vector μ_A . Unlike the BCB model, here it is not possible to drop out either μ_{nA} or μ_{sA} from the equation. The final result gives

$$k_{conv} = -\frac{\Delta\mu_n}{\Delta\mu_s} = \frac{(A - B - 1)s\mu_{nA} + \frac{1}{2}(b + B)s\mu_{sA}}{2(A + B - 1)s\mu_{nA} + (b + B)(-2 + 2A + 2B + s)\mu_{sA}}, \quad (3.55)$$

where a, b, A, B, s are the parameters in the transmission and reflection matrices of the generalized CISS model. This equation shows that a non-zero charge voltage difference ($\Delta\mu_n$) can give rise to a spin accumulation difference ($\Delta\mu_s$) across a generalized CISS molecule, and *vice versa* (spin-charge conversion). Interestingly, the conversion coefficient k_{conv} depends not only on the transmission and reflection matrices of the molecule, but also on the spin accumulation in the nodes connected to the molecule. If $s = 0$,

i.e. the molecule does not exhibit any CISS effect, the spin-charge conversion property also diminishes ($k_{conv} = 0$).

With these discussions, we demonstrated that a generalized CISS molecule shows differences from the simplified BCB model. Nonetheless, these differences are rather quantitative than qualitative, and are not easily measurable in experiments. Furthermore, the generalized model also introduces extra degrees-of-freedom to calculations as it uses four variables to describe a CISS molecule, compared to one in the BCB model. Having taken the above into consideration, in the main text we only showed the results of the BCB model.

Bibliography

- [1] S. A. Wolf, D. D. Awschalom, R. A. Buhrman, J. M. Daughton, S. Von Molnar, M. L. Roukes, A. Y. Chtchelkanova, and D. M. Treger, "Spintronics: a spin-based electronics vision for the future," *Science* **294**(5546), pp. 1488–1495, 2001.
- [2] R. Naaman and D. H. Waldeck, "Chiral-induced spin selectivity effect," *The Journal of Physical Chemistry Letters* **3**(16), pp. 2178–2187, 2012.
- [3] R. Naaman and D. H. Waldeck, "Spintronics and chirality: Spin selectivity in electron transport through chiral molecules," *Annual Review of Physical Chemistry* **66**, pp. 263–281, 2015.
- [4] B. Göhler, V. Hamelbeck, T. Z. Markus, M. Kettner, G. F. Hanne, Z. Vager, R. Naaman, and H. Zacharias, "Spin selectivity in electron transmission through self-assembled monolayers of double-stranded DNA," *Science* **331**(6019), pp. 894–897, 2011.
- [5] Z. Xie, T. Z. Markus, S. R. Cohen, Z. Vager, R. Gutierrez, and R. Naaman, "Spin specific electron conduction through DNA oligomers," *Nano Letters* **11**(11), pp. 4652–4655, 2011.
- [6] V. Kiran, S. P. Mathew, S. R. Cohen, I. Hernández Delgado, J. Lacour, and R. Naaman, "Helicenes—A new class of organic spin filter," *Advanced Materials* **28**, pp. 1957–1962, 2016.
- [7] M. Kettner, V. V. Maslyuk, D. Nürenberg, J. Seibel, R. Gutierrez, G. Cuniberti, K.-H. Ernst, and H. Zacharias, "Chirality-dependent electron spin filtering by molecular monolayers of helicenes," *The Journal of Physical Chemistry Letters* **9**(8), pp. 2025–2030, 2018.
- [8] K. Ray, S. P. Ananthavel, D. H. Waldeck, and R. Naaman, "Asymmetric scattering of polarized electrons by organized organic films of chiral molecules," *Science* **283**(5403), pp. 814–816, 1999.
- [9] I. Carmeli, V. Skakalova, R. Naaman, and Z. Vager, "Magnetization of chiral monolayers of polypeptide: a possible source of magnetism in some biological membranes," *Angewandte Chemie International Edition* **41**(5), pp. 761–764, 2002.
- [10] S. G. Ray, S. S. Daube, G. Leituz, Z. Vager, and R. Naaman, "Chirality-induced spin-selective properties of self-assembled monolayers of DNA on gold," *Physical Review Letters* **96**(3), p. 036101, 2006.
- [11] D. Mishra, T. Z. Markus, R. Naaman, M. Kettner, B. Göhler, H. Zacharias, N. Friedman, M. Sheves, and C. Fontanesi, "Spin-dependent electron transmission through bacteriorhodopsin embedded in purple membrane," *Proceedings of the National Academy of Sciences* **110**(37), pp. 14872–14876, 2013.
- [12] M. Á. Niño, I. A. Kowalik, F. J. Luque, D. Arvanitis, R. Miranda, and J. J. de Miguel, "Enantiospecific spin polarization of electrons photoemitted through layers of homochiral organic molecules," *Advanced Materials* **26**(44), pp. 7474–7479, 2014.
- [13] M. Kettner, B. Göhler, H. Zacharias, D. Mishra, V. Kiran, R. Naaman, C. Fontanesi, D. H. Waldeck, S. Sek, J. Pawłowski, *et al.*, "Spin filtering in electron transport through chiral oligopeptides," *The Journal of Physical Chemistry C* **119**(26), pp. 14542–14547, 2015.
- [14] K. Michaeli, V. Varade, R. Naaman, and D. H. Waldeck, "A new approach towards spintronics—spintronics with no magnets," *Journal of Physics: Condensed Matter* **29**(10), p. 103002, 2017.
- [15] O. B. Dor, S. Yochelien, S. P. Mathew, R. Naaman, and Y. Paltiel, "A chiral-based magnetic memory device without a permanent magnet," *Nature Communications* **4**, p. 2256, 2013.
- [16] P. C. Mondal, N. Kantor-Uriel, S. P. Mathew, F. Tassinari, C. Fontanesi, and R. Naaman, "Chiral conductive polymers as spin filters," *Advanced Materials* **27**(11), pp. 1924–1927, 2015.
- [17] V. Varade, T. Markus, K. Vankayala, N. Friedman, M. Sheves, D. H. Waldeck, and R. Naaman, "Bacteriorhodopsin based non-magnetic spin filters for biomolecular spintronics," *Physical Chemistry Chemical Physics* **20**(2), pp. 1091–1097, 2018.

- [18] B. P. Bloom, V. Kiran, V. Varade, R. Naaman, and D. H. Waldeck, "Spin selective charge transport through cysteine capped CdSe quantum dots," *Nano Letters* **16**(7), pp. 4583–4589, 2016.
- [19] S. P. Mathew, P. C. Mondal, H. Moshe, Y. Mastai, and R. Naaman, "Non-magnetic organic/inorganic spin injector at room temperature," *Applied Physics Letters* **105**(24), p. 242408, 2014.
- [20] K. M. Alam and S. Pramanik, "Spin filtering through single-wall carbon nanotubes functionalized with single-stranded DNA," *Advanced Functional Materials* **25**(21), pp. 3210–3218, 2015.
- [21] R. Gutierrez, E. Díaz, R. Naaman, and G. Cuniberti, "Spin-selective transport through helical molecular systems," *Physical Review B* **85**(8), p. 081404, 2012.
- [22] S. Yeganeh, M. A. Ratner, E. Medina, and V. Mujica, "Chiral electron transport: scattering through helical potentials," *The Journal of Chemical Physics* **131**(1), p. 014707, 2009.
- [23] J. Gersten, K. Kaasbjerg, and A. Nitzan, "Induced spin filtering in electron transmission through chiral molecular layers adsorbed on metals with strong spin-orbit coupling," *The Journal of Chemical Physics* **139**(11), p. 114111, 2013.
- [24] E. Medina, L. A. González-Arraga, D. Finkelstein-Shapiro, B. Berche, and V. Mujica, "Continuum model for chiral induced spin selectivity in helical molecules," *The Journal of Chemical Physics* **142**(19), p. 194308, 2015.
- [25] K. Michaeli and R. Naaman, "Origin of spin-dependent tunneling through chiral molecules," *The Journal of Physical Chemistry C* **123**(27), pp. 17043–17048, 2019.
- [26] V. V. Maslyuk, R. Gutierrez, A. Dianat, V. Mujica, and G. Cuniberti, "Enhanced magnetoresistance in chiral molecular junctions," *The Journal of Physical Chemistry Letters* **9**(18), pp. 5453–5459, 2018.
- [27] A.-M. Guo and Q.-F. Sun, "Spin-selective transport of electrons in DNA double helix," *Physical Review Letters* **108**(21), p. 218102, 2012.
- [28] A.-M. Guo and Q.-F. Sun, "Spin-dependent electron transport in protein-like single-helical molecules," *Proceedings of the National Academy of Sciences* **111**(32), pp. 11658–11662, 2014.
- [29] T.-R. Pan, A.-M. Guo, and Q.-F. Sun, "Spin-polarized electron transport through helicene molecular junctions," *Physical Review B* **94**(23), p. 235448, 2016.
- [30] J. H. Bardarson, "A proof of the Kramers degeneracy of transmission eigenvalues from antisymmetry of the scattering matrix," *Journal of Physics A: Mathematical and Theoretical* **41**(40), p. 405203, 2008.
- [31] S. Matityahu, Y. Utsumi, A. Aharony, O. Entin-Wohlman, and C. A. Balseiro, "Spin-dependent transport through a chiral molecule in the presence of spin-orbit interaction and nonunitary effects," *Physical Review B* **93**(7), p. 075407, 2016.
- [32] S. Matityahu, A. Aharony, O. Entin-Wohlman, and C. A. Balseiro, "Spin filtering in all-electrical three-terminal interferometers," *Physical Review B* **95**(8), p. 085411, 2017.
- [33] A.-M. Guo, E. Díaz, C. Gaul, R. Gutierrez, F. Domínguez-Adame, G. Cuniberti, and Q.-F. Sun, "Contact effects in spin transport along double-helical molecules," *Physical Review B* **89**(20), p. 205434, 2014.
- [34] M. Büttiker, "Role of quantum coherence in series resistors," *Physical Review B* **33**(5), p. 3020, 1986.
- [35] M. Büttiker, Y. Imry, R. Landauer, and S. Pinhas, "Generalized many-channel conductance formula with application to small rings," *Physical Review B* **31**(10), p. 6207, 1985.
- [36] M. Büttiker, "Four-terminal phase-coherent conductance," *Physical Review Letters* **57**(14), p. 1761, 1986.
- [37] M. Büttiker, "Symmetry of electrical conduction," *IBM Journal of Research and Development* **32**(3), pp. 317–334, 1988.
- [38] G. A. Prinz, "Magnetoelectronics," *Science* **282**(5394), pp. 1660–1663, 1998.
- [39] I. Adagideli, G. E. W. Bauer, and B. I. Halperin, "Detection of current-induced spins by ferromagnetic contacts," *Physical Review Letters* **97**(25), p. 256601, 2006.
- [40] F. J. Jedema, A. T. Filip, and B. J. van Wees, "Electrical spin injection and accumulation at room temperature in an all-metal mesoscopic spin valve," *Nature* **410**(6826), p. 345, 2001.
- [41] M. Drögeler, C. Franzen, F. Volmer, T. Pohlmann, L. Banszerus, M. Wolter, K. Watanabe, T. Taniguchi, C. Stampfer, and B. Beschoten, "Spin lifetimes exceeding 12 ns in graphene nonlocal spin valve devices," *Nano Letters* **16**(6), pp. 3533–3539, 2016.
- [42] J. Inglá-Aynés, M. H. D. Guimarães, R. J. Meijerink, P. J. Zomer, and B. J. van Wees, "24- μm spin relaxation length in boron nitride encapsulated bilayer graphene," *Physical Review B* **92**(20), p. 201410, 2015.
- [43] M. Gurram, S. Omar, S. Zihlmann, P. Makk, Q. C. Li, Y. F. Zhang, C. Schönenberger, and B. J. van Wees, "Spin transport in two-layer-CVD-hBN/graphene/hBN heterostructures," *Physical Review B* **97**(4), p. 045411, 2018.
- [44] D. Nürenberg and H. Zacharias, "Evaluation of spin-flip scattering in chirality-induced spin selectivity using the Riccati equation," *Physical Chemistry Chemical Physics* **21**(7), pp. 3761–3770, 2019.
- [45] L. Hu, H. Huang, Z. Wang, W. Jiang, X. Ni, Y. Zhou, V. Zielasek, M. G. Lagally, B. Huang, and F. Liu, "Ubiquitous spin-orbit coupling in a screw dislocation with high spin coherency," *Physical Review Letters* **121**(6), p. 066401, 2018.
- [46] R. Naaman and D. H. Waldeck, "Comment on "Spin-dependent electron transmission model for chiral molecules in mesoscopic devices"," *Physical Review B* **101**(2), p. 026403, 2020.

- [47] X. Yang, C. H. van der Wal, and B. J. van Wees, "Spin-dependent electron transmission model for chiral molecules in mesoscopic devices," *Physical Review B* **99**(2), p. 024418, 2019.
- [48] S. Dalum and P. Hedegård, "Theory of chiral induced spin selectivity," *Nano Letters* **19**(8), pp. 5253–5259, 2019.
- [49] D. Sánchez and M. Büttiker, "Magnetic-field asymmetry of nonlinear mesoscopic transport," *Physical Review Letters* **93**(10), p. 106802, 2004.
- [50] S. Datta, *Electronic transport in mesoscopic systems*, Cambridge University Press, 1997.
- [51] M. Ben-Chorin, F. Möller, and F. Koch, "Nonlinear electrical transport in porous silicon," *Physical Review B* **49**(4), p. 2981, 1994.
- [52] A. A. Middleton and N. S. Wingreen, "Collective transport in arrays of small metallic dots," *Physical Review Letters* **71**(19), p. 3198, 1993.
- [53] K. Michaeli, D. N. Beratan, D. H. Waldeck, and R. Naaman, "Voltage-induced long-range coherent electron transfer through organic molecules," *Proceedings of the National Academy of Sciences* **116**(13), pp. 5931–5936, 2019.
- [54] X. Yang, C. H. van der Wal, and B. J. van Wees, "Detecting chirality in two-terminal electronic nanodevices," *Nano Letters* **20**, p. 6148, 2020.
- [55] See Supplemental Material associated with the published version of this chapter at <http://links.aps.org/supplemental/10.1103/PhysRevB.99.024418>, where the transmission and reflection probabilities of each spin species are plotted as a function of t (BCB barrier transmission probability) for the FM-BCB and spin-valve geometries.

Chapter 4

Detecting chirality in two-terminal electronic nanodevices

Central to spintronics is the interconversion between electronic charge and spin currents, and this can arise from the chirality-induced spin selectivity (CISS) effect. CISS is often studied as magnetoresistance (MR) in two-terminal (2T) electronic devices containing a chiral (molecular) component and a ferromagnet. However, fundamental understanding of when and how this MR can occur is lacking. Here, we uncover an elementary mechanism that generates such an MR for nonlinear response. It requires energy-dependent transport and energy relaxation within the device. The sign of the MR depends on chirality, charge carrier type, and bias direction. Additionally, we reveal how CISS can be detected in the linear response regime in magnet-free 2T devices, either by forming a chirality-based spin-valve using two or more chiral components, or by Hanle spin precession in devices with a single chiral component. Our results provide operation principles and design guidelines for chirality-based spintronic devices and technologies.

This chapter is published as:

X. Yang, C. H. van der Wal & B. J. van Wees, "Detecting chirality in two-terminal elec-tronic nanodevices," *Nano Letters* **20**, 6148 (2020)

DOI:10.1021/acs.nanolett.0c02417

4 Recognizing and separating chiral enantiomers using electronic/spintronic technologies addresses fundamental questions of electronic charge and spin transport [1]. It can open up new avenues for chiral chemistry, and can bring chiral (molecular) structures into electronic and spintronic applications. This is enabled by the chirality-induced spin selectivity (CISS) effect [2–4], which describes the generation of a collinear spin current by a charge current through a chiral component (single molecule, assembly of molecules, or solid-state system). In two-terminal (2T) electronic devices that contain a chiral component and a single ferromagnet (FM), CISS is reported as a change of (charge) resistance upon magnetization reversal [5–12]. This magnetoresistance (MR) has been interpreted in analogy to that of a conventional spin valve, based on the understanding that both the FM and the chiral component act as spin–charge converters [13–18]. However, this interpretation overlooks the fundamental distinction between their underlying mechanisms — magnetism breaks time reversal symmetry, while CISS, as a spin-orbit effect, does not. In fact, Onsager reciprocity prohibits the detection of spin-orbit effects as 2T charge signals using a single FM in the linear response regime [19–22]. Therefore, it requires theories beyond linear response for possible explanations of the MR observed in CISS experiments [22–25].

Here we show that such a 2T MR can indeed arise from the breaking of Onsager reciprocity in the nonlinear regime. When the conditions for generating CISS in a chiral component are fulfilled, the emergence of the 2T MR requires two key ingredients: (a) energy-dependent electron transport due to, for instance, tunneling or thermally activated conduction through molecular orbitals; and (b) energy relaxation due to inelastic processes. Note that there exists an interesting parallel in chemistry, where absolute asymmetric synthesis is enabled by the lone influence of a magnetic field or magnetization in the nonlinear regime (details see Appendix A) [1, 26, 27].

Below, before demonstrating the emergence of 2T MR in the nonlinear regime and identifying key factors that determine its sign, we will first introduce a transport-matrix formalism unifying the description of coupled charge and spin transport in spin–charge converters such as a chiral component and an FM tunnel junction / interface (FMTJ). Afterwards, we will explore new device designs that make 2T electrical detection of CISS possible in the linear response regime, and reveal a chiral spin valve built without magnetic materials.

4.1 Transport matrix formalism beyond Landauer formula

The (spin-resolved) Landauer formula considers charge voltages as the driving forces for electronic charge and spin transport [28]. However, in a circuit with multi-

ple spin–charge converters, we must also consider the build-up of spin accumulations, which also drive the coupled charge and spin transport (details see Appendix B) [29, 30]. Here we include this (thermodynamic) spin degree-of-freedom by extending the Landauer formula using a Büttiker-type multi-terminal transmission analysis [31]. Building on this, we introduce a transport matrix formalism that describes the (thermodynamic) responses of generic spin–charge converters. The symmetry/asymmetry of these transport matrices in the linear/nonlinear response regime is fundamentally related to the (breaking of) Onsager reciprocity. It does not depend on specific microscopic mechanisms and is not restricted to the transmission analysis that we use (see Appendix B).

4.1.1 Spin–charge conversion in a chiral component

CISS arises from spin-orbit interaction and the absence of space-inversion symmetry. Further symmetry considerations require that the sign of the CISS-induced collinear spin currents must depend on the direction of the charge current and the (sign of) chirality. Note that the generation of CISS requires a nonunitary transport mechanism within the chiral component [32, 33], which we assume to be present (details see Appendix C). In an ideal case, as illustrated in Fig. 4.1, this directional, spin-dependent electron transport effectively allows only one spin orientation, say, parallel to the electron momentum, to transmit through the chiral component, and reflects and spin-flips the other [22]. The spin-flip reflection prevents a net spin current in and out of electrodes at thermodynamic equilibrium [34].

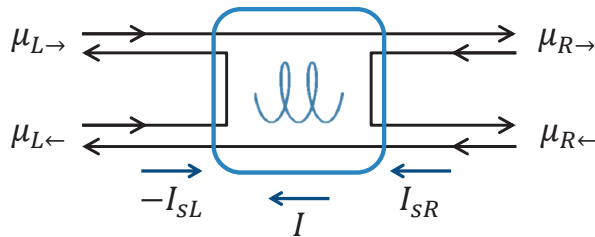


Figure 4.1: Illustration of CISS (ideal case). The directional electron transmission is spin-selective, and the unfavored spin is flipped and reflected. The chiral component is indicated by the blue helix, and is assumed to favor the transmission of electrons with spin parallel to momentum. The electrons on both sides (L and R) of the chiral component are labeled with their spin-specific (\rightarrow or \leftarrow) electrochemical potentials $\mu_{L(R)\rightarrow(\leftarrow)}$. At thermodynamic equilibrium, any net charge or spin current in and out of electrodes is forbidden, but when biased, the chiral structure supports a charge current I and collinear spin currents on both sides I_{sL} and I_{sR} . The positive currents are defined as right-to-left, i.e. when the (spin-polarized) electrons flow from left to right.

We first describe the directional electron transmission (\mathbb{T}) and reflection (\mathbb{R}) in a generalized chiral component using spin-space matrices introduced in Ref. 22. For right-moving (subscript \triangleright) electrons coming from the left-hand side of the component

$$\mathbb{T}_{\triangleright} = \begin{pmatrix} t_{\rightarrow\rightarrow} & t_{\leftarrow\rightarrow} \\ t_{\rightarrow\leftarrow} & t_{\leftarrow\leftarrow} \end{pmatrix}, \quad \mathbb{R}_{\triangleright} = \begin{pmatrix} r_{\rightarrow\rightarrow} & r_{\leftarrow\rightarrow} \\ r_{\rightarrow\leftarrow} & r_{\leftarrow\leftarrow} \end{pmatrix}, \quad (4.1)$$

where the matrix elements are probabilities of an electron being transmitted (t) or reflected (r) from an initial spin state (first subscript) to a final spin state (second subscript). For left-moving electrons, the corresponding matrices are the time-reversed forms of the above (details see Appendix D).

We extend the above coupled charge and spin transport by converting the spin-space matrices to transport matrices that link the thermodynamic drives and responses in terms of charge and spin. We define (charge) electrochemical potential $\mu = (\mu_{\rightarrow} + \mu_{\leftarrow})/2$ and spin accumulation $\mu_s = (\mu_{\rightarrow} - \mu_{\leftarrow})/2$, as well as charge current $I = I_{\rightarrow} + I_{\leftarrow}$ and spin current $I_s = I_{\rightarrow} - I_{\leftarrow}$. A subscript R or L is added when describing the quantities on a specific side of the component. With these, for a generalized case of Fig. 4.1, we derive (details see Appendix D)

$$\begin{pmatrix} I \\ -I_{sL} \\ I_{sR} \end{pmatrix} = -\frac{Ne}{h} \begin{pmatrix} t & s & s \\ P_r r & \gamma_r & \gamma_t \\ P_t t & \gamma_t & \gamma_r \end{pmatrix} \begin{pmatrix} \mu_L - \mu_R \\ \mu_{sL} \\ \mu_{sR} \end{pmatrix}, \quad (4.2)$$

where N is the number of (spin-degenerate) channels, e is elemental charge (positive value), and h is the Planck's constant. An electrochemical potential difference $\mu_L - \mu_R = -eV$ is provided by a bias voltage V . We name the 3×3 matrix the charge-spin transport matrix \mathcal{T} . All its elements are linear combinations of the spin-space \mathbb{T} and \mathbb{R} matrix elements, and represent key transport properties of the chiral component. For example, t is the (averaged) transmission probability, r is the reflection probability (note that $t + r = 2$ because we have treated the two spins separately), P_t and P_r are the CISS-induced spin polarizations of the transmitted and reflected electrons, respectively, γ_t and γ_r describe spin relaxation and spin transport generated by spin accumulations, and s is the charge current generated by the spin-charge conversion via CISS.

We are particularly interested in the symmetry of \mathcal{T} . Equation 4.2 fully describes the coupled charge and collinear spin transport through a (nonmagnetic) chiral component, which is subject to Onsager reciprocity in the linear response regime. This requires $\mathcal{T}_{ij}(\mathbf{H}, \mathbf{M}) = \mathcal{T}_{ji}(-\mathbf{H}, -\mathbf{M})$, where \mathbf{H} is the magnetic field and \mathbf{M} is the magnetization [35]. This then gives $P_t t = P_r r = s$. In later discussions we will connect the R -side of the chiral component to an electrode (reservoir), where $\mu_{sR} = 0$ and I_{sR} is irrelevant. The \mathcal{T} matrix then reduces to a 2×2 form (details see Ap-

pendix D)

$$\begin{pmatrix} I \\ -I_{sL} \end{pmatrix} = -\frac{Ne}{h} \begin{pmatrix} t & P_t t \\ P_t t & \gamma_r \end{pmatrix} \begin{pmatrix} \mu_L - \mu_R \\ \mu_{sL} \end{pmatrix}. \quad (4.3)$$

Note that t and γ_r do not depend on the (sign of) chirality, while P_t changes sign when the chirality is reversed.

4.1.2 Spin–charge conversion in a magnetic tunnel junction

To calculate the coupled charge and spin transport in a generic 2T circuit where an (achiral) ferromagnet is also present, we need to derive a similar \mathcal{T} matrix for an FMTJ. An FM breaks time-reversal symmetry and provides a spin-polarization P_{FM} to any outflowing charge current. Based on this, we obtain for the R -side of the FMTJ (details see Appendix E)

$$\begin{pmatrix} I \\ I_{sR} \end{pmatrix} = -\frac{N'e}{h} \begin{pmatrix} T & -P_{FM}T \\ P_{FM}T & -T \end{pmatrix} \begin{pmatrix} \mu_L - \mu_R \\ \mu_{sR} \end{pmatrix}, \quad (4.4)$$

where N' is the number of (spin-degenerate) channels, and T is the electron transmission probability accounting for both spins.

The matrix \mathcal{T} here also satisfies the requirement $\mathcal{T}_{ij}(\mathbf{H}, \mathbf{M}) = \mathcal{T}_{ji}(-\mathbf{H}, -\mathbf{M})$, where a reversal of \mathbf{M} corresponds to a sign change of P_{FM} .

4.2 Origin of MR – energy-dependent transport and energy relaxation

We model a generic 2T MR measurement geometry using Fig. 4.2(a). A FM and a chiral component are connected in series between two spin-unpolarized electrodes (L and R), and the difference between their electrochemical potentials $\mu_L - \mu_R = -eV$ drives charge and spin transport. We introduce a node between the FM and the chiral component, which is characterized by an electrochemical potential μ and a spin accumulation μ_s . It preserves the spin but relaxes the energy of electrons to a Fermi-Dirac distribution due to inelastic processes (e.g. electron-phonon interaction).

4.2.1 No MR in the linear response regime

The 2T conductance of this geometry in the linear response regime can be derived by applying continuity condition in the node for both the charge and spin currents, which gives (details see Appendix F)

$$G_{2T} = G_{2T}(P_{FM}^2, P_t^2), \text{ no } P_{FM}P_t \text{ term.} \quad (4.5)$$

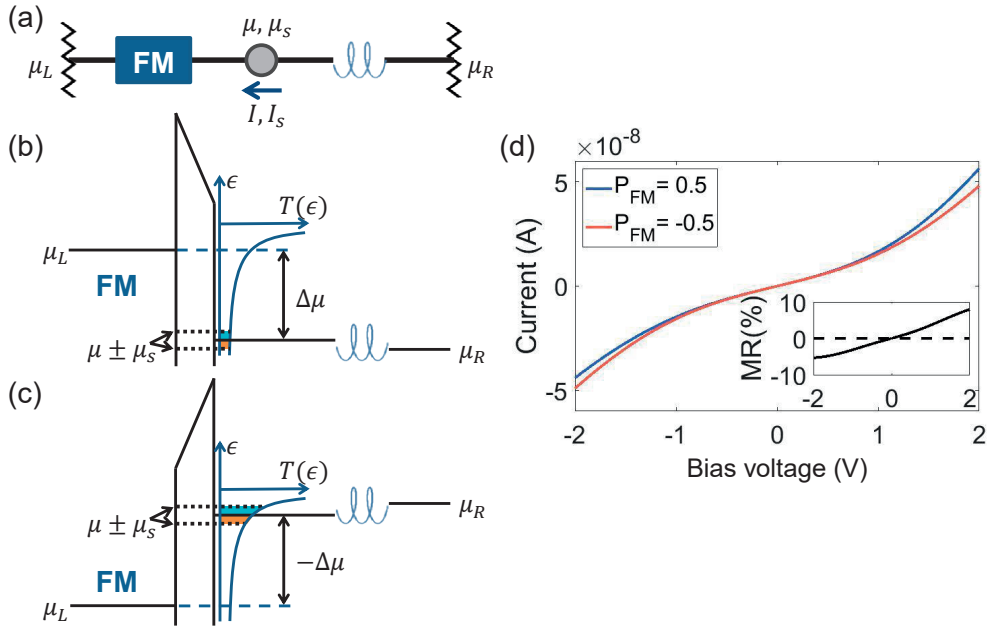


Figure 4.2: Origin of MR in a generic 2T circuit. (a). A 2T circuit containing an FM and a chiral component, connected by a node. The chiral component is assumed to favor the transmission of electrons with spin parallel to momentum. (b),(c). Schematic energy diagrams of tunneling at the FMTJ under forward [(b)] and reverse [(c)] biases. The energy-dependent tunnel transmission $T(\epsilon)$ is sketched in blue, and the tunnel current affected by the spin accumulation μ_s is illustrated by the color-shaded areas (cyan and orange). (d). Example I - V curves considering the nonlinear mechanism of (b)-(c), while keeping the transmission through the chiral component constant (details see Appendix G). Note that positive bias voltage corresponds to the reverse bias scenario depicted in panel (c). The MR ratio, defined as $(I_+ - I_-)/(I_+ + I_-)$, is plotted in inset. Here the subscript + or - denotes the corresponding sign of P_{FM} , with $P_{FM} > 0$ corresponding to a spin-right polarization for the injected electrons. The dashed line marks zero MR.

It depends on the polarizations P_{FM} and P_t only to second order, and does not depend on their product $P_{FM}P_t$. Therefore, the 2T conductance remains unchanged when the sign of either P_{FM} or P_t is reversed by the reversal of either the FM magnetization direction or the chirality. This result again confirms the vanishing MR in the linear response regime, as strictly required by Onsager reciprocity [22].

This vanishing MR can be understood as a result of two simultaneous processes. First, by the conventional description, the charge current through the chiral com-

ponent drives a collinear spin current and creates a spin accumulation in the node (spin injection by CISS), which is then detected as a charge voltage by the FM (spin detection by FM). This charge voltage indeed changes upon the FM magnetization reversal. However, this is always accompanied by the second process, where it is the FM that injects a spin current, and the Onsager reciprocal of CISS detects it as a charge voltage. This voltage also changes upon the FM magnetization reversal. In the linear regime, the two processes compensate each other, and the net result is a zero MR.

4.2.2 Emergence of MR in nonlinear regime

The key to inducing MR is to break the balance between the two processes, which can be done by using electrons at different energies for spin injection and spin detection. This requires the presence of energy relaxation inside the device, and it also needs the transport to be energy-dependent in at least one of the spin-charge converters. Note that the energy relaxation is crucial for generating MR, because Onsager reciprocity, which holds at each energy level, would otherwise prevent an MR even in the nonlinear regime despite the energy-dependent transport. We illustrate the emergence of MR using two types of energy dependence, (a) quantum tunneling through the FMTJ, and (b) thermally activated conduction through molecular orbitals. These two elementary examples reveal key factors that determine the sign of the nonlinear MR.

Example (a)

The asymmetric spin injection and spin detection in an FMTJ was previously discussed by Jansen *et al.* for an FM coupled to a semiconductor [36], and here we generalize it for our system. The energy diagrams for this tunneling process are sketched in Fig. 4.2(b)-(c) for opposite biases. The bias opens up an energy window $\Delta\mu = \mu_L - \mu$, and the electrons within this energy window contribute to the total charge current I . The energy distribution of the tunneling electrons follows the energy dependence of the tunnel transmission probability $T(\epsilon)$ (blue curve). Therefore, the electrons that contribute the most to the tunnel current I are those at the highest available energy, which are at μ_L (in the FM) under forward bias, and are at the spin-split electrochemical potentials $\mu \pm \mu_s$ (in the node) under reverse bias.

The spin injection process concerns the spin current I_s induced by the total charge current I through the FMTJ with spin polarization P_{FM} (assuming no energy dependence for P_{FM}). It is determined by the energy integral of $T(\epsilon)$ over the entire bias-induced window $\Delta\mu$, and is symmetric for opposite biases (assuming $\mu_s \ll \Delta\mu$). In contrast, the spin detection process, which concerns the spin accumulation μ_s in

the node at its highest energy μ (Fermi level), is not symmetric for opposite biases. Effectively, the spin accumulation describes the deficit of one spin and the surplus of the other, as illustrated by the orange- and blue-shaded regions under the $T(\epsilon)$ curve in Fig. 4.2(b)-(c), and therefore drives an (additional) charge current proportional to the area difference between the two regions. This detected charge current depends on the transmission probability at energy μ , and increases monotonically as the bias becomes more reverse.

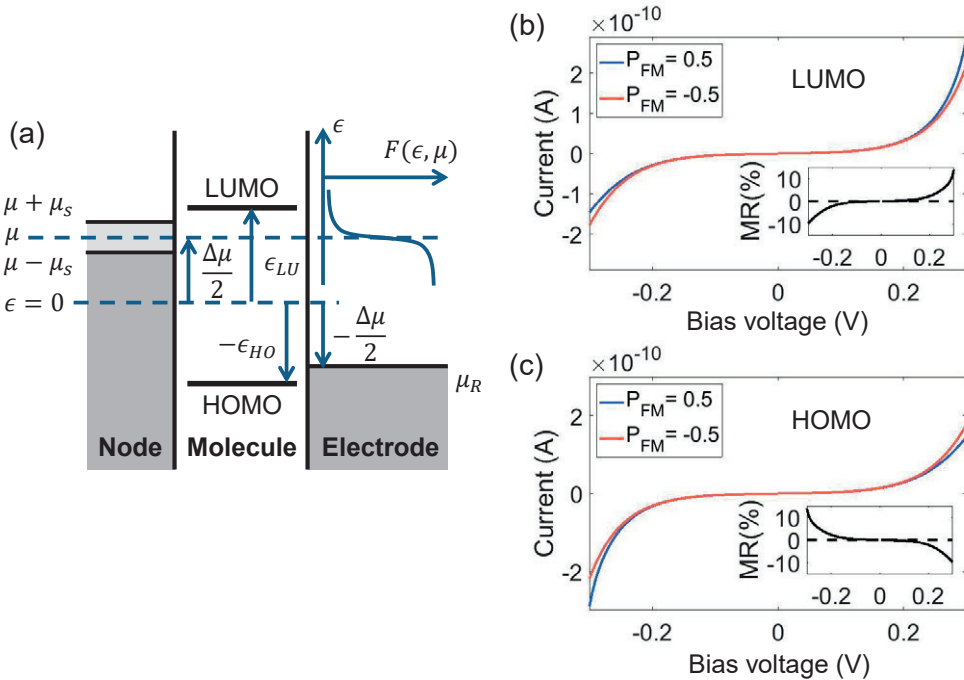


Figure 4.3: Generating MR by thermally activated conduction through molecular orbitals. (a). Schematic energy diagram of resonant transmission through molecular orbitals in a chiral component (molecule). The LUMO and HOMO levels and the bias-dependent electrochemical potentials are labeled, and the energy- and bias-dependent Fermi-Dirac function $F(\epsilon, \mu)$ is sketched in blue. (b)-(c). Example I - V curves and MR (inset) due to the resonant transmission through the LUMO [(b)] and the HOMO [(c)], for the same device geometry as in Fig. 4.2(a) but with the transmission of the FMTJ set constant. The chiral molecule is assumed to favor the transmission of electrons with spin parallel to momentum.

The different bias dependences for spin injection and detection break Onsager reciprocity for nonlinear response. This is also shown by the different off-diagonal

terms in the nonlinear transport equation (details see Appendix G)

$$\begin{pmatrix} I \\ I_s \end{pmatrix} = -\frac{N'e}{h} \begin{pmatrix} \bar{T}|_{\mu}^{\mu_L} & -P_{FM}T|_{\epsilon=\mu} \\ P_{FM}\bar{T}|_{\mu}^{\mu_L} & -T|_{\epsilon=\mu} \end{pmatrix} \begin{pmatrix} \mu_L - \mu \\ \mu_s \end{pmatrix}, \quad (4.6)$$

where $\bar{T}|_{\mu}^{\mu_L} = [1/(\mu_L - \mu)] \int_{\mu}^{\mu_L} T(\epsilon) d\epsilon$ is the averaged transmission over the energy window $\Delta\mu = \mu_L - \mu$, and $T|_{\epsilon=\mu}$ is the transmission evaluated at the Fermi level of the node $\epsilon = \mu$. In the linear response regime, when $\mu_L \approx \mu$, this equation returns to Eqn. 4.4.

The tunnel I - V and the MR due to this mechanism are illustrated in Fig. 4.2(d) using realistic circuit parameters (details see Appendix I). The MR ratio reaches nearly 10 % at large biases, but strictly vanishes at zero bias. Notably, the MR is positive under positive bias voltage (corresponds to reverse bias as in Fig. 4.2(c)), and it reverses sign as the bias changes sign.

Example (b)

The non-reciprocal spin injection and detection can also arise from the nonlinear transport through the chiral component. In principle, this could also be due to tunneling, but we focus here on another aspect, the Fermi-Dirac distribution of electrons. This is negligible when the transmission function $T(\epsilon)$ is smooth, as for the case of tunneling (thus we have assumed zero temperature for deriving Eqn. 4.6), but it becomes dominant when electron (or hole) transmission is only allowed at certain discrete energy levels or energy bands that are away from Fermi level, as for the case of conduction through molecular orbitals or through energy bands in semiconductors. We illustrate this in Fig. 4.3(a) considering the resonant transmission through the LUMO (lowest unoccupied molecular orbital) and the HOMO (highest occupied molecular orbital) of a chiral molecule (details see Appendix H). For spin injection, the generated spin current is proportional to the total charge current, which depends on the (bias-induced) electrochemical potential difference between the node and the right electrode, and is symmetric for opposite biases. In comparison, for spin detection, the spin-split electrochemical potentials in the node $\mu \pm \mu_s$ induce unequal occupations of opposite spins at each MO (depending on the MO position with respect to the node Fermi level μ), and it is not symmetric for opposite biases. This different bias dependence breaks Onsager reciprocity for nonlinear response, and gives rise to MR.

We consider the transmission through either only the LUMO or only the HOMO, and their example I - V curves and MR ratios are plotted in Fig. 4.3(b)-(c), respectively (details see Appendix I). The MR is able to reach tens of percent even at relatively small biases, and changes sign as the bias reverses. Remarkably, the bias dependence

of the MR is opposite for LUMO and HOMO, implying that the charge carrier type, i.e. electrons or holes, co-determines the sign of the MR. Again, the MR strictly vanishes as the bias returns to zero (linear response regime). An overview of the signs of MR is given in Appendix J.

4.3 Chiral spin valve

In the linear response regime, our formalism uses an antisymmetric transport matrix (opposite off-diagonal terms) to describe the coupled charge and spin transport through the FMTJ, and uses a symmetric one for the chiral component. The symmetries of these transport matrices are directly required by Onsager reciprocity, and have consequences when considering 2T circuits containing two generic spin-charge converting components, as illustrated in Fig. 4.4. If the two components are described by transport matrices with opposite symmetries, a 2T MR signal is forbidden in the linear response regime (Fig. 4.4(a)). This restriction is lifted if both components are described by matrices with the same symmetry. For example, in a conventional spin valve (Fig. 4.4(b)), the two FMs are both described by antisymmetric transport matrices, and the magnetization reversal of one FM indeed changes the 2T conductance even in the linear response regime.

A less obvious outcome of this symmetry consideration is that a combination of two chiral components (both described by symmetric matrices) can also form a spin valve, provided that at least one of them can switch chirality, such as a molecular rotor [37]. This is illustrated in Fig. 4.4(c)-(d), with example I - V curves in Fig. 4.4(f). In the linear response regime, this geometry already produces a nonzero chirality-reversal resistance (CRR, see figure caption for definition) ratio, which is further enhanced to tens of percent as the bias increases.

Finally, we introduce a 2T geometry that can detect the spin-charge conversion due to a single chiral component, as shown in Fig. 4.4(e). Here, a charge current through the chiral component can create a spin accumulation in the node (even in the linear response regime), which can then be suppressed using a perpendicular magnetic field due to Hanle spin precession. This results in a magnetic-field-dependent 2T conductance, and Fig. 4.4(g) shows the I - V curves for zero magnetic field (blue solid curve) and for when the field fully suppresses the spin accumulation (black dashed curve). The corresponding MR (inset) is nonzero even in the linear response regime, and can be enhanced by increasing bias.

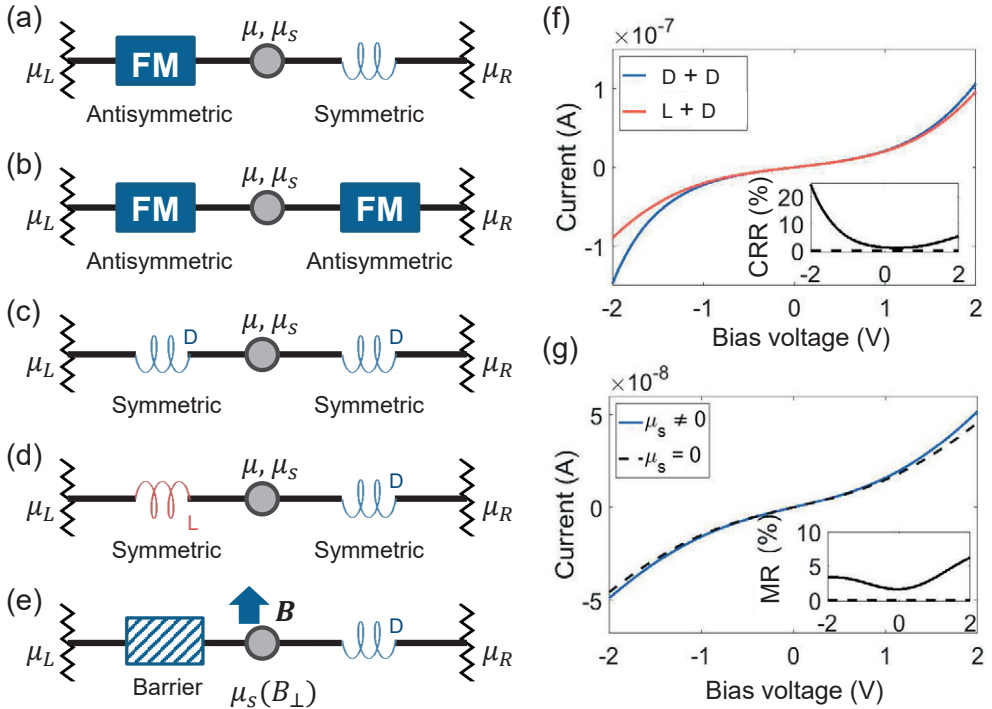


Figure 4.4: Generic 2T spin-valve device geometries with the symmetry of the charge–spin transport matrix labeled for each component. (a). The aforementioned FM–chiral geometry where MR signals are strictly forbidden in the linear response regime. (b). A FM–FM geometry, as in a conventional spin valve, where MR signals are allowed in the linear regime. (c),(d). A chiral–chiral geometry for using the same [(c)] and opposite [(d)] chiralities, as marked by color and labeled with D or L (here we assume the D-chiral component favors the transmission of electrons with spin parallel to momentum, and the L-chiral component favors the anti-parallel ones). The spin-valve effect can be achieved, even in the linear regime, by reversing the chirality of one component. (e). A geometry for directly probing the spin accumulation generated by a single chiral component. The perpendicular magnetic field B suppresses spin accumulation in the node via Hanle spin precession. (f). Example I - V curves for a chiral–chiral spin valve, with the two curves representing the geometries in panel (c) and (d) respectively. The corresponding chirality-reversal resistance (CRR) ratio, as defined by $CRR = (I_{DD} - I_{LD}) / (I_{DD} + I_{LD})$ (the two subscripts refer to the chiralities of the two chiral components), is plotted in the inset. (g). Example I - V for the geometry in panel (e), calculated for cases with μ_s either fully or not-at-all suppressed by Hanle precession. The corresponding MR is shown in inset, which is defined as the difference of the two curves divided by their sum.

4.4 Discussion

We explained that energy-dependent transport combined with energy relaxation can give rise to MR signals in 2T electronic devices containing an FM and a chiral component. We analyzed the (sign of) MR using two elementary examples: energy-dependent tunneling through FMTJ (plus a chiral component at linear response) and energy-dependent Fermi-Dirac distribution for thermally activated resonant transmission through the chiral component (plus an FMTJ at linear response). Here we note that other mechanisms such as electron-electron interaction may also play a role in electron transport through chiral molecules [38, 39]. This however does not affect our (qualitative) conclusions regarding the onset and the sign of MR, and can be quantitatively accounted for by deriving the transport matrix of the chiral component accordingly [40, 41] (see Appendix K).

We also assumed that the overall conduction through the circuit components is (phase) incoherent. In practice, coherent conduction mechanisms, such as direct tunneling from the FM into an MO of the chiral molecule, may also be present. For fully incoherent conduction, the chirality-based spin valve (Fig. 4.4(c-d)) resembles a conventional CPP GMR device [42], while if coherent tunneling dominates, it is comparable to a TMR device [43].

Finally, we draw attention to the sign of the nonlinear MR, which depends on the dominating nonlinear element, the bias direction, the charge carrier type, and the (sign of) chirality, as summarized in Appendix J. We have plotted the MR as a function of bias while assuming the chirality and the charge carrier type remain unchanged. However, in experimental conditions, it is possible that the charge carrier type switches when the bias is reversed, and consequently the MR can have the same sign for opposite biases. Such a bias-even MR is indeed in agreement with most experimental observations [5, 6, 8–12]. The experimental conditions concerning the vanishing MR in the linear regime are however not clear, since sometimes the currents are too low to be measured [5, 6, 9]. For experiments where a linear regime can be identified, some do show a strongly suppressed or vanishing MR [8, 12], while some do not [10, 11]. This inconsistency thus requires further investigation.

4.5 Appendices

A. Comparison to absolute asymmetric (chemical) synthesis

Absolute asymmetric synthesis refers to chemical reactions starting from achiral or racemic reactants but yield chiral products with a net enantiomeric excess. Generally, it requires the presence of a truly chiral external influence, which, according to Barron [1], is a physical quantity that can appear in two degenerate forms (e.g. opposite signs of one physical quantity, or parallel and anti-parallel alignments of two vectors),

which are interconverted by space-inversion but not time-reversal. Following this, the lone influence of a magnetic field, which reverses sign under time-reversal but not space-inversion, is not truly chiral, and therefore should not induce absolute asymmetric synthesis.

Just like Onsager reciprocity, this true-chirality consideration is based on microscopic reversibility, and therefore is only strict in the linear response regime (in the vicinity of thermodynamic equilibrium). Barron later pointed out that [44], in a chemical reaction that would yield a racemic mixture (of enantiomers), the presence of a magnetic field allows different reaction rates toward opposite enantiomers. This creates an enantiomeric excess away from equilibrium, which should eventually disappear as the system returns to equilibrium. However, if the nonequilibrium enantiomeric excess is amplified, for example by self-assembly or crystallization, absolute asymmetric synthesis is induced, and this was later demonstrated experimentally [26, 27].

This shows that a time-reversal-breaking influence (the magnetic field), albeit not being truly chiral, can distinguish and separate enantiomers away from thermodynamic equilibrium. By the same token, in the 2T circuit we discuss, the FM breaks time reversal symmetry and can therefore indeed distinguish enantiomers away from equilibrium, i.e. in the nonlinear regime. Therefore, the nonlinear conductance of the 2T circuit may depend on the chirality of the circuit component, as well as the magnetization direction of the FM.

B. Beyond the Landauer formula

The Landauer formula describes the electrical conductance of a conductor using its scattering properties [45]. Particularly, it expresses conductance in terms of transmission probabilities between electrodes, but does not require the use of reflection probabilities. Moreover, it considers that the charge (and spin) transport are solely driven by a charge bias, and neglects possible spin accumulations in the circuit [28]. For a 2T device, it allows two independent parameters (charge and spin transmission probability) for the description of coupled charge and spin transport.

We point out here that, a full description of the coupled charge and spin transport must extend beyond the conventional spin-resolved Landauer formula, and include also the (spin-flip) reflection terms and the build-up of spin accumulations, which also act as driving forces of the transport. This point was also earlier raised for a FM-normal metal system [29]. Following this, we need to characterize the (twofold rotationally symmetric) chiral component using four independent parameters, see the matrix in Eqn. 4.19, contrasting to the two parameters mentioned earlier.

Using this extended Landauer formula that is similar to a Büttiker multi-terminal analysis, we can fully (in terms of charge and spin) account for how a generic spin-charge converter responds to charge and spin driving forces. This response can be described using the transport matrices that our main text focused on. Note that although in this work we derive these transport matrices using the extended Landauer formula, the general validity of the transport matrix formalism is not limited by this extended Landauer formula. The transport matrices can be alternatively derived using other methods, and can be extended to the nonlinear regime by including energy or bias dependences. The symmetry/asymmetry of the transport matrix in the linear/nonlinear response regime is fundamentally related to the (breaking of) Onsager reciprocity, and does not depend on how the transport matrix itself is derived.

C. Nonunitarity for generating CISS and energy relaxation for generating MR

The generation of CISS requires the presence of nonunitary effects inside the chiral component, because the Kramers degeneracy would otherwise require equal transmission probabilities for opposite spin orientations [32, 33]. These nonunitary effects break the phase information of a transmitting electron, but does not necessarily alter its energy.

The presence of these nonunitary effects only allows the generation of CISS, but does not guarantee the generation of a 2T MR. These nonunitary effects do not (necessarily) break the Onsager reciprocity, and therefore a 2T MR is still forbidden in the linear response regime. Even when considering energy-dependent transport in the nonlinear regime ($|eV| > k_B T$), since at each energy level the Onsager reciprocity still holds, a 2T MR cannot arise.

The emergence of MR, as we discussed, requires energy relaxation in the device. These relaxation processes not only break the phase information, but also alter the energy of the electrons, and rearrange them according to Fermi-Dirac distribution. We have assumed that they do not change the spin orientation of the electrons. In principle, we can also include spin relaxation in the node, which we expect to reduce the MR without changing its sign.

D. Spin and charge transport in a nonmagnetic chiral component

In the main text we introduced the spin-space transmission and reflection matrices for the right-moving electrons in a (nonmagnetic) chiral component (Eqn. 1)

$$\mathbb{T}_{\triangleright} = \begin{pmatrix} t_{\rightarrow\rightarrow} & t_{\leftarrow\rightarrow} \\ t_{\rightarrow\leftarrow} & t_{\leftarrow\leftarrow} \end{pmatrix}, \quad \mathbb{R}_{\triangleright} = \begin{pmatrix} r_{\rightarrow\rightarrow} & r_{\leftarrow\rightarrow} \\ r_{\rightarrow\leftarrow} & r_{\leftarrow\leftarrow} \end{pmatrix}. \quad (4.7)$$

For the left-moving electrons, the matrices are the time-reversed form of the above

$$\mathbb{T}_{\triangleleft} = \begin{pmatrix} t_{\leftarrow\leftarrow} & t_{\rightarrow\leftarrow} \\ t_{\leftarrow\rightarrow} & t_{\rightarrow\rightarrow} \end{pmatrix}, \quad \mathbb{R}_{\triangleleft} = \begin{pmatrix} r_{\leftarrow\leftarrow} & r_{\rightarrow\leftarrow} \\ r_{\leftarrow\rightarrow} & r_{\rightarrow\rightarrow} \end{pmatrix}. \quad (4.8)$$

Note that these matrices are not suitable for describing magnetic components where time-reversal symmetry is not preserved, and we have assumed the chiral component is symmetric (i.e. a twofold rotational symmetry with axis perpendicular to the electron pathway, this ensures that for oppositely moving electrons, the spin polarization only changes sign).

We use spin-space column vector to describe electrochemical potentials and currents on both sides of the molecule, and following Ref.22 we have

$$\begin{pmatrix} I_{L\rightarrow} \\ I_{L\leftarrow} \end{pmatrix} = -\frac{Ne}{h} \left[(\mathbb{I} - \mathbb{R}_{\triangleright}) \begin{pmatrix} \mu_{L\rightarrow} \\ \mu_{L\leftarrow} \end{pmatrix} - \mathbb{T}_{\triangleleft} \begin{pmatrix} \mu_{R\rightarrow} \\ \mu_{R\leftarrow} \end{pmatrix} \right], \quad (4.9a)$$

$$-\begin{pmatrix} I_{R\rightarrow} \\ I_{R\leftarrow} \end{pmatrix} = -\frac{Ne}{h} \left[(\mathbb{I} - \mathbb{R}_{\triangleleft}) \begin{pmatrix} \mu_{R\rightarrow} \\ \mu_{R\leftarrow} \end{pmatrix} - \mathbb{T}_{\triangleright} \begin{pmatrix} \mu_{L\rightarrow} \\ \mu_{L\leftarrow} \end{pmatrix} \right], \quad (4.9b)$$

where N is the number of spin-degenerate channels.

We define charge electrochemical potential $\mu = (\mu_{\rightarrow} + \mu_{\leftarrow})/2$ and spin accumulation $\mu_s = (\mu_{\rightarrow} - \mu_{\leftarrow})/2$, as well as charge current $I = I_{\rightarrow} + I_{\leftarrow}$ and spin current $I_s = I_{\rightarrow} - I_{\leftarrow}$. We will describe both charge and spin in electrical units.

Following these definitions, we have

$$I = I_{L\rightarrow} + I_{L\leftarrow} = I_{R\rightarrow} + I_{R\leftarrow}, \quad (4.10a)$$

$$I_{sL} = I_{L\rightarrow} - I_{L\leftarrow}, \quad (4.10b)$$

$$I_{sR} = I_{R\rightarrow} - I_{R\leftarrow}, \quad (4.10c)$$

$$\mu_L = (\mu_{L\rightarrow} + \mu_{L\leftarrow})/2, \quad (4.10d)$$

$$\mu_R = (\mu_{R\rightarrow} + \mu_{R\leftarrow})/2, \quad (4.10e)$$

$$\mu_{sL} = (\mu_{L\rightarrow} - \mu_{L\leftarrow})/2, \quad (4.10f)$$

$$\mu_{sR} = (\mu_{R\rightarrow} - \mu_{R\leftarrow})/2. \quad (4.10g)$$

Combining Eqn. 4.9 and Eqn. 4.10, we can derive

$$\begin{pmatrix} I \\ -I_{sL} \\ I_{sR} \end{pmatrix} = -\frac{Ne}{h} \begin{pmatrix} t & s & s \\ P_r r & \gamma_r & \gamma_t \\ P_t t & \gamma_t & \gamma_r \end{pmatrix} \begin{pmatrix} \mu_L - \mu_R \\ \mu_{sL} \\ \mu_{sR} \end{pmatrix}, \quad (4.11)$$

which is Eqn. 2 in the main text, and $\mu_L - \mu_R = -eV$ is induced by a bias voltage V . The matrix elements are

$$t = t_{\rightarrow\rightarrow} + t_{\rightarrow\leftarrow} + t_{\leftarrow\rightarrow} + t_{\leftarrow\leftarrow}, \quad (4.12a)$$

$$r = r_{\rightarrow\rightarrow} + r_{\rightarrow\leftarrow} + r_{\leftarrow\rightarrow} + r_{\leftarrow\leftarrow} = 2 - t, \quad (4.12b)$$

$$\gamma_t = t_{\rightarrow\rightarrow} - t_{\rightarrow\leftarrow} - t_{\leftarrow\rightarrow} + t_{\leftarrow\leftarrow}, \quad (4.12c)$$

$$\gamma_r = r_{\rightarrow\rightarrow} - r_{\rightarrow\leftarrow} - r_{\leftarrow\rightarrow} + r_{\leftarrow\leftarrow} - 2, \quad (4.12d)$$

$$P_t = (t_{\rightarrow\rightarrow} - t_{\rightarrow\leftarrow} + t_{\leftarrow\rightarrow} - t_{\leftarrow\leftarrow})/t, \quad (4.12e)$$

$$P_r = (r_{\rightarrow\rightarrow} - r_{\rightarrow\leftarrow} + r_{\leftarrow\rightarrow} - r_{\leftarrow\leftarrow})/r, \quad (4.12f)$$

$$s = t_{\rightarrow\rightarrow} + t_{\rightarrow\leftarrow} - t_{\leftarrow\rightarrow} - t_{\leftarrow\leftarrow} \quad (4.12g)$$

$$= -r_{\rightarrow\rightarrow} - r_{\rightarrow\leftarrow} + r_{\leftarrow\rightarrow} + r_{\leftarrow\leftarrow}. \quad (4.12h)$$

For $r = 2 - t$ and the two expressions of s , we have used the condition of charge conservation

$$t_{\rightarrow\rightarrow} + t_{\rightarrow\leftarrow} + r_{\rightarrow\rightarrow} + r_{\rightarrow\leftarrow} = 1, \quad (4.13a)$$

$$t_{\leftarrow\rightarrow} + t_{\leftarrow\leftarrow} + r_{\leftarrow\rightarrow} + r_{\leftarrow\leftarrow} = 1. \quad (4.13b)$$

Among the above matrix elements, P_t , P_r , and s change sign when the chirality is reversed. For achiral components where there is no spin selective transport, we have $P_t = P_r = s = 0$, and the transport matrix is symmetric.

Note that in Eqn. 2 we have defined the vector of currents (thermodynamic response) using $-I_{sL}$ and I_{sR} , so that the transport matrix is symmetric in the linear response regime. Following this, as shown in Fig. 1, the chiral component acts as a source (or sink) of spin currents when biased.

We can rewrite γ_t and γ_r as transmission-dependent quantities

$$\gamma_r = r - (P_r r + s)/\eta_r - 2 = -t - (P_r r + s)/\eta_r, \quad (4.14a)$$

$$\gamma_t = -t + (P_t t + s)/\eta_t, \quad (4.14b)$$

where

$$\eta_r = \frac{r_{\leftarrow\rightarrow} - r_{\rightarrow\leftarrow}}{r_{\leftarrow\rightarrow} + r_{\rightarrow\leftarrow}}, \quad (4.15a)$$

$$\eta_t = \frac{t_{\rightarrow\rightarrow} - t_{\leftarrow\leftarrow}}{t_{\rightarrow\rightarrow} + t_{\leftarrow\leftarrow}}, \quad (4.15b)$$

are quantities between ± 1 and change sign under chirality reversal.

Next, for chiral components where P_t , P_r , and s are nonzero, the Onsager reciprocity requires the 3×3 matrix to be symmetric [35], which gives

$$P_t t = P_r r = s, \quad (4.16)$$

and therefore

$$t_{\rightarrow\leftarrow} = t_{\leftarrow\rightarrow}, \quad (4.17a)$$

$$r_{\rightarrow\rightarrow} = r_{\leftarrow\leftarrow}, \quad (4.17b)$$

$$t_{\rightarrow\rightarrow} - t_{\leftarrow\leftarrow} = r_{\leftarrow\rightarrow} - r_{\rightarrow\leftarrow}. \quad (4.17c)$$

These expressions show that, for any finite P_t (spin polarization of transmitted electrons), P_r (spin polarization of reflected electrons) must also be nonzero, which then requires the presence of spin-flip reflections [22]. This is again in agreement with the fundamental considerations based on zero charge and spin currents in electrodes at equilibrium.

Further, we obtain

$$\gamma_r = -(1 + 2P_t/\eta_r)t, \quad (4.18a)$$

$$\gamma_t = -(1 - 2P_t/\eta_t)t. \quad (4.18b)$$

which allows us to rewrite the transport matrix equation in terms of t

$$\begin{pmatrix} I \\ -I_{sL} \\ I_{sR} \end{pmatrix} = -\frac{Ne}{h} \begin{pmatrix} t & P_t t & P_t t \\ P_t t & -(1 + 2P_t/\eta_r)t & -(1 - 2P_t/\eta_t)t \\ P_t t & -(1 - 2P_t/\eta_t)t & -(1 + 2P_t/\eta_r)t \end{pmatrix} \begin{pmatrix} \mu_L - \mu_R \\ \mu_{sL} \\ \mu_{sR} \end{pmatrix}. \quad (4.19)$$

Note that P_t , η_t , and η_r all change sign when the chirality is reversed, and t , P_t/η_t , and P_t/η_r are always positive.

In later discussions we connect the right-hand side of the nonmagnetic component to an electrode (see Fig. 2(a)) where the spin accumulation μ_{sR} is zero and the spin current I_{sR} is irrelevant. This reduces the matrix equation to

$$\begin{pmatrix} I \\ -I_{sL} \end{pmatrix} = -\frac{Ne}{h} \begin{pmatrix} t & P_t t \\ P_t t & -(1 + 2P_t/\eta_r)t \end{pmatrix} \begin{pmatrix} \mu_L - \mu_R \\ \mu_{sL} \end{pmatrix}, \quad (4.20)$$

which is equivalent to Eqn. 3 in the main text.

E. Spin and charge transport at an achiral ferromagnetic tunnel junction/interface

In a FM, time-reversal symmetry is broken and the Kramers degeneracy is lifted. The FMTJ provides a spin polarization to any current that flows through, and reciprocally, it generates a charge voltage upon a spin accumulation at its interface. In terms of spin and charge transport, the FMTJ allows different conductances for electrons with opposite spins, and the difference depends on the spin polarization P_{FM} . Inside the FM spin relaxation is strong and the spin accumulation is considered zero. For our discussions, the FM is always connected to the left of the node, we thus only consider the R interface of the FM with a spin accumulation μ_{sR} . Following the discussion provided in Ref. 36, the spin-specific currents on the R -side are therefore

$$I_{\rightarrow} = -\frac{1}{e} G_{\rightarrow} [\mu_L - (\mu_R + \mu_{sR})], \quad (4.21a)$$

$$I_{\leftarrow} = -\frac{1}{e} G_{\leftarrow} [\mu_L - (\mu_R - \mu_{sR})], \quad (4.21b)$$

where $G_{\rightarrow(\leftarrow)}$ is the spin-specific tunnel conductance. We define the total conductance $G_{FM} = G_{\rightarrow} + G_{\leftarrow}$ and FM spin-polarization $P_{FM} = (G_{\rightarrow} - G_{\leftarrow})/(G_{\rightarrow} + G_{\leftarrow})$. We also introduce a transmission coefficient T ($0 \leq T \leq 2$) to distinguish G_{FM} from ideal transmission. The charge and spin currents on the R interface of the FM can thus be written as

$$\begin{pmatrix} I \\ I_{sR} \end{pmatrix} = -\frac{N'e}{h} \begin{pmatrix} T & -P_{FM}T \\ P_{FM}T & -T \end{pmatrix} \begin{pmatrix} \mu_L - \mu_R \\ \mu_{sR} \end{pmatrix}, \quad (4.22)$$

where N' is the number of spin-degenerate channels in the FMTJ.

This matrix gives the spin and charge response of the FMTJ, and unlike for a chiral molecule, this matrix fulfills the Onsager reciprocity by being antisymmetric (opposite off-diagonal terms), because upon magnetic field and magnetization reversal, the FM spin polarization P_{FM} changes sign [35].

F. Spin and charge transport in a generic 2T circuit

We consider a generic 2T circuit like the one shown in Fig. 2(a). Our goal here is to derive the quantities I , μ , and μ_s as a function of 2T bias $\mu_L - \mu_R$. We rewrite the transport matrices into conductance matrices, and obtain for the left and right side of the node

$$\begin{pmatrix} I \\ I_s \end{pmatrix} = -\frac{1}{e} \begin{pmatrix} G_1 & G_2 \\ G_3 & G_4 \end{pmatrix} \begin{pmatrix} \mu_L - \mu \\ \mu_s \end{pmatrix}, \quad (4.23a)$$

$$\begin{pmatrix} I \\ -I_s \end{pmatrix} = -\frac{1}{e} \begin{pmatrix} g_1 & g_2 \\ g_3 & g_4 \end{pmatrix} \begin{pmatrix} \mu - \mu_R \\ \mu_s \end{pmatrix}. \quad (4.23b)$$

At steady state the continuity condition requires the currents I and I_s are equal for both equations. This condition allows us to derive

$$\begin{aligned}\mu &= \mu_R + \frac{G_3(G_2 - g_2) - G_1(G_4 + g_4)}{f} (\mu_L - \mu_R) \\ &= \mu_L - \frac{g_3(g_2 - G_2) - g_1(G_4 + g_4)}{f} (\mu_L - \mu_R),\end{aligned}\quad (4.24a)$$

$$\mu_s = \frac{(G_3/G_1 + g_3/g_1)G_1g_1}{f} (\mu_L - \mu_R), \quad (4.24b)$$

$$I = \frac{G_1g_2g_3 + g_1G_2G_3 - G_1g_1(G_4 + g_4)}{f} (\mu_L - \mu_R), \quad (4.24c)$$

where the coefficient f is

$$f = (G_3 - g_3)(G_2 - g_2) - (G_1 + g_1)(G_4 + g_4). \quad (4.25)$$

Notably, f depends on $(G_3 - g_3)(G_2 - g_2)$, and for our linear-regime example using an FM with $G_2 = -G_3$ and a chiral component with $g_2 = g_3$, f only depends on $g_3^2 - G_3^2$, which does not change when either the FM magnetization or the chirality is reversed. Moreover, the charge current I only depends on g_3^2 and G_3^2 , and therefore remains unchanged under magnetization or chirality reversal. In contrast, the spin accumulation μ_s depends on G_3 and g_3 , and the charge distribution indicated by μ depends on G_3g_2 or g_3G_2 . Both μ_s and μ therefore indeed change upon magnetization or chirality reversal, and can be detected using three-terminal or four-terminal measurements.

If the two circuit components would both be FM (antisymmetric G and g matrices) or both be chiral (symmetric G and g matrices), then the coefficient f contains the cross products G_3g_2 and G_2g_3 , and therefore gives rise to a 2T current that does change upon magnetization or chirality reversal.

G. Reciprocity breaking by energy-dependent tunneling

Here we derive the energy dependence of the charge and spin tunneling through the FM interface following the discussion by Jansen *et al.* [36], and derive the subsequent nonlinear coupled charge and spin transport equations.

We consider a biased symmetric rectangular tunnel barrier with height Φ and width w between the FM and the node, as shown in Fig. 4.5(a). The reference energy $\epsilon = 0$ is chosen as the average of μ_L and μ , so that the average barrier height does not change with bias. The bias voltage $V = -\Delta\mu/e$ is applied, so that $\mu_L = \Delta\mu/2$, $\mu = -\Delta\mu/2$, $\mu_{\rightarrow} = -\Delta\mu/2 + \mu_s$, and $\mu_{\leftarrow} = -\Delta\mu/2 - \mu_s$. For simplicity, we assume the barrier height (evaluated at the center of the tunnel barrier) is constant, the tunneling is one dimensional, and the electrostatic potential drop across the tunnel barrier is exactly $-eV$.

The energy-dependent electron transmission function is

$$T(\epsilon) = 2 \exp\left(-\beta(\Phi - \epsilon)^{1/2}\right), \quad (4.26)$$

where $\beta = 2w\sqrt{2m/\hbar^2}$, with m being the (effective) electron mass and \hbar the reduced Planck's constant.

The total transmitted current is an energy-integral of two energy-dependent functions: (1). the transmission function $T(\epsilon)$, and (2) the voltage-dependent Fermi-Dirac distribution functions in both electrodes. The two parts dominate at different bias regimes with respect to the thermal activation energy $k_B T$, where k_B is the Boltzmann constant and T is temperature. For tunneling, typically we have $|eV| \gg k_B T$, and therefore we assume zero temperature for convenience. The Fermi-Dirac distribution functions then become Heaviside step functions with the step at μ_L for the left electrode and at μ_{\rightarrow} and μ_{\leftarrow} for the two spin species in the node.

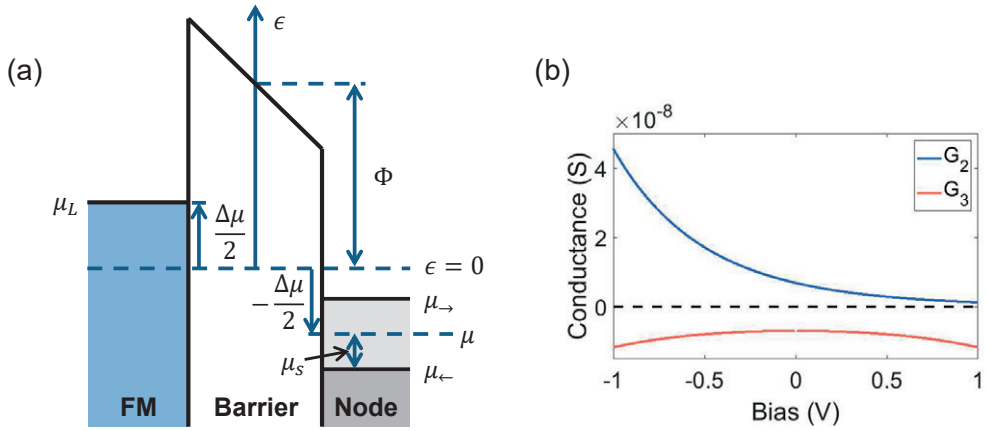


Figure 4.5: (a). Energy diagram of the tunnel barrier at the ferromagnet interface. Details see text. (b). Bias dependence of the off-diagonal elements of the conductance matrix describing tunneling through the FMTJ.

Assuming P_{FM} does not depend on energy, the energy-integrated tunnel current for each spin species through the FMTJ is

$$I_{\rightarrow}(\Delta\mu, \mu_s) = -\frac{N'e}{h} \frac{1 + P_{FM}}{2} \int_{\mu_{\rightarrow}}^{\mu_L} T(\epsilon) d\epsilon, \quad (4.27a)$$

$$I_{\leftarrow}(\Delta\mu, \mu_s) = -\frac{N'e}{h} \frac{1 - P_{FM}}{2} \int_{\mu_{\leftarrow}}^{\mu_L} T(\epsilon) d\epsilon. \quad (4.27b)$$

The range of the integrals can be rewritten as

$$\text{for } I_{\rightarrow} : \int_{\mu_{\rightarrow}}^{\mu_L} d\epsilon = \int_{\mu}^{\mu_L} d\epsilon - \int_{\mu}^{\mu_{\rightarrow}} d\epsilon, \quad (4.28a)$$

$$\text{for } I_{\leftarrow} : \int_{\mu_{\leftarrow}}^{\mu_L} d\epsilon = \int_{\mu}^{\mu_L} d\epsilon + \int_{\mu_{\leftarrow}}^{\mu} d\epsilon. \quad (4.28b)$$

We denote the two integrals on the right-hand side of the expressions $I_{\rightarrow(\leftarrow)}^{(1)}$ and $I_{\rightarrow(\leftarrow)}^{(2)}$ respectively, so that we have $I_{\rightarrow} = I_{\rightarrow}^{(1)} + I_{\rightarrow}^{(2)}$ and $I_{\leftarrow} = I_{\leftarrow}^{(1)} + I_{\leftarrow}^{(2)}$. The first integral $I_{\rightarrow(\leftarrow)}^{(1)}$ depends on the electrochemical potential difference across the barrier, $\Delta\mu$, and thus describes the bias-induced transport. In contrast, the second integral $I_{\rightarrow(\leftarrow)}^{(2)}$ depends on μ and μ_s in the node, and it vanishes when $\mu_s = 0$, and therefore it describes the spin-accumulation-induced correction to the first integral. We will treat the two integrals separately.

The bias-induced charge and spin currents are

$$\begin{aligned} I^{(1)} &= I_{\rightarrow}^{(1)} + I_{\leftarrow}^{(1)} \\ &= -\frac{N'e}{h} \int_{\mu}^{\mu_L} T(\epsilon) d\epsilon \\ &= -\frac{N'e}{h} (\overline{T})_{\mu}^{\mu_L} \Delta\mu, \end{aligned} \quad (4.29a)$$

$$\begin{aligned}
I_s^{(1)} &= I_{\rightarrow}^{(1)} - I_{\leftarrow}^{(1)} \\
&= -\frac{N'e}{h} P_{FM} \int_{\mu}^{\mu_L} T(\epsilon) d\epsilon \\
&= -\frac{N'e}{h} (P_{FM} \bar{T}|_{\mu}^{\mu_L}) \Delta\mu,
\end{aligned} \tag{4.29b}$$

where the averaged transmission within the bias window is defined as

$$\bar{T}|_{\mu}^{\mu_L} = \frac{1}{\Delta\mu} \int_{\mu}^{\mu_L} T(\epsilon) d\epsilon. \tag{4.30}$$

Note that when $\Delta\mu$ changes sign, the integral changes sign too, and therefore $\bar{T}|_{\mu}^{\mu_L}$ is an even function of $\Delta\mu$.

For the spin-accumulation-induced currents, we have

$$\begin{aligned}
I^{(2)} &= I_{\rightarrow}^{(2)} + I_{\leftarrow}^{(2)} \\
&= -\frac{N'e}{h} \left[-\frac{1+P_{FM}}{2} \int_{\mu}^{\mu_{\rightarrow}} T(\epsilon) d\epsilon + \frac{1-P_{FM}}{2} \int_{\mu_{\leftarrow}}^{\mu} T(\epsilon) d\epsilon \right] \\
&\approx -\frac{N'e}{h} (-P_{FM} T|_{\epsilon=\mu}) \cdot \mu_s,
\end{aligned} \tag{4.31a}$$

$$\begin{aligned}
I_s^{(2)} &= I_{\rightarrow}^{(2)} - I_{\leftarrow}^{(2)} \\
&= -\frac{N'e}{h} \left[-\frac{1+P_{FM}}{2} \int_{\mu}^{\mu_{\rightarrow}} T(\epsilon) d\epsilon - \frac{1-P_{FM}}{2} \int_{\mu_{\leftarrow}}^{\mu} T(\epsilon) d\epsilon \right] \\
&\approx -\frac{N'e}{h} (-T|_{\epsilon=\mu}) \cdot \mu_s,
\end{aligned} \tag{4.31b}$$

where the approximation is taken under the assumption that $\mu_s \ll \Delta\mu$, so that $T(\epsilon)$ is approximately a constant within the energy range from μ_{\leftarrow} to μ_{\rightarrow} , and thus they are evaluated at $\epsilon = \mu = -\Delta\mu/2$. The energy dependence of $I^{(2)}$ and $I_s^{(2)}$ follows that of $T(\epsilon)$ (Eqn. 4.26).

We can now rewrite Eqn. 4.29 and Eqn. 4.31 into matrix form

$$\begin{pmatrix} I \\ I_s \end{pmatrix} = -\frac{N'e}{h} \begin{pmatrix} \bar{T}|_{\mu}^{\mu_L} & -P_{FM} T|_{\epsilon=\mu} \\ P_{FM} \bar{T}|_{\mu}^{\mu_L} & -T|_{\epsilon=\mu} \end{pmatrix} \begin{pmatrix} \mu_L - \mu \\ \mu_s \end{pmatrix}, \tag{4.32}$$

which is Eqn. 6 in the main text. The different off-diagonal terms demonstrate the breaking of Onsager reciprocity in the nonlinear regime, since one of them depends on the integral of the transmission function, while the other depends on the transmission function itself. In the linear response regime ($\mu_L \approx \mu$), the two terms differ only by sign.

We write

$$\begin{pmatrix} I \\ I_s \end{pmatrix} = -\frac{1}{e} \begin{pmatrix} G_1 & G_2 \\ G_3 & G_4 \end{pmatrix} \begin{pmatrix} \mu_L - \mu \\ \mu_s \end{pmatrix}, \tag{4.33}$$

so that the matrix elements represent conductance, where $G_2 = (N'e^2/h) \cdot (-P_{FM} T|_{\epsilon=\mu})$ and $G_3 = (N'e^2/h) \cdot (P_{FM} \bar{T}|_{\mu}^{\mu_L})$. In Fig. 4.5(b), we plot G_2 and G_3 as a function of bias across the FMTJ ($(\mu_L - \mu)/e$) for $P_{FM} = -0.5$ and $N' = 1000$, values that are used to calculate the I - V curves in Fig. 2(d) (for other parameters see later in Appendix I).

Note that $G_2 = -G_3$ at zero bias, as required by Onsager reciprocity in the linear response regime. The breaking of reciprocity in the nonlinear regime is exhibited by the unequal absolute values of G_2 and G_3 away from zero bias. Here G_2 increases monotonically with decreasing bias, while G_3 is symmetric in bias and is minimum at zero bias.

H. Reciprocity breaking by thermally activated resonant transmission through molecular orbitals

We discuss here the effect of the Fermi-Dirac distribution of electrons using resonant transmission through discrete molecular orbitals (levels), specifically the lowest-unoccupied molecular orbital (LUMO) and the highest-occupied molecular orbital (HOMO). This is illustrated in Fig. 4.6(a). We assume here the LUMO and HOMO levels are fixed at energies ϵ_{LU} and $-\epsilon_{HO}$ respectively ($\epsilon_{LU}, \epsilon_{HO} > 0$), with $\epsilon = 0$ defined as the average of the two (charge) electrochemical potentials on both sides of the molecule. The nonlinearity is now assumed to be fully due to the Fermi-Dirac distribution $F(\epsilon, \mu)$, which is different for the node and the electrode, and is also different for the two spin species in the node when a spin accumulation is considered.

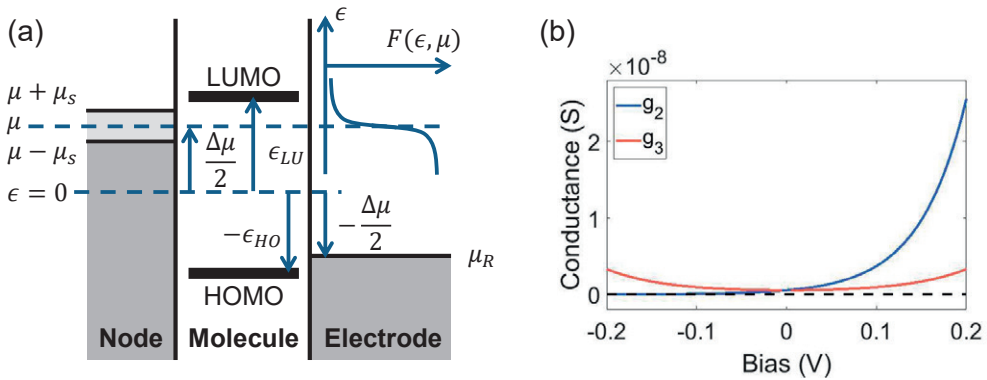


Figure 4.6: (a). Energy diagram of electron transmission through molecular levels. (b). Bias dependence of the off-diagonal elements of the conductance matrix describing thermally activated conduction through the LUMO.

Consider the geometry in Fig. 4.6(a), at a given bias $\Delta\mu$ and a spin accumulation μ_s in the node, the spin-specific Fermi-Dirac functions for the two spin species in the node are

$$F_{L\rightarrow}(\epsilon, \Delta\mu, \mu_s) = \frac{1}{\exp\left(\frac{\epsilon - \Delta\mu/2 - \mu_s}{k_B T}\right) + 1}, \quad (4.34a)$$

$$F_{L\leftarrow}(\epsilon, \Delta\mu, \mu_s) = \frac{1}{\exp\left(\frac{\epsilon - \Delta\mu/2 + \mu_s}{k_B T}\right) + 1}, \quad (4.34b)$$

where we used subscript L to denote the node because its located on the left side of the molecule.

The Fermi-Dirac function in the node (neglecting the spin accumulation) and in the right electrode are

$$F_L(\epsilon, \Delta\mu) = \frac{1}{\exp\left(\frac{\epsilon - \Delta\mu/2}{k_B T}\right) + 1}, \quad (4.35a)$$

$$F_R(\epsilon, \Delta\mu) = \frac{1}{\exp\left(\frac{\epsilon + \Delta\mu/2}{k_B T}\right) + 1}. \quad (4.35b)$$

We model the resonant transmission through the molecular orbitals as energy-dependent transmission probability $t(\epsilon)$ that is only nonzero at the LUMO and the HOMO levels, which it is described by

$$t(\epsilon) = t_{LU}\delta(\epsilon - \epsilon_{LU}) + t_{HO}\delta(\epsilon + \epsilon_{HO}), \quad (4.36)$$

where t_{LU} and t_{HO} are the transmission probabilities through the LUMO and the HOMO, respectively, and $\delta(\epsilon)$ is a Dirac delta function.

An exact calculation should separately address the two spin orientations separately, but for our assumption of $\mu_s \ll \Delta\mu$, we will directly start from the linear-regime equation of coupled charge and spin transport (Eqn. 4.20)

$$\begin{pmatrix} I \\ -I_{sL} \end{pmatrix} = -\frac{Ne}{h} \begin{pmatrix} t & P_t t \\ P_t t & -(1 + 2P_t/\eta_r)t \end{pmatrix} \begin{pmatrix} \mu - \mu_R \\ \mu_s \end{pmatrix}. \quad (4.37)$$

This gives the charge current I

$$I = -\frac{Ne}{h} [t(\mu_L - \mu_R) + P_t t(\mu_{L\rightarrow} - \mu_{L\leftarrow})/2], \quad (4.38)$$

where we used $\mu_{L\rightarrow} = \mu + \mu_s$ and $\mu_{L\leftarrow} = \mu - \mu_s$.

At finite temperature, the two terms in the square bracket on the right-hand side of the equation should each be replaced by an energy-integral of the electron transmission function modified by the voltage- and temperature-dependent Fermi-Dirac distributions in both electrodes. We denote the two terms $I^{(1)}$ and $I^{(2)}$, and the first term is

$$\begin{aligned} I^{(1)} &= \int_{-\infty}^{\infty} t(\epsilon) [F_L(\epsilon, \Delta\mu) - F_R(\epsilon, \Delta\mu)] d\epsilon \\ &= t_{LU} [F_L(\epsilon_{LU}, \Delta\mu) - F_R(\epsilon_{LU}, \Delta\mu)] \\ &\quad + t_{HO} [F_L(-\epsilon_{HO}, \Delta\mu) - F_R(-\epsilon_{HO}, \Delta\mu)]. \end{aligned} \quad (4.39)$$

We denote

$$\mathcal{F}_\epsilon(\Delta\mu) = \frac{1}{\Delta\mu} [F_L(\epsilon, \Delta\mu) - F_R(\epsilon, \Delta\mu)], \quad (4.40)$$

to highlight the transmission at energy ϵ and under bias $\Delta\mu$. In this manner, we can write

$$I^{(1)} = [t_{LU} \mathcal{F}_{\epsilon_{LU}}(\Delta\mu) + t_{HO} \mathcal{F}_{-\epsilon_{HO}}(\Delta\mu)] \Delta\mu. \quad (4.41)$$

Similarly, at finite temperature, the second term $I^{(2)}$ becomes

$$\begin{aligned} I^{(2)} &= \frac{P_t}{2} (t_{LU} [F_{L\rightarrow}(\epsilon_{LU}, \Delta\mu, \mu_s) - F_{L\leftarrow}(\epsilon_{LU}, \Delta\mu, \mu_s)] \\ &\quad + t_{HO} [F_{L\rightarrow}(-\epsilon_{HO}, \Delta\mu, \mu_s) - F_{L\leftarrow}(-\epsilon_{HO}, \Delta\mu, \mu_s)]). \end{aligned} \quad (4.42)$$

We define

$$\begin{aligned} \mathcal{F}'_{L,\epsilon}(\Delta\mu) &= \frac{1}{2\mu_s} [F_{L\rightarrow}(\epsilon, \Delta\mu, \mu_s) - F_{L\leftarrow}(\epsilon, \Delta\mu, \mu_s)] \\ &\approx \frac{\partial[F_L(\epsilon, \Delta\mu)]}{\partial\Delta\mu}, \end{aligned} \quad (4.43)$$

where the approximation is taken under the assumption of $\mu_s \ll \Delta\mu$.

With this, we have

$$I^{(2)} = P_t [t_{LU} \mathcal{F}'_{L,\epsilon_{LU}}(\Delta\mu) + t_{HO} \mathcal{F}'_{L,-\epsilon_{HO}}(\Delta\mu)] \mu_s. \quad (4.44)$$

Similarly, the expression of $-I_{sL}$ at finite temperature can also be derived from the linear regime expression. The nonlinear coupled spin and charge transport equation, due to the thermally activated resonant transmission via the LUMO and the HOMO levels, is therefore

$$\begin{pmatrix} I \\ -I_{sL} \end{pmatrix} = -\frac{Ne}{h} \mathcal{T} \begin{pmatrix} \mu - \mu_R \\ \mu_s \end{pmatrix}, \quad (4.45a)$$

where \mathcal{T} is

$$\begin{pmatrix} t_{LU} \mathcal{F}_{\epsilon_{LU}}(\Delta\mu) + t_{HO} \mathcal{F}_{-\epsilon_{HO}}(\Delta\mu) & P_t [t_{LU} \mathcal{F}'_{L,\epsilon_{LU}}(\Delta\mu) + t_{HO} \mathcal{F}'_{L,-\epsilon_{HO}}(\Delta\mu)] \\ P_t [t_{LU} \mathcal{F}_{\epsilon_{LU}}(\Delta\mu) + t_{HO} \mathcal{F}_{-\epsilon_{HO}}(\Delta\mu)] & -(1 + 2P_t/\eta_r) [t_{LU} \mathcal{F}'_{L,\epsilon_{LU}}(\Delta\mu) + t_{HO} \mathcal{F}'_{L,-\epsilon_{HO}}(\Delta\mu)] \end{pmatrix}, \quad (4.45b)$$

where we have assumed P_t, η_r do not depend on energy.

The breaking of reciprocity arises from the different forms of the off-diagonal terms of the transport matrix. While the bottom-left term scales with the electron occupation function, the top-right terms scales with its derivative. In the linear response regime, the two terms are equal and Onsager reciprocity is present.

If required, this nonlinear form can be easily extended to the 3×3 matrix for a generalized situation considering also a spin accumulation μ_{sR} on the right-hand side of the molecule. Then the third column will be modified similarly to the second column using the derivative of the electron occupation function in the right electrode $F_R(\epsilon, \Delta\mu)$.

Similar to the FMTJ, we can write the above equation into

$$\begin{pmatrix} I \\ -I_s \end{pmatrix} = -\frac{1}{e} \begin{pmatrix} g_1 & g_2 \\ g_3 & g_4 \end{pmatrix} \begin{pmatrix} \mu - \mu_R \\ \mu_s \end{pmatrix}, \quad (4.46)$$

where the matrix elements represent conductance. We plot the off-diagonal terms as a function of bias $((\mu - \mu_R)/e)$ for transmission only through the LUMO level ($t_{LU} = 1, t_{HO} = 0, \epsilon_{LU} = 0.6$ eV) for $P_t = 0.85$ and $N = 1000$, as shown in Fig. 4.6(b).

Note that $g_2 = g_3$ at zero bias, as required by Onsager reciprocity in the linear response regime. The reciprocity is broken as bias shifts away from zero, and the two conductance values are no longer equal. Here g_2 increases monotonically with bias, while g_3 is bias-symmetric and reaches minimum at zero bias.

I. Parameters for example I - V curves

(1) For calculating the I - V curves in Fig. 2(d) we have used the following parameters: Energy dependent FM tunnel transmission $T(\epsilon)$ for a tunnel barrier with height $\Phi = 2.1$ eV, and width $w = 1.0$ nm. The number of channels are set as $N' = 1000$ and $N = 5000$, the values are chosen taking into account the device length scale. For example, if using Ni as FM, when assuming each atom provides one channel, $N' = 1000$ corresponds to roughly an area of 100 nm^2 . The transmission through the chiral component is set linear and uses the same transmission value as the FM tunnel barrier at zero bias. The polarization values are $P_{FM} = \pm 0.5$, $P_t = 0.85$, and the quantity η_r is set as $\eta_r = 0.9$. The same parameters are used to obtain the conductances in Fig. 4.5(b).

(2) For calculating the I - V curves in Fig. 3(b-c) we have used the following parameters: Temperature at 300 K, the LUMO level at $\epsilon_{LU} = 0.6$ eV, and the HOMO level at $-\epsilon_{HO} = -0.6$ eV. For Fig. 3(b), the LUMO transmission $t_{LU} = 1$ and the HOMO transmission $t_{HO} = 0$, while for Fig. 3(c) the two values are interchanged. The number of channels are set as $N' = 1000$ and $N = 200$. The transmission through the FM tunnel barrier is set linear and uses the same transmission value as the FM tunnel barrier in case (1) at zero bias. The polarization values are $P_{FM} = \pm 0.5$, $P_t = 0.85$, and the quantity η_r is set as $\eta_r = 0.9$. The same parameters are used to obtain the conductances in Fig. 4.6(b).

(3) For the chiral spin valve in Fig. 4(f), we use the same tunnel transmission function and the same barrier parameters as in case (1) for both chiral components (both nonlinear), and do not consider the thermally activated molecular level transmission. The number of channels are set as $N' = 1000$ and $N = 20000$. The first chiral component has polarization ± 0.5 , and the second one 0.85 , both have $\eta_r = 0.9$.

(d) For the example in Fig. 4(g), the tunnel barrier uses the same parameters as the FMTJ in case (1), but has zero spin polarization. The chiral component transmission is set linear and uses the same set of parameters as in case (1). The dashed curve is obtained by forcing $\mu_s = 0$ for all bias values.

J. Sign of the nonlinear 2T MR

We summarize here, separately for the two nonlinear mechanisms, how the sign of the MR depends on the chirality, the charge carrier type, and the bias direction. First of all, we define the MR for the device in Fig. 2(a) following

$$MR = \frac{I_+ - I_-}{I_+ + I_-} \times 100\%, \quad (4.47)$$

where I_+ represents the charge current measured with the FM polarization $P_{FM} > 0$, which corresponds to a spin-right polarization of the injected electrons, and I_- corresponds to the current measured when the FM generates a spin-left polarization.

Table 4.1: Summary of the sign of MR for nonlinear tunneling through FMTJ

chirality	electron direction	carrier type	MR
D	CC to FMTJ	electron	+
L	CC to FMTJ	electron	-
D	FMTJ to CC	electron	-
L	FMTJ to CC	electron	+

Table 4.2: Summary of the sign of MR for nonlinear transmission through molecular orbitals

chirality	electron direction	carrier type	MR
D	CC to FMTJ	electron	+
L	CC to FMTJ	electron	-
D	FMTJ to CC	electron	-
L	FMTJ to CC	electron	+
D	CC to FMTJ	hole	-
L	CC to FMTJ	hole	+
D	FMTJ to CC	hole	+
L	FMTJ to CC	hole	-

For the bias direction, we describe it in terms of electron movement direction (opposite to charge current) with respect to the circuit components. For example, in Fig. 2(a), the positive bias voltage corresponds to an electron movement from the chiral component (CC) to the FMTJ.

For the (sign of) chirality, we label it as D and L. Here we (arbitrarily) assume that a D-chiral component favors the transmission of electrons with spins parallel to the electron momentum, while a L-chiral component favors the anti-parallel. The exact correspondence between the chirality and the favored spin orientation depends on the microscopic details of the spin orbit interaction.

According to these definitions, the sign of the MR is summarized in the above tables.

K. Beyond noninteracting-electron picture

In the main text, we analyzed two elementary sources of energy dependence to illustrate the onset of MR in nonlinear regime: (a) energy-dependent tunnelling through the ferromagnetic tunnel junction (Fig. 4.2), and (b) energy-dependent Fermi-Dirac distribution for molecular resonant transmission (Fig. 4.3). For convenience, both examples concentrated the role of electron-electron or electron-phonon interactions in the node for inducing energy relaxation, and considered a noninteracting-electron picture for transport through each individual circuit component. In practice, however, electron transport through chiral

molecules could also involve other many-body effects such as Coulomb blockade, Kondo effects, molecular deformation, and transport-induced chemical reactions [38, 39].

We emphasize here, in three aspects, that our qualitative conclusions are not restricted by the non-interacting-electron picture that we use. Moreover, our quantitative results can in principle be improved by including the many-body effects when deriving the transport matrices.

First, the transport matrix formalism we introduced is generally valid. It describes the coupled charge and spin transport in generic spintronic devices, which is (thermodynamically) driven by charge and spin chemical potentials. The symmetry/asymmetry of the transport matrices in the linear/nonlinear response regime is fundamentally related to the (breaking of) Onsager reciprocity. It does not depend on specific microscopic mechanisms. Based on this, we derived our main conclusion that MR signals can only arise in the nonlinear regime, and it requires energy-dependent transport and energy relaxation. This conclusion is therefore also fundamental and does not depend on detailed transport mechanisms.

Second, we identified how key factors such as bias direction, electron/hole transport, and chirality, determine the sign of the MR. These factors are also related to fundamental symmetry and the nature of electron transport, and do not depend on microscopic mechanisms.

Third, considering our two examples, the first one is unaffected by electron-electron or electron-phonon interactions in the chiral component because it operates in the linear response regime. In the second example where we consider energy-dependent transport through the chiral component, potential many-body effects may indeed change the energy and bias dependence of the nonlinear transport, and thereby quantitatively affect the MR in the nonlinear regime.

We point out here that our formalism can be extended to include the role of many-body effects or other nonlinear mechanisms by deriving the transport matrices accordingly [40, 41]. We encourage future studies to address these mechanisms to help identify their signatures in experimental results of the electrical detection of CISS.

Bibliography

- [1] L. D. Barron, "True and false chirality and absolute asymmetric synthesis," *Journal of the American Chemical Society* **108**(18), pp. 5539–5542, 1986.
- [2] R. Naaman, Y. Paltiel, and D. H. Waldeck, "Chiral molecules and the electron spin," *Nature Reviews Chemistry* **3**, pp. 250–260, 2019.
- [3] B. Göhler, V. Hamelbeck, T. Z. Markus, M. Kettner, G. F. Hanne, Z. Vager, R. Naaman, and H. Zacharias, "Spin selectivity in electron transmission through self-assembled monolayers of double-stranded DNA," *Science* **331**(6019), pp. 894–897, 2011.
- [4] A. Inui, R. Aoki, Y. Nishiue, K. Shiota, Y. Kousaka, H. Shishido, D. Hirobe, M. Suda, J.-i. Ohe, J.-i. Kishine, *et al.*, "Chirality-induced spin-polarized state of a chiral crystal CrNb₃S₆," *Physical Review Letters* **124**(16), p. 166602, 2020.
- [5] M. Suda, Y. Thathong, V. Promarak, H. Kojima, M. Nakamura, T. Shiraogawa, M. Ehara, and H. M. Yamamoto, "Light-driven molecular switch for reconfigurable spin filters," *Nature Communications* **10**(1), p. 2455, 2019.
- [6] H. Lu, J. Wang, C. Xiao, X. Pan, X. Chen, R. Brunecky, J. J. Berry, K. Zhu, M. C. Beard, and Z. V. Vardeny, "Spin-dependent charge transport through 2D chiral hybrid lead-iodide perovskites," *Science Advances* **5**(12), p. eaay0571, 2019.
- [7] A. C. Aragonès, E. Medina, M. Ferrer-Huerta, N. Gimeno, M. Teixidó, J. L. Palma, N. Tao, J. M. Ugalde, E. Giral, I. Díez-Pérez, *et al.*, "Measuring the spin-polarization power of a single chiral molecule," *Small* **13**(2), p. 1602519, 2017.
- [8] V. Kiran, S. P. Mathew, S. R. Cohen, I. Hernández Delgado, J. Lacour, and R. Naaman, "Helicenes—A new class of organic spin filter," *Advanced Materials* **28**, pp. 1957–1962, 2016.
- [9] Z. Xie, T. Z. Markus, S. R. Cohen, Z. Vager, R. Gutierrez, and R. Naaman, "Spin specific electron conduction through DNA oligomers," *Nano Letters* **11**(11), pp. 4652–4655, 2011.
- [10] R. Torres-Cavanillas, G. Escorcia-Ariza, P. C. Mondal, L. E. Rosaleny, S. Giménez-Santamarina, I. Brotons, M. Sesolo, M. Galbiati, S. Tatay, A. Gaita-Ariño, *et al.*, "Room temperature spin filtering in chiral metallopeptides," *arXiv:1905.09225*, 2019.

- [11] T. Liu, X. Wang, H. Wang, G. Shi, F. Gao, H. Feng, H. Deng, L. Hu, E. Lochner, P. Schlottmann, *et al.*, "Spin selectivity through chiral polyaniline monolayers on semiconductors," *arXiv:2001.00097*, 2019.
- [12] C. Kulkarni, A. K. Mondal, T. K. Das, G. Grinbom, F. Tassinari, M. F. Mabesoone, E. Meijer, and R. Naaman, "Highly efficient and tunable filtering of electrons' spin by supramolecular chirality of nanofiber-based materials," *Advanced Materials* **32**, p. 1904965, 2020.
- [13] K. Michaeli and R. Naaman, "Origin of spin-dependent tunneling through chiral molecules," *The Journal of Physical Chemistry C* **123**(27), pp. 17043–17048, 2019.
- [14] E. Medina, L. A. González-Arraga, D. Finkelstein-Shapiro, B. Berche, and V. Mujica, "Continuum model for chiral induced spin selectivity in helical molecules," *The Journal of Chemical Physics* **142**(19), p. 194308, 2015.
- [15] A.-M. Guo and Q.-F. Sun, "Spin-selective transport of electrons in DNA double helix," *Physical Review Letters* **108**(21), p. 218102, 2012.
- [16] M. S. Zöllner, S. Varela, E. Medina, V. Mujica, and C. Herrmann, "Insight into the origin of chiral-induced spin selectivity from a symmetry analysis of electronic transmission," *Journal of Chemical Theory and Computation* **16**(5), pp. 2914–2929, 2020.
- [17] E. Díaz, F. Domínguez-Adame, R. Gutierrez, G. Cuniberti, and V. Mujica, "Thermal decoherence and disorder effects on chiral-induced spin selectivity," *The Journal of Physical Chemistry Letters* **9**(19), pp. 5753–5758, 2018.
- [18] M. Geyer, R. Gutierrez, V. Mujica, and G. Cuniberti, "Chirality-induced spin selectivity in a coarse-grained tight-binding model for helicene," *The Journal of Physical Chemistry C* **123**(44), pp. 27230–27241, 2019.
- [19] L. Onsager, "Reciprocal relations in irreversible processes. I.," *Physical Review* **37**(4), p. 405, 1931.
- [20] M. Büttiker, "Symmetry of electrical conduction," *IBM Journal of Research and Development* **32**(3), pp. 317–334, 1988.
- [21] I. Adagideli, G. E. W. Bauer, and B. I. Halperin, "Detection of current-induced spins by ferromagnetic contacts," *Physical Review Letters* **97**(25), p. 256601, 2006.
- [22] X. Yang, C. H. van der Wal, and B. J. van Wees, "Spin-dependent electron transmission model for chiral molecules in mesoscopic devices," *Physical Review B* **99**(2), p. 024418, 2019.
- [23] S. Dalum and P. Hedegård, "Theory of chiral induced spin selectivity," *Nano Letters* **19**(8), pp. 5253–5259, 2019.
- [24] R. Naaman and D. H. Waldeck, "Comment on "Spin-dependent electron transmission model for chiral molecules in mesoscopic devices",," *Physical Review B* **101**(2), p. 026403, 2020.
- [25] X. Yang, C. H. van der Wal, and B. J. van Wees, "Reply to "Comment on "Spin-dependent electron transmission model for chiral molecules in mesoscopic devices",," *Physical Review B* **101**(2), p. 026404, 2020.
- [26] N. Micali, H. Engelkamp, P. G. van Rhee, P. C. M. Christianen, L. M. Scolaro, and J. C. Maan, "Selection of supramolecular chirality by application of rotational and magnetic forces," *Nature Chemistry* **4**(3), pp. 201–207, 2012.
- [27] K. Banerjee-Ghosh, O. B. Dor, F. Tassinari, E. Capua, S. Yochelis, A. Capua, S.-H. Yang, S. S. Parkin, S. Sarkar, L. Kronik, *et al.*, "Separation of enantiomers by their enantiospecific interaction with achiral magnetic substrates," *Science* **360**(6395), pp. 1331–1334, 2018.
- [28] M. Büttiker, Y. Imry, R. Landauer, and S. Pinhas, "Generalized many-channel conductance formula with application to small rings," *Physical Review B* **31**(10), p. 6207, 1985.
- [29] A. Brataas, Y. V. Nazarov, and G. E. W. Bauer, "Finite-element theory of transport in ferromagnet–normal metal systems," *Physical Review Letters* **84**(11), p. 2481, 2000.
- [30] R. Shekhter, O. Entin-Wohlman, and A. Aharony, "Mechanically controlled spin-selective transport," *Physical Review B* **90**(4), p. 045401, 2014.
- [31] M. Büttiker, "Four-terminal phase-coherent conductance," *Physical Review Letters* **57**(14), p. 1761, 1986.
- [32] J. H. Bardarson, "A proof of the Kramers degeneracy of transmission eigenvalues from antisymmetry of the scattering matrix," *Journal of Physics A: Mathematical and Theoretical* **41**(40), p. 405203, 2008.
- [33] S. Matityahu, Y. Utsumi, A. Aharony, O. Entin-Wohlman, and C. A. Balseiro, "Spin-dependent transport through a chiral molecule in the presence of spin-orbit interaction and nonunitary effects," *Physical Review B* **93**(7), p. 075407, 2016.
- [34] A. A. Kiselev and K. W. Kim, "Prohibition of equilibrium spin currents in multiterminal ballistic devices," *Physical Review B* **71**(15), p. 153315, 2005.
- [35] L. Onsager, "Reciprocal relations in irreversible processes. II.," *Physical Review* **38**(12), p. 2265, 1931.
- [36] R. Jansen, A. Spiesser, H. Saito, Y. Fujita, S. Yamada, K. Hamaya, and S. Yuasa, "Nonlinear electrical spin conversion in a biased ferromagnetic tunnel contact," *Physical Review Applied* **10**(6), p. 064050, 2018.
- [37] N. Koumura, R. W. Zijlstra, R. A. van Delden, N. Harada, and B. L. Feringa, "Light-driven unidirectional molecular rotor," *Nature* **401**(6749), pp. 152–155, 1999.
- [38] E. Díaz, A. Contreras, J. Hernández, and F. Domínguez-Adame, "Effective nonlinear model for electron transport in deformable helical molecules," *Physical Review E* **98**(5), p. 052221, 2018.
- [39] J. Fransson, "Chirality-induced spin selectivity: The role of electron correlations," *The Journal of Physical Chemistry*

- Letters* **10**(22), pp. 7126–7132, 2019.
- [40] M. Brandbyge, J.-L. Mozos, P. Ordejón, J. Taylor, and K. Stokbro, “Density-functional method for nonequilibrium electron transport,” *Physical Review B* **65**(16), p. 165401, 2002.
- [41] Y. Meir and N. S. Wingreen, “Landauer formula for the current through an interacting electron region,” *Physical Review Letters* **68**(16), p. 2512, 1992.
- [42] M. N. Baibich, J. M. Broto, A. Fert, F. N. Van Dau, F. Petroff, P. Etienne, G. Creuzet, A. Friederich, and J. Chazelas, “Giant magnetoresistance of (001) Fe/(001) Cr magnetic superlattices,” *Physical Review Letters* **61**(21), p. 2472, 1988.
- [43] J. S. Moodera, L. R. Kinder, T. M. Wong, and R. Meservey, “Large magnetoresistance at room temperature in ferromagnetic thin film tunnel junctions,” *Physical Review Letters* **74**(16), p. 3273, 1995.
- [44] L. D. Barron, “Reactions of chiral molecules in the presence of a time-non-invariant enantiomorphous influence: a new kinetic principle based on the breakdown of microscopic reversibility,” *Chemical Physics Letters* **135**(1-2), pp. 1–8, 1987.
- [45] R. Landauer, “Conductance determined by transmission: probes and quantised constriction resistance,” *Journal of Physics: Condensed Matter* **1**(43), p. 8099, 1989.

Chapter 5

Circuit-model analysis for spintronic devices with chiral molecules as spin injectors

Recent research discovered that charge transfer processes in chiral molecules can be spin selective and named the effect chiral-induced spin selectivity (CISS). Follow-up work studied hybrid spintronic devices with conventional electronic materials and chiral (bio-) molecules. However, a theoretical foundation for the CISS effect is still in development and the spintronic signals were not evaluated quantitatively. We present a circuit-model approach that can provide quantitative evaluations. Our analysis assumes the scheme of a recent experiment that used photosystem I (PSI) as spin injectors, for which we find that the experimentally observed signals are, under any reasonable assumptions on relevant PSI time scales, too high to be fully due to the CISS effect. We also show that the CISS effect can in principle be detected using the same type of solid-state device, and by replacing silver with graphene, the signals due to spin generation can be enlarged four orders of magnitude. Our approach thus provides a generic framework for analyzing this type of experiments and advancing the understanding of the CISS effect.

This chapter is published as:

X. Yang, T. Bosma, B. J. van Wees & C. H. van der Wal, " Circuit-model analysis for spintronic devices with chiral molecules as spin injectors," *Phys. Rev. B* **99**, 214428 (2019)

DOI: 10.1103/PhysRevB.99.214428

Electronic spin lies at the heart of spintronics due to its capability to convey digital information. In contrast, this quantum mechanical concept has found few applications in chemistry and biology as the energy states associated with opposite spin orientations are often degenerate. Molecular chirality, on the other hand, is thoroughly discussed in chemistry and biology but rarely concerned in spintronics. In the past decade, the two concepts have been increasingly linked together thanks to the discovery of the chiral-induced spin selectivity (CISS) effect, which describes that the electron transfer in chiral molecules is spin dependent [1–11]. This discovery not only provides new approaches to controlling chiral molecules [12] and understanding their interactions [13], but also opens up the possibility of small, flexible, and fully organic spintronic devices. Previously, organic materials were incorporated in spintronic devices as spin transport channels and spin-charge converters, but the conversion efficiency remained low [14–22]. Building on CISS, hybrid devices with efficient molecular spin injectors and detectors were realized [23–32]. However, a full understanding of the signals produced by these devices is still lacking, and thereby the understanding of CISS largely hindered.

We present here a circuit-model approach to quantitatively evaluating the spin signals measured from hybrid solid-state devices designed for studying the CISS effect. Similar approaches have been used for the analyses of spintronic devices with metallic and semiconducting materials [33–35]. They provided accurate descriptions of experimental results and have been extended to a wide range of device geometries. We apply here such modeling to devices with adsorbed molecular active layers instead of metal contacts. While generally applicable, we take the device reported in Ref. 26 as a case study for demonstrating our approach. In comparison to our recent analysis using electron-transmission modeling [36], the circuit-model approach is more suited for including a role for optically driven chiral molecules, and for electron transport outside the linear-response regime.

5.1 Circuit-model analysis

In the work of Ref. 26, cyanobacterial photosystem I (PSI) protein complexes were self-assembled on a silver- AlO_x -nickel junction and the orientation of PSI (*up* or *down*) was controlled by mutations and linker molecules. Figure 5.1 shows a device with PSI in the *up* orientation. Here, P700, the reaction center of PSI, was located adjacent to the silver layer. In P700, charge separation took place upon the illumination of a 660-nm laser during the experiments. It was described that the excited electron got transferred to the Fe_4S_4 clusters at the other end of PSI, and the hole left behind in P700 was refilled by an electron from silver. This process causes a net *upward* electron transfer from silver to PSI, which, before relaxation, results in a steady-state

increase of the silver surface potential, as was observed using a Kelvin probe [26]. In contrast, a device with PSI in the *down* orientation gave a decrease of silver surface potential upon light illumination, indicating a net *downward* electron transfer from PSI into silver. Both devices were then placed under laser illumination in the presence of an out-of-plane magnetic field which was used to set the magnetization of nickel in either the *up* or *down* direction. The charge voltage between silver and the nickel layer was monitored. The absolute value of this voltage was found to be always lower when the electron transfer direction and the magnetic field direction were parallel (both *up* or both *down*), and higher when they were anti-parallel (one *up* and one *down*). This magnetic field dependence suggested that the electron transfer process in PSI was spin selective, and the preferred spin orientation was parallel to the electron momentum. As PSI is one of Nature's two major light-harvesting centers, this intriguing result indicated that electron spins may also play a role in photosynthesis.

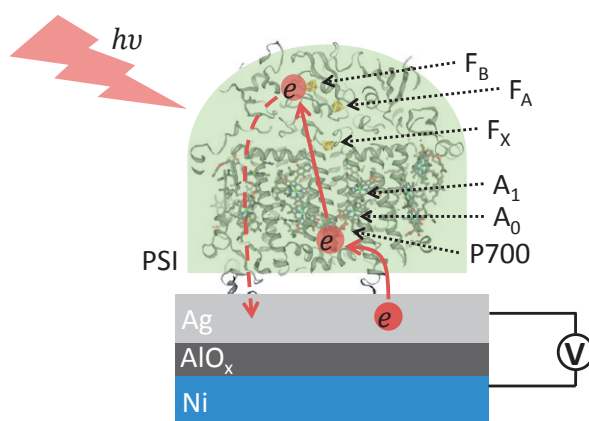


Figure 5.1: Electron transfer chain of PSI and the geometry of the solid-state device used in Ref. 26. The device was a stack of 150 nm of nickel, 0.5 nm of AlO_x, and 50 nm of silver. PSI was immobilized on top of the silver layer, and the voltage difference between the silver and the nickel was measured. PSI is represented by the green area, on which the structure of a part that contains the PSI electron transfer chain is overlaid. The structure highlights key cofactors such as Fe₄S₄ clusters (F_B, F_A and F_X), primary electron acceptors (A₁ and A₀), the reaction center (P700), and the chiral (helical) structural surroundings. Here PSI is in the *up* orientation, with P700 close to silver, and the Fe₄S₄ clusters at the far end. Red labellings mark the light induced electron transfer process, including the photon ($h\nu$) and the electron (e), the photo-excitation pathway (solid arrows) and the unknown relaxation pathway (dashed arrow). The protein structure is taken from the RCSB Protein Data Bank (PDB ID 1JB0 [37]).

However, an important question to address while considering this conclusion

is: How much of the observed magnetic-field-dependent signal was from CISS? To answer this question we need to understand the origin of the measured steady-state magnetic-field-dependent voltage. Upon photo-excitation charge carriers were transferred from silver to PSI. These carriers must relax back to silver via pathways inside PSI because there was no top electrode providing alternative pathways. Both the excitation and relaxation pathways might exhibit spin selectivity. Qualitatively, as long as the CISS effects in the two pathways do not cancel each other, a net spin injection into silver can be generated. This spin injection then competes with the spin relaxation process in silver, and results in a steady-state spin accumulation which can indeed be detected as a charge voltage between silver and the nickel layer [38].

To quantitatively evaluate this voltage signal, we adopt a two-current circuit model where spin transport is described by two parallel channels (spin-up and spin-down channels) [39, 40]. The two channels are connected via a spin-flip resistance R_{sf} , which characterizes the spin relaxation process in a nonmagnetic material. A derivation of R_{sf} and a more detailed introduction of the two-current model concept can be found in Appendix A. For a thin-film nonmagnetic material, we find

$$R_{sf} = 2 \cdot \frac{\lambda_{sf}^2}{d A_{rel} \sigma} \quad (5.1)$$

(assuming $d < \lambda_{sf}$ and $A_{rel} \gg \lambda_{sf}^2$), where λ_{sf} is the spin-relaxation length of the material, σ is the conductivity of the material, d is the thickness of the film, and A_{rel} is the relevant area of the film where spin injection occurs. Notably, R_{sf} is entirely determined by the properties of the material and the geometry of the device.

The role of PSI in the device can be characterized by two features. Firstly, due to the lack of a top electrode, there was (as a steady-state average) no net charge current flowing through PSI. Secondly, facilitated by CISS, PSI gave a net spin injection into silver. These two features resemble a pure spin-current source. Therefore, we model PSI as a pure spin-current source between the fully polarized spin-up (red) and spin-down (blue) channels, as shown in Figure 5.2A). Upon photo-excitation PSI sources an internal spin current I_{PSI} . The pathway with spin-flip resistance R_{sf-PSI} accounts for the spin relaxation inside PSI. At the PSI-silver interface the two channels encounter possibly spin-dependent contact resistances $R_{cPSI\uparrow}$ and $R_{cPSI\downarrow}$. The net spin current injected from PSI into silver is $I_s = \eta \cdot I_{PSI}$, ($-1 \leq \eta \leq 1$), with η being the fraction of the photo-induced spin current that actually contributes to the spin accumulation in silver. Generically, we regard PSI as a black box: a two-terminal unit that drives a spin current I_s , as shown in Figure 5.2B). This will later be linked and compared to known timescales for charge transfer processes inside PSI.

A circuit model for the entire device is shown in Figure 5.3. R_{Ag} is the spin-independent resistance (in the out-of-plane direction) of the silver layer. Inside the silver layer the spins can relax, as represented by a spin-flip pathway with resistance

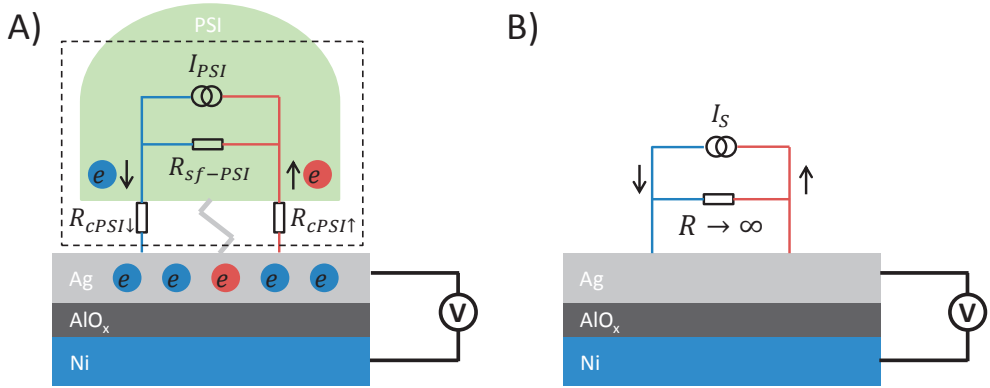


Figure 5.2: PSI modeled as a spin-current source. **A)** PSI compared to a pure spin-current source with a spin relaxation pathway. It creates spin accumulation in the silver layer upon light illumination. Spin-up electrons (red) are transferred from silver to PSI, while spin-down electrons (blue) are transferred back to silver. No charge current flows through PSI but a spin-down accumulation is created in silver. **B)** The model of panel **A)**, reduced to its net spin-injection effect. The contribution from each component in the dashed box in **A)** cannot be clearly distinguished, therefore we treat them together as an ideal spin-current source I_s with a parallel resistance R . Since the total impedance in PSI is much larger than that of silver, we consider $R \rightarrow \infty$. The net effect of this reduced model is to inject a spin current I_s into the silver layer. Here we show the drawing for one PSI unit, but the spin currents (I_{PSI} , I_s) concern the values for the entire PSI ensemble on the device.

R_{sf-Ag} . R_{cAg} is the contact resistance between silver and the voltage meter. In principle these contacts could provide an extra pathway for electron spins to relax, but in reality these contacts are located millimeters away from where spins are injected. This distance is much larger than the spin-relaxation length in silver (about 150 nm at room temperature) [41]. Therefore, the spin relaxation through these contacts is negligible and we can assume $R_{cAg} \rightarrow \infty$.

Underneath the silver layer is the the AlO_x tunnel barrier and the ferromagnetic nickel layer. In these layers electrons experience spin-dependent resistances: the tunnel resistance $R_{tun\uparrow(\downarrow)}$ and the contact resistance $R_{cNi\uparrow(\downarrow)}$ (which includes the out-of-plane resistance of the nickel layer). Note that here the subscript $\uparrow(\downarrow)$ refers to the corresponding spin-current channel, not to be confused with the magnetization direction of nickel which determines the values of $R_{tun\uparrow(\downarrow)}$ and $R_{cNi\uparrow(\downarrow)}$. These resistances can be combined using shorter notations $R_\uparrow = R_{tun\uparrow} + R_{cNi\uparrow}$ and $R_\downarrow = R_{tun\downarrow} + R_{cNi\downarrow}$. An interchange of the R_\uparrow and R_\downarrow values thus accounts for the reversal of the magnetization direction of nickel.

The magnetization direction of nickel can be described as being parallel (p) or

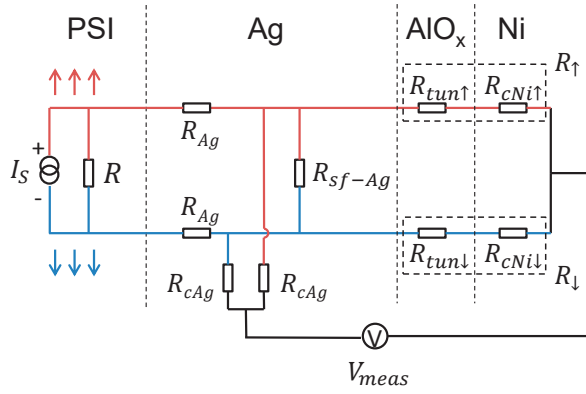


Figure 5.3: Two-current circuit model for the spintronic device of Ref.26 (symbols introduced in the main text). Different parts of the device are separated by dashed lines. Spin-up and spin-down current channels are distinguished by color. PSI is represented by a pure spin-current source as introduced in Figure 5.2B). The spin relaxation in silver is modeled as a pathway with spin-flip resistance R_{sf-Ag} connecting the two spin-current channels.

5

anti-parallel (*ap*) to the spin-up channel. For each case the reading of the voltage meter V_{meas} is

$$V_{meas}^{(p)} = \frac{1}{2} I_s (R_{\uparrow} - R_{\downarrow}) \frac{R_{sf-Ag}}{R_{\uparrow} + R_{\downarrow} + R_{sf-Ag}}, \quad (5.2a)$$

$$V_{meas}^{(ap)} = \frac{1}{2} I_s (R_{\downarrow} - R_{\uparrow}) \frac{R_{sf-Ag}}{R_{\uparrow} + R_{\downarrow} + R_{sf-Ag}}. \quad (5.2b)$$

The change in the measured voltage upon the reversal of the nickel magnetization is therefore

$$\begin{aligned} V_{diff} &= V_{meas}^{(ap)} - V_{meas}^{(p)} \\ &= I_s (R_{\downarrow} - R_{\uparrow}) \frac{R_{sf-Ag}}{R_{\uparrow} + R_{\downarrow} + R_{sf-Ag}} \\ &= I_s R_{eff}, \end{aligned} \quad (5.3)$$

where $R_{eff} = V_{diff}/I_s$ is an effective spinvalve resistance.

For the envisioned spintronic behavior in Ref. 26, this model captures all relevant aspects for spintronic signals in the linear transport regime, without making assumptions that restrict its validity. It is thus suited for describing the observed spin signals in a quantitative manner when the values of the circuit parameters are available. For the device described in Ref.26 we derive (see Appendix B)

$$R_{eff} \approx 15 \text{ m}\Omega. \quad (5.4)$$

Note that R_{eff} is fully determined by the properties of the Ag-AlO_x-Ni multilayer, and deriving its value does not use any estimates or assumptions concerning PSI. Furthermore, by carefully choosing material parameters, the estimate of R_{eff} is of great accuracy. This is also discussed in Appendix B.

The result for R_{eff} directly yields values for the injected spin current that was flowing in the experiment of Ref. 26. For the *up* orientation of PSI, the measured voltage difference V_{diff} was about 50 nV. Thus, the net spin current injected into silver must have been $I_s = V_{diff}/R_{eff} \approx 3 \mu\text{A}$. For the opposite PSI orientation, the measured V_{diff} was about 10 nV, and accordingly, $I_s \approx 0.6 \mu\text{A}$.

5.2 Discussion

Next, we turn these spin-current values into values for the timescale τ that must then hold for the charge excitation-relaxation process for illuminated PSI. Here τ can be understood as the time interval between two consecutive photo-excitation processes from the same PSI unit. By assuming that the intensity of the illumination is strong enough to drive all the PSI units in continuous excitation-relaxation cycles (saturated), we can write $i = -e/\tau$, where e is the elementary charge and i the photo-induced charge current in a PSI unit. The sum of all contributions i (sum over all PSI units) should then be high enough to provide the above I_s values. In order to check this, we will assume the highest number for PSI units that can contribute, and that they all maximally contribute. Therefore, we first assume that over the relevant area of the device the PSI units form a densely packed, fully oriented monolayer, and that all PSI units function identically. Secondly, we assume that photo-induced spin current from each PSI unit is fully injected into the silver layer, *i.e.* $\eta = 1$. Further, we assume that the polarization of the CISS effect in PSI is 50%, on par with the reported CISS polarization in other chiral systems [3, 8, 26]. For these assumptions we find (details in Appendix C) that for the *up* orientation of PSI, τ should not be larger than 100 ps. For the *down* orientation this limit is $\tau \leq 500$ ps. Note that the boundaries here correspond to the most ideal scenario, and in practice the required τ values could be much smaller than these boundaries.

We now compare these requirements for τ with the well-studied timescales of the electron transfer process in PSI. During photosynthesis, the photo-induced charge separation in PSI takes place at the primary donor P700. Electrons are then transferred through a series of acceptors along the electron transfer chain: A_0 , A_1 , and the Fe_4S_4 clusters F_X , F_A and F_B (see Figure 5.4) [37, 42, 43]. The initial electron transfer from P700 to A_1 is ultrafast (~ 30 ps), and further transfer to F_X happens in 20-200 ns. Then, the electron transfer from F_X through F_A to F_B typically takes 500 ns to 1 μs [43].

The requirements for τ values that we found are—regardless the PSI orientation—

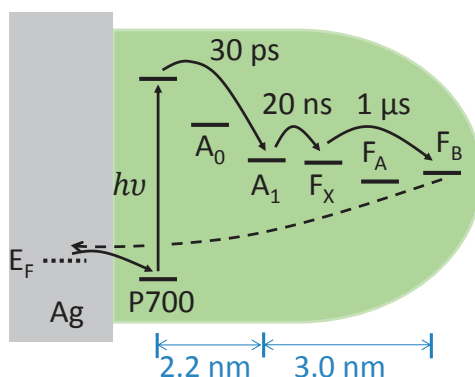


Figure 5.4: Electron transfer process and corresponding time scales in PSI, here depicted in a manner where the vertical placements of states reflect their energy levels. Here the PSI unit is in the *up* orientation. The excitation process is labeled by the black arrows with corresponding time scales marked. However, the relaxation process is unknown (dashed arrow). The blue scale shows the spatial distance between different parts of the electron transfer chain.

5

only compatible with the initial ultrafast electron transfer from P700 to A_1 . The subsequent steps are at least two orders of magnitude too slow. Thus, concluding that the observed signals fully result from the CISS effect requires the existence of an ultrafast relaxation process where electrons immediately return to P700 after their initial transfer from P700 to A_1 . This process does not exist in Nature, because it would stop the trans-membrane electron transfer in photosynthesis. We should, nevertheless, consider whether it can occur in the device, since PSI is there located in a very different environment.

In the solid-state environment, faster relaxation than in Nature could be due to, for instance, the use of linker molecules, the mutations of PSI, or the presence of silver (thanks to its high density of states). The linker molecules are unlikely to be the reason, because their size is significantly smaller than PSI, and the electron transfer chain is positioned deeply in the center of PSI (Figure 5.4). Moreover, it was stated in Ref.26 that the observed signals do not depend on the linker molecules.

The mutations and the metal substrate, on the other hand, could indeed affect the electron transfer. To assess the effects, we can draw direct comparisons between Ref.26 and Ref.44. In both works the same mutations of PSI were performed in order to covalently bind PSI to metal substrates (Ag and Au respectively). Ref. 44 found, for the bound PSI, the fastest excitation-relaxation cycle of around 15 ns. For Ref. 26 the value should be on the same order of magnitude due to the large similarities between the two experiments. However, this value is still two orders of magnitude slower than the most ideal scenario that we have assumed. Therefore, the CISS-

related spin signals in Ref. 26 was at least two orders of magnitude lower than the measured value. In fact, if we consider a realistic situation where PSI units do not form a fully-oriented and densely-packed layer on silver and $|\eta| < 1$, the actual CISS signals should be even smaller.

Although other mechanisms may still be at play [45, 46], they are not able to make up for the orders of magnitude of deviation. We thus conclude that the observed signals in Ref. 26 cannot be fully due to the light-induced spin injection from PSI, unless the very similar PSI conditions in Ref. 26 and Ref. 44 could lead to orders of magnitude of difference in PSI charge transfer time scales. This suggests that the magnetic-field dependence of the signals in Ref. 26 may predominantly originate from other effects. Some possible sources are discussed in Appendix D.

Nevertheless, our analysis shows that an experimental approach as in Ref. 26 is in principle suited for confirming spin signals with CISS origin. It also provides insight in how one can optimize this type of experiments towards a system that would yield CISS spin signals with a higher magnitude. The most direct improvement can be obtained via a system that has higher values for R_{sf} and R_{eff} in Eqs. (5.1)-(5.4). A good example to consider is to use graphene as replacement for the silver layer. This should boost the spin signals by four orders of magnitude, since it would increase the value of R_{eff} from ~ 15 m Ω to a value of ~ 0.5 k Ω (see Appendix B for details).

5.3 Conclusion

In summary, we introduced a two-current circuit-model approach to quantitatively assessing spintronic signals in hybrid devices which combine conventional electronic materials with (bio)organic molecules that are spin-active due to the CISS effect. As an example, we applied it to a case where the active layer has electrical contact only on one side, and we showed how the quantitative analysis can link the observed spin signals to charge excitation and relaxation times in the molecules. Our analysis showed that such devices can readily give spintronic signals that are strong enough for detection with current technologies. However, it also revealed that in the experiment of our case study (Ref. 26), the observed signals must have had strong contributions from other effects. Future experimental work should aim at separating other signals from signals given by CISS, and our circuit-model approach assists in designing these experiments. We also recommend using devices with nonlocal geometries in order to separate charge and spin signals [36, 38]. In these geometries, the spin signals can also be quantitatively assessed using our circuit-model approach.

5.4 Appendices

A. Two-current model and derivation of R_{sf}

In this section we use a simple example to introduce the concept of two-current circuit models [39, 40] and to illustrate what can be experimentally detected. Along the way we derive R_{sf} (Equation 5.1).

For describing spintronic signals, we use modeling where spin transport in conductors is described as two parallel channels each allowing only one type of spin (spin-up and spin-down channels, colored in red and blue respectively in Figure 5.5) [39, 40]. This allows us to separate the total electrical current I into spin-up and spin-down components: $I = I_{\uparrow} + I_{\downarrow}$. The difference between the two components is referred to as a spin current $I_{\uparrow\downarrow}$, with $I_{\uparrow\downarrow} = I_{\uparrow} - I_{\downarrow}$. A spin current injected into a non-magnetic material will result in a spin accumulation (chemical potential difference between the spin-up and spin-down channels) $\mu_{\uparrow\downarrow} = \mu_{\uparrow} - \mu_{\downarrow}$. Within the material spin accumulation decays exponentially over time due to spin relaxation mechanisms [47]. As an introduction to this type of modeling, we first show a simple case with a pure spin current in a nonmagnetic material, as shown in Figure 5.5. A pure spin current means that the net charge current $I = I_{\uparrow} + I_{\downarrow} = 0$. The spin relaxation is modeled as a pathway connecting the two channels, with a spin-flip resistance R_{sf} . The voltage difference between the two channels, as measured with fully spin-selective contacts, is therefore $V_{\uparrow\downarrow} = I_{\uparrow\downarrow} \cdot R_{sf}$.

Within the nonmagnetic material the steady-state spin accumulation is a balance between the spin injection due to $I_{\uparrow\downarrow}$ and the spin relaxation in the material. This is described as

$$0 = \frac{d\mu_{\uparrow\downarrow}}{dt} = -\frac{\mu_{\uparrow\downarrow}}{\tau_{sf}} + 2 \cdot \frac{I_{\uparrow\downarrow}}{e} \cdot \frac{1}{\nu_{3D} \cdot V_{rel}}, \quad (5.5)$$

where τ_{sf} is the spin-relaxation time in the material, ν_{3D} is the three-dimensional (3D) density of states (units of $\text{eV}^{-1} \text{m}^{-3}$), and V_{rel} is the relevant volume for the spin injection-relaxation balance in the material. The factor 2 arises from the fact that when one electron is transferred from the spin-down channel to the spin-up channel, the difference between the spin-up and spin-down population increases by two. The steady state solution for the measured voltage is

$$V_{\uparrow\downarrow} = \frac{\mu_{\uparrow\downarrow}}{e} = I_{\uparrow\downarrow} \cdot \frac{1}{V_{rel}} \cdot \frac{1}{\nu_{3D}} \cdot \frac{2\tau_{sf}}{e^2}. \quad (5.6)$$

For further analysis we also consider the role of the spin relaxation length of the material, $\lambda_{sf} = \sqrt{D \tau_{sf}}$, where D is the diffusion coefficient for electrons in the material. The Einstein relation gives

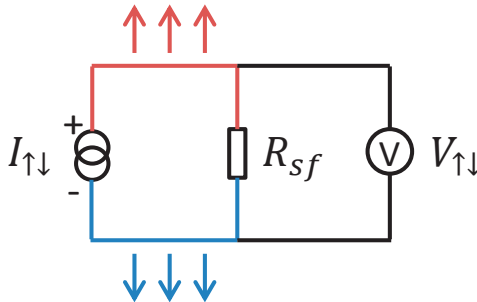


Figure 5.5: A circuit model considering the spin injection in a nonmagnetic conducting material. Spin-up and spin-down components are separated into red and blue channels. A pure spin current $I_{\uparrow\downarrow}$ is sourced between the two channels. Spin relaxation is modeled as a spin-flip resistance R_{sf} . The spin accumulation is measured as the signal $V_{\uparrow\downarrow}$ from a voltage meter that has fully spin-selective contacts.

$\sigma = e^2 \nu_{3D} D$, where σ is the conductivity of the material [38]. Consequently, Equation (5.6) becomes

$$V_{\uparrow\downarrow} = 2 I_{\uparrow\downarrow} \frac{\lambda_{sf}^2}{V_{rel} \sigma}, \quad (5.7)$$

and therefore:

$$R_{sf} = \frac{V_{\uparrow\downarrow}}{I_{\uparrow\downarrow}} = 2 \frac{\lambda_{sf}^2}{V_{rel} \sigma}. \quad (5.8)$$

We can see that the spin-flip resistance is completely determined by the properties of the material and the relevant volume concerned for each specific device.

Now we determine the relevant volume V_{rel} for a particular device geometry: a thin layer of a non-magnetic conducting material. The spin accumulation spreads out in a volume that is limited by either the spin relaxation length λ_{sf} , or the boundaries of the device, whichever is smaller. For the thin layer, we assume that the spin current is homogeneously injected from its top surface over a limited area, which is referred to as the relevant area A_{rel} . Spin accumulation then occurs in the thin layer within the area A_{rel} , as well as directly outside the boundaries of A_{rel} , up to a distance of $\sim \lambda_{sf}$. However, we consider here the situation where $A_{rel} \gg \lambda_{sf}^2$, and we can therefore neglect the spin accumulation outside A_{rel} . In the perpendicular direction we consider the case that the thickness of the layer $d < \lambda_{sf}$, which means that the spin-transport length is limited by the thickness of the layer rather than the spin relaxation length of the material. As a consequence, we have $V_{rel} = d A_{rel}$. Substituting this into Equation (5.8) gives

$$R_{sf} = 2 \frac{\lambda_{sf}^2}{d A_{rel} \sigma}. \quad (5.9)$$

When the thin layer (three-dimensional) is replaced by a truly two-dimensional material, such as graphene, the thickness of the material can no longer be defined. The material then has a two-dimensional density of states ν_{2D} (units of $\text{eV}^{-1} \text{m}^{-2}$), and one should use the Einstein relation for the 2D conductivity $\sigma_{2D} = e^2 \nu_{2D} D$. When assuming again $A_{rel} \gg \lambda_{sf}^2$, the spin-flip resistance for a 2D system is given as

$$R_{sf-2D} = 2 \frac{\lambda_{sf}^2}{A_{rel} \sigma_{2D}}. \quad (5.10)$$

B. Estimate for the value of R_{eff}

In this section we estimate a value for the effective spinvalve resistance R_{eff} . We first focus on a value for the experimental work of Ref. 26, and then on a similar system that has the silver layer replaced by graphene.

The tunneling resistance between silver and nickel was measured to be about 1 k Ω in Ref. 23, which used a device identical to that in Ref. 26. The change of this resistance under magnetization reversal, as characterized by its tunneling magnetoresistance ($\text{TMR} = (R_{\downarrow} - R_{\uparrow})/R_{\uparrow}$), depends on the spin polarization of nickel P_{Ni} , and does not depend on the magnetization axis. [48–50] It follows $\text{TMR} = 2P_{Ni}/(1 - P_{Ni})$, and takes a value of $\text{TMR} \approx 100\%$ for the $P_{Ni} \approx 33\%$ value used in Ref. 26. The actual TMR value may be lower than 100% because of temperature and bias voltage, but should be on the same order of magnitude. [50, 51] Moreover, taking the upper limit of TMR is consistent with us deriving the lower limit of I_s and the upper limit of τ . Therefore, we may assume $R_{\downarrow} = 1 \text{ k}\Omega$ and $R_{\uparrow} = 0.5 \text{ k}\Omega$. While this is an estimate, the value must be of the correct order of magnitude. Furthermore, later analysis will show that it is the spin-flip resistance of silver that governs the magnitude of the effective resistance R_{eff} .

To determine the spin-flip resistance of silver, we use the previously derived Equation (5.9). For the device we discuss, the thickness of the silver layer $d = 50 \text{ nm}$, the area of the junction $A_{rel} = 1 \mu\text{m} \times 1 \mu\text{m}$. For spin relaxation parameters we take reported values for a mesoscopic silver strip at room temperature $\lambda_{sf-Ag} \approx 150 \text{ nm}$, and $\rho_{Ag} = 1/\sigma_{Ag} \approx 50 \text{ n}\Omega \cdot \text{m}$. [41] We point out that these parameters are not only

affected by the material choice, but also by factors such as device geometry, fabrication techniques, and temperature [52]. The values we chose were reported for a device that had geometries very close to that used in Ref.26, was fabricated with the same technique, and was measured at the same temperature. With these, we get the spin-flip resistance in our model $R_{sf-Ag} = 45 \text{ m}\Omega$.

Substituting R_{sf-Ag} , together with the assumed R_{\uparrow} , R_{\downarrow} values in Equation 5.3 gives an effective resistance

$$R_{eff} \approx 15 \text{ m}\Omega. \quad (5.11)$$

Note that R_{eff} is fully determined by the properties of the Ag- AlO_x -Ni multilayer device, and estimating its value did not use any estimates or assumptions concerning PSI.

For the scenario where the silver layer is replaced by a graphene layer, we apply a similar analysis, while using Equation (5.10) instead of Equation (5.9). For graphene, typical material parameters are a square resistance of the order of 1 k Ω [53, 54], and a spin relaxation length of $\lambda_{sf} \approx 10 \text{ }\mu\text{m}$ [54, 55]. This gives $R_{sf-2D} \approx 1 \text{ M}\Omega$, and $R_{eff} \approx 0.5 \text{ k}\Omega$ for a device that is for other aspects identical to the device of Ref.26.

C. Analysis of compatible PSI excitation and relaxation times

In the main text we derived the I_s values without using any information about PSI. Here we analyze what the values mean in terms of photo-excitation and relaxation times of individual PSI units. We first assume that I_s is fully induced by the spin-selective electron transfer during photo-excitation and relaxation cycles in PSI. Then we examine the validity of this assumption by deriving (from I_s) the values of photo-excitation and relaxation times of individual PSI units. In the following discussion a few more assumptions are made. We carefully assume scenarios which consistently lead to the upper boundary of the photo-excitation-relaxation times. In the main text we showed that even this upper boundary is still too low to be realistic.

We write I_s as a sum of the contributions from individual PSI units,

$$I_s = \sum_{n=1}^N i_{s,n} \quad (5.12)$$

where i_s is the spin current injected from each PSI unit into silver, the index n runs over all individual PSI units, and N is the number of PSI units within the relevant area (area of the junction) A_{rel} . We assume that all PSI units are oriented in the same direction, so that each of them contribute equally to the total current I_s . Therefore, we have $i_{s,n} \equiv i_s$, hence

$$I_s = i_s \cdot N = i_s \cdot \rho \cdot A_{rel} \quad (5.13)$$

where ρ is the number density, or coverage, of PSI. To estimate the coverage we need to take into consideration the size of PSI units. Isolated cyanobacterial PSI systems usually appear in trimers with typical diameters of around 30 nm. This means three PSI units reside in an area of about 700 nm², or for convenience, approximately a coverage of $\rho = 0.004 \text{ nm}^{-2}$. Note that this is the highest possible coverage for a monolayer of PSI, since it corresponds to the entire silver surface being covered with a uniform, densely-packed PSI layer. We assume this maximum coverage for the entire junction area. We further assume that the total injected spin current I_s is equally contributed by all the PSI units. This gives us an estimate of the lower boundary of i_s , the spin-current injection per PSI unit. For the *up* orientation of PSI, we have $i_s \geq 750 \text{ pA}$. For the *down* orientation this lower limit is 150 pA.

Next, we analyze the magnitude of the charge current needed to produce this spin current via CISS effect. In our model, each PSI unit injects a spin current i_s into silver, which is a fraction of the total spin current i_{PSI} inside PSI. We have $i_s = \eta \cdot i_{PSI}$, with $-1 \leq \eta \leq 1$ being the fraction parameter. The value of η depends on the spin-relaxation process inside PSI. In order to obtain a lower estimate of i_{PSI} , we assume $\eta = 1$ (all the photo-induced spin current in PSI can be injected to the silver layer), hence

$i_{PSI} = i_s$. This spin current, i_{PSI} , is again a fraction of the charge current i induced by the continuous electron transfer during photo-excitation and relaxation cycles in a PSI unit. The conversion from a charge current into a spin current is due to the CISS effect and its efficiency is characterized by its polarization $P_{PSI} = i_{PSI}/i$. The CISS polarization of other chiral systems is reported to be about 50% [3, 8, 26], so here we adopt the same value. Taking the above into account, we can derive the lower boundary of the charge current driven by photo-excitation and relaxation processes in a PSI unit: $i \geq 1.5$ nA for the *up* orientation, and 300 pA for the *down* orientation.

Finally, we translate this current into a value for the excitation-relaxation time τ . Here, τ can be understood as the turn-over time, or the time interval between two consecutive photo-excitation processes from the same PSI unit. By assuming the intensity of the illumination is strong enough to drive all the PSI units in continuous excitation-relaxation cycles (saturated), we can write $i = -e/\tau$. A lower boundary of i corresponds to an upper boundary of τ . For the *up* orientation of PSI, $i \geq 1.5$ nA corresponds to $\tau \leq 100$ ps. For the *down* orientation the limit is $\tau \leq 500$ ps.

D. Possible origins of magnetic-field dependent signals in hybrid CISS devices

There are other effects that can give rise to the magnetic-field-dependent signals in devices as used in Ref. 26. One of these effects is the photo-response of silver. Any modification of the silver surface can change its work function. A work function as low as 1.8 eV was reported for modified silver surfaces [56, 57]. It is therefore possible that the adsorbed PSI units and binder molecules modified the silver surface in a way that photoemission was allowed at the photon energies used in the experiment. This photoemission can be spin polarized due to the spin-orbit effect in silver and possible spin-dependent scattering at the surface [58].

Alternatively, the signals could also arise from a pure charge effect. Even without photoemission, the change of silver work function can lead to a voltage signal in the Ni-AlO_x-Ag capacitor. This voltage signal may depend on illumination and magnetic field, because the adsorbed PSI (which modifies the silver surface and thus the voltage signal) is highly photo-sensitive and contains large iron clusters that may respond to magnetic field. In such a scenario (where spin transport does not play a role), the orientation of PSI can only affect the magnitude but not the sign of the magnetic-field dependence. In fact, this is indeed the case if one considers the full signals reported in Figure 2A(ii) and Figure 2B(ii) of Ref. 26 instead of only their absolute values. In both figures, the measured signals can be separated into two parts: a nonzero background and a magnetic-field-dependent component that shows a step upon magnetic-field reversal. Figure 2B(ii) differs from Figure 2A(ii) by having an opposite sign for the background and a smaller step size upon magnetic-field reversal. The directions of the steps (i.e. the signs of the magnetic-field dependence) in both figures are the same: Both signals shift tens of nanovolts to less positive (more negative) values when reversing the magnetic field from *down* to *up* direction. The opposite signs for the background can be explained by the opposite orientations of PSI (just as how the PSI orientation affected the silver surface potential measured with a Kelvin probe), whereas the change of step size may be given by the change of position of the iron clusters with respect to the silver surface.

Bibliography

- [1] K. Ray, S. P. Ananthavel, D. H. Waldeck, and R. Naaman, "Asymmetric scattering of polarized electrons by organized organic films of chiral molecules," *Science* **283**(5403), pp. 814–816, 1999.
- [2] S. Yeganeh, M. A. Ratner, E. Medina, and V. Mujica, "Chiral electron transport: scattering through helical potentials," *The Journal of Chemical Physics* **131**(1), p. 014707, 2009.

- [3] B. Göhler, V. Hamelbeck, T. Z. Markus, M. Kettner, G. F. Hanne, Z. Vager, R. Naaman, and H. Zacharias, "Spin selectivity in electron transmission through self-assembled monolayers of double-stranded DNA," *Science* **331**(6019), pp. 894–897, 2011.
- [4] Z. Xie, T. Z. Markus, S. R. Cohen, Z. Vager, R. Gutierrez, and R. Naaman, "Spin specific electron conduction through DNA oligomers," *Nano Letters* **11**(11), pp. 4652–4655, 2011.
- [5] A.-M. Guo and Q.-F. Sun, "Spin-selective transport of electrons in DNA double helix," *Physical Review Letters* **108**(21), p. 218102, 2012.
- [6] R. Gutierrez, E. Díaz, R. Naaman, and G. Cuniberti, "Spin-selective transport through helical molecular systems," *Physical Review B* **85**(8), p. 081404, 2012.
- [7] E. Medina, L. A. González-Arraga, D. Finkelstein-Shapiro, B. Berche, and V. Mujica, "Continuum model for chiral induced spin selectivity in helical molecules," *The Journal of Chemical Physics* **142**(19), p. 194308, 2015.
- [8] K. Michaeli, N. Kantor-Uriel, R. Naaman, and D. H. Waldeck, "The electron's spin and molecular chirality—how are they related and how do they affect life processes?," *Chemical Society Reviews* **45**(23), pp. 6478–6487, 2016.
- [9] S. Matityahu, Y. Utsumi, A. Aharoni, O. Entin-Wohlman, and C. A. Balseiro, "Spin-dependent transport through a chiral molecule in the presence of spin-orbit interaction and nonunitary effects," *Physical Review B* **93**(7), p. 075407, 2016.
- [10] R. Naaman and D. H. Waldeck, "Chiral-induced spin selectivity effect," *The Journal of Physical Chemistry Letters* **3**(16), pp. 2178–2187, 2012.
- [11] R. Naaman and D. H. Waldeck, "Spintronics and chirality: Spin selectivity in electron transport through chiral molecules," *Annual Review of Physical Chemistry* **66**, pp. 263–281, 2015.
- [12] K. Banerjee-Ghosh, O. B. Dor, F. Tassinari, E. Capua, S. Yochelis, A. Capua, S.-H. Yang, S. S. Parkin, S. Sarkar, L. Kronik, *et al.*, "Separation of enantiomers by their enantiospecific interaction with achiral magnetic substrates," *Science* **360**(6395), pp. 1331–1334, 2018.
- [13] R. Naaman, Y. Paltiel, and D. H. Waldeck, "Chirality and spin: A different perspective on enantioselective interactions," *CHIMIA International Journal for Chemistry* **72**(6), pp. 394–398, 2018.
- [14] W. J. M. Naber, S. Faez, and W. G. van der Wiel, "Organic spintronics," *Journal of Physics D: Applied Physics* **40**(12), p. R205, 2007.
- [15] V. A. Dediu, L. E. Hueso, I. Bergenti, and C. Taliani, "Spin routes in organic semiconductors," *Nature Materials* **8**(9), p. 707, 2009.
- [16] D. Sun, E. Ehrenfreund, and Z. V. Vardeny, "The first decade of organic spintronics research," *Chemical Communications* **50**(15), pp. 1781–1793, 2014.
- [17] V. Dediu, M. Murgia, F. Maticotta, C. Taliani, and S. Barbanera, "Room temperature spin polarized injection in organic semiconductor," *Solid State Communications* **122**(3–4), pp. 181–184, 2002.
- [18] Z. Xiong, D. Wu, Z. V. Vardeny, and J. Shi, "Giant magnetoresistance in organic spin-valves," *Nature* **427**(6977), p. 821, 2004.
- [19] L. Fang, K. D. Bozdag, C.-Y. Chen, P. Truitt, A. Epstein, and E. Johnston-Halperin, "Electrical spin injection from an organic-based ferrimagnet in a hybrid organic-inorganic heterostructure," *Physical Review Letters* **106**(15), p. 156602, 2011.
- [20] K. Ando, S. Watanabe, S. Mooser, E. Saitoh, and H. Sirringhaus, "Solution-processed organic spin-charge converter," *Nature Materials* **12**(7), p. 622, 2013.
- [21] D. Sun, K. J. van Schooten, M. Kavand, H. Malissa, C. Zhang, M. Groesbeck, C. Boehme, and Z. V. Vardeny, "Inverse spin Hall effect from pulsed spin current in organic semiconductors with tunable spin-orbit coupling," *Nature Materials* **15**(8), p. 863, 2016.
- [22] H. Liu, C. Zhang, H. Malissa, M. Groesbeck, M. Kavand, R. McLaughlin, S. Jamali, J. Hao, D. Sun, R. A. Davidson, *et al.*, "Organic-based magnon spintronics," *Nature Materials* **17**(4), pp. 308–312, 2018.
- [23] K. S. Kumar, N. Kantor-Uriel, S. P. Mathew, R. Guliamov, and R. Naaman, "A device for measuring spin selectivity in electron transfer," *Physical Chemistry Chemical Physics* **15**(42), pp. 18357–18362, 2013.
- [24] O. B. Dor, S. Yochelis, S. P. Mathew, R. Naaman, and Y. Paltiel, "A chiral-based magnetic memory device without a permanent magnet," *Nature Communications* **4**, p. 2256, 2013.
- [25] S. P. Mathew, P. C. Mondal, H. Moshe, Y. Mastai, and R. Naaman, "Non-magnetic organic/inorganic spin injector at room temperature," *Applied Physics Letters* **105**(24), p. 242408, 2014.
- [26] I. Carmeli, K. S. Kumar, O. Heifler, C. Carmeli, and R. Naaman, "Spin selectivity in electron transfer in photosystem I," *Angewandte Chemie International Edition* **53**(34), pp. 8953–8958, 2014.
- [27] N. Peer, I. Dujovne, S. Yochelis, and Y. Paltiel, "Nanoscale charge separation using chiral molecules," *ACS Photonics* **2**(10), pp. 1476–1481, 2015.
- [28] P. C. Mondal, N. Kantor-Uriel, S. P. Mathew, F. Tassinari, C. Fontanesi, and R. Naaman, "Chiral conductive polymers

- as spin filters," *Advanced Materials* **27**(11), pp. 1924–1927, 2015.
- [29] M. Eckshtain-Levi, E. Capua, S. Refaely-Abramson, S. Sarkar, Y. Gavrilov, S. P. Mathew, Y. Paltiel, Y. Levy, L. Kronik, and R. Naaman, "Cold denaturation induces inversion of dipole and spin transfer in chiral peptide monolayers," *Nature Communications* **7**, p. 10744, 2016.
- [30] G. Koplovitz, D. Primc, O. Ben Dor, S. Yochelis, D. Rotem, D. Porath, and Y. Paltiel, "Magnetic nanoplatelet-based spin memory device operating at ambient temperatures," *Advanced Materials* **29**(17), p. 1606748, 2017.
- [31] K. Michaeli, V. Varade, R. Naaman, and D. H. Waldeck, "A new approach towards spintronics–spintronics with no magnets," *Journal of Physics: Condensed Matter* **29**(10), p. 103002, 2017.
- [32] V. Varade, T. Markus, K. Vankayala, N. Friedman, M. Sheves, D. H. Waldeck, and R. Naaman, "Bacteriorhodopsin based non-magnetic spin filters for biomolecular spintronics," *Physical Chemistry Chemical Physics* **20**(2), pp. 1091–1097, 2018.
- [33] J. Banhart, H. Ebert, and A. Vernes, "Applicability of the two-current model for systems with strongly spin-dependent disorder," *Physical Review B* **56**(16), p. 10165, 1997.
- [34] A. Brataas, Y. V. Nazarov, J. Inoue, and G. E. W. Bauer, "Spin accumulation in small ferromagnetic double-barrier junctions," *Physical Review B* **59**(1), p. 93, 1999.
- [35] F. J. Jedema, M. S. Nijboer, A. T. Filip, and B. J. van Wees, "Spin injection and spin accumulation in all-metal mesoscopic spin valves," *Physical Review B* **67**(8), p. 085319, 2003.
- [36] X. Yang, C. H. van der Wal, and B. J. van Wees, "Spin-dependent electron transmission model for chiral molecules in mesoscopic devices," *Physical Review B* **99**(2), p. 024418, 2019.
- [37] P. Jordan, P. Fromme, H. T. Witt, O. Klukas, W. Saenger, and N. Krauß, "Three-dimensional structure of cyanobacterial photosystem I at 2.5 Å resolution," *Nature* **411**(6840), pp. 909–917, 2001.
- [38] F. J. Jedema, H. B. Heersche, A. T. Filip, J. J. A. Baselmans, and B. J. van Wees, "Electrical detection of spin precession in a metallic mesoscopic spin valve," *Nature* **416**(6882), pp. 713–716, 2002.
- [39] N. F. Mott and H. Jones, *The Theory of the Properties of Metals and Alloys*, ch. VII, pp. 270–271. Dover Publications Inc., New York, 1958.
- [40] A. Fert and I. A. Campbell, "Two-current conduction in nickel," *Physical Review Letters* **21**(16), p. 1190, 1968.
- [41] R. Godfrey and M. Johnson, "Spin injection in mesoscopic silver wires: Experimental test of resistance mismatch," *Physical Review Letters* **96**(13), p. 136601, 2006.
- [42] K. Brettel, "Electron transfer and arrangement of the redox cofactors in photosystem I," *Biochimica et Biophysica Acta (BBA)-Bioenergetics* **1318**(3), pp. 322–373, 1997.
- [43] K. Brettel and W. Leibl, "Electron transfer in photosystem I," *Biochimica et Biophysica Acta (BBA)-Bioenergetics* **1507**(1), pp. 100–114, 2001.
- [44] D. Gerster, J. Reichert, H. Bi, J. V. Barth, S. M. Kaniber, A. W. Holleitner, I. Visoly-Fisher, S. Sergani, and I. Carmeli, "Photocurrent of a single photosynthetic protein," *Nature Nanotechnology* **7**(10), pp. 673–676, 2012.
- [45] H. Nakayama, T. Yamamoto, H. An, K. Tsuda, Y. Einaga, and K. Ando, "Molecular engineering of Rashba spin-charge converter," *Science Advances* **4**(3), p. eaar3899, 2018.
- [46] M. Cinchetti, V. A. Dediu, and L. E. Hueso, "Activating the molecular spinterface," *Nature Materials* **16**(5), p. 507, 2017.
- [47] I. Žutić, J. Fabian, and S. D. Sarma, "Spintronics: Fundamentals and applications," *Reviews of Modern Physics* **76**(2), p. 323, 2004.
- [48] K. Takahashi, "Fundamentals of magnetoresistance effects," in *Spintronics for Next Generation Innovative Devices*, John Wiley & Sons, Ltd, 2015.
- [49] P. M. Tedrow and R. Meservey, "Spin-dependent tunneling into ferromagnetic nickel," *Physical Review Letters* **26**(4), p. 192, 1971.
- [50] J. S. Moodera, L. R. Kinder, T. M. Wong, and R. Meservey, "Large magnetoresistance at room temperature in ferromagnetic thin film tunnel junctions," *Physical Review Letters* **74**(16), p. 3273, 1995.
- [51] Y. Lu, X. W. Li, G. Xiao, R. A. Altman, W. J. Gallagher, A. Marley, K. Roche, and S. Parkin, "Bias voltage and temperature dependence of magnetotunneling effect," *Journal of Applied Physics* **83**(11), pp. 6515–6517, 1998.
- [52] J. Bass and W. P. Pratt Jr, "Spin-diffusion lengths in metals and alloys, and spin-flipping at metal/metal interfaces: an experimentalist's critical review," *Journal of Physics: Condensed Matter* **19**(18), p. 183201, 2007.
- [53] M. H. D. Guimarães, P. J. Zomer, J. Ingla-Aynés, J. C. Brant, N. Tombros, and B. J. van Wees, "Controlling spin relaxation in hexagonal BN-encapsulated graphene with a transverse electric field," *Physical Review Letters* **113**(8), p. 086602, 2014.
- [54] J. Ingla-Aynés, M. H. D. Guimarães, R. J. Meijerink, P. J. Zomer, and B. J. van Wees, "24- μm spin relaxation length in boron nitride encapsulated bilayer graphene," *Physical Review B* **92**(20), p. 201410, 2015.
- [55] N. Tombros, C. Jozsa, M. Popinciuc, H. T. Jonkman, and B. J. van Wees, "Electronic spin transport and spin preces-

- sion in single graphene layers at room temperature," *Nature* **448**(7153), p. 571, 2007.
- [56] C. N. Berglund and W. E. Spicer, "Photoemission studies of copper and silver: theory," *Physical Review* **136**(4A), p. A1030, 1964.
- [57] C. N. Berglund and W. E. Spicer, "Photoemission studies of copper and silver: experiment," *Physical Review* **136**(4A), p. A1044, 1964.
- [58] W. Kuch and C. M. Schneider, "Magnetic dichroism in valence band photoemission," *Reports on Progress in Physics* **64**(2), p. 147, 2001.

Chapter 6

Highly anisotropic and nonreciprocal charge transport in chiral van der Waals Tellurium

*S*olid-state electronics is keen to seek materials with low symmetry and low dimensionality for potential novel charge and spin transport properties. This consideration highlights a recently developed quasi-two-dimensional chiral van der Waals semiconducting material, Tellurene. Here we report for this material a giant mesoscopic conductance anisotropy that reaches 10^4 at cryogenic temperatures. Interestingly, the principal axis of the observed conductance anisotropy does not align with the principal symmetry axis of the crystal. Moreover, the chiral (inversion-asymmetric) crystal exhibits nonreciprocal (rectified) charge transport both for longitudinal and transverse conduction. Our results suggests broad application areas for the material, for example in piezoelectricity and non-linear electronics.

This chapter is being prepared as:

*X. Yang, T. S. Ghiasi, J. Momand, P. D. Ye, B. J. Kooi, C. H. van der Wal & B. J. van Wees
"Highly anisotropic and nonreciprocal charge transport in chiral van der Waals Tellurium"*

Layered van der Waals (vdW) materials have been incorporated in nano-electronic and spintronic devices for their functional properties such as magnetism, spin-orbit interaction, and optical response [1–3]. These properties often arise from their lowered dimensionality and low crystal symmetry, and can be imprinted into adjacent layers using heterostructure stacking [4]. Further lowering the dimensionality or crystal symmetry can enable additional novel properties and open up new application areas. For example, strong in-plane anisotropy can give rise to piezoelectricity for energy conversion [5], inversion asymmetry enables nonreciprocal (rectified) electronic responses, and chirality brings forward chemical and bio-organic applications [6] as well as chirality-induced spin selectivity (CISS) for spintronic technologies [7, 8].

These considerations inspire to explore the electronic properties of trigonal Tellurium (Te), which has a unique crystal structure consisting of a vdW stack of one-dimensional (1D) helical chains of Te atoms [9]. The semiconducting material was recently made into quasi-two-dimensional (2D) Tellurene flakes [10], and have been explored for its charge and spin transport properties [11–14].

The 1D nature of Tellurene suggests strong in-plane anisotropy for charge conduction, and the helical chain breaks inversion symmetry and introduces chirality. However, current experiments only found negligible in-plane anisotropy [10], and the nonlinear transport behaviors and chirality-related properties remain largely unexplored. Here, by reducing the size of the Tellurene electronic device, we uncover the expected giant in-plane charge transport anisotropy. Additionally, we investigate the nonreciprocal transport behaviors of the chiral crystal in terms of second-harmonic nonlinear response.

6.1 Highly anisotropic charge transport in Tellurene

6.1.1 Angle-resolved mesoscopic conductance

We use Tellurene single crystals that were grown in solution following procedures reported in Ref. 10. The helically winding chains (along c -axis) form a hexagonal stack (in the a - b plane) via vdW interaction, as illustrated in Fig. 6.1a-b. Within each chain, Te atoms form valence bonds with two nearest neighbors, and three Te atoms complete a helical turn [9]. Chains with the same handedness form enantiomeric single crystal flakes, but the as-grown solution is a racemic mixture of flakes with opposite chiralities.

Typically, the Tellurene single crystal flakes show elongated shape with parallel long edges, which are expected to be aligned with the trigonal principal axis (c -

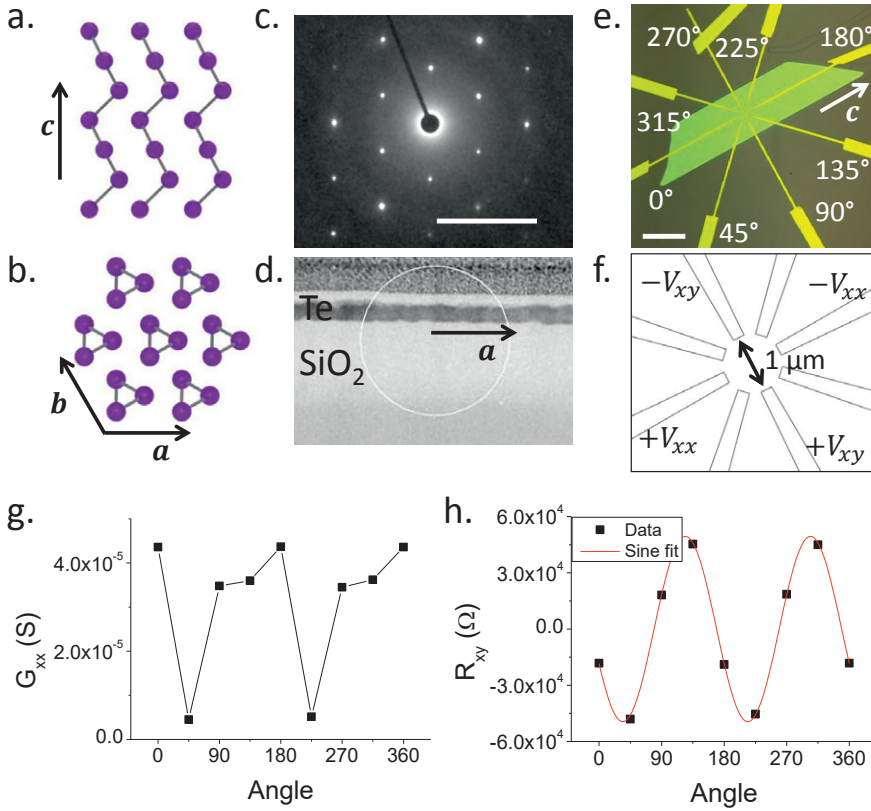


Figure 6.1: **a-b.** Crystal structure of trigonal chiral Tellurium (bulk space group $P3_121$ and $P3_221$ for opposite enantiomeric forms). It consists of helical chains curving around the c -axis (panel **a**). The chains are attached to each other via vdW binding and form a hexagonal stack in the a - b -plane (panel **b**). **c.** Selected-area electron diffraction (SAED) pattern and **d.** TEM image of a cross-sectioned Tellurene flake. The cut is taken perpendicular to the long parallel edges of a trapezoidal flake. The scale bar in panel **c** is 5 nm^{-1} , and the white circle with diameter of 125 nm in panel **d** indicate the region where SAED is taken. **e.** A typical trapezoidal flake, on which the device for conductance anisotropy measurements is made. Circularly patterned Ti-Au contacts are labeled by their angular direction with respect to the c -axis. The scale bar is $20 \mu\text{m}$. **f.** Conductance anisotropy measurement geometry. Four electrodes are used in each measurement, two for applying low-frequency ac voltage bias V_{xx} and measuring the longitudinal current I_{xx} , and the other two for measuring the transverse voltage response V_{xy} . **g-h.** Angular dependence of longitudinal conductance G_{xx} and transverse resistance R_{xy} at a temperature of 300 K. The red line in panel **h** is a sinusoidal fit.

axis) [10, 11]. This was confirmed by the selected-area electron diffraction (SEAD)

pattern obtained through a flake cross section (Fig. 6.1c), and the simultaneously obtained TEM image (Fig. 6.1d) reveals that the flake lies in the a - c plane, which we define as the in-plane orientation. All anisotropic behaviors herein are investigated within this plane.

We first studied the anisotropic electrical conduction in trapezoidal shaped Tellurene flakes, where eight circularly arranged Ti-Au electrical contacts were distributed according to crystallographic directions (see Fig. 6.1e and Methods). We applied voltage bias using the pair of opposing contacts ($\pm V_{xx}$) along a specific direction with respect to the crystal c -axis, and measured the subsequent longitudinal current (I_{xx}) and transverse voltage (V_{xy}) responses. The measurement geometry is illustrated (for the 0° direction) in Fig. 6.1f. For other angular directions, all four electrodes were rotated counterclockwise simultaneously. To ensure linear response, we used low-amplitude (5 mV), low-frequency (below 33 Hz) ac voltage bias, and registered the linear responses using lock-in amplifiers (see Methods). The obtained angular dependence of longitudinal conductance G_{xx} and transverse resistance R_{xy} at 300 K are plotted in Fig. 6.1g-h.

We highlight here three unusual observations. First, the direction measuring lowest conductance (along 45° and 225°) is not orthogonal to that measuring the highest (along 0° and 180°). This angular dependence significantly departs from a sinusoidal curve with 180° period, which is the requirement of the (2D) tensor-form of Ohm's law (see Appendix A). Second, the longitudinal conductance measured along 45° (225°) direction significantly differs from that measured along 135° (315°) direction, despite that the two directions appear equivalent considering the trapezoidal flake geometry. Third, although the transverse resistance does follow a sinusoidal dependence, it is nonzero even when the ac bias is applied along (or perpendicular to) the crystal c -axis.

These qualitative behaviors were also largely reproduced in another sample (see Appendix B), except that the lowest G_{xx} was measured along the 135° (315°) rather than the 45° (225°) direction.

To investigate the possible origin of these anomalies, we first examined the contact resistance and were able to exclude its dominant contribution to the observations (Appendix B). We could also exclude the role of the trapezoidal flake geometry because of the different behaviors along the 45° (225°) and the 135° (315°) directions. Moreover, we could rule out errors due to device fabrication by fitting the G_{xx} angular dependences with sinusoidal curves with 180° period. This yielded best fits with angular shifts larger than ± 10 degrees away from the c -axis (opposite signs for the two samples, and the absolute value varies depends on temperature). This is significantly larger than any (rotational) misalignment that could be identified from optical microscopic images (see e.g. Fig. 6.1e).

6.1.2 Inhomogeneity and chirality effects in 2D conduction

We attribute the observed behaviors to inhomogeneities within the micrometer-sized device and the chirality of the material.

Generally, the anisotropic charge transport in a 2D crystal is described by the (2D) tensor-form of Ohm's law for linear response

$$\mathbf{j} = \begin{pmatrix} \sigma_{xx} & \sigma_{xy} \\ \sigma_{yx} & \sigma_{yy} \end{pmatrix} \mathbf{E}, \quad (6.1)$$

where \mathbf{j} and \mathbf{E} are current density and electric field vectors defined in the x - y plane. In the absence of a magnetic field or magnetization, the conductivity tensor $(\sigma)_{ij}$ is always symmetric and can be diagonalized along a particular direction. For an achi-ral crystal, this direction is always parallel or perpendicular to the crystal principal axis; while for a chiral crystal, this direction can be rotated from the crystal principal axis by an angle, whose sign depends on the chirality. This rotation manifests as a finite transverse conduction when the driving bias is applied along the crystal principal axis. The sign of this transverse signal depends on the (sign of) chirality.

For the angle-resolved measurement geometry we used, the conductivity tensor description always predicts a 180° -periodic sinusoidal angular dependence for longitudinal and transverse responses, because \mathbf{j} and \mathbf{E} can always be decomposed into x - and y -components (see Appendix A).

Therefore, our repeatedly observed deviations from a sine curve suggest the presence of inhomogeneity within the Tellurene devices. This makes it improper to describe the charge transport in the device using the material-averaged property of conductivity. Instead, we must take into account the inhomogeneities and the subsequent irregular current paths within the mesoscopic device, and describe the charge transport using the directly measured conductances. It is important to realize that such significant inhomogeneity contributions were observed in micrometer-scale devices.

We attribute the inhomogeneities to mechanisms for conduction between the 1D helical Te chains (inter-chain conduction). Unlike the intra-chain (1D) transport through covalently bound Te atoms, the inter-chain conduction must overcome the vdW gap, and is expected to be orders of magnitude weaker [15]. However, the conductance we observed at 300 K was at the same order of magnitude along all angular directions. This suggests that the inter-chain conduction may be facilitated by extrinsic mechanisms, which may not be distributed following the crystal lattice. The inhomogeneous distribution of these conduction mechanisms causes irregular current paths, and can give rise to mesoscopic conductances with an angular dependence that deviates from a sinusoidal shape. This deviation was previously also observed in other materials using similar device geometries [16–18]. Note that the

180° periodicity is always guaranteed by the nature of linear response. In our devices, the presence of irregular current paths is further evidenced by the occasionally observed negative conductance values when using a four-terminal measurement geometry (Appendix C).

In addition to the inhomogeneity, the chirality of Tellurene eliminates the apparent mirror symmetry within the trapezoidal flake geometry, and thereby distinguishes the 45° (225°) direction from the 135° (315°) one, and also allows transverse conduction when bias is applied along the high symmetry axes. This is of the same symmetry origin as the aforementioned rotated conductivity tensor for chiral crystals, although here the conduction is not (perfectly) described by a tensor.

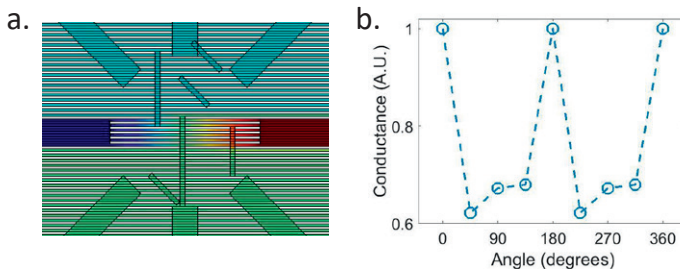


Figure 6.2: A conductor network model for the non-sinusoidal conductance anisotropy measured in inhomogeneous materials. **a.** The conductor network is formed by 1D (horizontal) chains and a few (partially tilted) channels for inter-chain conduction. The horizontal chains and the inter-chain channels are assumed to have different conductivity values. The network is contacted by eight circularly distributed electrodes. The color scheme describe the potential landscape when a bias is applied using the pair of horizontal electrodes (0° direction). **b.** The calculated angle-resolved 2T conductance probed using opposing pair of electrodes along different directions. The angles are defined in the same way as in Fig. 6.1e.

In order to illustrate this, we construct a conductor network model formed by horizontally aligned parallel 1D conductors, as shown in Fig. 6.2a. They are interconnected by arbitrarily distributed but (partially) orderly tilted channels with a different conductivity value, which mimic the inhomogeneous (extrinsic) inter-chain conduction mechanisms (see Methods). The tilting of the inter-chain channels introduces chirality. With this model, we simulate the angular dependence of G_{xx} , and can indeed qualitatively reproduce the anomalies discussed earlier (see Fig. 6.2b).

Note that in principle inhomogeneity alone can readily explain all the anomalies we observed, but the qualitative repetition in two samples suggests a potential role of their (opposite) chirality. The chirality distinguishes left from right, and this can in fact be identified from the crystal structure (projected on the a - c plane) shown in Fig. 6.1a. This symmetry aspect may therefore also be reflected in the distribution of

inter-chain conduction mechanisms. We emphasize that further evidence of this is still needed, for example, by verifying whether the two samples indeed had opposite chiralities.

6.1.3 Anisotropic temperature dependence

Next, we repeated the angle-resolved conductance measurement at different temperatures, and the results are shown in Fig. 6.3a-b.

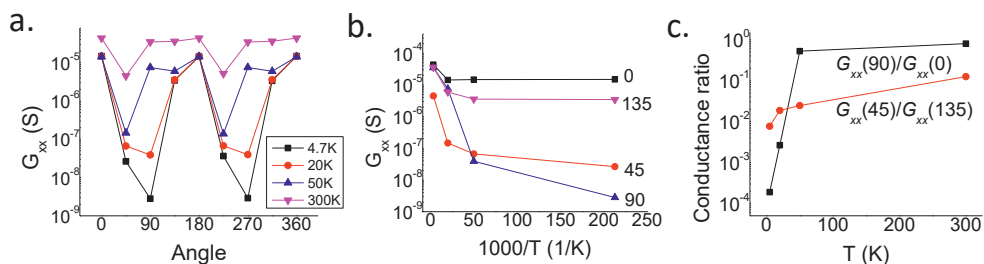


Figure 6.3: Anisotropic temperature dependence of longitudinal conductance. **a.** Angle-resolved longitudinal conductance measured at four different temperatures, plotted in log scale. The topmost curve (300 K) is the same as shown in Fig. 6.1g. **b.** Anisotropic temperature dependence of the longitudinal conductance, plotted for the four distinct angular directions in log scale. **c.** Temperature dependence of conductance ratios of two pairs of orthogonal directions, $G_{xx}(90^\circ)/G_{xx}(0^\circ)$ and $G_{xx}(45^\circ)/G_{xx}(135^\circ)$, plotted in log scale.

As shown in Fig. 6.3b, in all four distinct angular directions that we measured, the $2T$ conductance decreased with decreasing temperature, as expected from a semiconductor. This temperature dependence was also anisotropic. The G_{xx} along the 90° (270°) direction showed much stronger temperature dependence than along other directions. It reduced by five orders of magnitude, and changed from having the second highest value (slightly lower than along the c -axis) at room temperature to having the lowest at temperatures below 20 K. In contrast, the G_{xx} along the c -axis changed by less than one order of magnitude, and nearly remained constant below 50 K.

These temperature dependences are highlighted in Fig. 6.3c as two sets of conductance ratios between orthogonal crystal directions. The ratio $G_{xx}(90^\circ)/G_{xx}(0^\circ)$ is nearly unity for temperatures above 50 K, in agreement with previous results [10, 19]. Remarkably, it drops four orders of magnitude to about 10^{-4} at very low temperature (4.7 K). This strong anisotropy is comparable to other vdW materials such as (kish) graphite [15]. The ratio $G_{xx}(45^\circ)/G_{xx}(135^\circ)$ also changes with temperature, but only roughly by one order of magnitude.

This highly anisotropic temperature dependence can also be explained by the presence of extrinsic mechanisms for inter-chain conduction, which has a different temperature dependence from the intra-chain conduction.

Note that for trigonal Tellurium, which is an inversion-lacking Weyl semimetal [14, 20–22], there exists an intrinsic source of anisotropic temperature dependence of electrical conductivity [23]. However, this mechanism suggests that the conductance ratio between orthogonal directions scales linearly with temperature [23], which is not what we observed.

6.2 Nonreciprocal charge transport in Tellurene

6.2.1 Bias dependence of nonlinear charge transport

In order to further understand the conduction mechanisms, we measured the bias dependence of the charge transport at temperature of 50 K. This is done by applying a *dc* bias on top of the *ac* driving voltage, and recording the first and second order response in both longitudinal and transverse directions (see Methods and Appendix C). The results are shown in Fig. 6.4.

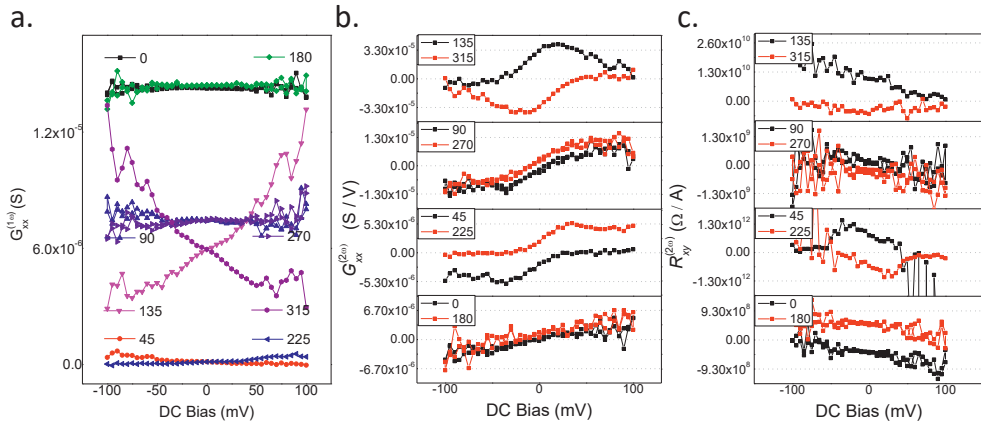


Figure 6.4: Angle-resolved bias dependence of first and second order responses in longitudinal and transverse directions. **a.** First order longitudinal conductance $G_{xx}^{(1\omega)} = I_{xx}/V_{xx}$. We have subtracted the mixing of second order response into the first order due to the *dc+ac* measurement technique [24]. **b.** Second-order longitudinal conductance coefficient $G_{xx}^{(2\omega)} = I_{xx}^{(2\omega)}/V_{xx}^2$. **c.** Second order transverse resistance coefficient $R_{xy}^{(2\omega)} = V_{xy}^{(2\omega)}/I_{xx}^2$. Each box in Panel **b** and **c** contains a pair of curves measured at opposite directions.

In Fig. 6.4a is the bias dependence of the first-harmonic longitudinal conduc-

tances (effectively the differential conductance, here noted as $G_{xx}^{(1\omega)}$) along different crystal directions. The bias dependence is again anisotropic. In directions along the c -axis (0° and 180°), the longitudinal conductances remain nearly unchanged within the bias range, while along other directions, the conductance changes monotonically with bias.

The presence of this bias non-even conductance, especially in the 45° (225°) and 135° (315°) directions, highlights the rectified (nonreciprocal) charge transport. Interestingly, the slopes for the 45° and 135° curves have opposite signs, and we suggest that their finite but incomplete compensation may be the reason for the finite but relatively weak bias dependence along the 90° (270°) direction.

These nonlinear behaviors are further detailed in the second-order responses of the crystal. For these measurements, we first confirmed the parabolic shape of the second-order I - V in all directions by sweeping the ac amplitude from 0 to 5 mV at zero dc bias. Then, we fixed the ac amplitude at 5 mV and swept the dc bias between ± 100 mV. Both the longitudinal (current) and transverse (voltage) second-order responses were measured, and the associated coefficients are plotted in Fig. 6.4b-c. The measurement geometry requires the two (180° -separated) curves within each box to overlap when both the horizontal and vertical axes reverse sign. This disqualifies the 135° and 315° transverse results for further analysis. We focus here only on the other valid curves.

We separately discuss the second-order longitudinal conductance $G_{xx}^{(2\omega)}$ and transverse resistance $R_{xy}^{(2\omega)}$ for each distinct angular direction. When the ac bias is applied along the c -axis (0° and 180°), both the $G_{xx}^{(2\omega)}$ and $R_{xy}^{(2\omega)}$ scale linearly with dc bias, but their slopes have opposite signs. Notably, $G_{xx}^{(2\omega)}$ vanishes at zero dc bias, in agreement with the flat $G_{xx}^{(1\omega)}$ bias dependence, while $R_{xy}^{(2\omega)}$ remains finite.

The orthogonal direction (90° and 270°) shows overall similar behaviors, but with a few differences. On one hand, the $G_{xx}^{(2\omega)}$ is nonzero at zero dc bias, and it reaches saturation at about 30 mV bias. The $R_{xy}^{(2\omega)}$, on the other hand, is much smaller at zero dc bias as compared to the c -axis direction.

For the 45° and 225° directions, $G_{xx}^{(2\omega)}$ also scales linearly with dc bias before reaching saturation at around 30 mV, where the $R_{xy}^{(2\omega)}$ shows a sharp turn and reverses its bias dependence before vanishing. Note that the $R_{xy}^{(2\omega)}$ here is three orders of magnitude larger than the 0° (180°) and 90° (270°) directions.

6.2.2 Discussion on nonlinear mechanisms

From a symmetry point of view, these nonreciprocal transport properties are indeed allowed in Tellurene because of its lack of inversion symmetry [25]. We interpret the observations as a combined result of intrinsic and extrinsic mechanisms.

The intrinsic nonlinearity can arise from the bias-dependent nonequilibrium band occupation in the material. What we measured here is a second-order current density (electron velocity) driven by an oscillating electric field under time-reversal invariant conditions. Here the intrinsic contribution has two aspects: firstly, the momentum-integrated group velocity of the Bloch electrons, and secondly, the momentum-integrated Berry curvature gradient over all occupied states [26, 27]. At zero dc bias, the first integral is required to vanish due to its odd k -dependence and the equal occupation of k and $-k$ states (time-reversal pairs) [27]. Therefore, the intrinsic nonlinear response at low bias is solely determined by the second integral, which is referred to as the Berry curvature dipole [27]. It gives rise to nonlinear transverse conduction in polar and inversion-lacking materials, which is termed the nonlinear anomalous Hall effect [27–29]. In a (quasi) 2D system, the anisotropy of this effect transforms as an in-plane vector, it should be strongest in one direction but vanishes in the orthogonal direction. This however does not (fully) describe our observations in Fig. 6.4c. Moreover, the magnitude of this effect in trigonal Tellurium is expected to be too small to observe [30].

When a dc bias is applied, the k and $-k$ states at the Fermi surface are no longer equally occupied, and therefore the group velocity integral becomes nonzero. This allows a second-order response that is odd in the dc bias in both the longitudinal and the transverse directions. This mechanism explains the linear bias dependence of $G_{xx}^{(2\omega)}$ and $R_{xy}^{(2\omega)}$ around zero bias in all (valid) directions, however, it does not explain their nonzero values at zero bias (equilibrium).

We attribute the finite equilibrium nonreciprocal transport, as well as other observed nonlinear features, to extrinsic mechanisms. The transverse response can arise from asymmetric disorder scatterings [31], which can add to the intrinsic Berry curvature dipole contribution and give rise to a nontrivial in-plane anisotropy. This disorder scatterings may also be reflected in the longitudinal response [32]. In addition, the longitudinal term may also be induced by, for instance, asymmetric potential profile for inter-chain conduction, or electron-electron interactions [33, 34].

6.3 Conclusion

In summary, we investigated the electrical transport properties of a quasi 2D van der Waals chiral crystal, Tellurene, and observed its giant conductance anisotropy of up to 10^4 . The anisotropy exhibited strong temperature dependence, suggesting a role of extrinsic conduction mechanisms in the crystal. There is also a nonreciprocal bias dependence associated with the charge transport, and we studied this as second-order longitudinal and transverse electrical responses. This can again largely

be accounted for by extrinsic conduction mechanisms.

Our results demonstrated the complexity of electrical conduction in low-symmetry, low-dimensional crystals, and highlighted the rich physics enabled in these materials. These phenomena can be potentially applied to piezoelectric and nonlinear electronic applications, but this requires further theoretical understandings. The applications can even be extended to the spin degree of freedom given the strong spin-orbit coupling of the material [11], and this directions should also be addressed in future researches.

6.4 Methods

Device fabrication. We transfer the solution-grown Tullurene flakes on a Si-SiO₂ (295 nm oxide) substrate using Langmuir-Blodgett transfer technique. Then we selected trapezoidal flakes that were around 50 nm thick for charge transport devices (Fig. 6.1e). On each flake, we deposited eight circularly arranged electrical contacts (5-nm Ti-50-nm Au), which were 45° separated from each other, as shown in Fig. 6.1e and f. The channel length between the two opposing contacts was 1 μm, and the width at the end of the contacts was 0.2 μm. The contacts were labeled by their angular orientation with respect to the *c*-axis, following a counterclockwise order. The measurement geometry is illustrated in Fig. 6.1f. At each angle, we applied longitudinal *ac* voltage bias with amplitude of 5 mV (root mean square) using V_{xx} electrodes, and used lock-in technique to measure simultaneously the linear response of longitudinal current I_{xx} (using the same electrodes) and the transverse voltage V_{xy} . When the angular direction of the measurement was changed, all four electrodes were rotated at the same time. The measurement direction was labeled using the same angular label of the $+V_{xx}$ electrode. The measurement geometry shown in Fig. 6.1f is for the 0° direction.

Electrical measurements. For the in-plane conductance anisotropy measurement, we characterized the *I-V* response in each angular direction by sweeping a low frequency (ranging from 3 to 33 Hz) *ac* bias V_{xx} from 0 to 5 mV, and at the same time measured the first-harmonic response of I_{xx} and V_{xy} using a lock-in amplifier (Stanford Research Systems SR830). The slopes of the linear *I-V* are used to extract the longitudinal conductance $G_{xx} = dI_{xx}/dV_{xx}$ and the transverse resistance $R_{xy} = dV_{xy}/dI_{xx}$. The angular dependence of both quantities are plotted in Fig. 6.1g-h for $T = 300$ K.

The same measurement geometry was used for the bias-dependent measurements, but in addition to the low frequency *ac* bias, a *dc* bias was applied on top using a voltage divider circuit (see Appendix C). The *ac* bias was kept at a constant amplitude of 5 mV, while the *dc* bias was swept between -100 and 100 mV. Both the first-harmonic and the second-harmonic responses of I_{xx} and V_{xy} were measured. These results were used to obtain the plots in Fig. 6.4. Note that the *dc+ac* measurement technique causes second-harmonic responses to mix into first-harmonic signals [24]. This mixing contribution has been subtracted for the curves in Fig. 6.4a.

Simulation details. The conductor network modeling in Fig. 6.2 was done with COMSOL Multiphysics 5.2a software. We simulated the circularly arranged electrode geometry, and between the top and bottom opposing electrodes we inserted 30 parallel elongated rectangular conducting channels to represent the 1D Te chains. Note that in the actual sample, 500 Te chains could fit in the distance between opposing electrodes [9]. We also introduced a few rectangles to make electrical contact between the parallel channels. They represent the extrinsic inter-chain conduction mechanisms. Their partially aligned tilting reflects the chirality of the material. The conductivity of the eight electrodes were set four orders of magnitude higher than that of the horizontal channels, which was again one order of magnitude higher than that of the inter-chain channels. The conductance was evaluated by applying a fixed current density

(against ground) using each opposing pair of electrodes, and the horizontal left-to-right current direction is considered 0° . Other angular directions were rotated in a counterclockwise fashion. The plotted mesoscopic conductance in Fig. 6.2b was the normalized result.

6.5 Appendices

A. 2D tensor-form Ohm's law

The 2D tensor-form Ohm's law describes a charge current density in response to a driving electric field, both are 2D (column) vectors. The (linear) response tensor connecting the two vectors is known as the conductivity tensor. This is given by (Eqn. 1 in the main text)

$$\begin{pmatrix} j_x \\ j_y \end{pmatrix} = \begin{pmatrix} \sigma_{xx} & \sigma_{xy} \\ \sigma_{yx} & \sigma_{yy} \end{pmatrix} \begin{pmatrix} E_x \\ E_y \end{pmatrix}, \quad (6.2)$$

where the x - and y -directions are defined by an external frame of reference, often the crystal structure of the conducting material.

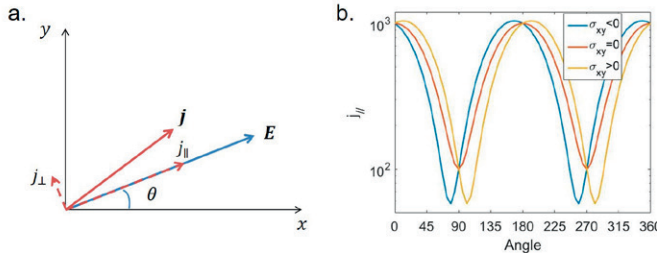


Figure 6.5: 2D tensor-form Ohm's law and the corresponding angular dependence of longitudinal conductance. **a.** Current density (\mathbf{j} in response to a driving electric field (\mathbf{E}), which is along the θ direction, in a 2D (x - y plane) anisotropic conducting material. **b.** The longitudinal (along the direction of the driving electric field) current density response as a function of angular direction θ (semi-log scale, arbitrary unit). The three curves represent conducting materials with $\sigma_{xy} = \sigma_{yx} < 0, = 0,$ and > 0 , respectively. All three are sinusoidal curves with a period of 180° .

We can rewrite the current density vector in terms of longitudinal (j_{\parallel}) and transverse (j_{\perp}) responses with respect to the driving electric field, which we assume is applied at an angle θ with respect to the x -direction, as illustrated in Fig. 6.5a.

However, the conductivity tensor is still defined in x - and y -terms because these directions are related to the material property. Therefore, we need to project the conductivity tensor from its original x - y frame of reference to a new frame of reference that is rotated (counterclockwise) by an angle θ . For this, we introduce a rotation operator of angle θ

$$R_{\theta} = \begin{pmatrix} \cos \theta & -\sin \theta \\ \sin \theta & \cos \theta \end{pmatrix}, \quad (6.3)$$

which satisfies $R_{\theta}^{-1} = R_{\theta}^T$ (where R_{θ}^T is the transpose of R_{θ}).

The 2D Ohm's law thus becomes

$$\begin{pmatrix} j_{\parallel} \\ j_{\perp} \end{pmatrix} = R_{\theta}^{-1} \begin{pmatrix} \sigma_{xx} & \sigma_{xy} \\ \sigma_{yx} & \sigma_{yy} \end{pmatrix} R_{\theta} \begin{pmatrix} E \\ 0 \end{pmatrix}, \quad (6.4)$$

where E is the length of \mathbf{E} .

This expression gives a j_{\parallel} that is a sinusoidal function of θ with a 180° period, as plotted in Fig. 6.5b (semi-log scale). The three curves in this figure correspond to situations where the unrotated conductivity tensor has its off-diagonal term $\sigma_{xy} = \sigma_{yx} < 0, = 0,$ and $> 0,$ respectively (assuming $\sigma_{xx} = 10 \sigma_{yy}$, and are kept unchanged for all three curves). At angles where j_{\parallel} takes maximum or minimum values, the rotated conductivity tensor becomes diagonal.

B. Results on another sample (Sample B) and effect of contact resistance

We performed the anisotropic conductance measurement on a different Tellurene flake using the same device and measurement geometry, and the results for three different temperatures are shown in Fig. 6.6a. For these results a gate voltage of -50 V was applied (see Appendix D). Similar to Sample A (main text), these results also show that the highest and lowest conductances are measured in non-orthogonal directions, and that the conductances are different along the 45° (225°) and 135° (315°) directions. Unlike Sample A though, here it is the 135° (315°) direction that has the lowest conductance.

The 90° (270°) direction again showed strongest temperature dependence with a change of about four orders of magnitude. However, the other directions also showed relatively strong temperature dependence, and as a result, the anisotropy ratio $G_{xx}(90^{\circ})/G_{xx}(0^{\circ})$ at 4 K is only roughly 10^{-2} .

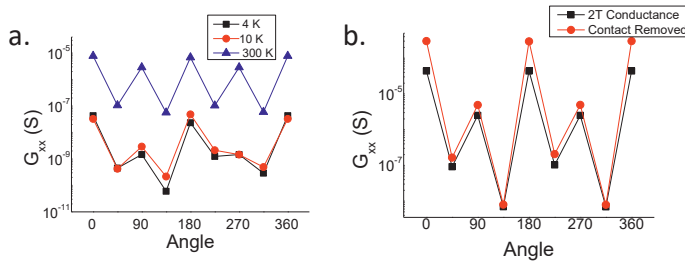


Figure 6.6: Anisotropic conductance measurements on Sample B. **a.** Angular dependence of the two-terminal G_{xx} at various temperatures. **b.** The two-terminal result of 300 K (black), as compared to when the electrical contact resistance is removed (red).

At 300 K, we checked the effect of contact resistance on this sample. We used a three-terminal technique, where we drive charge current between two electrodes, one of which is grounded, and then measure the voltage difference between a third reference electrode and the grounded electrode. This measurement was intended to determine the contact resistance of the grounded electrode. However, we found that depending on the reference electrode choice, the measured three-terminal resistance was different. This indicated that the sample itself was inhomogeneous, and therefore the three-terminal results contained not only the contact resistance, but also information on the conduction path. We thereby tried to use all available reference electrodes, and took the lowest measured resistance as an estimate for the contact resistance of the ground electrode. In this way, we estimated the upper limit of contact resistance for all eight electrode, and subtracted from the G_{xx} two-terminal measurement results. The angular dependence of G_{xx} before (black) and after (red) the subtraction are plotted in Fig. 6.6b.

C. Circuit geometry and additional results (Sample B)

We illustrate here the measurement geometry in Fig. 6.7a. Here we highlight the voltage divider circuit for the $dc+ac$ measurements in the green dashed box. During the experiments we used $R = 100 \Omega$. Using this circuit, we could apply a driving voltage of $V \approx V_{ac}/1000 + V_{dc}/100$ on the sample, and the subsequent responses were all measured at the ac frequency. Notably, we simultaneously measured the two-terminal current response I_{xx} , four-terminal longitudinal voltage responses (similar to a van der Pauw geometry) V_{xx-L} and V_{xx-R} , and four-terminal transverse voltage response V_{xy} .

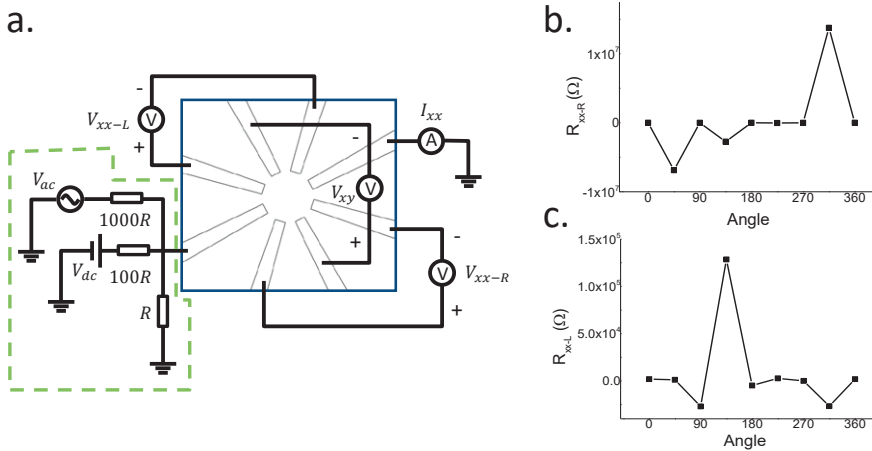


Figure 6.7: Measurement circuit and additional results. **a.** The circuit geometry for the conductance measurements. In the green dashed box is the voltage divider circuit for applying a $dc+ac$ driving voltage. The subsequent two-terminal charge current I_{xx} , transverse voltage response V_{xy} , longitudinal four-terminal (van der Pauw geometry) voltage responses V_{xx-L} and V_{xx-R} are measured at the ac frequency with a lock-in amplifier. All grounds are shared. When the angular direction is changed, all electrical contacts are changed simultaneously. **b-c.** The angular dependence of longitudinal van der Pauw voltage responses for Sample B at 4 K. These results are from the same set of measurements where the 4 K curve in Fig. 6.6a was obtained.

The longitudinal conductances G_{xx} that we showed in the main text were all determined using the two-terminal current response I_{xx} and the driving ac voltage $V_{ac}/1000$, instead of the four-terminal van der Pauw geometry that is commonly used for characterizing 2D conductors. This is because the van der Pauw geometry requires the samples to be homogeneous within the area of measurement, so that a (possibly anisotropic) conductivity tensor can be defined. However, as discussed in the main text, this is not the case for our samples. To illustrate this, we take the same set of measurements that gave the 4 K two-terminal G_{xx} curve in Fig. 6.6a, and use the simultaneously measured quantities to obtain the longitudinal four-terminal resistances $R_{xx-R} = V_{xx-R}/I_{xx}$ and $R_{xx-L} = V_{xx-L}/I_{xx}$, as shown in Fig. 6.7b-c. These results do not follow twofold sine curves, and can even provide negative resistance values. This is a further evidence for inhomogeneity-induced irregular current paths within the sample area.

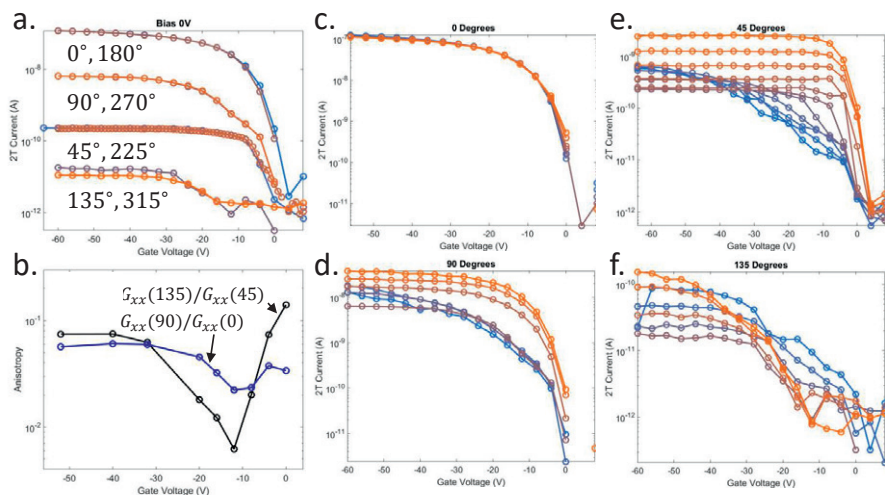


Figure 6.8: Gate and dc bias dependence measurement on Sample B. **a.** Gate dependence of G_{xx} at the four distinct angular directions, without applying and dc bias. **b.** Gate dependence of the conductance ratios $G_{xx}(90^\circ)/G_{xx}(0^\circ)$ and $G_{xx}(135^\circ)/G_{xx}(45^\circ)$, obtained from the data in Panel **a**. **c-f.** Gate dependence under dc biases, along the four distinct angular direction. The dc bias is swept with equal steps from positive (more orange) to negative (more blue) values, with a maximum current (absolute value) of 100 nA. (Thereby the maximum dc bias that was applied for the 0° direction was less than that along the 45° direction.)

D. Gate dependence (Sample B)

We performed gate dependence measurement on Sample B. The p -type semiconductor was turned on at negative gate voltages, and the longitudinal conductance G_{xx} is plotted against the gate voltage in Fig. 6.8. For Panels **a-b**, we only applied the ac driving bias to obtain the G_{xx} values, while for Panels **c-f**, we used a voltage divider circuit to apply a dc bias on top of the ac driving bias (see above Appendix C), in order to observe the bias-induced change to the gate dependences. Details of each panel is explained in the figure legend.

Bibliography

- [1] K. S. Burch, D. Mandrus, and J.-G. Park, "Magnetism in two-dimensional van der Waals materials," *Nature* **563**(7729), pp. 47–52, 2018.
- [2] T. S. Ghiasi, A. A. Kaverzin, P. J. Blah, and B. J. van Wees, "Charge-to-spin conversion by the Rashba–Edelstein effect in two-dimensional van der Waals heterostructures up to room temperature," *Nano Letters* **19**(9), pp. 5959–5966, 2019.
- [3] J. Quereda, T. S. Ghiasi, J.-S. You, J. van den Brink, B. J. van Wees, and C. H. van der Wal, "Symmetry regimes for circular photocurrents in monolayer MoSe_2 ," *Nature Communications* **9**(1), pp. 1–8, 2018.
- [4] K. Novoselov, A. Mishchenko, A. Carvalho, and A. C. Neto, "2D materials and van der Waals heterostructures," *Science* **353**(6298), p. aac9439, 2016.

- [5] T. I. Lee, S. Lee, E. Lee, S. Sohn, Y. Lee, S. Lee, G. Moon, D. Kim, Y. S. Kim, J. M. Myoung, *et al.*, “High-power density piezoelectric energy harvesting using radially strained ultrathin trigonal tellurium nanowire assembly,” *Advanced Materials* **25**(21), pp. 2920–2925, 2013.
- [6] F. Purcell-Milton, R. McKenna, L. J. Brennan, C. P. Cullen, L. Guillemeeny, N. V. Tepliakov, A. S. Baimuratov, I. D. Rukhlenko, T. S. Perova, G. S. Duesberg, *et al.*, “Induction of chirality in two-dimensional nanomaterials: chiral 2D MoS₂ nanostructures,” *ACS Nano* **12**(2), pp. 954–964, 2018.
- [7] R. Naaman, Y. Paltiel, and D. H. Waldeck, “Chiral molecules and the electron spin,” *Nature Reviews Chemistry* **3**, pp. 250–260, 2019.
- [8] X. Yang, C. H. van der Wal, and B. J. van Wees, “Detecting chirality in two-terminal electronic nanodevices,” *Nano Letters*, 2020.
- [9] A. Koma and S. Tanaka, “Etch pits and crystal structure of tellurium,” *Physica Status Solidi (b)* **40**(1), pp. 239–248, 1970.
- [10] Y. Wang, G. Qiu, R. Wang, S. Huang, Q. Wang, Y. Liu, Y. Du, W. A. Goddard, M. J. Kim, X. Xu, *et al.*, “Field-effect transistors made from solution-grown two-dimensional tellurene,” *Nature Electronics* **1**(4), p. 228, 2018.
- [11] Y. Du, G. Qiu, Y. Wang, M. Si, X. Xu, W. Wu, and P. D. Ye, “One-dimensional van der Waals material tellurium: Raman spectroscopy under strain and magneto-transport,” *Nano Letters* **17**(6), pp. 3965–3973, 2017.
- [12] S. Berweger, G. Qiu, Y. Wang, B. Pollard, K. L. Genter, R. Tyrrell-Ead, T. M. Wallis, W. Wu, P. D. Ye, and P. Kabos, “Imaging carrier inhomogeneities in ambipolar tellurene field effect transistors,” *Nano Letters* **19**(2), pp. 1289–1294, 2019.
- [13] G. Qiu, C. Niu, Y. Wang, M. Si, Z. Zhang, W. Wu, and P. D. Ye, “Quantum Hall effect of Weyl fermions in n-type semiconducting tellurene,” *Nature Nanotechnology* **15**, pp. 585–591.
- [14] M. Sakano, M. Hirayama, T. Takahashi, S. Akebi, M. Nakayama, K. Kuroda, K. Taguchi, T. Yoshikawa, K. Miyamoto, T. Okuda, *et al.*, “Radial spin texture in elemental tellurium with chiral crystal structure,” *Physical Review Letters* **124**(13), p. 136404, 2020.
- [15] D. Z. Tsang and M. S. Dresselhaus, “The c-axis electrical conductivity of kish graphite,” *Carbon* **14**(1), pp. 43–46, 1976.
- [16] E. Liu, Y. Fu, Y. Wang, Y. Feng, H. Liu, X. Wan, W. Zhou, B. Wang, L. Shao, C.-H. Ho, *et al.*, “Integrated digital inverters based on two-dimensional anisotropic ReS₂ field-effect transistors,” *Nature Communications* **6**, p. 6991, 2015.
- [17] Q. Zheng, P. Ren, Y. Peng, W. Zhou, Y. Yin, H. Wu, W. Gong, W. Wang, D. Tang, and B. Zou, “In-plane anisotropic Raman response and electrical conductivity with robust electron–photon and electron–phonon interactions of air stable MoO₂ nanosheets,” *The Journal of Physical Chemistry Letters* **10**(9), pp. 2182–2190, 2019.
- [18] X. Xu, Q. Song, H. Wang, P. Li, K. Zhang, Y. Wang, K. Yuan, Z. Yang, Y. Ye, and L. Dai, “In-plane anisotropies of polarized Raman response and electrical conductivity in layered tin selenide,” *ACS Applied Materials & Interfaces* **9**(14), pp. 12601–12607, 2017.
- [19] L. Rothkirch, R. Link, W. Sauer, and F. Manglus, “Anisotropy of the electric conductivity of tellurium single crystals,” *Physica Status Solidi (b)* **31**(1), pp. 147–155, 1969.
- [20] M. Hirayama, R. Okugawa, S. Ishibashi, S. Murakami, and T. Miyake, “Weyl node and spin texture in trigonal tellurium and selenium,” *Physical Review Letters* **114**(20), p. 206401, 2015.
- [21] K. Nakayama, M. Kuno, K. Yamauchi, S. Souma, K. Sugawara, T. Oguchi, T. Sato, and T. Takahashi, “Band splitting and Weyl nodes in trigonal tellurium studied by angle-resolved photoemission spectroscopy and density functional theory,” *Physical Review B* **95**(12), p. 125204, 2017.
- [22] T. Ideue, M. Hirayama, H. Taiko, T. Takahashi, M. Murase, T. Miyake, S. Murakami, T. Sasagawa, and Y. Iwasa, “Pressure-induced topological phase transition in noncentrosymmetric elemental tellurium,” *Proceedings of the National Academy of Sciences* **116**(51), pp. 25530–25534, 2019.
- [23] B.-J. Yang, M. S. Bahrmy, R. Arita, H. Isobe, E.-G. Moon, and N. Nagaosa, “Theory of topological quantum phase transitions in 3D noncentrosymmetric systems,” *Physical Review Letters* **110**(8), p. 086402, 2013.
- [24] J. Shan, F. K. Dejene, J. C. Leutenantsmeyer, J. Flipse, M. Münzenberg, and B. J. van Wees, “Comparison of the magneto-Peltier and magneto-Seebeck effects in magnetic tunnel junctions,” *Physical Review B* **92**(2), p. 020414, 2015.
- [25] Y. Tokura and N. Nagaosa, “Nonreciprocal responses from non-centrosymmetric quantum materials,” *Nature Communications* **9**(1), pp. 1–14, 2018.
- [26] G. Sundaram and Q. Niu, “Wave-packet dynamics in slowly perturbed crystals: Gradient corrections and Berry-phase effects,” *Physical Review B* **59**(23), p. 14915, 1999.
- [27] I. Sodemann and L. Fu, “Quantum nonlinear Hall effect induced by Berry curvature dipole in time-reversal invariant materials,” *Physical Review Letters* **115**(21), p. 216806, 2015.
- [28] Q. Ma, S.-Y. Xu, H. Shen, D. MacNeill, V. Fatemi, T.-R. Chang, A. M. M. Valdivia, S. Wu, Z. Du, C.-H. Hsu, *et al.*,

- "Observation of the nonlinear Hall effect under time-reversal-symmetric conditions," *Nature* **565**(7739), p. 337, 2019.
- [29] K. Kang, T. Li, E. Sohn, J. Shan, and K. F. Mak, "Nonlinear anomalous Hall effect in few-layer WTe₂," *Nature Materials* **18**(4), p. 324, 2019.
- [30] S. S. Tsirkin, P. A. Puente, and I. Souza, "Gyrotropic effects in trigonal tellurium studied from first principles," *Physical Review B* **97**(3), p. 035158, 2018.
- [31] Z. Z. Du, C. M. Wang, S. Li, H.-Z. Lu, and X. C. Xie, "Disorder-induced nonlinear Hall effect with time-reversal symmetry," *Nature Communications* **10**(1), pp. 1–6, 2019.
- [32] P. Olbrich, L. Golub, T. Herrmann, S. Danilov, H. Plank, V. Bel’Kov, G. Mussler, C. Weyrich, C. Schneider, J. Kampmeier, *et al.*, "Room-temperature high-frequency transport of Dirac fermions in epitaxially grown Sb₂Te₃- and Bi₂Te₃-based topological insulators," *Physical Review Letters* **113**(9), p. 096601, 2014.
- [33] T. Christen and M. Büttiker, "Gauge-invariant nonlinear electric transport in mesoscopic conductors," *EPL (Europhysics Letters)* **35**(7), p. 523, 1996.
- [34] M. Büttiker, "Capacitance, admittance, and rectification properties of small conductors," *Journal of Physics: Condensed Matter* **5**(50), p. 9361, 1993.

Chapter 7

Enhancing and rectifying electron transport through a biomolecular junction comprising Photosystem I and graphene

Biological systems provide a large pool of chiral materials. Understanding the electrical properties of these materials opens up possibilities for bio-organic opto-electronic, photo-voltaic, or spintronic applications. For this purpose, here we incorporate natural photosynthetic protein complex Photosystem I (PSI) onto graphene electrodes, and investigate the electron transport through the biomolecular junction. Comparing to earlier researches, we significantly enhanced and rectified the electron transport by using phage-displayed peptides as binders between PSI and graphene. Further, we studied how the electron transport through the junction is affected by mechanical contact. Our results provide insights for future device designs involving large bio-organic systems.

This chapter is being prepared as:

X. Yang, T. Bosma, E. B. P. Brul, A. Kunzendorf, P. I. Gordiichuk, A. Herrmann, B. J. van Wees & C. H. van der Wal, "Enhancing and rectifying electron transport through a biomolecular junction comprising Photosystem I and graphene"

Chirality is abundant in natural bio-organic systems. Understanding its role in various biological processes is not only fundamentally interesting, but also important to the development of nature-inspired technologies. For example, the chirality of a photosynthetic membrane protein complex, photosystem I (PSI), reportedly induces spin-polarized electron transfer during its photo-excitation and relaxation cycles [1]. This suggests a role of electronic spin in photosynthesis, and hints potential opto-spintronic applications for PSI [2]. Additionally, PSI is one of the most efficient light-harvesting systems to date. It has a quantum efficiency of nearly 100% [3, 4], which contributes to the overall high efficiency of photosynthesis [5, 6], and shows application prospects in fields like photovoltaics and opto-electronics [7–13]. Because of this, PSI has been incorporated onto electrodes to understand its electron transport properties and to pave way for future applications. The desired electrode should be optically transparent and support efficient electronic charge and spin transport, and is thereby often chosen as graphene [14–17]. However, the electron transport across the PSI-graphene biomolecular junction has remained poor, hindering further technological developments.

Here we enhance the electron transport in PSI-graphene junctions by modifying PSI with phage-displayed peptides. This is demonstrated on commercially available CVD (chemical vapor deposition) graphene, and the electron transport is characterized using conductive atomic force microscopy (cAFM) techniques.

7

7.1 Binding PSI onto graphene using peptides

7.1.1 Sample preparation

For our research, cyanobacterial PSI was extracted and purified following the procedure described in Ref. 13. These PSI units typically appear as trimers with diameters of around 25 nm and heights of around 7 nm [13, 18]. They were kept in Buffer A (see Experimental Section) at a concentration of 1 μM before use.

To form biomolecular junctions, the PSI units were immobilized onto graphene surfaces in two steps. First, the PSI-Buffer A solution was mixed with a phosphate-buffered saline (PBS) solution that contained the peptides (see later discussions for details on peptides). This gave a mixed solution with PSI concentration of 0.1 μM and a desired PSI:peptide ratio. Second, the graphene substrate (graphene on SiO_2) was immersed in the mixed solution for a period of time for immobilization. Both steps were performed in the dark to minimize optical activity of PSI. Both the PSI-to-peptide ratio and the incubation time were varied for optimization, which concluded a 1 : 1 ratio and a 2-hour incubation time.

After immobilization, the graphene substrate was cleaned with water (Milli-Q) and then blown dry with gentle nitrogen flow. This treatment was intended to remove any excess PSI or peptides while keeping the immobilized ones on the graphene surface. The surface profiles and the subsequent electrical measurements were then measured with an AFM (Bruker MultiMode 8).

7.1.2 Peptide improves PSI coverage

Figure 7.1 shows the surface profiles of control samples prepared using only the peptides (a) and only the PSI (b), and the sample prepared using both (c). Figure 7.1a reveals nonuniform structures with height variation of around 1 nm, which likely corresponds to aggregated peptides. Figure 7.1b shows scattered grainy structures that resemble the shape and height of PSI. In comparison, Figure 7.1c, which corresponds to a sample prepared with 1 : 1 PSI-to-peptide ratio and an incubation time of 2 hours, shows similar grainy structures as in Fig. 7.1b, but as a densely packed monolayer. This indicates an improved PSI coverage due to the use of peptides. This region exhibits a high PSI number density (coverage) of around $1000 \mu\text{m}^{-2}$. However, we found that for the same sample and other samples prepared using the same peptide (GGD, see Table 7.1 for details), the PSI coverage was not uniform across the entire sample surface. We explain this as a consequence of the washing and drying procedures where nonuniform mechanical interactions took place due to water and air flow.

For comparison, we tested four other different sequences of peptides: HGI, IGH, IGG, GGI, as introduced in Table 7.1. They all contained two functional segments, one that was previously developed using phage display to bind to PSI with a controlled orientation [19], and another (two variants) which was reported to bind to graphene [20, 21]. These segments were linked to each other with glycine G (either one or three units). These peptide structures were designed in order to serve as binders between PSI and graphene.

Using each of these peptides, we immobilized PSI following the same procedure as described above. Then we performed AFM scans (size $3 \mu\text{m}$ by $3 \mu\text{m}$) at five random locations on each sample in order to analyze the average number density of immobilized PSI units. All the four peptides yielded uniform PSI coverage, with HGI being the highest at $22.67 \mu\text{m}^{-2}$ (see Table 7.1). This is however still much lower than the maximum coverage of about $1000 \mu\text{m}^{-2}$ observed on the GGD samples, which are although highly nonuniform.

It is worth noting that the GGD peptide contained a segment that has inverted sequence as compared to the phage-displayed PSI-binding segment used in other peptides [19]. It was likely that this sequence inversion affected the binding rate and binding strength between the peptide and the PSI [22–24]. For the other peptides, it

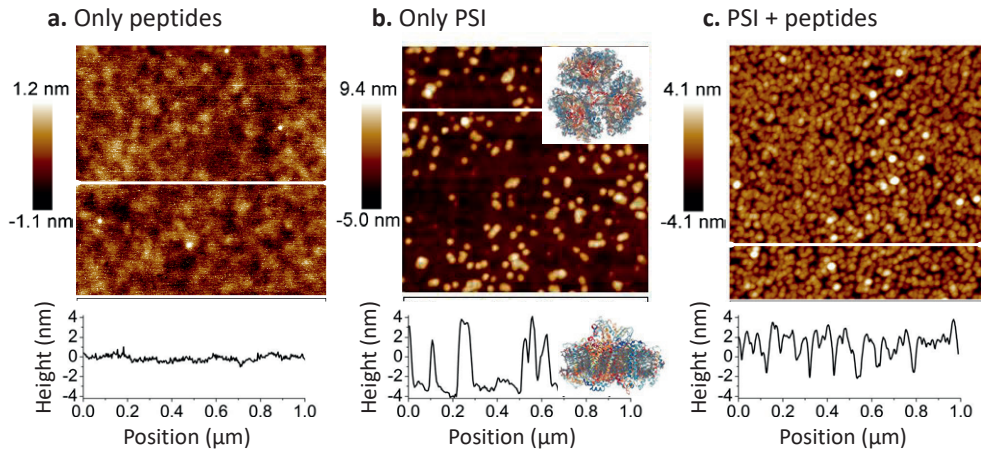


Figure 7.1: AFM height profile of CVD graphene substrates after being immersed 2 hours in **a.** a peptide solution, **b.** a PSI solution, and **c.** a PSI + peptide (1:1) mixed solution. A line profile (white line) parallel to the AFM scan direction is shown below each surface map. The scales of all line profiles are set equal. The structure of a PSI trimer is shown as insets in **b.**, where the top inset shows the top-view of a PSI trimer with a diameter of about 25 nm; and the bottom inset shows the side-view of a PSI monomer with a height of about 8 nm). PSI structure is taken from RCSB PDB (1JB0) [18]. The peptide used was GGD (see Table 7.1). [Change fig label Height]

7

Table 7.1: Comparison of immobilized PSI number density for different binding peptides.

Peptide name	Peptide sequence	PSI coverage (μm^{-2})
HGI	HSSYWYAFNNKT-GGG-IQAGKTEHLAPD	22.67
IGH	IQAGKTEHLAPD-GGG-HSSYWYAFNNKT	6.22
IGG	IQAGKTEHLAPD-G-GAMHLPWHMGTL	8.11
GGI	GAMHLPWHMGTL-G-IQAGKTEHLAPD	8.89
GGD	GAMHLPWHMGTL-G-DPALHETKGAQI	up to 1000*

* Among the five randomly chosen regions, some showed densely packed PSI like in Figure 7.1c, but some were completely empty.

was possible that the binding properties of either segment was affected when combining them into one peptide using a few glycine units. The exact impact was however unclear.

7.2 Enhanced and rectified PSI-graphene electron transport

7.2.1 Point-and-shoot technique for I - V characterization

The densely covered region obtained using the GGD peptide allowed us to perform electrical measurements on the PSI-graphene biomolecular junction, and this was done using conductive AFM (cAFM) techniques. We used Pt/Ir coated AFM probes and the Bruker MultiMode 8 was operated in PeakForce Tunneling AFM (PF-TUNA) mode. The geometry and the electrical wiring of this measurement is shown in Figure 7.2a. We first used a *Point and Shoot* method. The sample height profile was scanned with a controlled tip-sample contact force of no more than 1 nN. Then, according to this height profile, we positioned the AFM probe over individual PSI units and ramped down until a contact force of 10 nN. At this position, a bias sweep between ± 1 V was applied and the current through the junction was measured. One of the I - V curves obtained using this method is shown in Figure 7.2b.

The curve in Figure 7.2b exhibits rectified I - V behavior, and the rectification is quantified with

$$\mathfrak{R} = -\frac{I_{-0.5}}{I_{0.5}} \quad (7.1)$$

where $I_{-0.5}$ and $I_{0.5}$ are the currents measured at a sample bias of -0.5 V and 0.5 V, respectively. These bias voltages were phenomenologically chosen to be at the region where all (valid) I - V curves are nonlinear and do not reach the instrumental limit (within roughly ± 550 nA under our settings). For the GGD sample, majority of the I - V showed rectifications of $\mathfrak{R} > 1$.

This rectified electron transport was previously attributed to the orientation of PSI, because the internal electric dipole of PSI (which is determined by its structure) would induce asymmetric electron transfer [7, 25]. This would imply that the GGD peptide helped control the orientations of the bound PSI.

We also observed an exceptionally high charge current through the PSI-graphene junction. It often reached about 100 nA (at ± 0.5 V sample bias), significantly higher than previously reported PSI junctions using other binding molecules or other substrates [14–17, 19, 25].

We emphasize here two aspects about this high conductance. First, it was measured across a biomolecular junction with a thickness of around 8 nm. This strongly suggests that the electron transport happens via a conduction pathway, rather than by completely tunneling through the entire junction. Second and more importantly, the high conductance (as compared to other works using binding molecules other than peptides) indicated that the peptides helped enhance the electrical conduction through the junction. This could be due to the selective binding of the peptide to

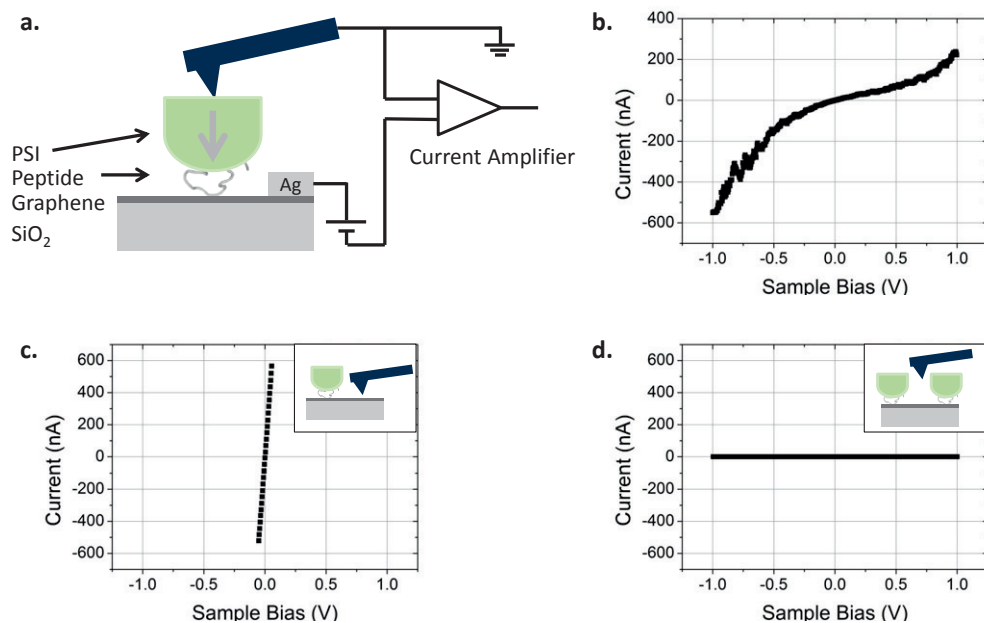


Figure 7.2: Geometry of the cAFM measurements and typical *I-V* curves obtained from the measurements. **a.** The wiring of the PF-TUNA mode used for cAFM measurements, illustrating the configuration of an AFM tip directly placed on top of a PSI unit, which has an internal electric dipole moment indicated by the gray arrow, and **b.** the *I-V* curve obtained for this configuration. **c.** The *short-circuit* configuration where the tip is in contact with the graphene substrate (inset), and its corresponding *I-V* curve. **d.** The *open-circuit* configuration where the AFM tip is not in contact with any conductive material (inset), and its corresponding *I-V* curve.

one end of the electron transfer chain within PSI, as was initially designed [19]. Consequently, it may provide an electron transfer path between PSI and graphene, and thereby enhance the conduction through the entire junction.

Note that two other types of *I-V* curves were also often measured. One is a *short-circuit* curve, as shown in Figure 7.2c. This linear *I-V* behavior was obtained when the AFM tip was placed in a region without PSI coverage, and can be explained by the direct contact between the tip and the graphene substrate. The other is an *open-circuit* flat line, which was caused by poor tip-sample contact, as shown in Figure 7.2d. The poor contact could be due to wearing off of the tip coating, ramping onto nonconductive parts of PSI or contaminants on the sample, noneffective binding between PSI and graphene, or denaturation of PSI.

7.2.2 Random positioning method for statistical confirmation

In order to statistically confirm the role of peptides in the PSI-graphene junction, we took a *Random Positioning* approach, where we performed ramping and subsequent I - V sweeps at a large number of random positions on a GGD sample within a region that was densely covered by PSI. (For control experiment, we also chose a densely packed region on a sample where PSI was deposited onto graphene without using peptides.) With this approach, we were able to exclude the influence of subjective selection of measurement positions and systematic errors associated with the positioning of the AFM probe. After obtaining a large amount of I - V curves, we removed *short-circuit* and *open-circuit* ones in order to account for only the effectively bound PSI units (see Experimental Section), and left 648 (out of 5436, yield of 11.92%) valid I - V curves for the GGD sample, and only 142 (out of 2126, yield of 6.67%) for the control sample. For all valid curves, we took the logarithm value of the $|I_{-0.5}|$ (without unit) and \Re , and plotted their distributions as 2D histograms, as shown in Figure 7.3.

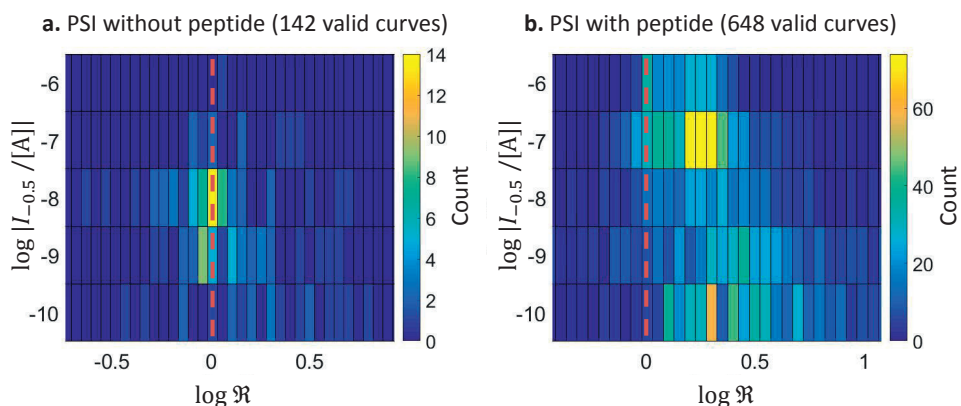


Figure 7.3: 2D histograms for $\log |I_{-0.5}/[A]|$, which denotes the logarithm (base 10) of the current value (in Ampere), and $\log \Re$, for the samples of PSI on graphene prepared **a.** without and **b.** with peptides. Red dashed lines show $\log \Re = 0$, which indicates symmetric IV.

The results strongly suggest an enhanced and rectified electron transport across the PSI-graphene junction due to the use of peptides: First of all, the use of peptides nearly doubled the yield of valid I - V curves, indicating the ability of peptides in improving the electrically active binding between PSI and graphene. Secondly, the use of peptides introduced a clearly rectified I - V behavior by shifting $\log \Re$ values from centered around 0 to around 0.3, confirming the role of peptides in altering the electron transport properties of the junctions. Finally, comparing the most probable current magnitude in the two histograms, the use of peptides increased the $|I_{-0.5}|$ by

roughly one order of magnitude, suggesting a significant enhancement of electrical conduction through the junctions.

We point out that the current limit of the system was around ± 550 nA, thus currents with higher magnitudes ($\log |I_{-0.5}/[A]| > -6.3$) were removed during data filtering and were not accounted for in the statistics. Taking this into account, the actual enhancement of the current magnitude could be larger than shown here. Furthermore, it was not necessarily the case that the rectification was caused by the peptide orienting PSI, as was previously discussed [7, 26]. This could alternatively be explained as electrode and electrical interface effects, such as asymmetric electrode materials [27], asymmetric coupling at the molecule-electrode interfaces [28, 29], and asymmetric tunnel barriers at the interfaces [30].

It is worth noting that both the $\log |I_{-0.5}|$ and $\log \mathcal{R}$ showed large scatters. The current magnitude, especially, spanned over the entire range the instrument could measure (four orders of magnitude). This adds complexity to understanding the electrical coupling between the PSI and the graphene substrate. We attribute this large span to two mechanisms. First, as a result of random positioning, the AFM tip was not guaranteed to land exactly atop the PSI electron transfer chain. The relative position affects the effective contact area and the exact electron transport path, and consequently, the measured current magnitude. Secondly, the contact force between the AFM tip and PSI might fluctuate during the data acquisition processes. Although the force was set to be kept constantly at 10 nN, the actual value could be different due to environmental disturbances and instabilities of the AFM stage. This second aspect is further investigated in the next section.

7.3 Mechanical tuning of PSI-graphene electron transport

We studied the impact of contact-force on I - V curves on a single PSI unit (bound on graphene using the GGD peptide). First, we performed a zoom-in height profile scan to have only one PSI unit in the image (Figure 7.4a). Then, we ramp the AFM probe at the center of the PSI unit (indicated by marker in Figure 7.4a) to repeat *Point and Shoot* at a set of gradually increasing contact forces. At each contact force, we obtained an I - V curve, as plotted in Figure 7.4b. In the end, we scanned again the height profile to make sure the PSI unit was still in the image (Figure 7.4c), confirming that the AFM stage had not drifted and thus all the I - V curves were measured on the same PSI unit. These results showed that the PSI I - V strongly depended on the contact force, and higher contact forces gave steeper I - V curves.

We calculated the resistance of PSI within the linear regime (between ± 0.05 V

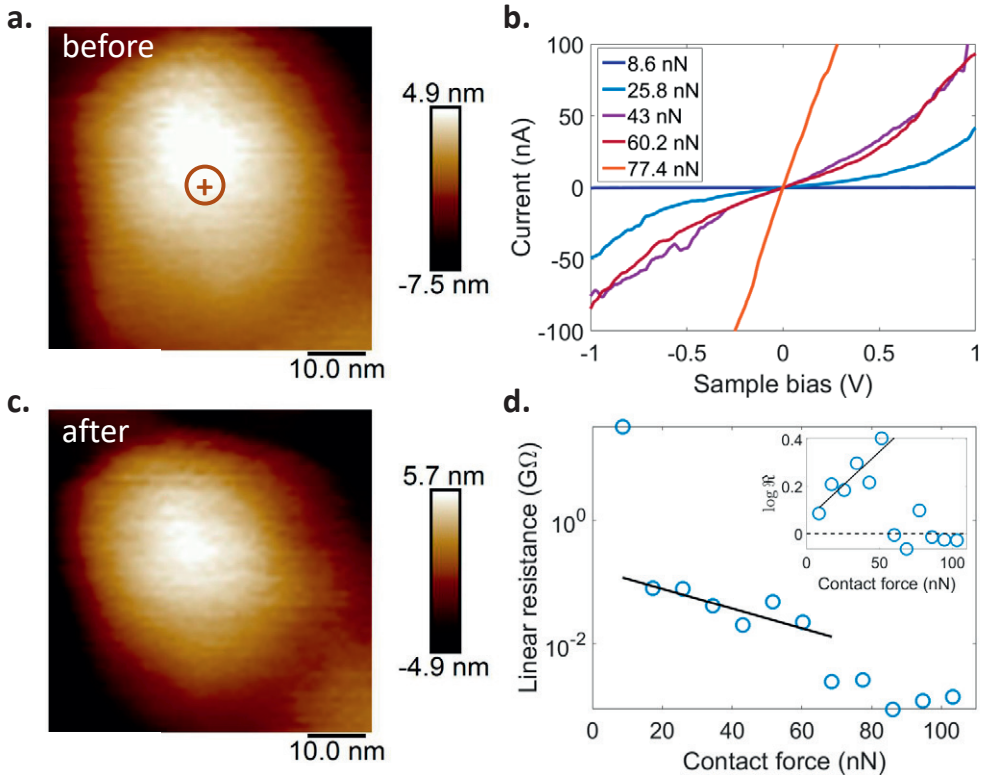


Figure 7.4: Force dependence of I - V curves across a PSI-graphene junction. **a.** Height profile scan of a single PSI unit, before I - V sweeps. The marker indicates where the tip is ramped for all I - V sweeps. **b.** Selected I - V sweeps at the marker location under different contact forces, in the experiment the forces were ramped from low to high. **c.** Height profile scan of the same PSI unit, after all I - V sweeps. **d.** Resistance at the zero-bias (linear) regime (obtained from the I - V curves between ± 0.05 V sample bias) as a function of applied contact force, plotted in log scale. The black line is an exponential fit for forces between 10 and 65 nN. Inset: Force dependence of $\log \mathfrak{R}$, the black line is a linear fit for forces below 65 nN, and dashed line marks $\log \mathfrak{R} = 0$, which corresponds to nonrectified IV.

sample bias) and plotted it as a function of contact force, see Figure 7.4d. The force dependence shows two regimes. For forces lower than 65 nN, there is a clear trend of decreasing resistance with increasing contact force, and the dependence is roughly exponential (black line, note the semi-log scale). However, for higher forces, the resistance jumps down to about 10^{-3} G Ω , and the force dependence becomes unclear.

We also calculated the rectifications of these I - V curves at ± 0.5 V sample bias, and plotted $\log \mathfrak{R}$ against the contact force in the inset of Figure 7.4d. We observe

here the same two force regimes. For forces lower than 65 nN, \mathfrak{R} increases exponentially with increasing contact force (black line, note the plotted $\log \mathfrak{R}$ value), while for higher forces $\log \mathfrak{R}$ jumps to around zero.

We explain the trends at lower forces as results of PSI deformation, and the separation of regimes as a structural breakdown of PSI. For lower forces, increasing contact force causes larger deformation, which could shorten the distance between the two electrodes (tip and graphene), and subsequently reduce the barrier width for any associated tunneling. Also, larger deformation could enlarge the contact area between PSI and the tip, providing more channels for conduction. These combined give rise to a lower electrical resistance. At the same time, in the nonlinear regime where the rectification was evaluated, the shortened channel length can also lead to an increased electric field across the junction (at a given bias voltage). This may amplify any asymmetric transport behavior either due to the electrical interfaces or due to the internal electric dipole associated with PSI orientation, and therefore increase the rectification \mathfrak{R} . The breakdown of these trends at about 65 nN can be attributed to an inelastic structural damage of PSI. This structural change is also evidenced by the height difference of the same PSI unit before and after taking the series of I - V curves. In Figure 7.4a (before measurements), the height variation within the scan area is about 12.4 nm, while in Figure 7.4c (after measurements) it is about 10.6 nm.

The above force dependence demonstrates that the electrical properties of PSI or a PSI-graphene junction are highly sensitive to mechanical interactions. On one hand, this provides an extra degree-of-freedom to tune the electrical properties of such a junction for potential applications such as force sensing. On the other hand, it also demonstrates complication for designing devices based on such biomolecular materials.

Furthermore, these force dependences show that results from the common experimental technique, cAFM, can be strongly affected by the environment. For example, the fluctuations of temperature and humidity may cause the AFM stage to drift, hence may change the contact force. It is therefore more complicated than commonly expected to conduct systematic electrical measurements with cAFM. One should always take into account the tip-sample contact force, and rely mainly on statistical results rather than individual I - V curves. For instance, during our *Random Positioning* experiments (including the control experiment), the AFM system was identically prepared before data acquisition and was kept in the same environment, and each measurement session took the same amount of time. Therefore, for all samples, the systematic instability of the contact force should be comparable, and this is supported by the similar levels of scatters in the two panels in Figure 7.3. As a result, it was proper to compare the centers of distribution in these two figures.

7.4 Conclusion

In summary, with the use of peptides that were partially developed using phage display, we successfully obtained a monolayer of Photosystem I trimers on graphene surfaces, and at the same time observed significant enhancement of electrical transport across the biomolecular junction. Our statistical results showed at least a one-order-of-magnitude increase of tunneling current and an introduction of rectified current-voltage (I - V) behavior due to the use of peptides. This is possibly due to the direct bindings of the peptides to the PSI electron transfer chain and graphene, and thereby altered the electrical properties of both the electrical interfaces and the entire junction itself. Further, we found that the current magnitude and the rectification were both affected by the tip-sample contact force, and we observed a breakdown of PSI at a force of about 65 nN. We also discussed that cAFM measurements on large biomolecular junctions must be based on proper statistical approaches that consider the tip-sample contact force.

Overall, the peptides provide a new tool to incorporate photosynthetic protein complexes onto solid-state devices while maintaining a good electrical coupling between the two parts. Similar techniques can be applied to other large protein complexes too. Further research should improve the coverage of the protein complexes by tuning the sequence of the peptides, and focus on the potential applications of these hybrid devices, for example, in the field of opto-electronics, photovoltaics, or spintronics.

7.5 Methods

Photosystem I cultivation, extraction and purification were done following the procedure reported in Ref. 13. The purified PSI was kept in Buffer A (20 mM HEPES, 10 mM MgCl₂, 10 mM CaCl₂, 500 mM Mannitol) and 0.3% DDM, and was stored in the dark at -80°C at a PSI trimer concentration of $1\ \mu\text{M}$.

Peptides: Lyophilized peptides with $> 90\%$ purity were purchased from two companies. Peptide GGD was from Proteogenix and the others were from Caslo. All peptides were kept in PBS at $5\ \mu\text{M}$ prior to immobilization.

PSI immobilization: The PSI and peptide solution were defrosted in the dark in ice before being mixed and further diluted with PBS. The final solution had the PSI and the peptide both at $0.1\ \mu\text{M}$ concentration. This solution was then shaken at 500 rpm at 4°C in the dark for 1 hour. Afterwards, a piece of CVD graphene on SiO₂ sample (purchased from Graphenea, cut into 2.5 mm by 5 mm shape) was immersed in the solution and incubated for 2 hours. During incubation, the system was kept at room temperature in the dark. After the incubation the samples were gently taken out of the solution and rinsed with Milli-Q water before being blown-dry with gentle nitrogen flow. The sample was then immediately kept in the dark until further measurements, which for our case varies between 1 and 24 hours.

AFM measurements: After immobilization the sample was glued to a stainless steel sample plate, and the sample plate was brought into electrical contact to the graphene surface with silver paste. The sample was then scanned in PeakForce TUNA mode with a Bruker Multimode 8, using Bruker's PFTUNA probes ($f_0 = 70\ \text{kHz}$, $k = 0.4\ \text{N/m}$). During AFM scans all light sources in the environment (apart from the red laser in the AFM scanning head) were turned off, and the scanning head opening was covered with a

stainless steel cover piece. The images and I - V curves were analyzed with the NanoScope Analysis 1.8 software.

Data filtering for statistics: After obtaining a large number of I - V curves, we filter out *short-circuit* and *open-circuit* ones. Here, *short-circuit* curves were defined as those in which $I_{-0.5}$ or $I_{0.5}$ reached the current limit of the AFM (the highest positive or lowest negative current that the system could measure), which was roughly ± 550 nA for the settings we used. *Open-circuit* curves accounted for two cases: first, those in which $I_{-0.5}$ and $I_{0.5}$ were equal (the value was often not zero due to system offset); and secondly, those in which the maximum absolute value of the curve was smaller than the resolution of the current meter (the minimum current that the system could detect, roughly 30 pA for our settings).

Bibliography

- [1] I. Carmeli, V. Skakalova, R. Naaman, and Z. Vager, "Magnetization of chiral monolayers of polypeptide: a possible source of magnetism in some biological membranes," *Angewandte Chemie International Edition* **41**(5), pp. 761–764, 2002.
- [2] X. Yang, T. Bosma, B. J. van Wees, and C. H. van der Wal, "Circuit-model analysis for spintronic devices with chiral molecules as spin injectors," *Physical Review B* **99**(21), p. 214428, 2019.
- [3] W. Haehnel, "Photosynthetic electron transport in higher plants," *Annual Review of Plant Physiology* **35**(1), pp. 659–693, 1984.
- [4] K. Brettel and W. Leibl, "Electron transfer in photosystem I," *Biochimica et Biophysica Acta (BBA)-Bioenergetics* **1507**(1), pp. 100–114, 2001.
- [5] W. S. Chow, A. Melis, and J. M. Anderson, "Adjustments of photosystem stoichiometry in chloroplasts improve the quantum efficiency of photosynthesis," *Proceedings of the National Academy of Sciences* **87**(19), pp. 7502–7506, 1990.
- [6] C. Klughammer and U. Schreiber, "An improved method, using saturating light pulses, for the determination of photosystem I quantum yield via P700+ absorbance changes at 830 nm," *Planta* **192**(2), pp. 261–268, 1994.
- [7] I. Lee, J. W. Lee, and E. Greenbaum, "Biomolecular electronics: vectorial arrays of photosynthetic reaction centers," *Physical Review Letters* **79**(17), p. 3294, 1997.
- [8] R. Das, P. J. Kiley, M. Segal, J. Norville, A. A. Yu, L. Wang, S. A. Trammell, L. E. Reddick, R. Kumar, F. Stellacci, N. Lebedev, J. Schnur, B. D. Bruce, S. Zhang, and M. Baldo, "Integration of photosynthetic protein molecular complexes in solid-state electronic devices," *Nano Letters* **4**(6), pp. 1079–1083, 2004.
- [9] S. A. Trammell, L. Wang, J. M. Zullo, R. Shashidhar, and N. Lebedev, "Orientated binding of photosynthetic reaction centers on gold using Ni-NTA self-assembled monolayers," *Biosensors and Bioelectronics* **19**(12), pp. 1649–1655, 2004.
- [10] S. A. Trammell, A. Spano, R. Price, and N. Lebedev, "Effect of protein orientation on electron transfer between photosynthetic reaction centers and carbon electrodes," *Biosensors and Bioelectronics* **21**(7), pp. 1023–1028, 2006.
- [11] I. Carmeli, L. Frolov, C. Carmeli, and S. Richter, "Photovoltaic activity of photosystem I-based self-assembled monolayer," *Journal of the American Chemical Society* **129**(41), pp. 12352–12353, 2007.
- [12] D. Gerster, J. Reichert, H. Bi, J. V. Barth, S. M. Kaniber, A. W. Holleitner, I. Visoly-Fisher, S. Sergani, and I. Carmeli, "Photocurrent of a single photosynthetic protein," *Nature Nanotechnology* **7**(10), pp. 673–676, 2012.
- [13] P. I. Gordichuk, G.-J. A. H. Wetzelaer, D. Rimmerman, A. Gruszka, J. W. de Vries, M. Saller, D. A. Gautier, S. Catarci, D. Pesce, S. Richter, P. W. M. Blom, and A. Herrmann, "Solid-state biophotovoltaic cells containing photosystem I," *Advanced Materials* **26**(28), pp. 4863–4869, 2014.
- [14] D. Gunther, G. LeBlanc, D. Prasai, J. R. Zhang, D. E. Cliffl, K. I. Bolotin, and G. K. Jennings, "Photosystem I on graphene as a highly transparent, photoactive electrode," *Langmuir* **29**(13), pp. 4177–4180, 2013.
- [15] S. C. Feifel, H. Lokstein, M. Hejazi, A. Zouni, and F. Lisdat, "Unidirectional photocurrent of photosystem I on π -system-modified graphene electrodes: nanobionic approaches for the construction of photobiohybrid systems," *Langmuir* **31**(38), pp. 10590–10598, 2015.
- [16] S. C. Feifel, K. R. Stieger, H. Lokstein, H. Lux, and F. Lisdat, "High photocurrent generation by photosystem I on artificial interfaces composed of π -system-modified graphene," *Journal of Materials Chemistry A* **3**(23), pp. 12188–12196, 2015.
- [17] E. Darby, G. LeBlanc, E. A. Gizzie, K. M. Winter, G. K. Jennings, and D. E. Cliffl, "Photoactive films of photosystem I on transparent reduced graphene oxide electrodes," *Langmuir* **30**(29), pp. 8990–8994, 2014.
- [18] P. Jordan, P. Fromme, H. T. Witt, O. Klukas, W. Saenger, and N. Krauß, "Three-dimensional structure of cyanobacterial photosystem I at 2.5 Å resolution," *Nature* **411**(6840), pp. 909–917, 2001.
- [19] P. Gordichuk, D. Pesce, O. E. Castañeda Ocampo, A. Marozzi, G.-J. A. H. Wetzelaer, A. Paul, M. Loznik,

- E. Gloukhikh, S. Richter, R. C. Chiechi, and A. Herrmann, "Orientation and incorporation of photosystem I in bioelectronics devices enabled by phage display," *Advanced Science* **4**(5), p. 1600393, 2017.
- [20] Y. Cui, S. N. Kim, S. E. Jones, L. L. Wissler, R. R. Naik, and M. C. McAlpine, "Chemical functionalization of graphene enabled by phage displayed peptides," *Nano Letters* **10**(11), pp. 4559–4565, 2010.
- [21] S. N. Kim, Z. Kuang, J. M. Slocik, S. E. Jones, Y. Cui, B. L. Farmer, M. C. McAlpine, and R. R. Naik, "Preferential binding of peptides to graphene edges and planes," *Journal of the American Chemical Society* **133**(37), pp. 14480–14483, 2011.
- [22] E. Kaiser and F. Kezdy, "Amphiphilic secondary structure: design of peptide hormones," *Science* **223**(4633), pp. 249–255, 1984.
- [23] Y. Venkatachalapathi, M. C. Phillips, R. M. Epanand, R. F. Epanand, E. M. Tytler, J. P. Segrest, and G. Anantharamaiah, "Effect of end group blockage on the properties of a class A amphipathic helical peptide," *Proteins: Structure, Function, and Bioinformatics* **15**(4), pp. 349–359, 1993.
- [24] M. D. Fletcher and M. M. Campbell, "Partially modified retro-inverso peptides: development, synthesis, and conformational behavior," *Chemical Reviews* **98**(2), pp. 763–796, 1998.
- [25] O. E. Castañeda Ocampo, P. Gordiichuk, S. Catarci, D. A. Gautier, A. Herrmann, and R. C. Chiechi, "Mechanism of orientation-dependent asymmetric charge transport in tunneling junctions comprising photosystem I," *Journal of the American Chemical Society* **137**(26), pp. 8419–8427, 2015.
- [26] C. Krzeminski, C. Delerue, G. Allan, D. Vuillaume, and R. Metzger, "Theory of electrical rectification in a molecular monolayer," *Physical Review B* **64**(8), p. 085405, 2001.
- [27] J. Pan, Z. Zhang, K. Ding, X. Deng, and C. Guo, "Current rectification induced by asymmetrical electrode materials in a molecular device," *Applied Physics Letters* **98**(9), p. 092102, 2011.
- [28] S. Sherif, G. Rubio-Bollinger, E. Pinilla-Cienfuegos, E. Coronado, J. C. Cuevas, and N. Agrait, "Current rectification in a single molecule diode: the role of electrode coupling," *Nanotechnology* **26**(29), p. 291001, 2015.
- [29] I. Díez-Pérez, J. Hihath, Y. Lee, L. Yu, L. Adamska, M. A. Kozhushner, I. I. Oleynik, and N. Tao, "Rectification and stability of a single molecular diode with controlled orientation," *Nature Chemistry* **1**(8), p. 635, 2009.
- [30] P. Kornilovitch, A. Bratkovsky, and R. S. Williams, "Current rectification by molecules with asymmetric tunneling barriers," *Physical Review B* **66**(16), p. 165436, 2002.

Closing remark – Spinchiraltronics

T*his thesis began with two fundamental questions concerning the theoretical and experimental development of chirality-induced spin selectivity (CISS). After approaching these questions from a solid-state spintronics point of view, here we conclude the thesis by answering them. With this, we illustrate a systematic approach to further study CISS, and envision a future where additional controls and functionalities are enabled by bridging chirality and spin in electronic devices.*

8.1 Conclusion

A brief recap

We first briefly review the main conclusions of each chapter.

In Chapter 2, we learned that the concepts of chirality and spin are related to the fundamental symmetries of space and time. From this symmetry perspective, we discussed how the observations of CISS differ from other physical phenomena related to chirality or spin, such as electron helicity dichroism, the electrical magnetochiral effect, or the Edelstein effect.

In Chapter 3, we revealed that the commonly used two-terminal electronic devices are fundamentally unable to detect CISS in the linear response regime. Here we particularly emphasized the distinctions between the electrical detection of CISS in electronic devices and the generation of CISS within chiral materials. We also highlighted differences between experiments within the linear response regime and those in the nonlinear regime.

In Chapter 4, we pointed out that energy-dependent electron transport combined with energy relaxation can enable the two-terminal electrical detection of CISS. Using examples of tunneling and thermally activated molecular resonant transmission, we underlined key ingredients that determine the sign of typical two-terminal electrical signals.

In Chapter 5, we addressed another type of electronic device that contained an optically responsive chiral component. We quantitatively analyzed how electrical signals in this type of devices can be translated to spin-related information.

In Chapter 6, we built electronic devices using a chiral van der Waals solid-state material, Tellurene. We highlighted electron transport properties that are related to its strong anisotropy and low crystal symmetry.

In Chapter 7, we characterized the electron transport through a biomolecular junction comprising a chiral photosynthetic protein complex, photosystem I. We demonstrated techniques that can significantly modify the electronic properties of this junction.

Answering the questions

Now we look at the two questions this thesis set out to answer (Section 1.4).

1. How does chirality interact with spin on a microscopic level?

This question concerns the mechanism of generating a spin imbalance by electron transmission through a chiral system. Although obtaining such a microscopic pic-

ture was not our goal, we are nevertheless able to provide insights based on the knowledge obtained through this thesis.

(a) What are the fundamental restrictions?

Due to the Kramers degeneracy of transmission eigenfunctions (Chapter 2), it is fundamentally forbidden for a chiral system to exhibit spin-selective electron transmission, unless there exists a nonunitary mechanism within the chiral system (Chapter 3 and 4).

(b) Can we confirm the spin-orbit origin?

In most of our theoretical analyses, we have indeed assumed CISS to be a spin-orbit effect that is present in the linear response regime (Chapter 3 and 4). However, the experimental situation for this is still unclear (note that this does not affect the conclusions of Chapter 3 and 4). It is therefore important that future experiments directly address CISS in the linear response regime to obtain a clearer picture.

(c) Can we distinguish CISS from other spin-charge conversion mechanisms?

Based on current descriptions, there are key differences between CISS (if present in the linear response regime) and other spin-charge conversion mechanisms that are relevant to spintronics. First, compared with magnetism, CISS does not break time reversal symmetry (Chapter 2). Second, compared with spin-orbit effects such as spin Hall effect and Rashba-Edelstein effect, CISS produces a collinear alignment between spin and charge currents (Chapter 2-4).

2. How does this interaction generate signals observed in various types of experiments?

This question concerns the experimental detection of CISS. It was thoroughly discussed in this thesis with a focus on electron transport experiments.

(a) What are the requirements for experimental geometries?

In Chapter 3 and 4 we discussed that the typical two-terminal spin-valve type of electronic devices can only detect CISS in the nonlinear regime. In order to detect CISS in the linear response regime, one has to use either a multi-terminal geometry (Chapter 3 and 5), or a two-terminal geometry that does not rely on magnetization reversal for generating charge signals (Chapter 4).

(b) Can the magnetic-field- or magnetization-dependent signals be interpreted as due to electronic spin?

For an ideal spin-valve type of device (Chapter 3 and 4), the observed magnetoresistance (MR) in the nonlinear regime is indeed related to the spin-charge conversion by CISS. If this conversion mechanism had not existed, the MR signals would have vanished. However, the value of the MR ratio cannot be directly translated to the spin polarization generated by CISS. The MR is co-determined by other factors such as the spin polarization of the ferromagnet.

In realistic situations, the presence of a magnetic field or an incomplete magnetization reversal could change the picture. For example, in Chapter 5 we discussed a possible charge contribution to the observed spintronic signals.

(c) How to better characterize CISS using (other) spintronic experiments?

A pressing issue regarding CISS experiments is the insufficient direct observation in the linear response regime. This needs to be addressed using new types of experimental geometries. For example, the multi-terminal geometries introduced in Chapter 3, or the Hanle precession or chiral spin valve geometry introduced in Chapter 4. At the same time, it is also important to repeat existing experimental methods (e.g. magnetic conducting atomic force microscopy or two-terminal spin valve device) with a broader range of chiral molecules, and to correlate the quantitative observations to various material properties (e.g. HOMO-LUMO gap or specific optical rotation).

8.2 Further questions

As mentioned in Chapter 1, CISS is a growing field with a growing amount of questions. The more of which we try to answer, the more new ones arise. Here we name a few questions that future researches should address.

First of all, how to consistently describe CISS in photoemission and transport experiments? Can we find an experimental observable that is suited for both the single-electron and the thermodynamical pictures? If so, how does this observable depend on temperature and electron energy?

Next, how to consistently describe CISS in different chiral materials? Is it possible to define a material property that on one hand describes CISS, and on the other hand directly relates to other characteristic chiral properties, such as the specific optical rotation? If so, how would this property then depend on temperature and electron energy, and how can it be deduced from the molecular (crystal) structure of the material?

Further, what is the dynamics of CISS? Can we investigate CISS using time-resolved experiments, such as ultrafast optics? Correspondingly, can we obtain a frequency-domain spectrum of CISS? If so, how would it differ from the chiral optical rotation and circular dichroism spectra of the same chiral material?

Moreover, does CISS have a role in nature? Would it be possible that the biological homochirality has given electronic spin an essential role in natural processes, such as photosynthesis? Or conversely, could CISS have helped the formation of homochirality itself?

Last but not the least, how can we use CISS to better control electronic spin in electronic devices? Can we combine chirality with other electrical, thermal, or opti-

cal effects to improve the properties of spintronic devices? Can we gain even more control by tuning chirality itself?

8.3 Outlook – Spinchiraltronics

We now envision a future where chirality is deeply connected with spin in electronic devices for information technologies. This is of particular importance thanks to the abundance of chiral materials.

As mentioned in Chapter 1 and 7, nearly all naturally occurring biological molecules (or molecular complexes) are chiral and exist only in one enantiomeric form. Surveying this rich library could reveal a large pool of easily accessible functional materials with electronic properties that are suitable for device-based applications.

Also, there are solid-state materials that are chiral and have novel electronic properties, such as the Tellurene introduced in Chapter 6. These materials can be processed with existing nano-fabrication technologies and can be readily incorporated in complex nano-electronic and spintronic devices.

Another source of chirality is related to the increasingly popular van der Waals materials, which can be stacked to form heterostructures to enrich their functional properties. For them, twisted heterostructure-stacking introduces chirality, and the chiral stack can be further processed for device fabrication. The chirality introduced in this way can be tuned by controlling the twisting angle and the layered materials that are involved, which opens up a new degree of freedom for designing novel spintronic devices.

We should not forget that chirality itself also has a binary nature, which can be used to encode and decode digital information. In Chapter 4 we envisioned a chiral spin valve that makes use of optical molecular switches, which can change chirality under light illumination. Integrating this class of molecular materials into solid-state spintronic devices would not only enable the control of the binary state of chirality, but also evoke on-demand tuning of all chirality-induced spintronic phenomena. This paves way for a whole new area of spintronics where chirality is put into action on a fundamental level – an area that can be called spinchiraltronics.

Summary

The concepts of chirality and spin are constantly encountered in our everyday life, and at the same time, they are related to the most fundamental aspects of nature. Chirality is the geometrical property of a stationary object that makes it distinguishable from its own mirror image. A pair of chiral enantiomers is analogous to a pair of hands — they are mirror images of each other but cannot be made to exactly overlap — and they are often referred to using the corresponding handedness. Spin is a quantum mechanical concept that relates to the magnetic property of electrons. It can be envisioned as the rotational motion of an electron around its own axis, and the orientation of this axis can be controlled magnetically.

Chiral molecules are the foundation of life. Nearly all naturally occurring and biologically active molecules are chiral and exist in only one enantiomeric form. For example, the DNA double helix that encodes genetic information for all living organisms are uniformly right-handed, all the natural sugars are also right-handed, and 19 out of the 20 natural amino acids are left-handed (the other one is not chiral). Electronic spin is the origin of ferromagnetism, which has enabled a broad range of applications from compass needles to computer hard drives. Today, as the conventional silicon-based electronics technologies are approaching fundamental limits, scientists are looking into new alternatives that use the electronic spin not only to store digital information, but also to process it — a field known as spintronics.

On a fundamental level, chirality and spin both manifest nature's most elementary symmetries, or rather, the lack thereof. Chirality relates to the broken symmetry of space, as it makes it possible to distinguish between left and right (handednesses), while spin relates to the broken symmetry of time, since it allows to differentiate between opposite directions of motion (clockwise vs. counterclockwise rotations). Opposite chiral enantiomers are interconverted by space-inversion, while opposite spin orientations are interconverted by time-reversal.

The significance of chirality and spin have long been recognized, but in separate

fields and mostly for unrelated applications. This has been changed by the discovery of the chirality-induced spin selectivity (CISS) effect. It describes that, as electrons pass through a chiral (helical) structure (molecule), a spin polarization (imbalance between opposite spin orientations) arises. If the chiral molecule is replaced by its opposite enantiomer, the preferred spin orientation also reverses. CISS has attracted increasing research attention thanks to its direct relevance to fundamental symmetries of nature and applications in fields across physics, chemistry, and biology. However, 20 years after its discovery, the microscopic origin of CISS remains a mystery, and detailed understanding of key experimental results is still lacking.

There are various types of experiments designed to demonstrate CISS, and many of them involve the thermodynamic transport of electrons. These experiments usually make use of micrometer- or even nanometer-scale electronic devices comprising a chiral (molecular) component, electrical contacts, and often a ferromagnet (FM) to control or detect the spins. By driving a charge current through such devices and measuring the subsequent voltage drop, one obtains the resistance for electron transport. This resistance is often reported to change when the magnetization direction of the FM is flipped, generating a magnetoresistance (MR) signal.

The MR signal is characteristic for spintronic devices since it reveals information about coupled charge and spin transport, and it is key to the understanding of experimental results related to CISS. The first part of this thesis focuses on this MR signal in spintronic devices used in CISS experiments, and explains theoretically when and how the MR can arise, and what it can tell us about the CISS effect.

Understanding the signal

Although the microscopic mechanism of CISS remains largely unclear, we can nevertheless turn to fundamental laws that govern electron transport for insights into the MR signal. In particular, we look at the Onsager reciprocity, which describes symmetry relations between coupled thermodynamic processes. In an electronic/spintronic device, when the roles of voltage and current probes are interchanged, and at the same time all magnetic fields and magnetizations are reversed, the Onsager reciprocity requires that the measured resistance must remain the same in the linear response regime (at sufficiently low bias). This robust fundamental symmetry requirement directly implies that in electronic devices that are usually used for CISS experiments, where a single FM and chiral component are connected in series between two electrodes (two-terminal, 2T), the MR signal must remain zero in the linear response regime.

Starting from this, we introduce an electron-transmission model to describe chiral molecules in electronic devices as generic circuit components where electrons can either transmit through or be reflected back. CISS then implies that the elec-

tron transmission probabilities must be spin-dependent. This generic and conceptual description, when combined with Onsager reciprocity and time-reversal symmetry, immediately reveals that there must be certain dephasing mechanisms for the transmitted electrons, and there must be a spin-flip process for electrons reflected off the chiral component. This understanding allows us to use elementary spin-space electron transmission and reflection matrices to describe a chiral component, and to analyze signals generated by it when placed into an electronic device together with other (possibly magnetic) components. This also provides a framework for analyzing whether CISS can generate signals in more complex electronic devices (e.g. with multiple FMs or chiral components, or with more than two electrodes), and if so, how such signals depend on the spin-polarizing strength of the chiral component.

Next, we extend this rather microscopic picture of electron transmission and reflection to a more macroscopic one of thermodynamic driving forces and responses. Here the driving forces are charge and spin electrochemical potential differences, and the responses are charge and spin currents. With this, the descriptions of a chiral (nonmagnetic) component and an (achiral) magnetic components can be unified using a transport matrix formalism, where the former is described by a symmetric transport matrix, and the latter by an asymmetric one. The symmetry of these transport matrices is directly imposed by Onsager reciprocity. This description reveals in detail why the MR signal cannot arise in 2T devices with one chiral component and one FM in the linear response regime. It is a result of the exact compensation of two simultaneous processes: first, spin injection by the chiral component and spin detection by the FM, and second, spin injection by the FM and spin detection by the chiral component. This result then suggests a way to induce the desired MR signal — by breaking the symmetry between these two processes in the nonlinear regime, which can happen when the transport is energy-dependent and is subject to energy relaxation. We demonstrate the emergence of MR due to this mechanism using examples of energy-dependent quantum tunneling and energy-dependent resonant transmission through molecular orbitals, and we indeed can largely reproduce experimentally observed current-voltage characteristics. Furthermore, this understanding of nonlinear MR enables us to identify key factors that codetermine the sign of the MR signal, which include bias direction, charge carrier type, and the chirality.

Based on this understanding of spintronic signals in electronic devices that contain chiral components, we propose new device geometries that can better separate CISS-related signals from other (mostly charge) signals, and can do so even in the linear response regime. These include multiterminal nonlocal geometries where charge and spin signals are spatially separated, and novel magnet-free 2T geometries that uses solely chiral components for spin injection and detection. This therefore provides operation principles and design guidelines for future CISS experiments using electronic devices.

To obtain a more quantitative understanding, we introduce a circuit model approach that uses elementary circuit analysis to relate experimentally observed charge signals to possible spin-dependent processes within an electronic device. To illustrate this approach, we analyze an experimental geometry that was earlier used to demonstrate CISS in a bio-organic photosynthetic protein complex, photosystem I (PSI). Our results conclude that the signals observed in that experiment cannot be interpreted as fully due to the CISS effect that causes spin-polarized photo-excitations inside PSI complexes.

Experimental explorations

The second part of this thesis shows results of two distinct experiments where we incorporate chiral materials into electronic devices. The first experiment uses a chiral solid-state van-der-Waals (vdW) semiconductor, tellurene. It is a thin-flake single crystal, and each flake consists of parallel-aligned, vdW-bound one-dimensional helical chains of tellurium atoms. With this material, we fabricate mesoscopic electronic devices using nano-fabrication technologies, and we measure the anisotropic electron transport properties of this material using a lock-in technique that can separately address linear and nonlinear responses. We observe a strong in-plane anisotropy for the linear electrical conduction in this material, and we identify a signature that may relate to the chirality of the material. At the same time, we also observe an anisotropic temperature dependence of this linear conductance and a nonreciprocal electrical conduction (exhibited as second-order response), which is linked to the lack of inversion symmetry of the chiral tellurene material. These results provide insight into the electron transport within this material, and help with the design and understanding of more complex electronic/spintronic device geometries involving tellurene.

In the second experiment, we develop a technique that uses an engineered chain of amino acids (peptides) to immobilize the chiral bio-organic photosynthetic protein complex PSI onto a single layer of carbon atoms (graphene). We electrically contact the PSI units with a few-nanometer-scale conductive probe, and drive electron transport through the PSI-peptide-graphene junction. We use a random-positioning approach to statistically analyze results obtained on a large number of PSI units, and discover that the introduction of peptide significantly enhances the electrical conduction through the junction, and at the same time introduces a rectified (asymmetric) current-voltage profile. This conduction and rectification can further be tuned mechanically by applying a force on PSI using the conductive probe. These results shed light on possibilities of using complex bio-organic materials for electronic applications.

All in all, this thesis combines theoretical and experimental work to gain new understanding of the rich physics introduced by chirality and spin in electronic devices. The results presented here pave the way for future developments that employ these two elementary concepts for electronic/spintronic applications.

Samenvatting

In ons dagelijks leven worden we voortdurend geconfronteerd met de concepten chiraliteit en spin, tegelijkertijd zijn zij verwant aan de fundamenteelste aspecten der natuur. Chiraliteit is de geometrische eigenschap van een vast object die het te onderscheiden maakt van zijn spiegelbeeld. Een paar chirale enantiomeren is te vergelijken met een paar handen – zij zijn elkaars spiegelbeeld, maar kunnen niet zo worden gevormd dat zij exact overlappen – en vaak wordt naar hen verwezen als links- of rechtshandig. Spin is een kwantummechanisch concept dat betrekking heeft op de magnetische eigenschappen van een elektron. Het kan worden gezien als de roterende beweging van een elektron om zijn eigen as waarbij de richting van de as magnetische kan worden bepaald.

Chirale moleculen zijn de fundamenteen van het leven. Bijna alle natuurlijk voorkomende en biologisch actieve moleculen zijn chiraal en bestaan alleen maar in één enantiomerische vorm. De DNA dubbele helix waarin voor alle levende organismen de genetische informatie in gecodeerd is, is rechtshandig, ook alle natuurlijke suikers zijn rechtshandig en 19 van de 20 natuurlijke aminozuren zijn linkshandig (de overige is niet chiraal). Elektron spin is de oorsprong van ferromagnetisme, dat een brede reeks aan toepassingen, van kompas naalden tot harde schijven van een computer, vindt. Hedentendage, terwijl de traditionele, op silicium gebaseerde elektronica technologie haar fundamentele grenzen nadert, onderzoeken wetenschappers nieuwe alternatieven die de elektron spin niet louter voor het opslaan van digitale informatie benutten, maar ook voor het verwerken ervan – een discipline beter bekend als spintronica.

Fundamenteel gezien manifesteren zowel chiraliteit als spin de elementairste symmetrieën der natuur, of beter gezegd, het gebrek eraan. Chiraliteit toont de symmetriebreking van ruimte, daar het mogelijk maakt te onderscheiden tussen links- en rechts(handigheid). Onderwijl toont spin de symmetriebreking van tijd, aangezien deze het mogelijk maakt het verschil tussen tegenovergestelde bewegingsrichtingen

(met-de-klok-mee ten opzichte van tegen-de-klok-in) te onderscheiden. De tegenovergestelde chirale enantiomeren zijn onderling converteerbaar door middel van ruimte-inversie, terwijl tegenovergestelde spin oriëntaties converteerbaar zijn door middel van tijd-omkering.

Niettemin is voor geruime tijd het belang van chiraliteit en spin voornamelijk alleen in andere disciplines en niet verwante toepassingen bekend. Dit veranderde na de vondst van het 'chirality-induced spin selectivity' (CISS) effect. Dit beschrijft dat wanneer een elektron zich door een chirale (helische) structuur (molecuul) beweegt er een spin polarisatie (een onevenwichtigheid tussen de beide spin oriëntaties) ontstaat. Wanneer het chirale molecuul wordt vervangen door zijn tegenovergestelde enantiomeer, draait ook de verkozen spin oriëntatie om. CISS wekt groter wordende wetenschappelijke belangstelling, wat te danken is aan haar directe relevantie voor fundamentele symmetrieën der natuur en toepassingen in disciplines verspreid over natuurkunde, scheikunde en biologie. Echter, 20 jaar na haar ontdekking blijft de microscopische oorsprong een raadsel en een diepgaand begrip van de voornaamste experimentele resultaten ontbreekt nog steeds.

Verschillende type experimenten zijn ontworpen om CISS te demonstreren, velen dezes hebben betrekking tot thermodynamisch transport van elektronen. Deze experimenten maken meestal gebruik van micrometer- of zelfs nanometerschaal elektronische schakelingen om een chiraal moleculaire component, elektrische contacten en vaak een ferromagneet (FM), om controle te krijgen over de spin of om hem te detecteren, te compromitteren. Door een ladingsstroom door zo'n schakeling te sturen en vervolgens het potentiaal verschil te meten kan de weerstand voor elektrontransport verkregen worden. Voor deze weerstand wordt vaak gevonden te veranderen wanneer de magnetisatie oriëntatie wordt omgekeerd, een magnetoweerstand (MW) signaal genererend.

De MW is kenmerkend voor een spintronische schakeling, omdat het informatie over de koppeling tussen lading- en spintransport blootstelt, en het is de sleutel tot het begrijpen van de resultaten uit CISS experimenten. Het eerste deel van dit proefschrift focust zich op dit MW signaal in spintronische schakelingen in deze experimenten en verklaart theoretisch wanneer en hoe de MW kan ontstaan en wat het ons kan vertellen over het CISS effect.

Begrip van het signaal

Ofschoon het microscopische mechanisme achter CISS grotendeels onduidelijk blijft, kunnen we desalniettemin kijken naar de fundamentele wetten in elektrontransport om inzicht te verkrijgen in het MW signaal. In het bijzonder wordt de Onsager reciprociteit beschouwd, waarin de symmetrieën tussen gekoppelde thermodynamische processen worden beschreven. In een elektronische/spintronische schakeling,

waarbij de rollen van spanning en stroom sondes worden uitgewisseld en waarbij tegelijkertijd alle magnetische velden en magnetisaties worden omgekeerd, verlangt de Onsager reciprociteit dat de gemeten weerstand ten alle tijden gelijk blijft in het lineaire response stelsel (bij spanning die gering genoeg is). Dit sterke fundamentele symmetrie vereiste dicteert dat in de elektronische schakelingen gewoonlijk benut voor CISS experimenten, waarin een enkele FM en een chiraal component in serie zijn verbonden tussen twee elektroden (tweepuntsmeting, 2T), het MW signaal nul moet blijven in het lineaire response stelsel.

Met dit als beginpunt introduceren we een elektron transmissiemodel om chirale moleculen in elektronische schakeling te beschrijven als generieke componenten waar elektronen ofwel doorgezonden kunnen worden, ofwel teruggekaatst kunnen worden. De CISS sluit dan in dat de elektron transmissiewaarschijnlijkheden spin afhankelijk betamen te zijn. Deze generieke en conceptuele beschrijving, wanneer het wordt samengenomen met de Onsager reciprociteit en tijdsomkeringsymmetrie, verraad meteen dat er een zekere defaseringsmechanisme moet bestaan voor de doorgezonden elektronen. Hierbij dient er zich een spin-flip voor te doen voor de van de chirale component weerkaatste elektronen. Dit begrip geeft ons de mogelijkheid om elementaire spin-ruimte elektrontransmissie en reflectie matrixen aan te wenden om een chiraal component te beschrijven en de daardoor gegenereerde signalen te analyseren wanneer het op een elektronische schakeling is geplaatst samen met een andere (mogelijk magnetisch) component. Dit verschaft ons het raamwerk om te kunnen analyseren of CISS signalen kan opwekken in complexere elektronische schakelingen (zoals meerdere FM'en of chirale componenten of meer dan twee elektrodes) en indien mogelijk hoe zulke signalen afhangen van de sterkte van de spinpolarisatie van het chirale component.

Vervolgens breiden we de nogal microscopische voorstelling van elektron transmissie en reflectie uit tot een macroscopischer geheel met thermodynamische drijfkrachten en responsen. De drijvende krachten zijn hierbij de lading en spin elektrochemische potentiaal verschillen en de responsen zijn de ladings- en spinstromen. Met gebruikmaking hiervan kunnen de beschrijving van een chiraal (niet magnetische) component en een (achiraal) magnetische component worden samengevoegd in een transport matrix vorm, waarbij het eerst genoemde is beschreven door een symmetrische transport matrix en het laatst genoemde door een asymmetrische. De symmetrie van deze transport matrixen is opgelegd door de Onsager reciprociteit. Deze beschrijving toont in detail waarom het MW signaal niet kan ontstaan in een 2T schakeling met één chiraal component en één FM in het lineaire response stelsel. Het is een resultaat van de exacte tegenwicht van twee gelijktijdige processen: als eerste, spininjectie door het chirale component en spindetectie door de FM, en als tweede, spininjectie door de FM en spindetectie door het chirale component. Dit resultaat stelt voor een manier om het gewenste MW signaal te induceren – door het breken

van de symmetrie tussen deze twee processen in het non-lineaire stelsel, wat gedaan kan worden wanneer het transport energie afhankelijk is en is onderworpen aan energierelaxatie. Wij tonen de verschijning van de MW aan door dit mechanisme gebruikmakend van energieafhankelijk kwantumtunnelen en energieafhankelijke resonante transmissie door moleculaire orbitalen en we kunnen daadwerkelijk grotendeels de experimenteel geobserveerde stroom-spanning karakteristieken reproduceren. Bovendien staat dit begrip van de non-lineaire MW ons toe om de knelpuntfactoren die mede het teken van het MW signaal (de richting van de stroom in beschouwing nemend), de ladingsdrager en chiraliteit bepalen, te kunnen identificeren.

Op basis van dit begrip van spintronische signalen in elektronische schakelingen die chirale componenten bevatten, stellen we nieuwe schakelingsgeometrieën voor die signalen door CISS beter kunnen onderscheiden van andere (meestal ladings) signalen, zelfs tot in het lineaire response stelsel. Zij omvatten meerpuntse niet-lokale geometrieën waarbij ladings- en spinsignalen fysiek gescheiden zijn en nieuwe magneetvrije 2T-geometrieën die uitsluitend chirale componenten gebruiken voor spininjectie en detectie. Dit verschaft basisprincipes en ontwerprichtlijnen voor toekomstige CISS-experimenten met elektronische schakelingen.

Om meer kwantitatief inzicht te krijgen, introduceren we een benadering met een circuitmodel dat elementaire circuitanalyse gebruikt om de experimenteel waargenomen ladingssignalen te linken aan mogelijke spinafhankelijke processen binnen een elektronisch schakeling. Om deze benadering te illustreren, analyseren we een experimentele geometrie die eerder werd gebruikt om CISS te demonstreren in een bio-organisch fotosynthetisch eiwitcomplex, fotosysteem I (PSI). Uit onze resultaten concluderen wij dat de signalen die in dat experiment zijn waargenomen niet volledig door het CISS-effect dat spin-gepolariseerde foto-excitaties in PSI-complexen veroorzaakt, kunnen worden verklaard.

Experimentele onderzoek

Het tweede deel van dit proefschrift toont de resultaten van twee verschillende experimenten waarbij we chirale materialen in elektronische schakeling integreren.

Het eerste experiment maakt gebruik van een chirale van-der-Waals (vdW) halfgeleider, tellurene. Dat is een monokristallijne structuur waarbij elke laag bestaat uit parallel uitgelijnde, vdW-gebonden eendimensionale spiraalvormige ketens van telluriumatomen. Met dit materiaal fabriceren we mesoscopische elektronische schakelingen gebruikmakend van nanofabricage technologieën en wij meten de anisotrope elektrontransporteigenschappen van dit materiaal met behulp van de lock-in techniek die afzonderlijk lineaire en niet-lineaire reacties kan aanspreken. We zien een sterke anisotropie in-het-vlak voor de lineaire elektrische geleiding in dit materi-

aal en we onderscheiden een eigenschap die mogelijk verband kan houden met de chiraliteit van het materiaal. Tegelijkertijd zien we ook een anisotrope temperatuurafhankelijkheid in de lineaire geleiding en een niet reciproke elektrische geleiding (zich manifesterend als tweede-orde respons), die verband houdt met het gebrek aan inversiesymmetrie in het chirale tellurene. Deze resultaten geven begrip van het elektronentransport in dit materiaal en dragen bij aan het ontwerpen en bevatten van complexere elektronische/spintronische schakelingsgeometrieën waarbij tellurene gebruikt wordt.

In het tweede experiment ontwikkelen we een techniek die een ontworpen keten van aminozuren (peptiden) gebruikt om het chirale bio-organische fotosynthetische eiwitcomplex PSI te fixeren op een enkele laag koolstofatomen (grafeen). We maken elektrisch contact met de PSI-laag via een geleidende sonde van enkele nanometers en zenden de elektronen door de PSI-peptide-grafeen verbinding. Hier exploiteren we een methode van willekeurige positionering om de resultaten die op een groot aantal verschillende PSI-lagen zijn verkregen statistisch te analyseren. We ontdekken dat het introduceren van de peptide de elektrische geleiding door de PSI-peptide-grafeen verbinding aanzienlijk verbetert en tegelijkertijd een gelijkgerichte (asymmetrische) stroom-spanning curve toont. Deze geleiding en rectificatie kan verder mechanisch worden afgestemd door een kracht op PSI uit te oefenen met behulp van de geleidende sonde. Deze resultaten werpen het licht op de mogelijkheden om complexe bio-organische materialen te gebruiken voor elektronische toepassingen.

Samenvattend, dit proefschrift combineert theoretisch en experimenteel werk om nieuw inzicht te bekomen in de rijke natuurkunde ingewijd door chirale en spin in elektronische schakelingen. De resultaten die hier worden gepresenteerd leiden de weg naar toekomstige ontwikkelingen die deze twee elementaire concepten benutten voor elektronische/spintronische toepassingen.

Acknowledgements

Finally, we are here, ending this rather technical thesis with a little emotional touch. I'm not sure which one is more difficult to write though, a hundred-page book about molecules and electrons, or a few-line story about you — who helped me immensely along this PhD journey.

Caspar, thank you for everything, really. All this would not have started without you. It was in April 2013 when I first met you, when you grilled me with quantum physics questions during my topmaster interview. Looking back, I was probably at my scientific worst, struggling to draw lines between the unfamiliar words entering my ears and the vague concepts in my brain. Yet, you gave me a chance to improve, and you later did so repeatedly by supervising my master's thesis and providing me with an intriguing PhD topic to explore. You encouraged and trusted me to teach and supervise students, to reach out and seek collaborations, to attend conferences and present research, and to learn about languages and culture. When confused, I would always turn to you and you would always give me a direction. I can't imagine what my PhD trajectory would have been like without your guidance, and I am so proud of and so grateful for what we have accomplished.

Bart, thank you so much for making my PhD such a complete and joyful learning experience. You taught me with your own daily action what scientific excellence truly is: it's not only about always producing highest-quality research, but also about standing firmly against any scientific misconduct, advising scientific policies for the benefit of society, teaching and motivating young scientists, and leading and managing a diverse research group. This is probably the most valuable lesson a young scientist like me could ever wish to learn, and I truly appreciate and admire you for that. Besides, I'm also extremely grateful for all our enlightening discussions, for the endless ideas you had on my PhD project, for the opportunities you gave me to speak at great conferences on your behalf, and, of course, for all the nice beers (particularly in quantity) and chit-chats we enjoyed.

I give my sincere acknowledgements to the members of my assessment committee for taking the time and effort to evaluate my thesis. Dear **Ben**, it is a great honour to have you both in my assessment committee and as a collaborator. Thank you for all the inspiring and motivating discussions we had, they have always been fruitful and valuable to me. **Yamamoto sensei**, thank you for being such a warm and welcoming host in Okazaki. I had a wonderful time visiting your group, and truly enjoyed the insightful discussions with you and your team. **Herre**, it was a great pleasure meeting you in Leiden. I was very enlightened by your experimental approach towards CISS, and I hope to see your exciting results soon.

My thesis would not have been completed without these collaborators: **Peide Ye, Bart Kooi, Andreas Herrmann, Jamo, Mark, Pavlo, and Andreas K.** Thank you all for the timely help and great collaboration experience. Pavlo, thank you so much for showing me around Chicago, and I wish you great success in your career. AK, thank you for being so well-organized and so decisive. I learned a lot from you.

The knowledge I learned during a recent trip to Japan greatly helped improve this thesis, and I would also like to thank the people who made this trip so unforgettable. **Gerrit**, conversations with you have always been enlightening and enjoyable. Thanks for all the detailed discussions we had both in Sendai and in many other locations, both on science and on other interesting matters. **Saitoh sensei**, it was highly inspiring to discuss with you, and thank you for kindly guiding me around University of Tokyo and around your labs. **Iwasa sensei**, thank you for being a great host and for showing me your exciting library of materials. I am also thankful for all the intriguing questions and discussions with **Otani sensei, Yaroslav, Oiwa sensei, Suda san, Hirobe san, and Weichao**. Last but not least, **Koichi**, it was such a fun time attending your PhD graduation party. Thank you for the wonderful night-out. Of course, also thank you for showing me in and around Sendai. Now you've become Oyanagi sensei, I wish you great success with your future career in Morioka.

This thesis would not have been the same without the help from many others at the Zernike Institute for Advanced Materials. **Marcos**, thank you both for the sharp scientific input and valuable career advices. Your PhD defence was one of the first that I attended, and now at the time I'm finishing mine, you are back in Groningen to start your own group. I'm always touched and motivated by your enthusiasm for science, and I'm sure you will have great success. **Justin**, I always enjoyed our interactions, and I learned so much when teaching solid-state physics with you, thank you immensely for that. **Tamalika**, thank you for maintaining a friendly touch both inside and outside workspace. **Meike**, thank you for the great discussions we had, and for always being there when my students need a second examiner. **Miki**, thank you for helping me with evaporating molecules and handling the AFM systems. **Ryan**, it was a great time doing my small research project in your group playing with EGaIn, thank you for the opportunity. I would also like to thank **Chao, Parisa,**

Olga, Ali, Theodosis, Nico, Brian, Minpeng, Fan, Xiaotian, Evgeniia, Machteld, Aisha, Maria, Arunesh, Saurabh for the always timely and friendly support and interactions. Also a big thanks to the students I supervised, **Evelien, Mikhail, Elias, Floris, Frits, Luna, and Ocid**, your effort is greatly appreciated.

Next, dear QD team, thank you for all the support and company over the past years. **Tom**, you were the first student I supervised, and somehow you tolerated that experience and still decided to join the team and became a great colleague and friend. Thank you for being around with a bright smile all these years, and good luck with finishing your thesis. **Olger**, you were such a great supervisor and motivated me so much during my master's research, and I'm still thankful for that experience. **Jakko, Sander, and Gerjan**, you left the QD team a great legacy: a frank, cheerful, and supportive vibe, and I can't thank you enough for that. **Joop and Freddie**, great job bringing brotherhood into QD (FND), and wish you all the best with your PhD.

Then there is the great FND. Firstly, a big thanks to my officemates for bearing with me for such a long time. **Ludo**, it was both delightful and enlightening to share office with you. I've always admired your perfect work-life balance, highly efficient working style, and enthusiasm for communicating science to public. **Kumar**, you were a great officemate, always suited up and always willing to offer help. **Anouk**, it always impresses me how you manage to keep up with going to the gym, playing tennis, and at the same time being so hard-working. **Eswara**, thanks for recently joining the office and wish you all the best.

Many years at FND means many years of greatest memories. **Jorge**, you were a wonderful host in Madrid, and those cocktails you made were awesome. I enjoyed your humour so much, although I'm not sure that's a good thing. Oh, also thank you for dedicatedly making tongue twisters with my name. **Talieh**, we've shared so many great memories, those experiments in the lab, those gossips over lunch, those Swiss mountain hikes. Thanks for being there. **Julian**, you too were always around. You are such a wonderful man that takes my jokes well. Thank you for all the joy you brought along. **Obed**, you are such a cheerful person that always arrives with a big smile and some vibrant music, and that heaven-level picanha. Thanks for all the unforgettable moments. **Frank**, you somehow always carry energy and motivation with you. It's always been fun when you are around, both at work and during beers and pizzas. Thanks a lot. **Pep**, I can't overstate how much I missed our lunches with you, and your adiabatically evolving orange. **Christian**, thanks for the dinners at your place and the balcony drinks at mine. Hope Bavaria has been treating you well. I still owe you a visit. **Alexey**, thank you for being so sharp on both scientific and technical issues, and for having the coldest humour that is sometimes so infectious. **Jantje, Antonio, Sid, Mallik, Roald, Tian, and Crystal**, it was always great to chat with you guys about all sorts of issues, and those conversations always end

with a smile. **Ping**, it's amazing to see how you can balance research and motherhood so well. I wish you and Zhilan brightest future. **Xiangyang**, it's impressive how broad your interest is, I expect to see a painting of miumiu from you soon. **Jan** and **Eric**, the new and old social managers, thanks for all the effort you put into to cheer up the group. **Lei** and **Juan**, you are such a sweet couple, and I wish you both carrying a big smile everyday. **Cristhian**, I appreciate your strong interest in my research topic and the sincere attitude you have, all the best in Germany. **Anna**, **Job**, **Arjan**, **Madhu**, thank you guys for bring extra joy to the great group. Of course, all this cannot be maintained without the support from **Anna McEwan**, **Feitze**, **Johan**, **Tom Schouten**, **Hans**, **Herman**, **Arjun**, and **Martijn**, thank you so much. **Martijn**, my gratitude for you also include beer supports. All the best in Norway.

I intentionally skipped two important ones, my dear paranymphs Carmem and Dennis. Thank you for taking this challenging task. **Carmem**, you were my student, but I would learn just as much from you as you did from me. That year was probably the most frustrating time of my PhD, but your presence made it so much easier and happier. Thanks enormously for that. Of course, thank you for all the moments thereafter, for all the good laughs and complaints we shared. **Dennis**, thank you for translating my summary into Dutch and carrying a lamp over hundreds of kilometers for me. Technically you were also my student, the one that stood out immediately. I'm so glad and grateful that you chose to share an office with me and affected me with your frankness and optimism.

Then there are my nano buddies. Two years of fighting together gave us such a strong bond, which I truly cherish. I'm so grateful that we all decided to do PhD in Groningen. **Jing**, my dear officemate, you brought so much happiness to me, and I'm so happy you now found something that suits you better. **Arijit**, **Geert**, we all ended up in FND and became great neighbours. **Arijit**, thanks for taking up my jokes well. **Geert**, thanks for the social events we organized together and the thorough political discussions. **Wytse**, **Henrieke**, thanks for our collaboration attempts. **Sasha**, it was great discussing about teaching with you. **Tenzin**, **Xinkai**, thank you for the continued scientific and casual discussions throughout the PhD years. **Yuchen**, thank you for always being the Master Chef. **Azadeh**, **Dima**, **Natasha**, **Hendrik**, thank you all for the amazing memories together. **Azadeh**, I admire how brave you are, stay strong and all the best.

There are many other great people outside FND that I have enjoyed so much great time with. **Zahra**, you are such a sweet and lovely person. I've always enjoyed the time we spent together, no matter it's a deep philosophical discussion (which you are so bad at) or a cozy gossip session with a fine glass of wine (which you are

so good at). I admire your espresso-making and gardening skills. I'm so grateful that you take my bad jokes well and can always return an equally bad one. Thank you for being there. **Alessio**, my snooker buddy, concerto host, secret trip crew, thank you so much for always being the cool dude and for bringing so much fun. Those memories will never fade. **Désirée, Alberto, Vincent**, my memories of that Peruvian trip and many Groningen night-outs are still so vivid, I loved every minute of your company. Désirée, a special thanks to your never-ending bubbling energy, which cheers me up all the time.

Steven, Ahmed, Diana, Morten, Els, Kiran, that Gopher board year together was such a great experience, thank you all for that. Els, a special thanks for finding me a beautiful apartment and for the many beer events. Ahmed, I always enjoyed our conversations and golf practices. Let's keep that up. **Ante, Elwin, Markus, Lisa K, Esther, Antonija, Daniela M, Estefanía, Maik, Joana, Paolo, Monique**, without your constant support, those Gopher events would have failed so badly. Estefanía, it's always nice chatting with you, all the best with your teaching career. **Cassia, Lisa, Eric C**, our international dinners must continue on, those evenings are always so much fun. **Musty, Solmaz, Aga, Jhonatan, Anne-Claire, Isa**, the PhD day organisation was also such a challenging but great memory, thank you all for sharing this together.

Jin, thank you so much for always being my great life-choice advisor and an excellent chef and host. Our paths have overlapped so much, and now you are defending your PhD one week before me, all the best with that and with everything thereafter. **Yanxi and Qihong**, thank you for the priceless time that we enjoyed great laughter together by making fun of each other, all the best with moving on in your life on opposite sides of the world. **Jingjin, Yingfen**, it was always fun when you guys were around. Yingfen, I still miss that tasty egg dishes you made.

Marina, you are the first person I met in Groningen, and my best photography model. I enjoyed every minute that you were around, especially when we celebrated our birthdays together. **Nicky**, thanks for always bringing me the coolest technology updates and the Hema theme tune whistling. Wish you two all the best together. **Daniela**, I still remember us practicing broken Dutch together. I'm so thankful having met you during my first days in Groningen, and so happy that our friendship could last even after you moved away for so long. **Sander**, thank you for being a great housemate, those off-shore stories were always cool to hear. **Ziyuan**, thank you for offering me shelter and for the deep discussions on life and society. Wish you well in Shenzhen. **Qianli, Chuangxin**, my old mates, thanks for hosting me in Toronto. You always have a roof wherever I am. **Haotian, Jinhao, Zemin**, we are almost brothers, those old good memories will never die, right?

Now, my fantastic four, or as my mom puts it, the 'gang of four'. We've had so

many memories together, in so many places around the world. If I can predict one thing about the future, it's that our friendship will never end. **Sonia**, you appeared since my first day in Groningen, and somehow got stuck around. That completely changed my life and I appreciate it immensely. You are my teacher in European culture, my library studying pal, my fashion advisor, my travel agent, my (absolutely best) project manager, my driver, and that list goes on and on. You are definitely not just 'slightly above average'. You made my life in Europe so much more enjoyable, and even got me a whole Spanish family. I don't think my vocabulary contains any word that could even remotely express my thankfulness to you, so just let me say it in a simple way, thank you so much! **Irene**, you are such a wonderful person despite having an obsession with chicken nuggets. I love it how you can be so cheerful in one second and super stressed in the next. We've shared so much together that even when I was moving, half of the stuff were yours, and I'm sure there are a lot more to come. Thank you for always being in those precious moments. Oh, also thank you for getting me my youngest Instagram followers yet. I'm really proud and happy for how brave and positive you are, and I'm sure you will accomplish great things both in research and in life. **Ryan**, man, you've been such a great housemate (for almost never being there), and such a great host (for never showing me around Denver despite I passed by twice). But hey, who cares. After so many years of sharing the same roof we are still close friends, that says enough. For real, I really appreciate the time we shared, especially that almost-dying hike in Germany. I'm always impressed by your enthusiasm towards work and I have learned a lot from you. I'm sure your career will be a great success too. Oh, and I won't laugh at you for spending so much time on your PhD thesis any more, I promise.

Finally, my dear parents. Any glossy word becomes pale in front of the unconditional love and support you gave me. You've always encouraged me to make my own decisions, even if that would mean me leaving home to study in another city at the age of 16. I know that decision was a tough one for you, but that experience was the key to where I am today. **Mom**, you've always been the strict one, teaching me about discipline and goal of life. You've also always been the caring one, reminding me to put on an extra jacket and treat myself well. Thank you for all the love and care. **Dad**, you've always respected my opinions and decisions, giving me access to the things and knowledge I wanted, and allowing me to freely explore. Thank you for all the trust and support. Mom and Dad, it was your love, care, trust, and support that shaped me, and I'm so proud of that. I love you so deeply, eternally.

Xu Yang
Warsaw, Poland
August 6, 2020

List of publications

1. **A symmetry perspective of chirality, spin, and chirality-induced spin selectivity**

Xu Yang, Bart J. van Wees & Caspar H. van der Wal
in preparation

2. **Highly anisotropic and nonreciprocal charge transport in chiral van der Waals Tellurium**

Xu Yang, Talieh S. Ghiasi, Jamo Momand, Peide D. Ye, Bart J. Kooi, Caspar H. van der Wal & Bart J. van Wees
in preparation

3. **Enhancing and rectifying electron transport through a biomolecular junction comprising Photosystem I and graphene**

Xu Yang, Tom Bosma, Elias B. P. Brul, Andreas Kunzendorf, Pavlo I. Gordichuk, Andreas Herrmann, Bart J. van Wees & Caspar H. van der Wal
in preparation

4. **Detecting chirality in two-terminal electronic nanodevices**

Xu Yang, Caspar H. van der Wal & Bart J. van Wees
Nano Letters **20**, 6148 (2020) [DOI: 10.1021/acs.nanolett.0c02417]

5. **Reply to “Comment on ‘Spin-dependent electron transmission model for chiral molecules in mesoscopic devices’ ”**

Xu Yang, Caspar H. van der Wal & Bart J. van Wees

Phys. Rev. B **101**, 026404 (2020) [DOI: 10.1103/PhysRevB.101.026404]

6. Circuit-model analysis for spintronic devices with chiral molecules as spin injectors

Xu Yang, Tom Bosma, Bart J. van Wees & Caspar H. van der Wal

Phys. Rev. B **99**, 214428 (2019) [DOI: 10.1103/PhysRevB.99.214428]

7. Spin-dependent electron transmission model for chiral molecules in mesoscopic devices]

Xu Yang, Caspar H. van der Wal & Bart J. van Wees

Phys. Rev. B **99**, 024418 (2019) [DOI: 10.1103/PhysRevB.99.024418]

Editors' suggestion

Curriculum Vitae

杨旭
Yang, Xu

26 November 1990 Born in Baiyin, Gansu, China

Education

- 09/2015 - 09/2019 Ph.D. research in the group Physics of Nanodevices
Zernike Institute for Advanced Materials, University of
Groningen, the Netherlands
Promoters: Prof. C.H. van der Wal and Prof. B.J. van Wees
This thesis
- 09/2013 - 07/2015 M.Sc. Nanoscience (Topmaster)
University of Groningen, the Netherlands
Thesis: *"Controlling optical interactions with divacancy spin ensembles in silicon carbide – towards a quantum memory"*
- 09/2009 - 06/2013 B.Sc. Applied Physics
University of Science and Technology of China, Hefei, China
Thesis: *"Compact-designed interferometer for laser plasma diagnostics"*
- 09/2006 - 07/2009 The High School Attached to Northwest Normal University,
Lanzhou, China